**Max-Planck-Institut für Metallforschung**
Stuttgart

# Towards Spin Injection into Silicon

**Saroj Prasad Dash**

Dissertation
an der
**Universität Stuttgart**

Bericht Nr. 203
August 2007

# Towards Spin Injection into Silicon

von der Fakultät Mathematik und Physik der Universität Stuttgart

zur Erlangung der Würde eines Doktors der

Naturwissenschaften (Dr. rer. nat.) genehmigte Abhandlung

vorgelegt von


# Saroj Prasad Dash

aus Bhubaneswar/Indien


| | |
|---|---|
| Hauptberichter: | Prof. Dr. H. D. Carstanjen |
| Mitberichter: | Prof. Dr. G. Denninger |
| Mitprüfer: | Prof. Dr. G. Mahler |

| | |
|---|---|
| Tag der Einreichung: | 16.05.2007 |
| Tag der mündlichen Prüfung: | 09.08.2007 |


**MAX-PLANCK-INSTITUT FÜR METALLFORSCHUNG, STUTTGART**

Stuttgart 2007

***… Dedicated to my family***
***and***
***teachers …***

# Contents

# Chapter 1

# Introduction

## 1.1 Motivation

Since the invention of the transistor, the conventional way of improving the functionality of electrical circuits remained the traditional downscaling of device dimensions, following Moore's prediction [1.1]. However, in near future the existing device architectures as well as the material properties will reach their fundamental limitations for downscaling. The ‘red brick wall’ defined by the Semiconductor Industry Association (SIA) and the International Technology Roadmap for Semiconductors (ITRS) indicates the point at which there is no known solution for most of the technical difficulties, and a research breakthrough is needed. Yet scientists believe that we are being offered an unprecedented opportunity to define a radically new class of devices that would exploit the idiosyncrasies of the quantum world to provide unique advantages over the existing technologies, having thus far relied on purely charge-based devices.

One such idiosyncrasy is a quantum property of the electron known as spin [1.2]. Devices that rely on the electron spin to perform their functions is the foundation of spintronics (spin-electronics). The electron spin is either +1/2 or -1/2: in other words, an electron can rotate either clockwise or anticlockwise around its own axis with constant frequency. The two possible spin states naturally represent the "0" and "1" states in logical operations. The ability to exploit this spin in semiconductors promises new logic devices with enhanced functionality, higher speed and reduced power consumption - and might spark off a revolution in semiconductor industry [1.3]. Such a spin transistor topped the hype cycle for emerging technology in 2005 and is expected to come to productivity after 10 years.

The first semiconductor-based device utilizing the electron spin in order to change its electrical properties was proposed in 1990 as an 'electronics analogue of the electro-optic modulator' [1.4]. In its functionality it resembles both the conventional FET transistor and the GMR device. It consists of two ferromagnetic contacts on both sides of a 2-dimensional electron gas (2DEG), separated over a distance $L < l_{sf}$, where $l_{sf}$ is the spin flip length in a 2DEG (see Fig. 1.1). Under the application of an electrical bias, depending on the relative magnetization and character of the density of states in the left and right ferromagnetic (FM) metals, the spin polarized electrons originating from the first ferromagnetic metal (FM 1) can be either accepted or rejected by the second one (FM 2), resulting in a high or low magnetoresistance, respectively. Moreover, the traditional gating of the channel allows additional control over the carrier concentration and also the spin precession in the channel.

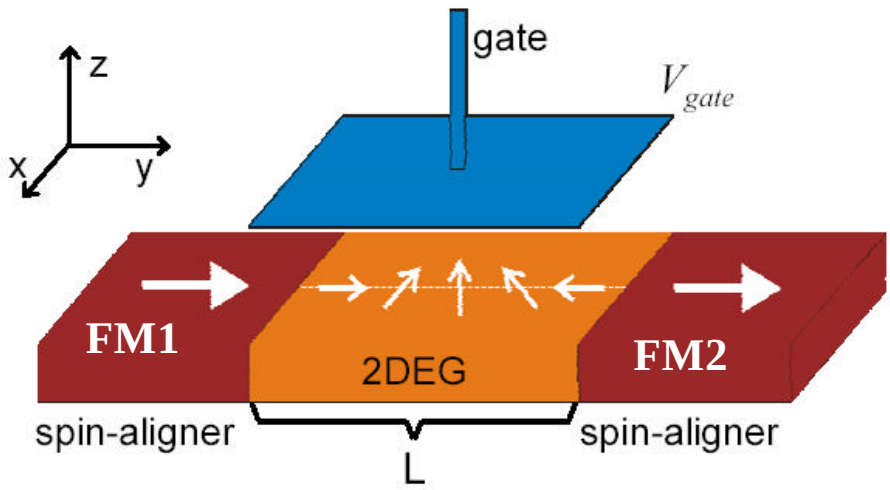


Fig. 1.1: Spin-FET structure, in which spin polarized electrons are injected from FM1 (source) and collected by FM 2 (drain) depending upon the relative magnetization of both FMs. The gate voltage can manipulate the spin and hence the spin polarized carrier concentration [1.4].

Unfortunately, preliminary experiments have shown that electrical spin injection and detection in semiconductors from a ferromagnetic metal in direct electrical contact is not a trivial task. Until very recently, only, one of the fabricated devices, for electrical injection and detection of spin polarized electrons on the ferromagnetic metal/semiconductor interface have been able to show clear spin injection effects [1.5, 1.6]. Some of the claimed results of spin injection effects were attributed to stray Hall effect and scientists were not able to separate out the spin injection signal, which was very small [1.7]. In 2000, the theoretical analysis of spin injection began to catch up with the experimental work. Schmidt and co-workers proposed

that the conductivity mismatch between the ferromagnetic metal and the semiconductor was the fundamental obstacle for the detection of spin injection into a semiconductor in the diffusive regime [1.8]. Rashba *et al.* picked up where Schmidt *et al.* finished, by proposing a solution to the problem of the conductivity mismatch by replacing the direct metal semiconductor diffusive contact by an artificial resistance, a metal-insulator-semiconductor contact or a metal-semiconductor Schottky contact [1.9]. The tunnel contact has the ability to support the considerable difference in electrochemical potential under the conditions of slow spin relaxation and allows for efficient spin injection. But until very recently, nobody was able to detect spin polarized electrons in semiconductors by electrical means [1.6]. The electrical signal received from the detector is believed to be overshadowed by various spurious effects like anomalous magnetoresistance (AMR) and stray Hall effects [1.7].

However, the well known correlation between the spin polarization of injected electrons and the polarization of the emitted light provide a unique opportunity for the optical investigation of electrical spin injection into semiconductors in a light emitting diode (Spin LED) type heterostructure across a single ferromagnet / semiconductor interface [1.10]. In parallel to Rashba's theoretical effort, Zhu *et al.* were able to show a spin injection effect of 2 % in a spin LED structure with a Fe-GaAs Schottky contact [1.11]. The spin injection efficiency was low in this case, but later on Hanbicki *et al*. were able to show spin injection efficiencies up to 32 % by tailoring the Schottky barrier into a tunnel barrier with a heavily doped GaAs surface layer [1.12]. A spin injection effect of 20% was also observed with an $AlO_x$ tunnel barrier in between CoFe and GaAs [1.13]. The highest spin injection efficiency (~ 50 %) was observed in Feb-2005 by the IBM spintronics group taking advantage of coherent tunneling of spin-polarized electrons from CoFe through a single crystalline MgO tunnel barrier in a GaAs LED structure [1.14]. In parallel to this spin injection could also be successfully realized using diluted magnetic semiconductors (DMS) as spin aligners [1.15]. These DMS also overcome the conductivity mismatch problem (observed in the case of ferromagnetic metal / semiconductor heterostructures) by ensuring that the resistivity of the materials on both sides of the interface are comparable in magnitude. All these results were obtained by using LED structures in the detector geometry. Although optical methods have been used to reveal much of the underlying physics of spin dynamics and transport in direct band gap semiconductors, electrical spin detection remained a significant problem, also for direct band gap semiconductors. Recent progress using the epitaxial Fe/GaAs for non-local detection of spin diffusion with voltage sensing is encouraging [1.6]. In Feb-2007 the authors observed a clear spin valve signal at 50 K and the spin injection efficiency was found to be

around 2 %. By this non-local measurement, they could avoid all spurious effects like anisotropic magnetoresistance and Hall effect [1.6].

## 1.2 Subject of this thesis

Silicon would be ideally suited for spin electronics applications because of its promising attributes suggesting a long spin life time: Zero nuclear spin for the most abundant isotope $Si^{28}$, crystal lattice inversion symmetry maintaining spin-degenerate bands, and low spin orbit interaction [1.16]. The latter is due to the inversion symmetry of the diamond lattice, which drastically reduces spin orbit coupling. The spin lifetime in Si exceeds those in zinc blend III-V semiconductors by many orders of magnitude. Due to the presence of low spin orbit coupling in Si, the manipulation of spin polarized electrons and its precession can not be achieved by application of a perpendicular electric field (so called Rashba effect). However, the electrons can be made to precess by application of a small perpendicular magnetic field. A realization of spin injection into Si would not only reduce the constraints for devices in terms of critical dimensions or temperatures, but also enhance the probability of a short time to market. Compared to the III-V or II-VI semiconductors, much less effort has been devoted to spin injection into Si. The reason is its indirect band gap structure, which precludes optical detection of spin injection. This is not a major draw back, since electrical detection can be readily used in silicon through a spin collector electrode in a non-local geometry and a proper design of magnetic contacts to exclude spurious effects like stray Hall effect and anomalous magnetoresistance. This concept has already been realized in case of spin injection into metallic systems (Al and Cu) from Co electrodes [1.17, 1.18] and, most recently, into GaAs from Fe electrodes in a tailored Schottky contact [1.6]. As understood, the spin injection can be done using three concepts: (i) spin injection through a Schottky contact, (ii) spin injection through a tunnel barrier, and (iii) spin injection using diluted magnetic semiconductors (DMS) as spin aligner.

Taking into account the large spin coherence length in silicon and its technological importance, I started my work with the aim to achieve electrical injection and detection of spin polarized electrons in Si. In this thesis, three different concepts of spin injection into Si are studied: ***(i) spin injection through a ferromagnet-Si Schottky contact, (ii) Spin injection using a MgO tunnel barrier in between the ferromagnet and Si, and (iii) spin injection using Mn doped Si (DMS) as spin aligner.***

## 1.3 Outline of this thesis

After this introduction, fundamental aspects of spin injection into semiconductors, which are important in the context of this work, are reported in ***chapter 2***. Furthermore, different problems and their solutions that arise in spin injection experiments are addressed.

In ***chapter 3***, the more uncommon experimental techniques and experimental set-ups used in this thesis are described.

As a first step of the experimental work of this thesis, ferromagnet-Si interfaces, which are important for spin injection through a **Schottky contact**, are investigated in ***chapter 4 and 5***. Most theoretical treatment begins by assuming an ordered interface, so that the electron momentum parallel to the interface plane is conserved. Real ferromagnetic metal-Si interfaces are, however, very complicated and their properties strongly depend on the preparation of the semiconductor surface and interface reactions. The technologically important materials Co and Fe grown by MBE on a clean Si (100) surface are considered. If a small amount of Co or Fe (~ $10^{20}$ $cm^{-3}$) diffuses into the Si, each such Co or Fe atom will be likely to carry a local magnetic moment, oriented randomly with respect to the magnetization direction, and will scatter electrons between the two different spin channels, thereby degrading the injected spin polarization. Also from another point of view it is important to know whether Co and Fe diffuse into silicon: if it is energetically preferable to do so, it is not possible to prevent it, but if it is due to the growth process, one could change it if necessary. The real challenge in this research would be to find a magnetically sharp Co-Si and Fe-Si interface.

Therefore, structure, interface and magnetism of MBE-grown Co and Fe thin films on clean Si (100) were studied. The results of these studies are presented in ***chapters 4***. From the results of these studies it will be clear that there is strong intermixing at the interface, which is fatal for spin injection experiments. In order to understand the processes going on at the interface in atomic detail, Co and Fe thin films on Si (100) were investigated at very initial stages of growth by high-resolution RBS (HRBS) and presented in ***chapter 4***. The knowledge gained from these experiments was helpful to improve the interface quality. In ***chapter 5*** the *non equilibrium ways* to suppress the silicide formation at the interface, such as (i) low temperature growth and (ii) surfactant mediated growth are reported. In this way the silicide formation at the interface can be minimized but could not be stopped completely. So Schottky contacts apparently should not be used for spin injection into Si.

In order to circumvent the problem of the Schottky contact, a **MgO tunnel barrier** between the FM and Si is used in a second step. The tunnel barrier has three advantages: (i) It

forms a chemical barrier between the FM and the Si, (ii) it is a good spin-selective tunnel resistance, and (iii) a tunnel barrier can be formed at both injector and detector ends. In ***chapter 6*** the ways how to fabricate ultra thin (~ 2nm) crystalline tunnel barriers with a sharp interface on Si (100) and results of these experiments are presented. A spin injection and detection device using such a tunnel barrier on Si is also proposed.

In a third part of the thesis, a new material system is explored by doping Si with Mn. This **diluted magnetic Si** can be very efficiently used as spin injector. Such diluted ferromagnetic semiconductors overcome the conductivity mismatch problem by ensuring that the resistivities of the materials on both sides of the interface are comparable in magnitude. In ***chapter 7*** of this thesis the magnetic and structural properties of Mn doped Si are investigated: (i) by doping Si with Mn by ion implantation and (ii) by doping Si with Mn by solid state diffusion. Very initial stages of growth have also been studied for the case of Mn on Si (100) for a detailed understanding of the involved atomic processes. Mn in Si is a new material system and more detailed investigations are needed before using it for spin injection.

Finally, a brief summary of this work is given in ***chapter 8***.

# Chapter 2

# Spin injection into semiconductors

One of the key problems of spintronics is the development of efficient methods of injection and detection of spin-polarized carriers. Hence, various techniques for spin injection and detection have been adopted, perhaps culminating in the development of diluted magnetic semiconductors as injectors [2.1]. The aim of this chapter is to introduce the field of spin injection and detection in semiconductors.

## 2.1 Ferromagnetism and spin polarization

For the elementary ferromagnetic transition metals Fe, Co and Ni, the 3d-spin sub-bands are shifted with respect to each other ("exchange splitting") due to the presence of the exchange interaction. This exchange splitting of 3d bands gives rise to a finite magnetization in thermodynamic equilibrium [2.2]. The spin-splitting leads to a different density of states in the electronic system and, hence forth, to a different number of spin-up and spin-down electrons at the Fermi level as shown in Fig. 2.1 [2.3].

The spin polarization of electrons at the Fermi level can be defined as

$$P = \frac{N^{\uparrow}(E_f) - N^{\downarrow}(E_f)}{N^{\uparrow}(E_f) + N^{\downarrow}(E_f)} \tag{2.1}$$

Here $N^{\uparrow}(E_f)$ and $N^{\downarrow}(E_f)$ are the densities of states of spin-up and spin-down electrons at the Fermi level, respectively.

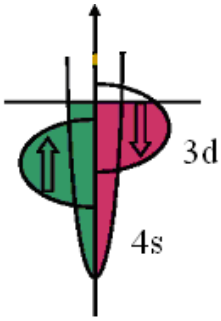


Fig. 2.1: A simplified band structure of ferromagnet showing imbalance in spin-up and spin-down electron density of states at the Fermi level.

### 2.1.1 Spin current

Often one finds the argument that this spin asymmetry in the density of states is the reason for the observed spin current in ferromagnets. But since the current in a solid is the product of density of states and mobility of the charge carriers, also the mobility plays an important role. And, as it turns out, the mobility plays the important role in transition metal ferromagnets [2.3]. As follows from band structure calculations, d-band electrons are more localized and exhibit a larger effective mass than s-electrons. The resulting mobility of s-electrons is so much bigger that mainly itinerant s-electrons carry the electrical current when an electrical bias is applied across such a ferromagnetic metal. Moreover, as the densities of states for spin-up and spin-down electrons in the d-band of ferromagnetic metals differ significantly, the s-electrons in the two spin sub-bands experience different scattering, thus resulting in different mobilities for spin-up and spin-down electrons [2.4]. As a result, the current in ferromagnetic metals is carried by spin polarized s-electrons. The ferromagnetic metal is having different bulk conductivities for spin-up and spin-down electrons:

$$s_{\uparrow,\downarrow} = e^2 N_{\uparrow,\downarrow} D_{\uparrow,\downarrow} \tag{2.2}$$

Here $s_{\uparrow,\downarrow}$ is the spin dependent conductivity, $e$ the electronic charge, $N_{\uparrow,\downarrow}$ the spin dependent DOS, and $D_{\uparrow,\downarrow}$ the spin dependent diffusion constant. The latter is given by $D_{\uparrow,\downarrow}$ = $1/3\, v_{f\uparrow,\downarrow} l_{e\uparrow,\downarrow}$, where $v_{f\uparrow,\downarrow}$ is the spin dependent Fermi velocity and $l_{e\uparrow,\downarrow}$ the spin-dependent electron mean free path.

Due to different conductivities for up-spin and down-spin electrons, Fert and Campbell used the idea of a ‘two-channel model’ [2.5]. This model treats spin-up and spin-down electrons as different families between whom there is rarely any interchange of personnel (i.e. spin-flip scattering) at least on the brief time scale defined by all the other processes in the

system. So the current flow in the ferromagnet for the spin-up and spin-down channels is different.

$$j_{\uparrow,\downarrow} = \frac{s_{\uparrow,\downarrow}}{e}\frac{\partial m_{\uparrow,\downarrow}}{\partial x} \tag{2.3}$$

Here $j_{\uparrow,\downarrow}$ are the spin-up and spin-down current densities, $m_{\uparrow,\downarrow}$ the spin dependent electrochemical potential and $x$ the spatial distance over which the current flows.

### 2.1.2 Spin polarization of current

The spin polarized electrons flow in a ferromagnet due to mobility asymmetry (indirectly due to DOS asymmetry) under biased conditions. The bulk current polarization of a ferromagnetic metal is then defined as

$$a_F = \frac{j_\uparrow - j_\downarrow}{j_\uparrow + j_\downarrow} \tag{2.4}$$

The spin polarization of the current densities in such ferromagnets was measured by Andreev reflection in quantum point contact and found to be 45 % for Fe, 42 % for Co and around 27 % for Ni at room temperature [2.6].

## 2.2 Concepts of spin injection and detection in semiconductors

### 2.2.1 Concept of electrical spin injection into semiconductors

Arnov and Pikus suggested in 1976 that the spin polarization in a ferromagnet can be injected into semiconductors by passage of a current through the ferromagnet/semiconductor interface [2.7]. The diffusion of electrons and their drift in an electric field spread the spin polarization region into the semiconductor. The degree of polarization of electrons in such a flux is governed by their polarization in the ferromagnet. As the conductivities for the spin-up and spin-down electrons in a ferromagnetic metal are unequal, the usual charge current ($I_\uparrow + I_\downarrow$) is accompanied by a spin current ($I_\uparrow - I_\downarrow$).

The spins injected into a semiconductor are maximum (“accumulated”) near the interface. The amount of spin accumulation depends on the net spin injection rate at the interface and the spin-flipping rate in the semiconductor (Fig. 2.2). The spin accumulation decays exponentially away from the interface on a length scale called the ‘spin diffusion length’ [2.8].

The spin diffusion length is defined as $l_{sd} = \sqrt{\frac{v_F t_{\uparrow\downarrow} l}{3}}$ (2.5)

Here $v_F$ is the Fermi velocity, $t_{\uparrow\downarrow}$ the spin-flip time, and $l$ the normal mean free path of electron scattering.

The magnitude of the spin accumulation density $n$ at a distance $x$ from the interface can be written:

$$n = n_0 e^{-\frac{x}{l_{sd}}} \quad (2.6)$$

But the electrical detection of such spin injection into semiconductors came out to be very difficult until recently. The difficulties in the realization and proposed solutions will be discussed extensively in section 2.3 of this chapter.

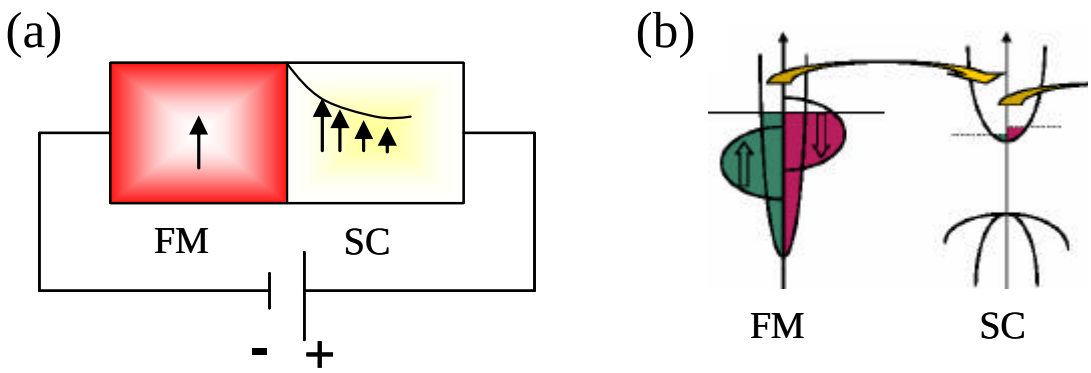


Fig. 2.2: **(a)** Illustration of the spin accumulation and its decay at the ferromagnet/semiconductor interface. **(b)** Band diagram showing the DOS asymmetry in the semiconductor due to spin injection.

### 2.2.2 Importance of crystal orientation on spin injection efficiency

Some of the key factors for spin-polarized carrier injection include interface, band structure, and impurities. Experimental work on spin injection in ZnMnSe/AlGaAs(100) structure showed that interface defects such as stacking faults, limit the spin injection efficiency in diffusive transport, and thus are a potential source of spin scattering [2.9]. Recent theoretical work suggests that matching the symmetry of the transport bands across the spin injecting interface can play a significant role [2.10]. In the ideal limiting case of ballistic transport where *k*-parallel is conserved, these calculations indicate that spin injection from Fe into GaAs is strongly enhanced for Fe/GaAs (100) interface where the transport band symmetries are matched, but suppressed for the Fe/GaAs (110) interface, where the band symmetries are poorly matched. In an experimental effort Li *et al.* examined the role of interface orientation

and band matching on the spin injection process in Fe/AlGaAs/GaAs spin-LED structure [2.11]. The maximum electron spin polarization measured in the (110) spin-LEDs (13%) is less than 1/2 of that obtained in similar (100) structures (32%).

Silicon is a semiconductor with the diamond structure and a lattice constant of 5.43 Å. Between the valence band and conduction band there is an indirect band gap of 1.12 eV at room temperature. In the conduction band of Si there are 6 minima at an energy $E_c$ on the positive and negative *x*, *y* and *z* axes in *k*-space (Fig. 2.3). Spin polarized electrons only with enough energy and with the right momentum can be injected into Si [2.12]. An incoming electron should find a corresponding state in one of the 6 conduction bands in order to be collected. This means that there should be a state with the same parallel momentum as in the ferromagnet. In Fig. 2.3, the 6 band minima in *k*-space are projected on the interface plane for the case of Si (100) and (111). As seen in the figure, only Si (100) has available states at $k_y = 0 = k_z$. If an electron is coming perfectly perpendicular to the interface it needs to go into a state with $k_y = 0 = k_z$ for Si [2.13]. This is only possible in the case of Si (100), but not of Si (111). But as a result of inelastic scattering in the ferromagnetic metal film or at the ferromagnetic metal-semiconductor interface, injected spin polarized electrons even can go to $k_y$, $k_z$ ? 0 states [2.13].

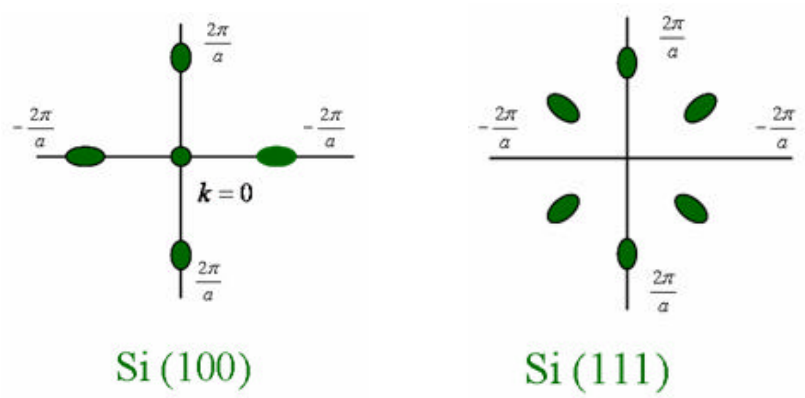


Fig. 2.3: The projection of the 6 band minima in *k*-space for Si (100) and (111). For Si (100), two minima (at $k_x = \pm \frac{2p}{a}$) coincide at $k_y = 0 = k_z$ in this projection.

### 2.2.3 Spin relaxation in semiconductors

The spin accumulation in a semiconductor due to spin injection decays, starting at the interface, because of spin relaxation [2.14]. There are four proposed ways by which conduction electrons of metals and semiconductors relax: (a) The Elliott-Yafet mechanism,

(b) The D'yakonov-Perel' mechanism, (c) The Bir-Aronov-Pikus mechanism, and (d) hyperfine-interaction [2.14].

*Elliot-Yafet (EY) Mechanism:* Elliot first suggested that conduction electron spin relaxation occurs via momentum scattering by phonons or non-magnetic impurities. Momentum scattering occurs when lattice ions or phonons bring on spin-orbital coupling in the electron wave function. This spin-orbital coupling introduces wave functions of opposite spin. EY mechanism is based on the fact that in real crystals, Bloch state are not spin eigen states since the lattice-ion-induced spin-orbit interaction mixes the spin-up and spin-down states. These combinations of spin-up and spin-down momentum lead to relaxation of electron spin. The mechanism is dominant in small-gap semiconductors with large spin-orbit splitting [2.14].

*D'yakonove-Perel' (DP) Mechanism***:** This mechanism comes into play, when the systems lack inversion symmetry in its crystal structure [2.14]. Absence of inversion symmetry leads to spin splitting of the conduction band for $k$ ? 0, i.e. spin–up and spin-down electrons even having the same momentum state, have different energies. This splitting is equivalent to the presence of an effective magnetic field around which electron spins precess with Larmor frequency. The interaction of the electron spin with this internal magnetic field causes flipping of the electron spin. This mechanism plays an important role with the increase in temperature and the increase of the band gap [2.14].

*Bir-Aronov-Pikus (BAP) Mechanism:* The holes also possess spin [2.15]. The spin of a hole can exchange with that of conduction electrons. These exchanges proceed through scattering and lead to spin relaxation of conduction electrons in p-doped semiconductors [2.14, 2.15]. Holes have shorter spin coherence times, and spin exchange between electrons and holes is very effective. Ultimately, it will lead to spin decoherence. This mechanism is of importance at low temperatures [2.14].

*Hyperfine-interaction Mechanism*: Hyperfine-interaction comes from the magnetic interaction between the magnetic momentum of nuclei and electrons. In semiconductor heterostructures, this mechanism is responsible for spin dephasing of localized or confined electron spins [2.14, 2.15].

GaAs has no inversion symmetry in its lattice structure; hence the DP mechanism is the main mechanism for spin dephasing in GaAs. Silicon, however, has inversion symmetry

and as a result, the DP mechanism is absent. In n-type semiconductors, the holes rapidly recombine with the high number of electrons, and the BAP mechanism is not valid for this. In the case of p-type semiconductors and intrinsic semiconductors the BAP mechanism becomes important. Hence, in lightly doped and n-Si, the EY mechanism should dominate [2.14].

### 2.2.4 Concepts of electrical spin detection in semiconductors

The first semiconductor-based device utilizing the electron spin for changing its electrical properties was proposed in 1990 as an 'electronics analogue of the electro-optic modulator' [2.16]. In its functionality it resembles both the conventional FET transistor and the GMR device. This device consists of two ferromagnetic contacts, separated by a semiconductor channel (over a distance $L < l_{sf}$, where $l_{sf}$ is spin flip length in the semiconductor) and a gate electrode that controls electric field in a conduction channel in the semiconductor [see Fig. 2.4 (a)].

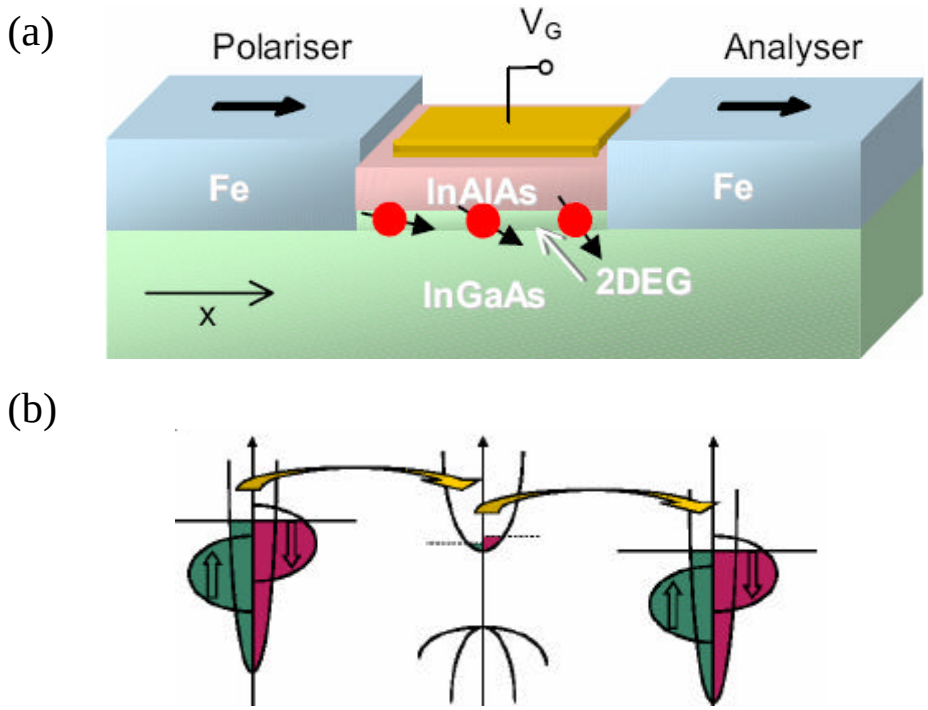


Fig. 2.4: **(a)** Spin-FET structure, in which spin polarized electrons are injected from the polarizer (FM1) and collected by the analyzer (FM2), depending upon the relative magnetization of both the FMs. The gate voltage can manipulate the spin and, hence, the spin-polarized carrier concentration. **(b)** Parallel configuration: Spin up electrons injected from FM 1 across the semiconductor encounter a large number of unoccupied states in the spin up band of the FM 2, giving rise to high conductance. A simplified band diagram is shown here.

One electrode acts as a polarizer, the other as analyzer (similar to source and drain of a field effect transistor). The polarizer emits electrons with their spins oriented along the direction of the electrode's magnetization, while the analyzer (with the same electrode magnetization) acts as a spin filter and accepts electrons with the same spin preferentially. In the "conduction" channel, the gate electrode produces a field that forces the electron spins to preces, just like the precession of a spinning top under the force of gravity (Rashba effect, due to large spin orbit coupling). The electron current is then modulated by the degree of precession of the electron spin introduced by the gate field: The passage of an electron through the analyzer is more preferable for the spin of the electron parallel to the magnetization direction of the analyzer than for the anti-parallel case.

This Datta-Das effect should be most visible for narrow band-gap semiconductors such as InGaAs, which have relatively large spin-orbit interactions (that is, a electric field introduced by the gate voltage has a relatively large effect on the electron spin). Despite several years of effort, however, the effect has yet to be convincingly demonstrated experimentally.

In the materials like Si and GaAs, where the spin orbit coupling is very weak, such a manipulation of the spin direction is not possible by the application of an electric field. However the electrons can be accepted or rejected by changing the magnetization of the two ferromagnetic electrodes. When both the ferromagnetic electrodes are parallel, the injected electrons can be accepted, giving rise to low resistance. For antiparallel alignment of both ferromagnetic electrodes, the electrons will not find available states and, hence, the electrons will be rejected giving rise to high resistance across the device. However, due to fundamental problems in detection of such spin injection, electrical spin transport properties could not be demonstrated convincingly. In the next section the origin of such problems and proposed solutions to circumvent the problem will discussed.

## 2.3 Fundamental problems in spin injection and detection in semiconductors

### 2.3.1 Problems in electrical detection *(conventional geometry)*

The simplest detection device for spin polarization would be the classical spin valve [Fig. 2.5 (a)]. In this device the spin polarized electrons are injected from the first ferromagnetic electrode (FM1) into the semiconductor and are detected at the (second electrode second

ferromagnetic electrode, FM2). For parallel magnetization of the two FM electrodes the injected spin polarized electrons face a low resistance and for antiparallel alignment of the two electrodes a high resistance. The change in the voltage drop across the device structure for parallel and antiparallel alignment of the two ferromagnetic electrodes should in principle give the value of spin injection.

The first experimental attempt to fabricate and investigate electrical spin injection into semiconductors was made by Hammar *et al.* [2.17]. They used NiFe as ferromagnetic contact with an InAs 2DEG. Ferromagnetic metals form Ohmic contacts with InAs due to the presence of a large number of surface states. The changes in resistance amounted to 0.8 %. They were obtained by changing the relative magnetization of the two ferromagnetic contacts. The interpretation of these electrical spin transport measurements was complicated because of *anisotropic magnetoresistance* in the electrodes, local *Hall effects* and other extrinsic contributions to the signal [2.18]. These spurious effects give rise to a large background resistance as compared to the spin valve resistance in conventional geometry.

### 2.3.2 Solution of the electrical detection problem: *non-local geometry*

***(Separation of charge and spin current)***

A second geometry, which is referred to as the non-local geometry, was invented by Johnson in 1985 for the case of spin injection into Al [2.19]. It is shown in Fig. 2.5(b). Such a non local measurement avoids spurious effects like magnetoresistance of ferromagnetic electrodes and stray Hall effect by placing a spin detection electrode outside the path of the charge current. In this geometry spin polarized electrons are injected from the first ferromagnetic electrode (FM 1) into the semiconductor (SC) and will flow to contact 1. The injected spin current causes a stationary spin accumulation in the semiconductor and the densities of the spin-up and spin-down electrons in the SC become unequal. This imbalance in spin population in the semiconductor diffuses in either way and will extend over a characteristic spatial length given by the spin flip length. If the second ferromagnet (FM 2) is lying within the spin diffusion length in the semiconductor (from FM 1), it can detect a voltage which is due to spin imbalance in the semiconductor which persists up to the FM 2. For different magnetization directions of the two ferromagnetic electrodes a change in voltage can be measured. The contact 2 should be placed far away; beyond the spin diffusion length in the semiconductor. Following this non-local measurement geometry, the electrical spin injection and detection has been successfully demonstrated in metallic systems and, most recently, it is

realized for the case of semiconductors (GaAs) [2.20, 2.21]. But the realization of such a structure with Si has remained a challenge.

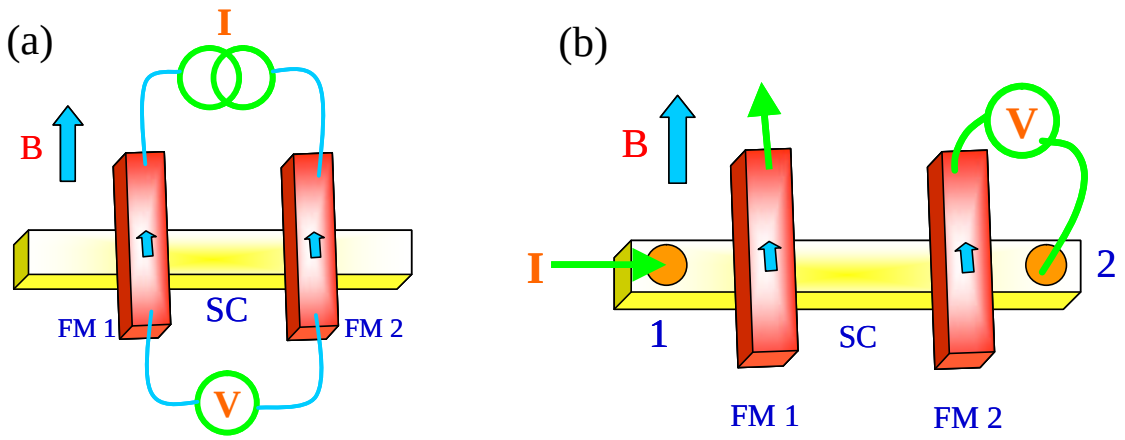


Fig. 2.5: **(a)** Conventional geometry for spin valve structure. **(b)** Non-local geometry for the spin valve structure. FM 1 and FM 2 are two ferromagnetic electrodes and SC is the semiconductor channel.

### 2.3.3 Problems in spin injection with Ohmic contact

Attempts to repeat this experiment, taking special care for the elimination of the different side effects, were performed by different groups. In these experiments devices with different ferromagnetic contacts (Co, Ni, NiFe) on InAs 2DEG, which give rise to Ohmic contacts, were fabricated [2.22]. Measurements in so called non-local geometry [Fig 2.5(b)], where there is no electrical current in the second detecting ferromagnetic metal and, hence, no major side effects, could not reveal any signal which could be attributed to spin polarized transport in any single one of these devices [2.22]. However fabricating and measuring a pure spin valve effect remained a challenge for a long period of time. Even the failure of detecting any spin valve signal in non-local geometry raised the doubt about spin injection in an Ohmic contact.

It was found that the injected spin polarized electrons could not be detected experimentally in a semiconductor (SC) with Ohmic contact (*diffusive regime)* due to the large difference in the band structure and the large conductivity mismatch between the FM and the SC. In the experiments done on these systems, a current flow from FM1 into the SC channel and a change in voltage due to a stationary spin accumulation were measured between FM2 and the SC. In a FM there is a spin dependent resistance (the voltage drops for up and down spin electrons are different), but in a SC the resistances for spin up and spin down

electrons are the same. So what one measures effectively is the voltage difference between up and down spin electrons in the FM, which is very small and could not be detected. That's why no spin accumulation voltage could be measured in the *diffusive regime*. This problem is known as the conductivity mismatch problem [2.23].

### 2.3.4 Solutions for efficient spin injection

It was proposed that the conductivity mismatch problem can be circumvented if the resistance of the spin-selective interface resistance dominates, for example by insertion of a spin dependent tunnel barrier between the FM and the SC [2.24]. The large and spin-dependent resistance of the tunnel barrier will give rise to a measurable voltage drop across the device due to non-equilibrium spin accumulation in the SC. This fact is explained in Fig. 2.6 based on the two-spin channel model in FMs.

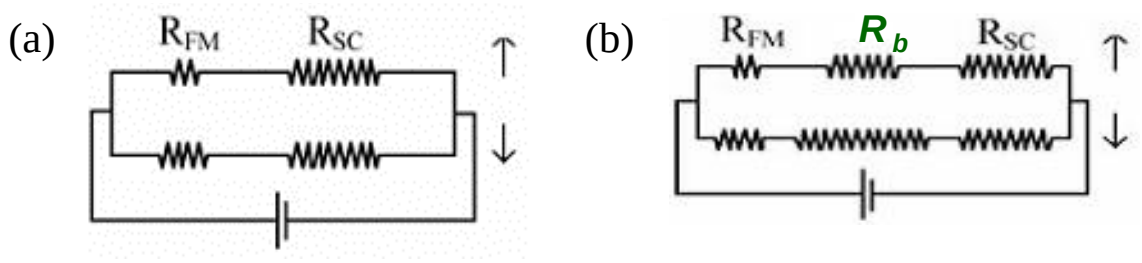


Fig. 2.6: **(a)** Spin injection in the diffusive regime: The voltage difference between up and down spin electrons (indicated by arrows) in a FM is very small and could not be measured. **(b)** Spin injection through a tunnel barrier: The large spin-dependent resistance of the tunnel barrier will give rise to a measurable voltage drop across the device.

The proposed solutions for measurable spin injection are using *i)* a *Schottky contact* in the tunnelling regime or ii) a *tunnel barrier* between the FM and the SC. The third concept consists in using iii) a *diluted magnetic semiconductor* (DMS) as injector, which has almost the same resistance as the semiconductor. Hence, no conductivity mismatch problem arises.

### 2.3.5 Failure of detecting spin injection by electrical means

Measurements by Hammar *et al*. of spin injection by using a tunnel barrier in non-local geometry have not observed a clear spin valve signal [2.25]. Also fabricating a device for measurements in non-local geometry on semiconductors remained a difficult task. A number of issues have been defined for a non-local spin injection device.

(i) *Spin dependent interface resistance*: A quality tunnel barrier with atomically sharp interfaces with the ferromagnetic metal injector and the semiconductor is important for efficient spin injection. Schottky barriers can also act as effective tunnel barriers by heavily doping the semiconductor surface layer.
(ii) *Channel length*: Coherently polarized electrons injected from a source at $x = 0$ lose their net polarization via spin flipping processes. For diffusive (ballistic) transport, the distance between source and drain must be less than the spin-diffusion length.
(iii) *High signal-to-noise ratio*: The effects due to spin polarization (spin valve effect) may be much smaller than the background voltages associated with the charge transport. A geometry (non-local) that can minimize the background is highly advantageous.

## 2.4 Optical detection of spin injection

Unfortunately, the preliminary experiments have shown that electrical spin injection into a semiconductor in a direct electrical contact is not a trivial task [2.25]. GaAs and other III-V semiconductors are already known for their ability to efficiently convert angular momentum of light into electron spin and vice versa. Further, as there is a known correlation between spin polarization of injected charges and the polarization of the emitted light, they provide a unique opportunity for optical investigation of electrical spin injection into semiconductors. The spin LED utilizes the intrinsic properties of III-V semiconductors to efficiently transfer electron angular momentum into angular momentum of the emitted light. Thus the change in the magnetization state of the ferromagnetic injector provides control over the polarization state of the injected electrons and, hence, over the polarization of the optical output [2.26].

Three concepts of spin injection have been successfully realized by optical detection in a LED structure. Such injection has been demonstrated by analyzing the circular polarization of photons that are generated after recombination of the injected electrons with holes in a quantum-well layer inside the semiconductor.

### 2.4.1 Spin injection through a tailored Schottky barrier

In the case of GaAs there is a natural Schottky barrier with a height $\approx$ 0.5 to 0.8 eV with a FM (Fe, Co, Ni) and a width $\geq 30$ nm for a doping concentration of $N_d \leq 10^{17}$ cm$^{-3}$. The spin injection from the FM into n-GaAs corresponds to a reverse current in the Schottky junction, which is usually negligible due to the large height and width of the depletion region.

Therefore a $n^{++}$-GaAs layer between the FM and the n-GaAs should be used to increase the spin injection current. Hanbiki *et al.* used such a tailored Fe-GaAs Schottky contact (Fig. 2.7) on a LED structure to achieve a spin injection efficiency of ~32 % [2.27].

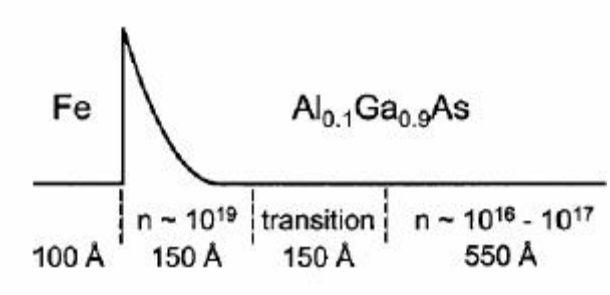


Fig. 2.7: Spin injection from Fe into GaAs through a tailored Schottky barrier [2.27].

## 2.4.2 Spin injection through a tunnel barrier

The 2nd concept is using tunnel barriers like $Al_2O_3$ or MgO in between the ferromagnet and semiconductors [2.28, 2.29]. Using a tunnel barrier has the advantages that it has a good spin-selective resistance and acts as a chemical barrier between ferromagnet and semiconductor. Using an $Al_2O_3$ tunnel barrier, around 20 % spin injection efficiency was detected in a GaAs LED system. The spin-injection efficiency has been improved dramatically by inserting a crystalline MgO tunnel barrier between the ferromagnetic contact and the semiconductor. The authors found a spin polarization of about 50%, which is independent of temperature [2.29]. This value is larger than the spin polarization at the Fermi energy inside the ferromagnetic metal, emphasizing the spin-selective property of the MgO tunnel barrier. The band model of such a tunnel contact for spin injection is shown in Fig. 2.8.

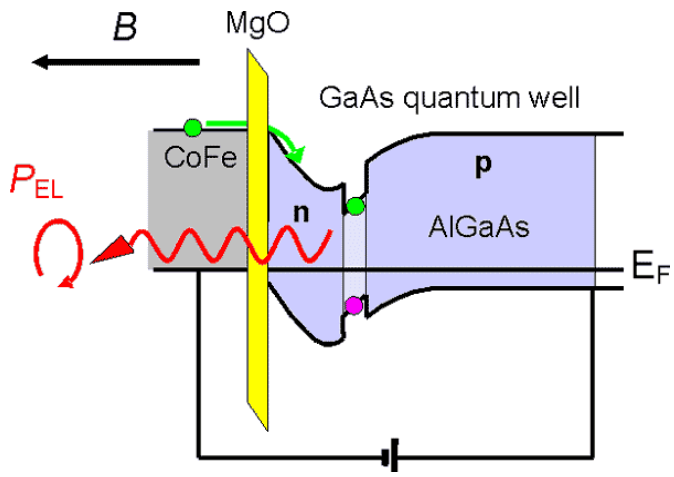


Fig. 2.8: Spin injection from CoFe into GaAs through a MgO tunnel barrier [2.29].

### 2.4.3 Spin injection from diluted magnetic semiconductors

As we have seen above, the problem of the detection of injected spin polarized electrons originates from the conductivity mismatch of the ferromagnetic metal and the semiconductor. One can think of two solutions. One was proposed by Rashba [2.24] to use a tunnel junction, the other is to use a ferromagnetic semiconductor source with almost similar conductivity as the semiconductor. The concept of using a diluted magnetic semiconductor with small amount of Mn ions as spin aligner was pioneered in 1998 and high degrees of spin polarization achieved in this way [2.30]. Spin polarized holes were injected from GaMnAs into the active region of a spin LED (InGaAs/GaAs quantum well). Unpolarized electrons were supplied by the n-type GaAs substrate. Spin polarized holes from GaMnAs and unpolarized electrons from n-GaAs combine in the active region to produce electroluminescence (Fig. 2.9).

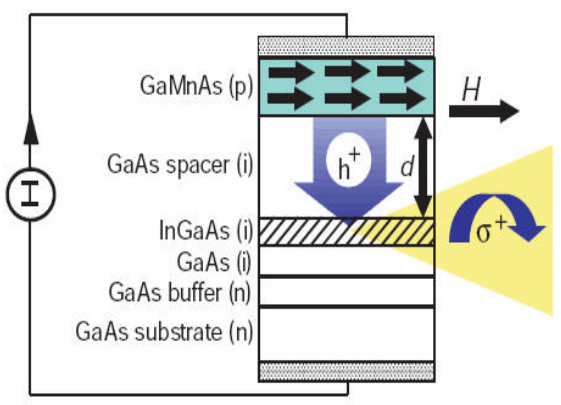


Fig. 2.9: Spin-injection from a diluted magnetic semiconductor (GaMnAs) into GaAs [2.30].

### 2.4.4 The problem with Si

Unfortunately, the optical detection of spin injection is possible only for direct band gap semiconductors. An indirect band gap and a weak spin-orbit coupling preclude conventional optical methods for the detection of spin polarized electrons in Si. The electrical measurement is the only method for the detection of spin injection into Si [2.14]. On the other hand, spintronic devices should not have to rely on optics. A purely electrical method for injecting spin-polarized electrons into semiconductors is needed to guarantee the success of spintronics - and has provided a surprisingly difficult challenge.

## 2.5 Imaging spin injection into a semiconductor through a Schottky contact

Recently Crooker *et al.* directly imaged electrical spin injection and accumulation in GaAs from a Fe electrode [2.31]. The spin polarized electrons were injected through a Fe/GaAs Schottky tunnel barrier and the component of the magnetization perpendicular to the GaAs channel was imaged by scanning Kerr microscopy. Fig. 2.10 shows that injected spins are accumulated near the interface and decay with distance due to spin relaxation in GaAs.

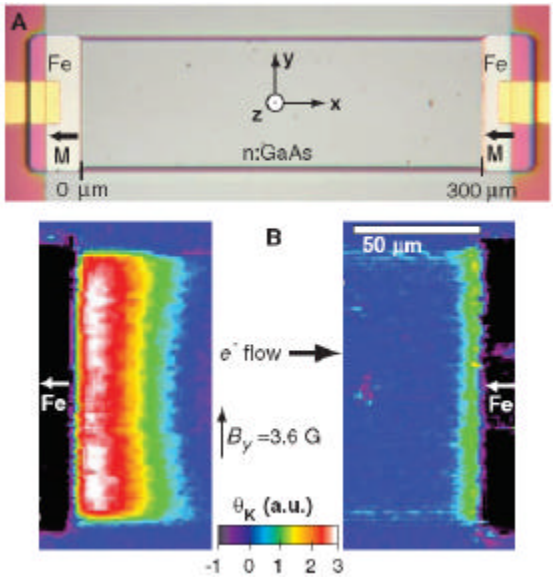


Fig. 2.10: **(a)** Photo-micrograph of the spin injection device. Spin polarized electrons are injected from Fe into GaAs. **(b)** Image of the perpendicular component of spin accumulation in a GaAs channel by a scanning Kerr microscope [2.31].

## 2.6 Successful detection of spin injection by electrical means

As mentioned in the previous sections, the ability to inject, modulate and detect spin polarized carriers electrically is a long-standing goal in semiconductor spintronics. The most recent studies by Lou *et al*. successfully demonstrated the electrical detection of spin injection into GaAs through a tailored Schottky contact using a non-local measurement (shown in Fig. 2.11) [2.21]. Spin polarized electrons were injected from the ferromagnetic Fe contact 3 (injector) through a tunneling Schottky barrier into GaAs.

The injected spin current causes a stationary spin accumulation in GaAs and the densities of the spin-up and spin-down electrons in the GaAs become unequal. This imbalance

in spin population diffuses in either way. The amount of spin imbalance that diffused to the Fe contact 4 (detector), can be detected. For parallel and anti-parallel alignment of the two contacts the authors could measure different voltages due to the spin imbalance in GaAs. The voltage difference can be written as:

$$V_{\uparrow\downarrow} - V_{\uparrow\uparrow} = \frac{2hP_{Fe}P_{GaAs}E_f}{3e} \tag{2.6}$$

Here $h$ is the spin transmission efficiency of the interface ~ 0.5, e the electronic charge, $P_{Fe}$ the spin polarization in Fe ~ 0.42, $E_f$ the Fermi energy and $P_{GaAs}$ the spin polarization in GaAs to be calculated.

A voltage change of $V_{\uparrow\downarrow} - V_{\uparrow\uparrow} = 15$ µV at the detector corresponds to $P_{GaAs}$ = 0.02, when the distance $\Delta x$ between the two ferromagnetic electrodes amounts to $\Delta x = 12$ µm.

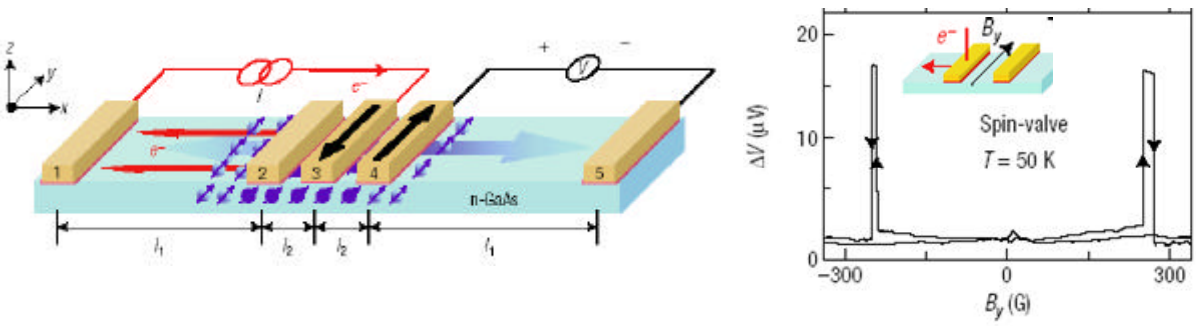


Fig. 2.11: Schematic diagram of the spin injection structure in non-local geometry and the observed spin valve signal for parallel and anti-parallel magnetic configuration of the injector and detector contacts [2.21].

By this non-local measurement, the authors could avoid all spurious effects like anisotropic magnetoresistance and Hall effect. The spin polarization measured in this experiment ($P_{GaAs}$ = 0.02) is the pure spin signal due to the presence of a spin imbalance in the GaAs channel at the detector Fe contact which is 12 µV away from the spin injecting Fe contact [2.21].

### 2.6.1 Manipulation of spins in semiconductors

Lou *et al*. could also show that by applying a small perpendicular magnetic field to the device (without changing the magnetization of the electrodes) the spin polarized electrons precess and dephase showing modulation and suppression in the spin valve signal [2.21]. This effect

(Hanle effect) again shows that what was measured in non-local measurement is the effect only due to spin injection. Fig. 2.12 shows the Hanle signal for parallel and anti-parallel magnetic alignment of the electrodes.

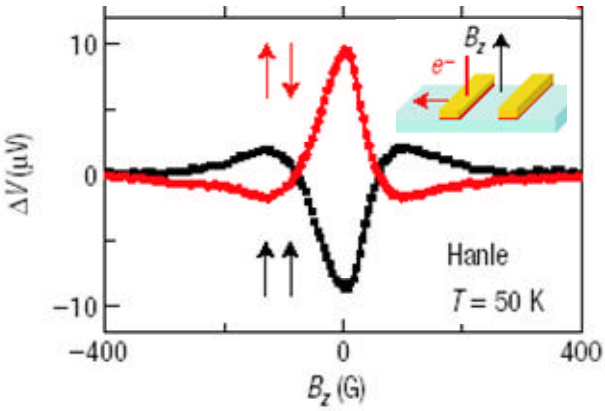


Fig. 2.12: Hanle effect: Non-local spin valve signal versus the small perpendicular magnetic field for both parallel and antiparallel magnetic configuration of the injector and detector contacts [2.21].

## 2.7 Subject of this thesis: Spin injection into Si

In addition to its central role in conventional electronics, silicon has spin-dependent properties (long spin relaxation and decoherence time) that could be particularly useful in spin-based quantum information processing. Si is a very attractive material for studying spin transport due to its inversion symmetry in its lattice structure giving rise to low spin orbit coupling and, hence, long spin coherence lengths [2.14]. Unfortunately, an indirect band gap and a weak spin-orbit coupling preclude conventional optical methods for detection of spin polarized electrons in Si [2.14]. The electrical measurement is the only method available for detection of spin injection into silicon by measuring the resistance across the device for parallel and anti–parallel magnetic configuration of the ferromagnetic contacts, as realized for the case of metallic systems and GaAs [2.19-2.21]. Some schemes use ferromagnetic metal–Si hybride structures for electrical injection and detection in conventional geometry, where the authors could not separate out spurious effects as discussed in the previous section [2.32-2.35]. However, material difficulties such as the *formation of silicides* and a *poor interface quality* are compounded with difficulties in making a *good tunnel junction* and preclude spin injection experiments [2.36, 2.37]. Consequently, it remains a challenge to quantify the degree to which spurious effects like the stray Hall effect and the anomalous magnetoresistance effect would compete with the signals that might be attributed to spin injection. Fabricating a device structure for the measurement in non-local geometry on Si has remained a difficult task, too.

In this section different concepts of spin injection into Si, its possibilities, and the difficulties for its realization will be discussed.

### 2.7.1 Spin-diffusion length in Si

As discussed in section 2.2.3, the spin flipping in lightly doped n-Si is mainly due to EY mechanism. The EY mechanism is described by the equation

$$\frac{1}{t_{sf}} = A\left(\frac{\Delta}{\Delta + E_g}\right)^2\left(\frac{E_g}{e_e}\right)^2\frac{1}{t_e} \tag{2.7}$$

Here $t_{sf}$ is the spin relaxation time, $t_e$ the momentum scattering time, $\Delta$ the spin splitting of the valance band, $e_e$ the kinetic energy of the electrons, and $E_g$ the width of the energy gap. $A$ is a parameter, dependent upon the scattering mechanism, and close to unity in all cases considered.

The spin diffusion length in the so called "current perpendicular-to-the-plane (CPP) geometry" is defined as

$$l_{sd} = \sqrt{Dt_{sf}} = \sqrt{\frac{mkT}{e}t_{sf}} \tag{2.8}$$

Here D is the electron diffusion constant, $t_{sf}$ the above mentioned spin relaxation time and $m$ the mobility. D and $m$ are related by the Einstein relation: $D = \frac{mkT}{e}$.

Inserting the value of the spin flip time from equation 2.7 and mobility ($m = \frac{et_e}{m_e^*}$) into 2.8, the spin diffusion length in Si can be written as:

$$l_{sd} = \frac{m}{e}\left(\frac{\Delta + E_g}{\Delta}\right)\left(\frac{E_g}{e_e}\right)\sqrt{\frac{kTm_e^*}{A}} \tag{2.9}$$

For the calculation of the spin diffusion length in Si as a function of temperature and doping, the following assumptions were taken [2.38]:

i) The band gap decreases slightly with temperature, therefore reduces the spin diffusion length.

ii) The band gap does not change significantly below the doping level of $N_d > 10^{19}$ $cm^{-3}$. So this influence is neglected in this analysis.

iii) The kinetic energy of the electrons in Si is taken to be the thermal energy $kT$.

iv) The effective mass of the electrons is assumed to stay constant with doping and temperature. In reality it would increase slightly with temperature and doping, leading to a small increase in the spin diffusion length. However, this change is small and considered negligible, here.

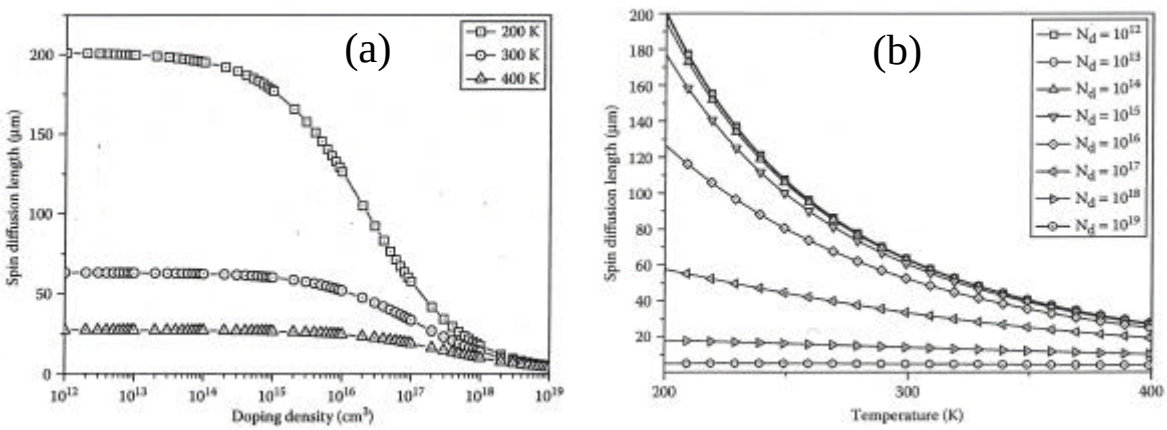


Fig. 2.13: **(a)** Spin-diffusion length vs. doping density in Si at 200 K, 300 K and 400 K. **(b)** Spin-diffusion length vs. temperature in Si for $N_d = 10^{12}$ to $10^{17}$ cm$^{-3}$ [2.38].

Spin-diffusion lengths vs. doping density and spin-diffusion lengths vs. temperature are shown in Figs. 2.13 (a) and (b), respectively. The general trend of the spin-diffusion length follows that of the mobility. An increase in the doping concentration at a given temperature results in the reduction of the carrier mobility and, hence, the mean relaxation time and spin diffusion length. The calculated spin diffusion lengths are long, 62.5 µm for a doping density ($N_d$) of $10^{14}$ cm$^{-3}$ ($t_{sf}$ =1.1 µs) at room temperature [2.38]. The length scale is large compared to conventional complementary metal-oxide-semiconductor (CMOS) devices and is promising for room temperature silicon-based spin-electronics devices. In p-type Si, the holes will interact with the conduction electrons and may cause additional spin relaxation via the *BAP* mechanism and have lower spin diffusion lengths [2.14].

### 2.7.2 Concepts of spin injection into Si

As already discussed in section 2.4 of this chapter the spin injection into semiconductors can be done in three different ways: by using

(i) a Schottky barrier,

(ii) a tunnel barrier and

(iii) diluted magnetic semiconductors.

In the next sections it will be shown how much these concepts are relevant to the case of spin injection into Si.

### 2.7.3 FM-Si Schottky barrier for spin injection

In the case of Si there is a natural Schottky barrier with a height $\approx$ 0.5 to 0.8 eV with FM (Fe, Co, Ni) and a width $\geq 30$ nm for a doping concentration of $N_d \leq 10^{17}$ cm$^{-3}$. The spin injection from a FM into Si corresponds to a reverse current in the Schottky junction, which is usually negligible due to the large height and width of the depletion region. Therefore a *d* doped n$^+$-Si layer ($N_d^+ \geq 10^{20}$ cm$^{-3}$) between the FM and Si should be used to increase the spin injection current. This *d* doped layer sharply reduces the thickness of the barrier and increases its tunneling transparency [2.39]. Similar doping profiles are also needed for the detector junction. The energy band diagram of such a FM - n$^+$ Si - n Si- n$^+$ Si -FM structure in reverse biased condition is shown in Fig 2.14.

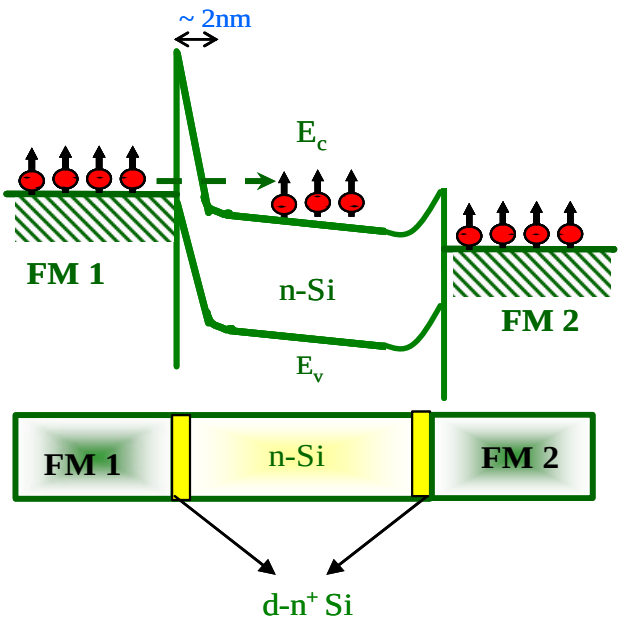


Fig. 2.14: Energy band diagram of the FM - n$^+$ Si - n Si - n$^+$ Si - FM heterostructure in reverse bias condition.

**Issues in spin injection and detection through Schottky contact with Si**

*(a) Interface*: In a heterostructure of a ferromagnetic thin film on a Si substrate, any structural disorder at the interface would drastically reduce the spin polarization at the interface and, hence, the spin injection efficiency [2.32 - 2.37]. If a small amount of Co or Fe (~ $10^{20}$ cm$^{-3}$) diffuses into the Si, each such Co or Fe atom will be likely to carry a local magnetic moment

oriented randomly with respect to the magnetization direction and will scatter electrons between the two different spin channels, thereby degrading the injected spin polarization. Therefore, in order to be able to control and improve the interface, a detailed understanding of such interfaces on atomic scale is necessary. *The real challenge in this field is to find a magnetically sharp FM-Si interface.*

In chapter 4 such ferromagnet-Si interfaces will be discussed. There it is shown that a thick disordered interface consisting of different silicide layers forms at room temperature. Approaches were taken for tackling this interface problem by growing ferromagnetic metal on a Si (100) surface at low temperature or by using a surfactant layer to reduce segregation of atoms from the substrate.

*(b) Absence of tunnel barrier at the detector end:* It is not possible to obtain a Schottky barrier at both ends (injector and detector). When the injection is done by reverse biasing the injector FM-Si Schottky contact, the detector end will be automatically forward biased (having a no Schottky barrier, see Fig. 2.14). So both the spin-up and the spin-down electrons from the semiconductor will enter the detector without spin filtering (besides a small effect due to filtering by the second ferromagnet). This will end up with detecting both spin directions and a reduction in the spin detection efficiency. The low spin polarization as observed by Lou *et al*. by injection and detection through a Schottky contact in GaAs may be due to the absence of a tunnel barrier at the detector end [2.21].

The other way to get rid of both problems is to use a tunnel barrier between the FM and Si for spin injection.

### 2.7.4 FM-Tunnel barrier-Si for spin injection

On the other hand, ultra thin tunnel barriers ($Al_2O_3$ and MgO) have proven to be the quality spin-selective tunnel barriers in a prototype GaAs system [2.28, 2.29]. Using a tunnel barrier has three advantages: (i) It forms a chemical barrier between the FM and the Si, (ii) it is a good spin-selective tunnel resistance, and (iii) tunnel barriers can be formed at both ends, the injector and the detector end. Even with a thin tunnel barrier at the interface, a Schottky barrier is formed due to band bending of the semiconductor. The formation of a Schottky barrier at the interface originates from an inability of the ultra thin tunnel barrier to support the difference in potentials between the Si and the FM on the other side of the tunnel barrier. Tunnel barriers would need to be at least 200 nm thick for typical doping levels in Si, in order

to support the potential difference without any band bending [2.39]. The thick Schottky barriers at the interface have a detrimental effect on the spin injection. As discussed for the case of a Schottky contact, a *d* -doped $n^+$-Si layer ( $N_d^+ \geq 10^{20}$ $cm^{-3}$) between the FM and Si should be used to increase the spin injection current. This *d* -doped layer sharply reduces the thickness of the barrier and increases its tunnelling transparency. Similar doping profiles are also needed for the detector junction. The energy band diagram of such a FM-I-$n^+$Si-nSi-$n^+$Si-I-FM structure in reverse biased condition is shown in Fig 2.15.

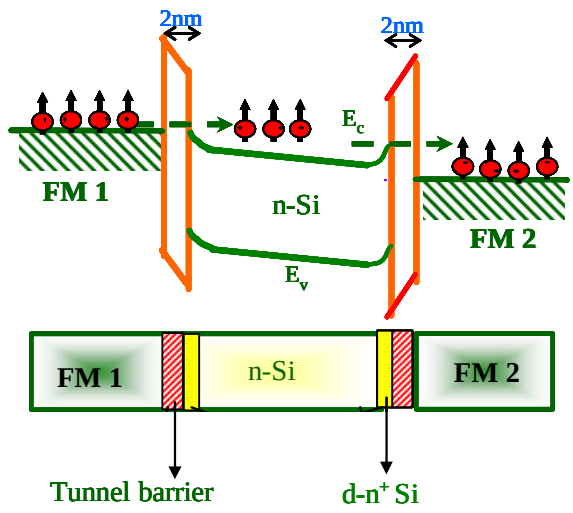


Fig. 2.15: Energy band diagram of FM-I-$n^+$Si-nSi-$n^+$Si-I-FM in reverse bias condition.

**Issues in spin injection and detection through a tunnel contact with Si**

*(a) Crystalline tunnel barrier for coherent spin injection:* When an $Al_2O_3$ tunnel contact is used for spin injection, the maximum spin polarization that can be achieved might be limited by the tunneling spin polarization from the ferromagnetic metal. For instance, for 3-*d* transition metals and their alloys, the tunneling spin polarization is normally no more than 50% when an $Al_2O_3$ tunnel barrier is used [2.28]. This is because of the amorphous nature of $Al_2O_3$ causes scattering and depolarization of spin polarized carriers.

An alternative approach for increasing the spin polarization is to use a crystalline MgO tunnel barrier. Using first-principle calculations, the tunneling spin polarization of a Fe/MgO(100)/Fe structure was predicted to be very high due to coherent tunneling of spin polarized electrons [2.40]. It was found that in such a structure, the tunneling magnetoresistance ratio is in excess of 1000% for an MgO (100) barrier of ~ 20 atomic planes. Experimentally, the tunneling spin polarization of CoFe/MgO junctions was measured using superconducting tunneling spectroscopy [2.41]. A large polarization (85%) was

obtained, indicating that very efficient spin injection is possible using a CoFe/MgO tunnel injector. In chapter 6 of this thesis, the fabrication of such a crystalline MgO tunnel barrier on Si for coherent transport of spin polarized carriers is presented.

*(b) Uniform tunnel barrier without pin holes:* The requirement for low-resistance tunnel junctions pushes the barrier thickness to lower length scales, making barrier pinholes a real and significant problem. The relative contributions from the two conduction channels - elastic tunneling through the insulating spacer and ballistic spin polarized transport through the narrow pinhole shorts - can change as the temperature and applied bias are varied and can also change the sign of the magnetoresistive response [2.42]. In chapter 6 of this thesis the fabrications of crystalline pin-hole free MgO (1.5 nm) tunnel barriers on silicon will be discussed.

*(c) Thermal stability of ferromagnetic metals on MgO tunnel barriers:* A thermal stability study of the ferromagnetic metals on thin tunnel junctions is of significance, due to compatibility issues with existing complementary metal-oxide semiconductor CMOS processes, i.e. for the production of magnetic random access memories and for sensor applications where high-temperature operation can be important. On the other hand the thermal stability of magnetic tunnel junctions is of considerable interest because their performance has been shown to be improved by annealing [2.43]. The thermal stability of MBE-grown ferromagnet-MgO tunnel junctions on Si (100) are studied up to 450°C for 30 min using *in situ* high resolution Rutherford backscattering (HRBS).

*(d) Optimization of resistance-area product:* Fert and Jaffer calculations reveal that a reasonable value of the magnetoresistance (MR) can only be obtained in the FM/I/Si/I/FM structure if the resistance-area (RA) product of both the FM/I/Si contacts is in a relatively narrow range [2.44].

Considering Co as ferromagnet and n-type Si with a resistivity of $10^{-2}$ O m, a carrier concentration (n) of $3\times10^{21}$ $m^{-3}$, and a spin relaxation time ($t_s$) of 7 ns, the spin diffusion length can be calculated at room temperature as

$$l_{sd}^{n} = \sqrt{\frac{k_B T t_{sf}}{2ne^2 r_n}} = 4.3\times10^{-6}\ \text{m} \tag{2.10}$$

In order to observe the MR response, the tunnel barrier resistance $R_b$ (the RA product of the tunnel contact) should be in the range of $r_n t_n < R_b < r_n (l_{sf}^n)^2 / t_n$. Here $t_n$ is the channel length of Si [2.45].

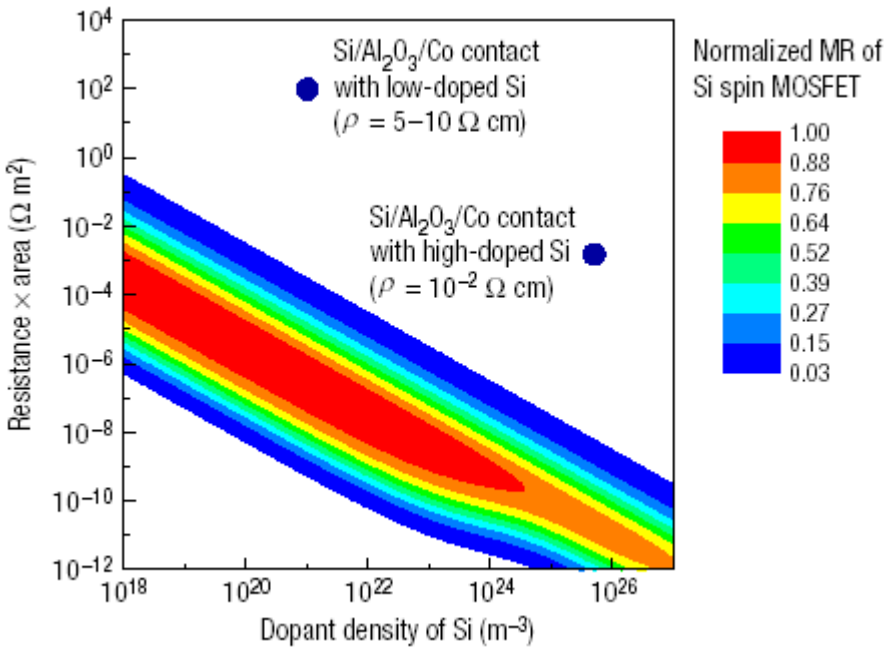


Fig. 2.16: Calculated MR of FM/I/Si/I/FM spin MOSFET structure as a function of the contact resistance-area product and the Si dopant density. The color legend shows the value of the normalized MR [2.45].

The optimum range of the RA product of the contact for a high MR is shown in Fig. 2.16 as a function of the dopant density of Si [2.45]. This calculation was done using a Si channel of 100 nm length and a spin life time of the electrons in Si of 7 ns at 300 K. Generally, the spin life time of electrons in semiconductors is reduced at higher dopant density. It should be noted that the experimentally observed RA product values by Min *et al.* for $Co/Al_2O_3/Si$ on low-doped and high-doped Si (shown in Fig. 2.16) are far from the required range for the observation of a spin injection effect [2.45].

The issue of tailoring the resistance-area product of the tunnel contact has been addressed by heavily doping the Si surface layer, decreasing the oxygen content in the tunnel barrier and scaling the tunnel barrier thickness to sub-nanometer regime in chapter 6 of this thesis.

*(e) Spin injection through tunnel barrier in non-local geometry:* Sample preparation, a device design for spin injection into Si through a tunnel barrier, and its non-local detection have also been proposed in chapter 6.

### 2.7.5 Diluted magnetic silicon for spin injection

Instead of contacting the semiconductor with a ferromagnetic metal, the contact could be made with another semiconductor - one with magnetic properties. This solves the conductivity mismatch problem by ensuring that the resistivities of the materials on both sides of the interface are comparable in magnitude [2.46]. Doping of semiconductors with magnetic 3d transition metal impurities has attracted much interest. Since it has long been known that Mn impurities can have a high magnetic moment, research is focused on Mn-doped semiconductors [2.1]. The spin injection using diluted magnetic semiconductors (DMS) as spin aligners has met with grate success. Spin-polarized currents of 90 % have been observed by this method [2.46]. The mostly studied DMS material GaMnAs has a Curie temperature well below room temperature. Now researchers are hunting for finding a DMS material with high Curie temperature, preferably well above room temperature.

Making Si a ferromagnetic semiconductor at room temperature by doping it with Mn to achieve the dominance of the long-range ferromagnetic interaction over the short-range anti-ferromagnetic interaction can be promising for spin injection into Si. Interestingly Mn-doped Si shows ferromagnetic order with a Curie temperature above room temperature in $Si_{0.95}Mn_{0.05}$ films [2.47], $Mn^+$-implanted Si [2.48], and $Mn^+$-implanted Si nano wires [2.49]. This ferromagnetic order is believed to be due to long range interaction of Mn atoms, mediated by carriers in the Si matrix. Carrier-mediated ferromagnetism has great potential for making spin field effect transistors [2.50].

**Issues in Mn-doped Si**

*(a) Positions occupied by implanted Mn in Si lattice:* Motivated by research on other diluted magnetic semiconductors, it had been believed that substitutional Mn is crucial for ferromagnetism. However, these substitutional Mn impurities in Si are energetically less stable than the interstitial ones [2.51]. In a most recent study by density functional theory, it has been shown that for the case of Si, interstitial Mn atoms also show ferromagnetic ordering, which agrees quite well also with experimental observation [2.52].

To find out whether the Mn atoms are in interstitial or substitutional positions after annealing in the implanted samples, RBS-channeling experiments were performed, which are presented in chapter 7 of this thesis.

*(b) Carrier-mediated ferromagnetism:* The nature and origin of this ferromagnetism, as well as its carrier mediation in Mn-doped Si still are points of discussion. Bolduc *et al*. [2.48]

reported that in Mn-implanted samples the ferromagnetic exchange is hole mediated by comparing n-type Si ($10^{15}$ $cm^{-3}$) and p-type Si ($10^{19}$ $cm^{-3}$), where the carrier concentrations in n-Si and p-Si are quite different. There remains, however, the problem, if the ferromagnetism is only hole mediated, then n-Si should not show ferromagnetism. In another study Liu *et al*. [2.53] have shown that Mn and B-doped Si (which is p-type) show hole-mediated ferromagnetism. n-type Si samples were not studied in their work.

To obtain information about the origin of the ferromagnetism of Mn-implanted Si (hole mediated or electron mediated), Mn ions of a fluence of $1\times10^{17}$ ions/$cm^2$ were implanted into $p^+$ Si (Boron: $1\times10^{19}$ atoms/$cm^2$), p Si (Boron: $1\times10^{15}$ atoms/$cm^2$) and n Si (Phosphorus: $1\times10^{15}$ atoms/$cm^2$) samples.

*(c) Magnetic moment of Mn and Si:* To reveal the microscopic origin of magnetism that occurs in this DMS, X-ray magnetic circular dichroism (XMCD) spectroscopy [2.54] has been used to study the magnetic moments of Mn atoms in the Si lattice (spin and orbital magnetic moments separately).

In chapter 7 of this thesis, the studies on structural and magnetic properties of Mn-doped Si samples are presented, mainly addressing the above mentioned issues.

# Chapter 3

# Experimental techniques and sample preparation

In this chapter, the sample preparation and the experimental techniques used for the investigations of such samples are described. The ferromagnet-Si (100) interfaces were prepared using molecular–beam epitaxy and *in situ* analyzed by high-resolution Rutherford back scattering spectroscopy. The magnetic properties of these samples were analyzed by superconducting quantum interference device (SQUID) magnetometer.

## 3.1 Molecular beam epitaxy (MBE)

As discussed in chapter 2 of this thesis, an atomically sharp ferromagnet-Si interface is needed for spin injection into Si. Preparing well-defined heterostructures on a nanometer scale has not only led to fundamentally new phenomena but has also initiated new technologies. **M**olecular **B**eam **E**pitaxy (MBE) is a well-established technique to grow such heterostructures under very clean and controlled conditions. Due to the low energy of the evaporated atoms (~ 1 eV), the add-atoms land softly on the substrate giving a very sharp and ordered interface and allowing to perform various surface and interface sensitive studies [3.1, 3.2].

### 3.1.1 Film deposition and growth modes

The growth mode of a thin film determines it's structural and magnetic and interface properties. A first distinction can be done between those films which present a polycrystalline structure and those which grow as mono-crystals; in this latter case one speaks of epitaxial

growth. Three different growth modes, depending on the lattice parameters and surface energies of adsorbate and substrate, can be qualitatively classified (see also Fig. 3.1):

1) *island* or Vollmer-Weber (VW) growth mode: this kind of growth is characterized by the formation of a conglomerate of atoms (islands) on the surface instead of atomic layers
2) *layer-by-layer* or Frank-Van der Merwe (FM) growth mode: in this case each atomic layer starts to grow after the previous one is completed
3) *layer and island* or Stransky-Krastanov (SK) growth mode: in this last mode islands start to form after one or more atomic layers are completed.

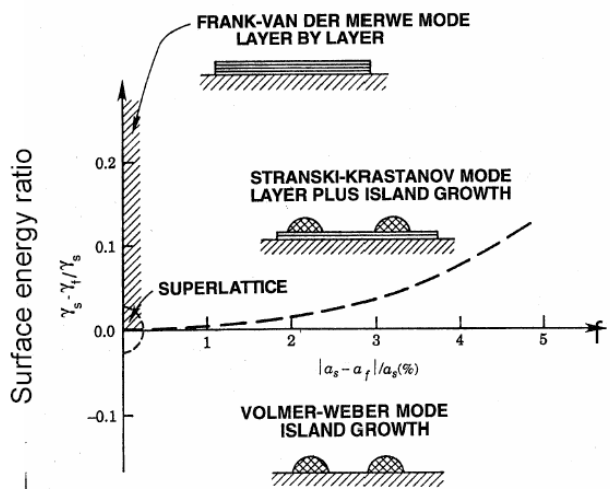


Fig. 3.1: Different growth modes of thin films depending upon the surface energy ratio $(g_s - g_f)/g_s$ and the lattice mismatch between the grown film and the substrate $(a_s - a_f)/a_s$. Here *s* = substrate, *f* = film [3.2].

One of the key factors to understand the different growth modes is the difference between the lattice parameters of the film and the substrate; as a matter of fact, once the atoms of the films start to deposit on the surface, they aim to reproduce the two-dimensional pattern of the substrate; doing this they inevitably increase the elastic-deformation energy of the film, due to the difference with the lattice parameter of the substrate. If the difference is small, then the film can grow with the lattice parameter of the substrate even to higher thicknesses (pseudo-morphic growth); on the contrary, if the difference is big, the film starts to grow with its own lattice parameter from the very first layer. In the intermediate case there could be a transition between these two growth modes, starting at a critical thickness when the elastic stress becomes greater than the adhesion force between the film and the substrate [3.1, 3.2].

### 3.1.2 Interfaces

In the case of ferromagnetic metals, thin metal films can even react with single-crystal Si at room temperature [3.3]. Therefore, whenever a ferromagnetic transition metal is used on Si, its interface with Si is actually replaced by a silicide-Si interface. How the covalent bonds in Si can be broken at such a low temperature is an intriguing question. As it is kinetically impossible, some new low-energy processes are believed to be occurring at the interface (see chapter 4) [3.4] . The diffused-in ferromagnetic metal atoms present in these silicide phases may be the main cause for spin flip scatting at the interface, when spin polarized electrons are injected from the ferromagnet into Si [3.5].

## 3.2 High resolution Rutherford back scattering spectrometry

Obtaining a detailed understanding of the atomistic structure at buried interfaces responsible for electronic and magnetic properties is very important for the realization of spin injection into Si. In general, the atomic structure and composition of the ferromagnetic metal-Si interface are not known up to the level of precision needed. In the case of the interface for which there may be mixing of many atomic layers needs to be better understood for its improvement. High resolution Rutherford backscattering is a very promising for addressing such buried-interface problems in atomic detail. In particular the *in situ* deposition experiments in ultra-high vacuum feasible with this technique help in better understanding of ferromagnetic metal-Si interfaces at very initial stages of growth.

High resolution Rutherford backscattering is used as a non-destructive method for elemental depth analysis with monolayer depth resolution. High resolution was obtained by using a high-resolution spectrometer and grazing-angle incidence. Using $N^+$ ions gives an even higher depth resolution than $He^+$ ions, because of the larger stopping power. This new technique, called high-resolution RBS (HRBS), realizes quantitative layer-by-layer analysis, essentially without destruction of specimens.

### 3.2.1 Principle of HRBS

HRBS involves the measurement of the number and energy distribution of energetic ions (usually MeV light ions such as $He^+$, $N^+$) backscattered from atoms within the near-surface region of solid targets. From such measurements it is possible to determine both the atomic mass and concentration of elemental target constituents as a function of depth below the surface [3.6].

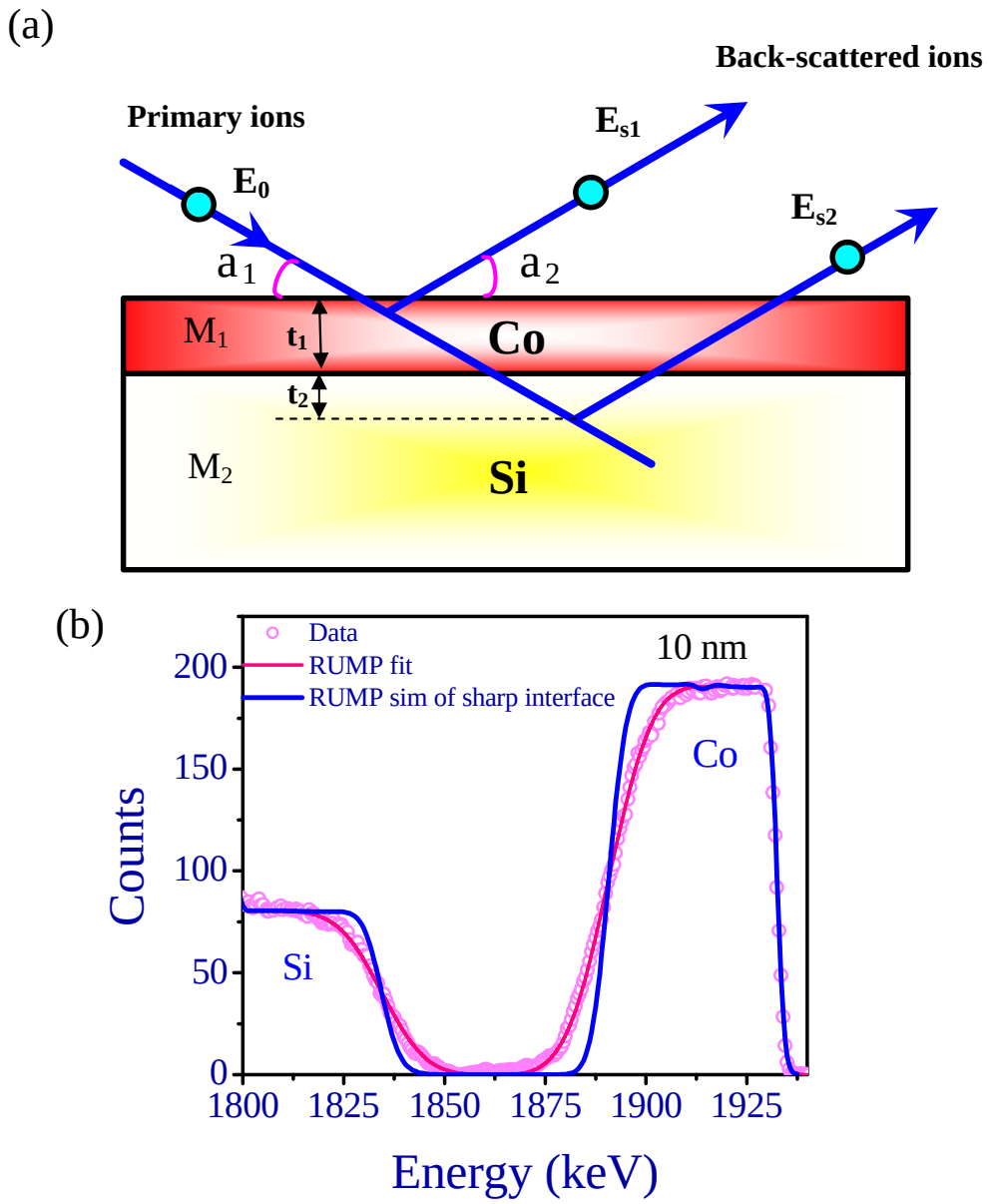


Fig. 3.2: **(a)** Schematic diagram of an HRBS-experiment. **(b)** Corresponding energy spectrum of a Co thin film on a Si substrate. For comparison the RUMP simulation of a sharp Co-Si interface is shown which reveals that interdiffusion of Co and Si has occurred at the interface. (2 MeV $He^+$ ion beam at an incidence angle of 19° and at a scattering angle of 38° is used for this experiment.

In the analysis of high-resolution Rutherford backscattering (HRBS) a sample is exposed to a beam of ions with mass $M_1$ (He or N particles) at a grazing incidence angle $a_1$ with a well defined energy $E_0$ (in the order of MeV). Those ions that undergo elastic coulomb collisions with sample atoms are recorded with an electrostatic spectrometer and a position-sensitive detector which is positioned at an angle $a_2$ (see Fig. 3.2(a)). The ions undergoing a collision with a heavy target atom loose less energy than ions colliding with a target atom of

lower atomic mass. This fact is frequently used in HRBS experiments to analyze the atoms of the sample under investigation. In addition both primary ions and the scattered ions loose energy on their way through the sample, depending on the stopping power, which yield the depth information needed for depth profiling [3.6].

A typical HRBS spectrum, as met during this work repeatedly, is shown in Fig. 3.2 (b). A thin over-layer of atoms (Co) with high atomic mass ($M_1$) is on the top of the bulk substrate (Si) which is of lower atomic mass ($M_2$). In the energy spectrum of backscattered particles the thin film of heavy atoms lead to a peak which is well separated from the particles scattered by the light atoms of the substrate. The high-energy edge of the paek corresponds to atoms on the surface. Due to energy loss of ions traversing the Co film, ions scattered from the atoms deeper in the sample appear at lower energies in the spectrum. In this way the thickness of the Co film is determined to be 10 nm. As shown in the figure, the spectrum can be fitted with the program RUMP to obtain the composition and depth structure of the sample [3.7]. For comparison the RUMP simulation of a sharp Co-Si interface is shown which reveals that interdiffusion of Co and Si has occurred at the interface.

### 3.2.2 The high resolution electrostatic spectrometer

The scattering chamber for the HRBS experiments is equipped with a high-resolution electrostatic spectrometer. This can be rotated to access a large variety of scattering angles. With this setup scattering experiments can be done with an energy resolution corresponding to a depth resolution of less than one monolayer [3.8, 3.9].

The spectrometer consists essentially of three parts (see Fig. 3.3): (i) an electrostatic lens system, (ii) the analyzer and (iii) a one-dimensional position-sensitive detector. (i) The lens system (four quadrupole lenses and one hexapole) focuses particles emitted parallel to the optical axis of the instrument onto the entrance slit of the analyzer. This design allows for extended samples and beam spots without spoiling the energy resolution of the instrument due to kinematic errors. The hexapole corrects for curved imaging of the slit by the analyzer. (ii) The analyzer is a 100° cylindrical condenser (cylindrical sector field) of 700 mm radius and 19.8 mm gap width. With the maximum voltage of 60 kV applied to the condenser plates, 2 MeV particles can be analyzed, which doubles with double charge state. Since deflecting and focusing do not depend on the particle's mass, heavy particles of the same energy can be analyzed. The simultaneously available energy window amounts to 1.7 % of the analyzed energy; the energy resolution of the instrument is better than $3\times10^{-4}$ (iii) for the detection of

the particles, one-dimensional position-sensitive silicon surface barrier detectors are used with lengths of typically 15 mm. [3.8, 3.9].

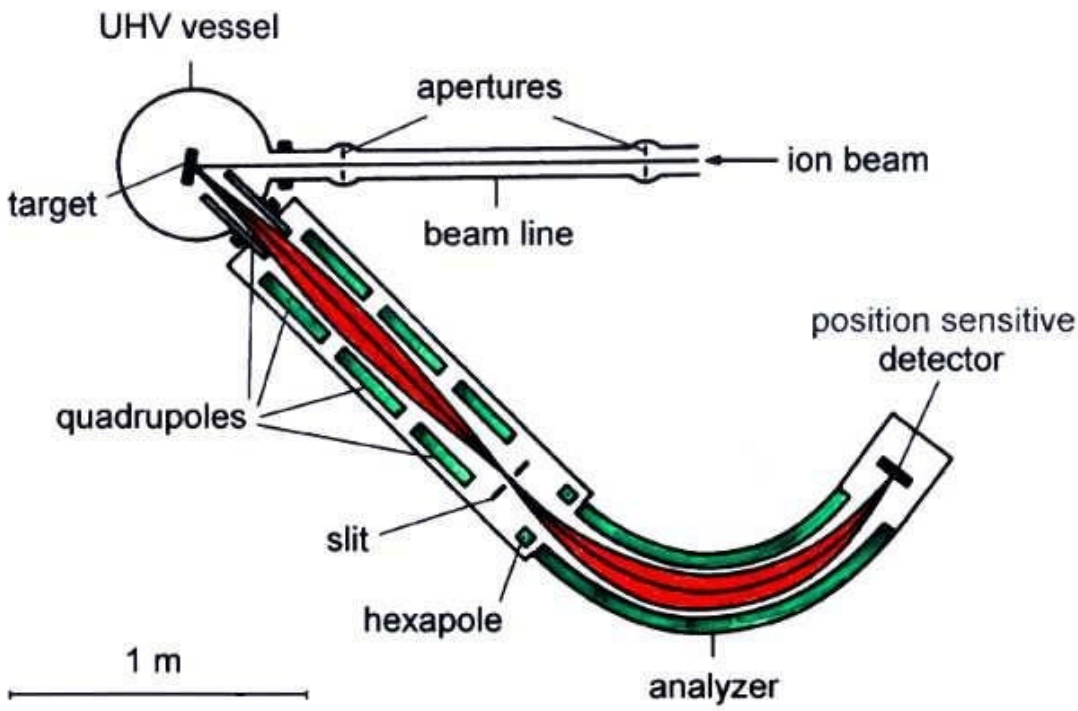


Fig. 3.3: Schematic drawing of the electrostatic spectrometer and the scattering chamber set up at the Pelletron accelerator of the Max Planck Institute for Metals research, Stuttgart [3.8].

### 3.2.3 Monolayer resolution with HRBS *(Counting individual atom layers in graphite)*

The result shown in Fig. 3.4 is a recent experiment on highly oriented pyrolytic graphite (HOPG) by high-resolution Rutherford backscattering spectroscopy (HRBS). By using an ion beam of 2 MeV $N^+$, up to five individual monolayers could be identified in the HRBS spectrum from such a sample, which clearly demonstrates that monolayer depth resolution is possible with this device.

For the experiments square discs of HOPG supplied by Advanced Ceramics were used. The samples had the dimensions 12 × 12 × 2 $mm^3$ and a mosaic spread of 0.4°. Before use for the experiment a notch was made at one corner of the sample and the sample subsequently cleaved along this notch by a stream of pressurized air. The samples were then mounted in the UHV scattering chamber and annealed at 400 °C for about 1 hr before the measurement. During the measurements a pressure of $1 \times 10^{-9}$ mbar was maintained. In Fig.

3.4 the increased height of peak 1 is due to the fact that the N ions (here in fact $N^{4+}$ ions were counted, i.e. ions which leave the sample in charge state 4) leave the sample after the violent backscattering collision in rather high charge states which survive only when coming from the very surface.

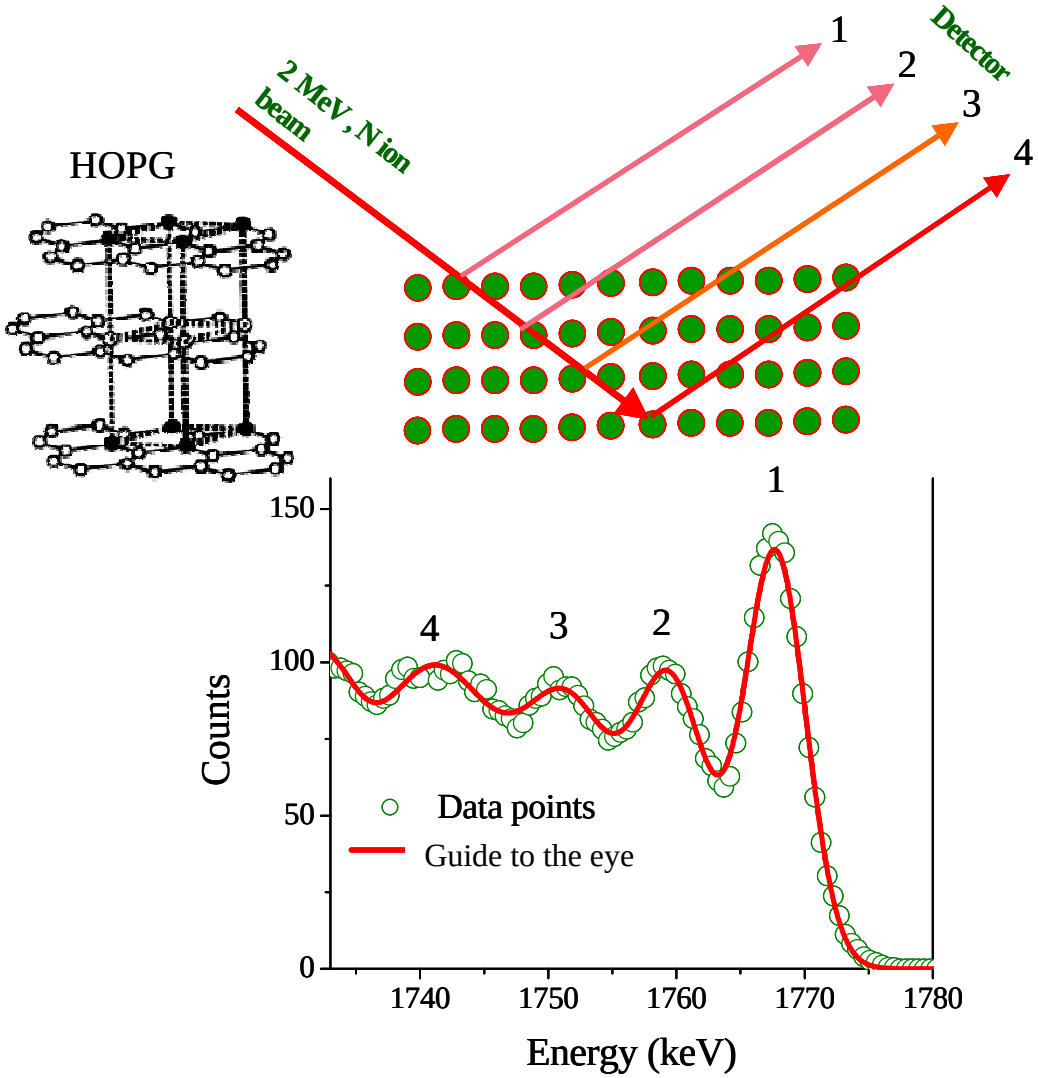


Fig. 3.4: High energy resolution RBS spectrum from a HOPG sample. The first five carbon layers of the sample are well resolved. (Incident beam: 2 MeV $N^{+}$ ions, analyzed ions: $N^{4+}$, scattering angle: 7°, angles of incidence and exit: 3.5° each).

### 3.2.4 Analysis of initial stages of growth

It was demonstrated in the previous section by using HOPG as an example that monolayer resolution can be achieved. As shown by Kimura *et al.* by using HRBS technique different

growth modes of thin films can be distinguished [3.10]. Fig.3.5 shows typical examples of Frank-van der Merwe mode (FM mode) and Volmer-Weber mode (VW mode). In the FM mode, atomic layers of the grown crystals can be resolved as separate peaks on the HRBS spectrum. On the other hand, in the VW mode, the energies of the ions scattered from the same atomic layer are not always the same. As shown in Fig 3.5(b), the energy of the ion scattered at B is smaller than that scattered in C, because the path length of the ion scattered in B is longer than that of the ion scattered in C. Consequently, the HRBS spectrum does not show separated peaks but shows a broad peak with rounding off of the high-energy edge.

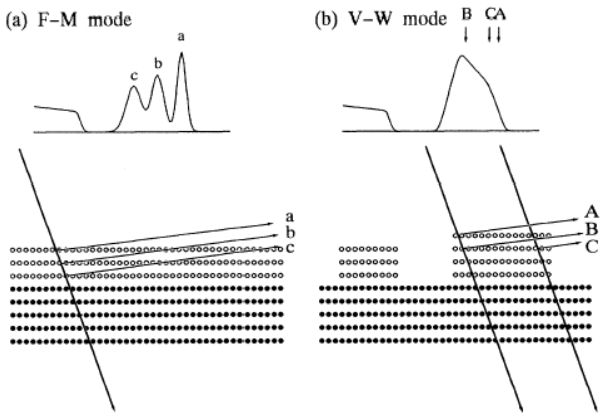


Fig. 3.5: HRBS spectra expected for FM and VW growth modes. The FM growth mode shows sharp peaks arising from the individual atom layers while the VW mode leads to a rounding off of high-energy edge [3.10].

## 3.3 Silicon surface preparation

Surface structural disorder, defined as any disruption of perfect order in the surface, influences a wide variety of surface kinetic, electronic, magnetic and chemical properties. Schottky barrier properties and interface magnetism are very likely to be modified by the surface preparation conditions. That’s why a detailed understanding of the FM-Si interface is needed when growing FM on clean Si surfaces. In this sub-chapter the Si surface preparation and the *in situ* characterization procedures are summarized.

There have been innumerable studies of Si surfaces. All use one of several surface preparation processes. These can be categorized roughly as follows: (i) chemical etching with subsequent high temperature (>1000 °C) anneal in UHV, (ii) sputter etching and annealing to a variety of temperatures up to 1250 °C, and (iii) pure annealing treatments of a sample that has not been chemically or sputter cleaned. Combinations of these treatments have also been used. In our experiments we have used the process (i) [3.11].

### 3.3.1 Steps for cleaning silicon

The clean Si surface was prepared for our experiments by a two-step procedure: (i) by first chemical cleaning (Shiraki cleaning procedure [3.11]) which leaves an oxide layer on the Si surface and then (ii) by thermal cleaning in UHV in steps as discussed below:

**UHV thermal cleaning procedure**

1. Out-gassing of the sample at 450 °C over night (10 hr),
2. Heating to 800 °C for 1 hr,
3. Flash heating to 1050 °C several times for short periods at time (~ 1 min.),
4. Cooling slowly at a rate < 2 °C/sec to room temperature.

### 3.3.2 Si cleaning and *in situ* XPS measurements

*In situ* measurements were done at each step of the UHV cleaning procedure. The measurements were performed in an Omicron UHV surface science chamber. XPS measurements with a Mg $K_a$ line were performed on a Si surface at each step of the cleaning procedure, as shown in Fig. 3.6(a). Just after chemical cleaning, O 1s and C 1s peaks could be observed indicating the presence of C and O on the Si surface. After degassing at 450 °C for 10 hr, carbon was removed as seen from the disappearance of the C 1s peak in the XPS spectra. This indicates that C was only on the surface. After this degassing step oxygen is still on the surface. It disappears after heating the Si sample at 800 °C for 1 hr [O 1s peak in Fig. 3.6(a)]. The Si peak intensity also increases, indicating a clean Si surface. The magnified spectrum of the Si 2p line just after chemical cleaning and after thermal cleaning is shown in Fig. 3.6 (b) and (c). A hump on the left side of the Si 2p XPS spectrum in Fig. 3.6 (b) shows the presence of oxygen bonded to silicon on the chemically cleaned sample. After heating at 800 °C for 1 hr the left shoulder of the Si 2p line disappears. This is the indication of the disappearance of chemisorbed oxygen on the Si surface [Fig. 3.6 (c)].

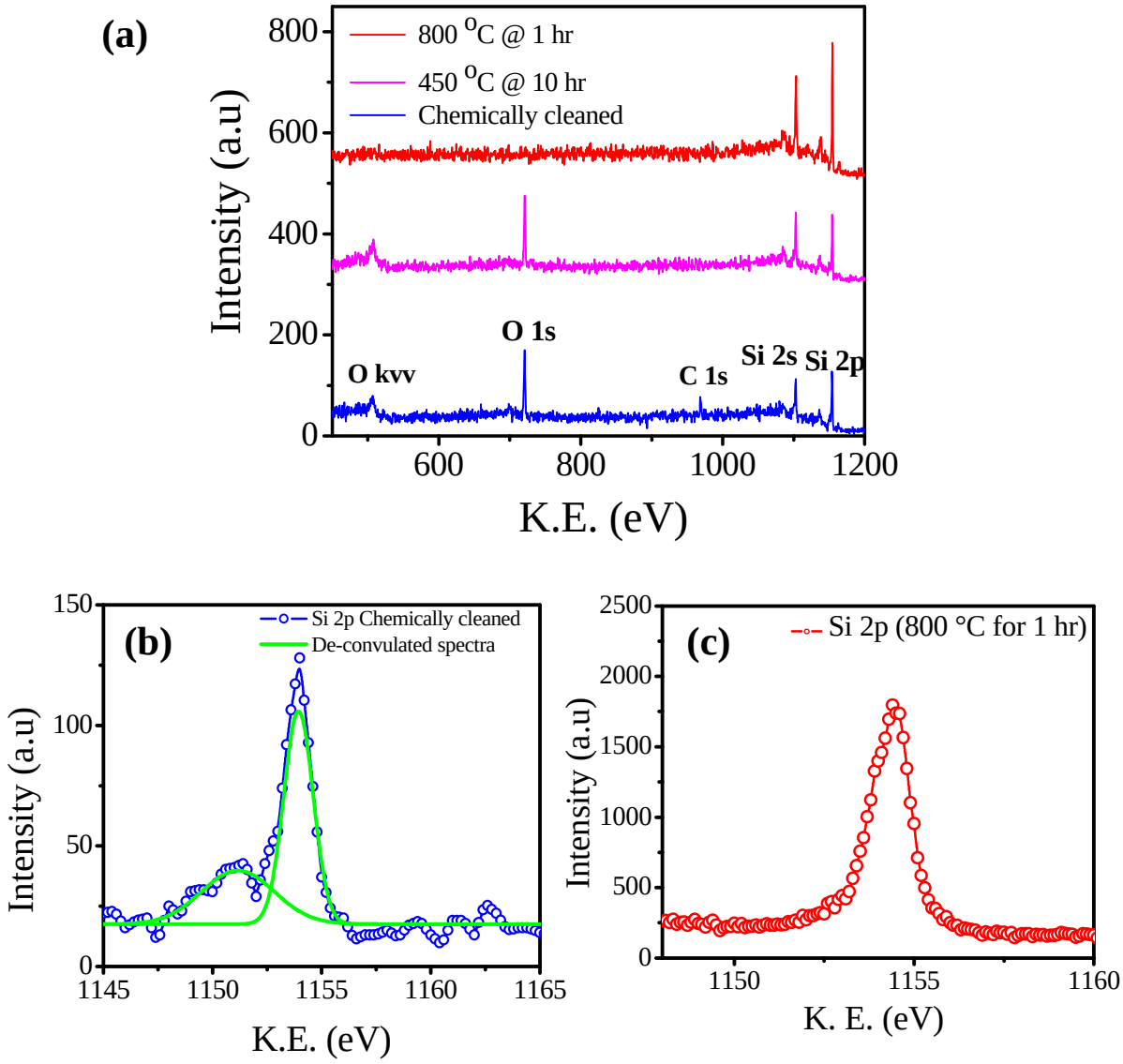


Fig. 3.6: **(a)** XPS spectra of a Si surface cleaned by thermal desorption of C and O. Blue line: As freshly prepared and oxidized by chemical means, showing the O kvv Auger line at 510 eV, XPS lines of O 1s at 720 eV, C 1s at 965 eV, Si 2s at 1100 eV and Si 2p at 1150 eV. Magenta line: heated at 450 °C for 10 hr, the C 1s peak disappears. Red line: heated at 800 °C for 1 hr, the O 1s peak disappears. **(b, c)** Magnified Si 2p XPS spectra (b) as prepared (c) heated at 800 °C for 1 hr.

### 3.3.3 Si surface cleaning and *in situ* HRBS measurements

In another experiment a Si (100) surface was prepared and analyzed using HRBS to probe the surface cleanness. Fig. 3.7 shows the HRBS spectra and RUMP simulations of the chemically prepared Si surface (red) and after thermal cleaning (blue curve) at 1050 °C. Here we use 1 MeV He ions at the scattering angle of 38 deg. The oxide thickness before the thermal cleaning was found to be 8 nm. Thus we were able to prepare clean Si (100) surfaces following these cleaning procedures. These procedures are nicely reproducible and provide

the good Si surfaces which are the most important requirements for studies of the ferromagnet-Si (100) interface.

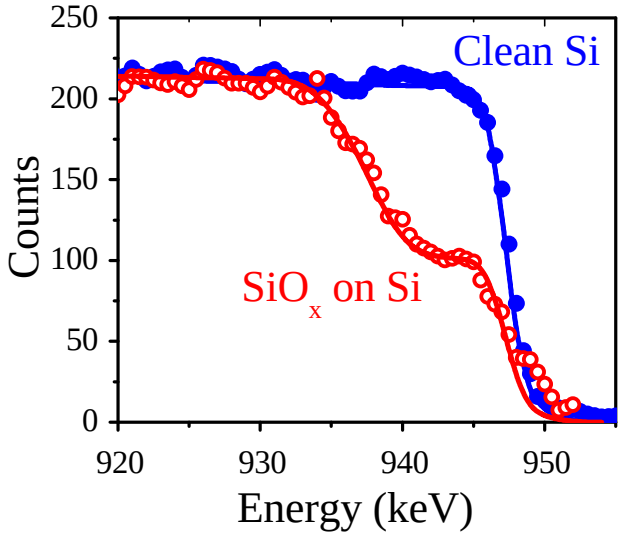


Fig. 3.7: HRBS spectra and RUMP simulations of a Si surface after Shiraki cleaning (open circles) and after thermal cleaning at 1050 ℃ (solid circles).

## 3.4 Experimental set-up for *in situ* HRBS experiments

Figure 3.8 shows the experimental arrangement for our *in situ* HRBS measurements described in the subsequent experimental chapters. In these measurements the surface cleanness of the Si sample was verified by HRBS. Co/Fe with high purity *(4N)* was evaporated from a high temperature effusion cell on to the clean Si (100) surface which was kept at room temperature. The evaporation rate was about 0.05 ML/min (1 ML = $6.87\times10^{14}$ atoms/cm$^2$). The deposition rate was measured by a quartz microbalance and calibrated by HRBS with an accuracy of about 5%. HRBS with monolayer depth resolution is achieved by the use of the high-resolution spectrometer described in section 3.2.2. Grazing incidence of the ion beam on the target (2° to 3°) provides an even improved depth resolution. Different coverages of ferromagnetic metals on Si (100) were investigated by 2 MeV $N^+$ ions at the incidence angle of ~ 2.5° to the surface and at the scattering angle of 37.5°.

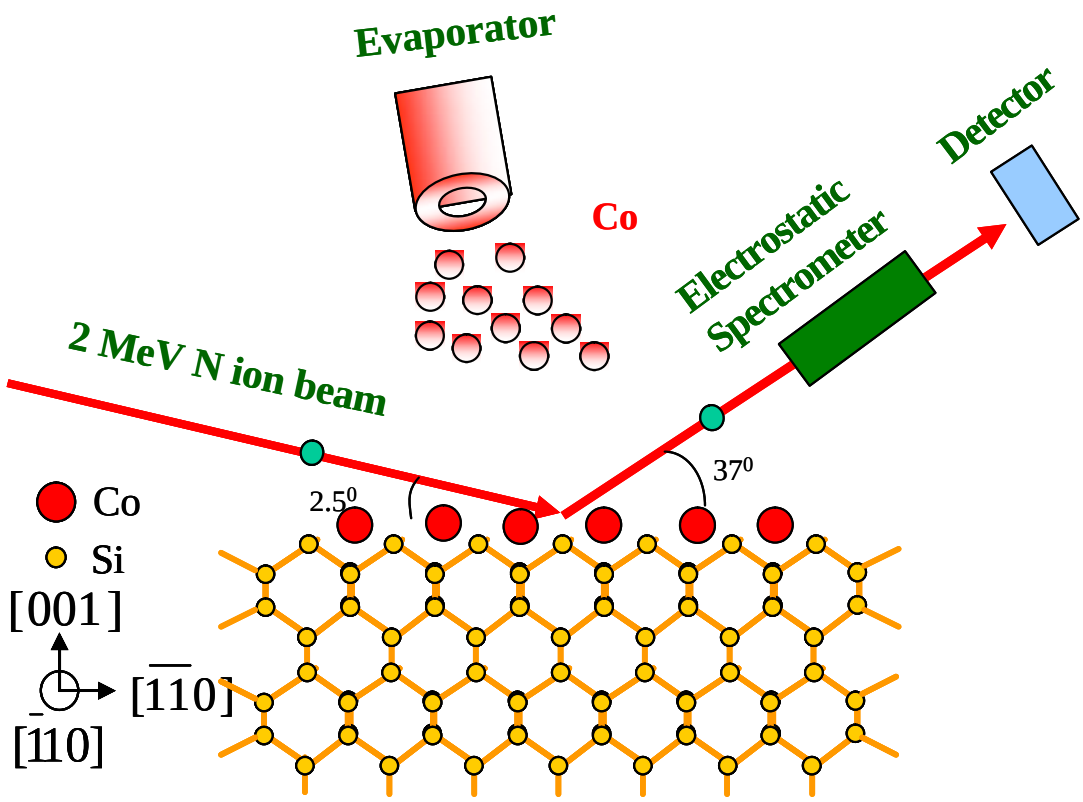


Fig. 3.8: Experimental set-up for *in situ* HRBS experiments. The figure shows the sample geometry, evaporation source, incident beam, electrostatic spectrometer and detector used for most of the experiments.

Combining the high-resolution spectrometer and $N^+$ ions (providing a higher stopping power and, hence, depth resolution), experiments with monolayer depth resolution could be performed. The preparation chamber was equipped with multiple evaporation sources for producing multiple layered structures and analyzing it without breaking the vacuum. The chamber was also equipped with sample heater and cooling stages for sample cleaning, high temperature growth, and low temperature growth of ferromagnetic metals on Si. Also arrangements were made for *in situ* oxidation and reactive molecular beam epitaxy for the preparation of tunnel barriers. The effusion cells were outgassed before each experiment and no O or C contaminations were found during evaporation.

## 3.5 Superconducting quantum interference device (SQUID) magnetometry

High sensitivity is needed when samples with low intrinsic magnetic moment or low mass are measured. In ultra thin films, for instance, the mass may be smaller than 1 µg. Such samples can be measured very accurately with a SQUID magnetometer. High sensitivity is possible because this SQUID device responds to a fraction of the flux quantum. The SQUID magnetometer used in this work is based on a field probe that consists of two Josephson junctions forming a superconducting ring [Fig. 3.9(a)].

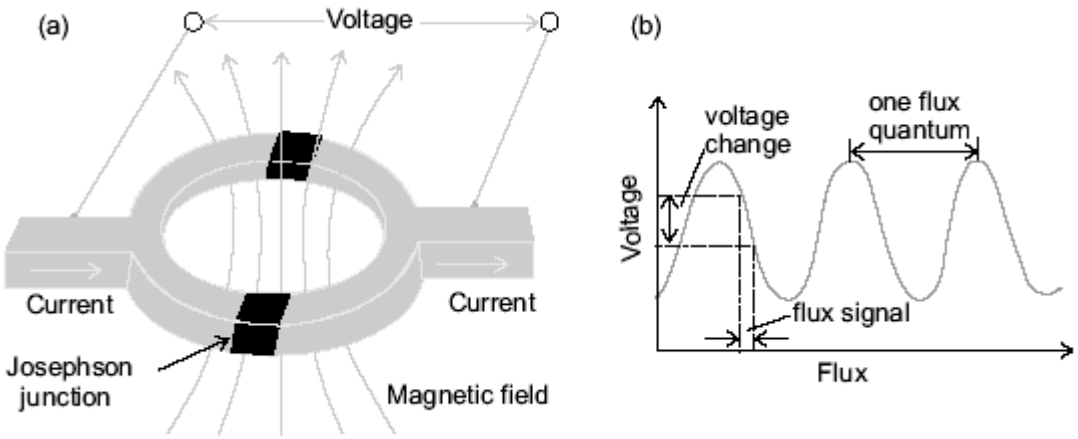


Fig. 3.9: SQUID measurement principle: **(a)** Two Josephson junctions forming a superconducting ring, which provides information about the change in flux. **(b)** The output voltage as a function of flux [3.13].

Applying a current to the SQUID activates Cooper pairs to tunnel across the junctions as long as the critical current does not surpassed in each of the junctions. When a magnetic field is applied to the ring, it alters the flow of the Cooper pairs, causing a change in the quantum mechanical phase difference across each of the two junctions. These phase changes, in turn, cause as well the current through the device as the circular current in the ring to oscillate in anti-phase between a maximum and a minimum value with increasing magnetic field. The maxima (or minima) occur when the flux administered to the SQUID equals an integral number of flux quanta through the ring. The minima (or maxima) correspond to half-integral numbers of quanta. In practice, one does not measure the current but rather the voltage across the SQUID. The voltage also swings back and forth under a steadily changing magnetic field [Fig. 3.9(b)]. This quantum interference effect provides us with a digital magnetometer, where each digit represents a flux quantum. The use of the lock-in amplification technique combined with a flux-locked feedback loop allows to measure even small fractions of one flux quantum.

In essence, the SQUID is a flux-to-voltage transducer, converting a tiny change in magnetic flux into a voltage. Field changes as low as $10^{-11}$ Gauss are measurable in this way.

The main components of a SQUID magnetometer are: (a) a superconducting magnet for applying an external magnetic field to the sample, (b) a superconducting detection coil where the sample is slowly pushed in and out (inductively coupled to the sample), (c) a SQUID connected to the detection coil, and (d) a superconducting magnetic shielding to shield the SQUID sensor from the fluctuations of the ambient magnetic field of the place where the magnetometer is located and from the large magnetic field produced by the superconducting magnet. A measurement is done in this equipment by moving the sample through the second-order gradiometer. The changing magnetic flux during the motion of the sample induces an electric current in the pick-up coil system. Since a SQUID works as a highly linear current to voltage converter, the variations in the current in the detection coil produce a corresponding variation in the SQUID output voltage which is proportional to magnetic moment of the sample [3.12, 3.13].

# Chapter 4

# Ferromagnet - Si Schottky contact at room temperature for spin injection

Injecting spin polarized electrons from a ferromagnet (FM) into Si through a Schottky contact and harnessing the spin degree of freedom in addition to the charge have both fundamental and technological importance [4.1]. Co and Fe having nearly 45 % spin polarization at room temperature and Si having a long spin coherence length are the attractive candidates for spin injection experiments [4.2]. There exists a Schottky barrier with ferromagnetic metals (Fe, Co, Ni) for a nominal doping concentration of Si. The large height and width of the depletion region precludes spin injection in reverse bias mode. Therefore a $n^+$-Si layer between FM and Si should be used to increase the spin injection current. As discussed in chapter 2 the main problem for spin injection across a Schottky contact is the need for atomically sharp FM-Si interfaces. The challenge to grow such a heterostructure with sharp interface is to reduce interface reactions [4.3]. In such a heterostructure of a ferromagnetic thin film on a Si substrate, any structural disorder at the interface would drastically reduce the spin polarization at the interface and, hence, the spin injection efficiency [4.4]. If a small amount of Co or Fe (~ $10^{20}$ $cm^{-3}$) diffuses into the Si, each such Co or Fe atom will be likely to carry a local magnetic moment oriented randomly with respect to the magnetization direction and will scatter electrons between the two different spin channels, thereby degrading the injected spin polarization. Therefore, in order to be able to control and improve the interface, a detailed understanding of such interfaces on atomic scale is necessary.

This chapter is dedicated to the study of such ferromagnetic metal (Co and Fe) - Si (100) interface structures at room temperature.

# 4.1 Co-Si (100) interface at room temperature

## 4.1.1 Structure, interface and magnetism of Co thin films on Si (100)

As mentioned in the introduction, the ferromagnet-Si interface microstructure determines the polarized spin injection efficiency. So obtaining an atomistic understanding of the effects of buried interfaces on magnetic properties is very important for spin injection across the interfaces. In this section a detailed study of the structure, interface and magnetism of 10 nm Co on clean Si (100) is reported. Special attention has been given to study the buried Co-Si (100) interface and its magnetic properties by HRBS and SQUID magnetometer respectively.

**Experimental**

n-type Si (100) samples were cleaned by flash heating in a UHV chamber. Surface cleanness and structure were checked with AES, RHEED or HRBS. The Co films were grown by molecular beam epitaxy on cleaned Si (100) surfaces at room temperature. The deposition rate (1 ML/min) was measured by a quartz microbalance and calibrated by HRBS (accuracy within 5%). The surface structure of this 10 nm Co film was probed by RHEED, then the film was capped with 2 nm Ag. XRD-pole figures were measured for analyzing the structure of the Co thin film. A Quantum design SQUID magnetometer was used to study magnetic properties of the Co thin film. The buried Co-Si interface of a separately prepared sample was investigated by *in situ* HRBS experiments.

**Structure**

The cleaned Si (100) surface showed crystalline structure and a flat surface from *in situ* RHEED measurements. After evaporation of a 10 nm Co thin film, the RHEED pattern showed a fuzzy pattern with a signature of an hcp (0001) surface structure [shown in Fig. 4.1. (a)]. In order to determine whether the film was single crystalline or highly oriented, an XRD pole figure has been acquired using a four-circle diffractometer, which can reveal information regarding in-plane crystallinity. Figure 4.1. (b) shows an X-ray pole figure measured with Cu $K_a$ (?=1.5405Å) radiation. The pole figure is drawn as contour map of the X-ray intensity as a function of *?* (radial axis, from 0 to 90°) and *f* (circumferential axis, 0 to 360°). A combined pole-figure analysis of the Co (0001) and Si (400) reflections from the sample [Fig. 4.1. (b)]

shows a strong hcp (0001) fiber texture of the Co film grown on Si (100). The ring with small peaks in the pole figure is an indication of the preferred in plane orientation of some grains.

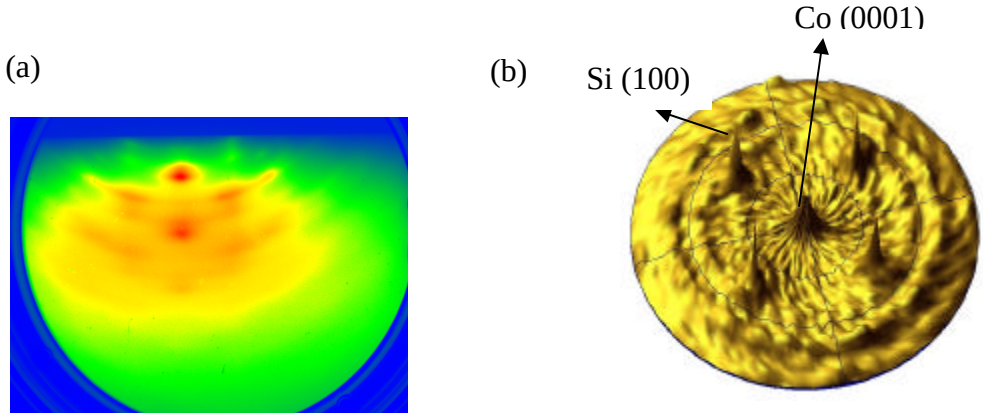


Fig. 4.1: **(a)** RHEED pattern of 10 nm Co on a cleaned Si (100) substrate **(b)** Pole figure recorded with the Co (0002) reflections. The four peaks at symmetrical positions are due to the Si (100) substrate.

**Magnetic properties**

Magnetization curves (M vs H) at 5 K and 300 K for the 10 nm Co film on Si with 2 nm Ag capping are shown in Fig. 4.2. The diamagnetic signal due to Si and Ag was subtracted from the measured data to get the magnetization of the 10 nm Co thin film. The saturation magnetizations are 1142 kA/m and 1130 kA/m at 5 K and 300 K, respectively. The coercive field of the Co film is 98.36 Oe at 300 K and 600 Oe at 5 K. The hysteresis loop deviates from a standard shape at low temperatures. Two coercive fields could be found at 203 Oe and 1506 Oe for the 5 K measurement which is an indication of an additional magnetic phase present in the sample. The magnetic moment of Co was calculated taking the thickness calibration value from the HRBS data (all Co atoms were taken into account). The magnetic moment per Co atom is found to be 1.3 $\mu_B$, which is less than the bulk cobalt magnetization value of 1.7 $\mu_B$ [4.5]. This reduction in magnetic moment and the existence of a new magnetic phase at low temperature may be due to interface effects. Therefore it carries importance to study inter-diffusion and mixing phenomena at such interfaces.

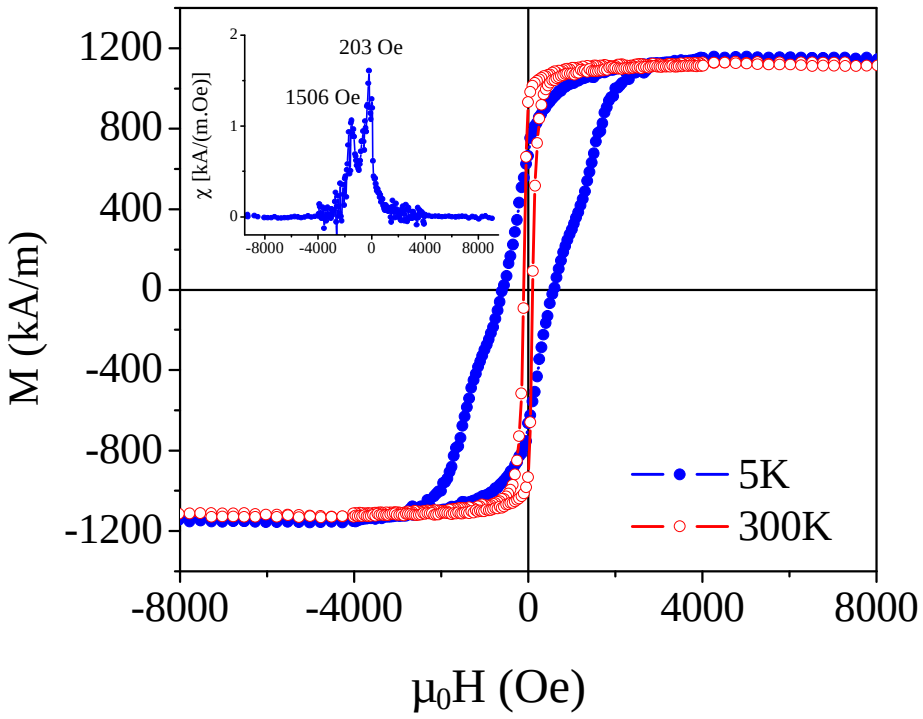


Fig. 4.2: Magnetization loops obtained from a 10 nm Co film on Si (100) at 5 K and 300 K. The **inset** shows the differential curve (susceptibility) of the 5 K magnetization curve, clearly showing the two magnetic phases.

**Interface**

The Co-Si interface structure was studied on an *in situ* prepared Co thin film on Si (100) using 2 MeV $He^+$ ions at an incidence angle of 5° and scattering angle of 37.5°. The results are shown in Fig. 4.3 (a). For 23 ML of evaporated Co on Si (100), only 6 ML of pure metallic Co grow on the surface, followed by $Co_2Si$, CoSi and $CoSi_2$ like phases at the interface. The thickness of the silicide layers at the interface is calculated by a RUMP simulation. The total amount of Co atoms found in the interface silicide layer is 16.87 ML. This means that pure metallic Co grows only for coverages grater than 16.87 ML. The thickness is smaller than in the results of Meyerheim *et al.* (19 ML) [4.6]. The Co in these silicides is distributed over a thickness of 32 ML (24.2 Å) and forms silicides of various compositions. The thicknesses of the silicide layers (from surface to interface) amount to: $Co_2Si$ : 3.26 Å, CoSi : 18.77 Å, and $CoSi_2$ : 2.2 Å.

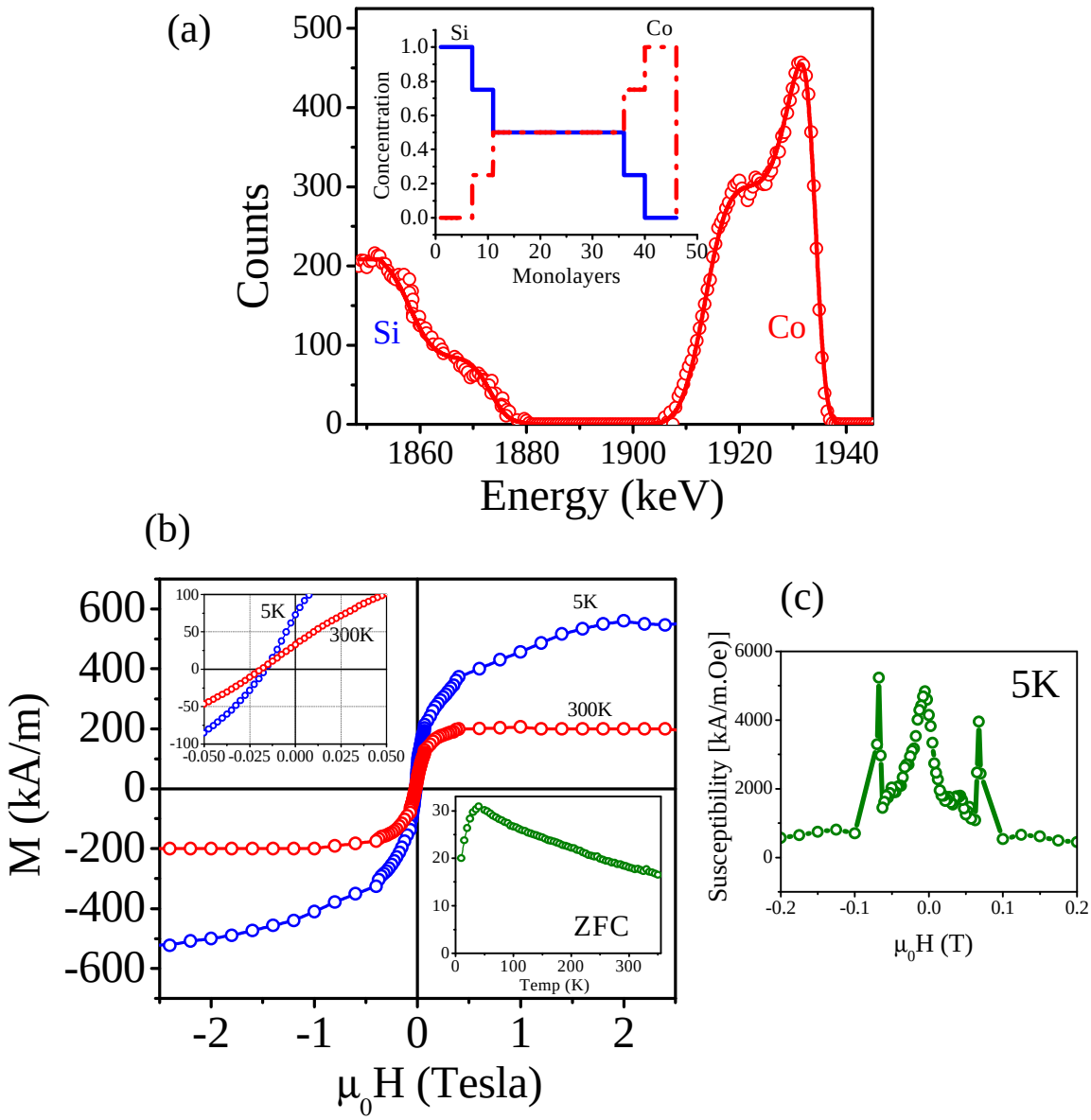


Fig. 4.3: **(a)** Si and Co backscattering spectra (circles) and RUMP simulation (solid line) for the coverage of 23.42 ML of Co on Si (100) evaporated at room temperature using 2 MeV He ions at an incidence angle of 5°. The *inset* shows the interface composition of both Si and Co as obtained from a RUMP simulation. **(b)** Magnetic measurements of 17 ML of Co on Si (100). Magnetization curves at 5 K and 300 K. (**Upper inset**) Magnified version of magnetization curve showing clear remanence and coercive fields. (**Lower inset**) The increase of magnetization up to T = 40 K in the zero field cooled curve indicates a presence of an anti ferromagnetic phase in the sample. **(c)** The differential curve of the 5 K magnetization curve, clearly showing three magnetic phases.

The elemental distribution of Si and Co at the interface for 23.4 ML of evaporated Co on Si is shown in the inset of Fig. 4.3 (a). This disordered Co-Si interface is the main reason for non-epitaxial growth of Co films and magnetic properties which is different from Co bulk material. Comparing the SQUID and HRBS data it is clear that the Co atoms in the silicide

phases carry different magnetic moments and behave differently in the applied magnetic field than Co atom in a pure Co thin film.

**Magnetic properties of interface silicide layer**

As understood from the growth of Co on Si (100), metallic Co starts to grow after 17 ML of evaporated Co. To study the magnetic properties of silicide layers formed at the interface at room temperature, 17 ML of Co was evaporated on Si (100) and capped with 3 nm of Au. So the sample must have consumed all Co to form silicide-like phases at the interface. The magnetization curves of this sample were measured at 5 K and 300 K and are shown in Fig. 4.3 (b). The sample is magnetic above room temperature. The sample also shows remanence of $M_R$ = 31.8 kA/m and coercive field of $\mu_0H$ = 0.019 Tesla at room temperature. Furthermore the temperature dependence of magnetization at zero applied field shows a peak at 40 K [Lower inset of Fig. 4.3 (b)]. This gives clear evidence that there is an antiferromagnetic phase present in the sample. The formation of any extra magnetic phase have resulted in a peak in the ZFC curve due to ‘blocking’ mechanism owing to the competition between the thermal energy and the magnetic anisotropy energy. Also the magnetization curve at 5 K shows multiple features and saturates at large applied fields in comparison to 300 K. The multiple features in the magnetization is more clear when the differential curve (susceptibility) vs. applied field is plotted [see Fig. 4.3 (c)]. From the figure it is clear that their exists three magnetic phases. So these silicide phases at the interface which are showing ferromagnetic order even at room temperature are fatal for spin injection experiments.

To improve the Co-Si interface it is necessary to understand the atomic processes going on at the interface in detail, starting at the very initial stages of growth. It is important to know, how it is possible that such a thick silicide phase forms at the interface at room temperature. Since the energy needed to remove a Si atom from a low index plane is equal to large fraction of formation energy of a vacancy in Si (about 3.5 eV). So kinetically it is almost impossible to release Si atoms at room temperature. Therefore Tu proposed the existence of some low-energy process which enables Si atoms to break away easily from the lattice [4.7]. The mixing at the interface requires the jumping of Si atoms away from the Si lattice or jumping of metal atoms into the Si or both. Since the Si jumping is energetically unfavorable at room temperature, they assumed that jumping of metal atoms into Si occurs first. They argued that the jumping can only occur via interstitial defects. The formation of metal

interstitial in Si weakens the Si-Si bond strength so that Si atom can break away from their lattice more easily. To study this postulate and the atomic processes going on at the interface, the *in situ* HRBS experiments were carried out for the growth of Co and Fe on Si (100) at very initial stages, which are presented in next two sections.

## 4.2 Initial stages of growth of Co on Si (100) at room temperature: *Subsurface enrichment of Co*

The phenomena observed at the initial stages of Co deposition on a Si substrate seem to be unique and depend on the preparation conditions. About the *growth mode* of Co on Si, Cho *et al.* [4.8] concluded that the Co atoms grow in a layer-by-layer mode, without any interdiffusion, whereas Meyerheim *et al.* [4.6] and Rangelov *et al.* [4.9] could see the in-diffusion of Co atoms for coverages higher than 0.5 ML of Co. About the *atomic positions* of Co atoms on Si (100), Scheuch *et al.* [4.10], Meyerheim *et al.* [4.6] and Gomoyunova *et al.* [4.11] found that Co is adsorbed in fourfold hollow sites (nearly in plane, $d_{\perp} \approx 0$) in every second [110] row of the Si (100) surface. The sites (sites A in the inset of Fig. 4.4(a)) are one of the low-energy sites according to density functional calculations [4.12]. In contradiction, Cho *et al*. [4.8] found that the preferred adsorption sites are on top of a Si dimer ($T_4$ sites) and sites spanning the [110] trench (HB-sites). However density functional calculations [4.12] suggested that the $T_4$ and HB sites are energetically unfavorable. Concerning the positions of the diffused Co atoms, Meyerheim *et al.* [4.6] could distinguish between several stages of growth. In the regime of 0.5 to 2.5 ML, Co atoms diffuse into the Si lattice occupying interstitial sites, for the regime above 2.5 ML the substitution of the Si host atoms by Co takes place, and for coverages above 19 ML a locally ordered metallic overlayer starts to grow.

Controversies still exist about the growth mode of Co: Does there exist a critical coverage of Co for the in-diffusion of Co and the out-diffusion of Si atoms? How thick is the silicide layer formed at the interface? What is the chemical composition of the interface layer, and which are the diffusing species at different stages of growth? In this section, some of these controversies have been addressed by an *in situ* investigation of the growth of Co (0.08 ML to 2.93 ML) on Si (100) at room temperature with HRBS.

## Experimental

The *in situ* HRBS measurements were carried out in an ultra high vacuum (UHV) system consisting of a preparation chamber, connected to a Pelletron accelerator, and an electrostatic spectrometer [4.13] for energy analysis of scattered 2 MeV $N^+$ ions at an incidence angle of 2.5° to the sample surface and a scattering angle of 37.5°. n-Si (100) samples with resistivity 4-10 O cm (P doped) were cleaned in UHV by flash heating at 1050 °C. The surface cleanness of the Si samples was verified by HRBS measurements. In the experiment Co (0.08 to 2.93 ML, 1 ML = $6.87\times10^{14}$ atoms/cm$^2$) was evaporated from an effusion cell on to the clean Si (100) surface at room temperature. Before use the effusion cell was outgassed; no C or O contaminants were found during evaporation. HRBS spectra were taken at different stages of Co deposition. The evaporation rate (0.05 ML/min) was calibrated by HRBS with an accuracy of about 5%. Each HRBS spectrum was taken on a new spot (size ~ 1 mm$^2$) to minimize the influence of radiation damage.

## Results and discussion

### Submonolayer coverage

The HRBS spectra for the evolution of the Co distribution are shown in Fig. 4.4(a) for Co coverages of 0.08-1.19 ML. The spectra exhibit two distinct peaks. A first peak between 1805 and 1815 keV is due to $N^+$ ions backscattered by Co atoms adsorbed on the Si surface, the second peak in the range 1785-1800 keV is due to Co atoms which diffused into the Si bulk. In order to obtain more detailed information about the Co depth distribution, the Co spectra were simulated by the program RUMP [4.14]. In these simulations the sample was subdivided into thin sublayers of the thickness of $6.87\times10^{14}$ atoms/cm$^2$ [this is the atomic density of the Si (100) planes]. The composition of each sublayer was varied and the HRBS spectrum calculated for the assumed Co depth distribution until good agreement with the experimental data was achieved. It is to be noted that one can exclude the growth of islands during Co deposition: From an Auger study Gallego *et al*. derive layer-by-layer growth of Co with some Si intermixed during deposition at room temperature [4.15]. Also from the HRBS data themselves this can be excluded: When island growth occurs, shadowing effects become visible in the spectra at glancing incidence, resulting in a “rounding off” of the high-energy edge of the spectra (see ref. 4.16). No such effects are seen in HRBS spectra shown in Fig. 4.4(a). However, the clusters of Co which were incorporated inside the Si lattice could not be

excluded. Most probably such clusters are present at very low coverage. In this case the concentrations given in the following are average concentrations of Co, averaged over the individual layers.

Figure 4.4(b) shows the Co concentration in the different sublayers as obtained from the RUMP simulations for Co coverage below about 1 monolayer (0.08 ML to 1.19 ML). The $0^{th}$ layer is the topmost layer; -1, -2, -3, and -4 are subsequent layers below the surface. According to my data, already at coverages as low as 0.08 ML, Co atoms are found to have diffused in the Si bulk up to the $-4^{th}$ layer. They form a subsurface maximum in the Co concentration which shifts into the Si bulk with increasing coverage. Meyerheim *et al.* [4.6] could observe in-diffusion of Co atoms only for coverages greater than 0.5 ML and Cho *et al.* [4.8] could not see any diffused Co atoms in the Si lattice for 0.6 and 1.9 ML coverage. This might be due to the fact that HRBS is by far more sensitive at small concentrations than the techniques used by these authors. My results are, however, consistent with the suggestion by Horsfield *et al*. [4.17], based on a theoretical study, that bulk diffusion of Co in Si should be very fast, possibly faster than surface diffusion, and the experimental observation of Lee *et. al.* [4.18] who finds that bulk diffusion is much faster than surface diffusion at high temperature. My observations find the same for small coverages even at room temperature. It is to be noted that these findings resemble the growth of Ge on Si (100), where the Ge atoms were found up to $4^{th}$ layer inside the Si lattice [4.19].

For the further discussion, we follow the result given in literature that the surface Co atoms are positioned in the surface Si plane (on fourfold hollow sites) and diffused-in Co atoms occupy tetrahedral interstitial sites for less than 2.5 ML of deposited Co [see inset of Fig. 4.4(a)] [4.6, 4.11]. Following this model the depth scale of the Co distribution can be rewritten. Each layer then contains exactly $6.87\times10^{14}/cm^2$ Si atoms (one (100) layer in Si); the Co concentration just adds up. Figure 4.4(c) shows the Co distribution in the Si lattice as calculated in this way. Since the Co concentration in each layer is very small, the new distribution is not much different from that of Fig. 4.4(b), but the depth scale is now given in units of (100) Si monolayers. As Fig. 4.4(c) shows, at 0.08 ML, 0.22 and 0.3 ML coverages the $-1^{st}$ Si layer is not occupied by Co atoms. This depletion of subsurface layers persists up to higher coverages (about 1ML) now extending also to other layers. The depletion is followed by a subsurface peak in the Co concentration. Both depletion (min.) and maximum (max.) shift towards larger depths in the Si bulk with increasing Co coverage. Their dependencies on the Co coverage are shown in Fig. 4.5(d) (full squares and open circles). They are the reasons for the double peak structure found in the HRBS experiments.

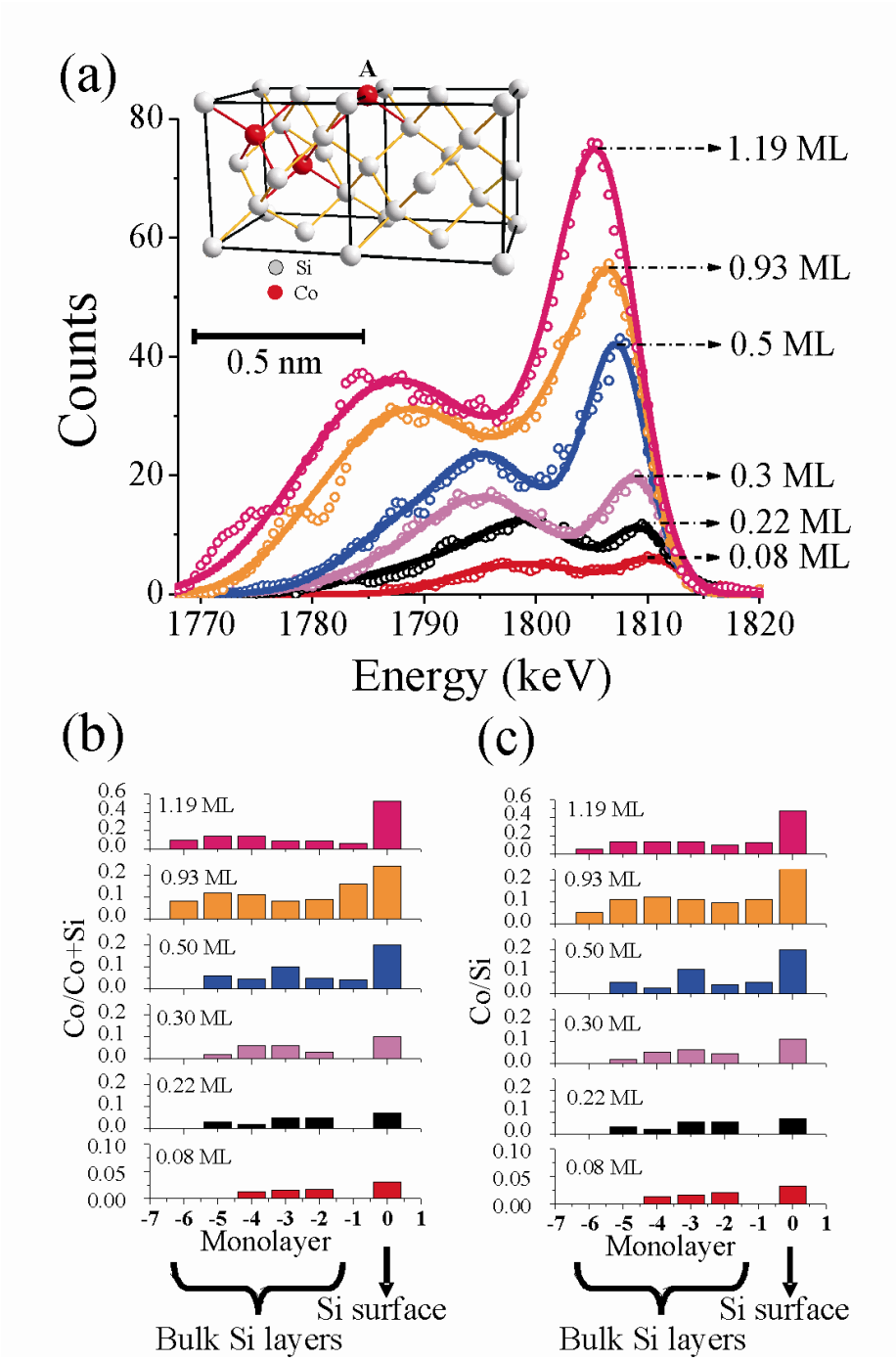


Fig. 4.4: Co on Si (100), submonolayer coverage (0.08-1.19 ML). **(a)** Co edge of HRBS spectra (circles) and RUMP simulation (solid lines). The peaks between 1805 and 1815 keV are due to backscattering from Co at the surface. The other peak in the range of 1785-1800 keV is due to Co atoms in the Si bulk. The inset shows the tetrahedral sites of Si lattice. Site 'A' is the fourfold hollow site at the Si surface favored as adsorption site for Co atoms. **(b)** Co concentration (Co atoms per total number of atoms) in subsequent layers (each $6.87\times10^{14}$ atoms/cm$^2$ thick) of the sample as obtained from the RUMP simulation. The 0$^{th}$ layer is the topmost Si layer; -1, -2, -3, -4, and -5 are subsequent layers in bulk. Note: the y axes for 0.08 ML and 1.19 ML are having scales different from others. **(c)** Co concentration (Co/Si) in the various Si (100) layers of the Si crystal as derived from the RUMP simulations. Each layer consists of $6.87\times10^{14}$ atoms/cm$^2$ Si plus some Co atoms. Hence the distributions slightly differ from that of Fig. 1b. Note: the y axis for 0.08 and 1.19 ML have scales different from others.

This is similar to the recent results about a subsurface Au-enriched phase in a liquid AuSi alloy [4.20]. In these systems such a configuration is stabilized by the minimization of the free energy, essentially consisting of atomic binding and surface energies, and the entropy of mixing. In solids strain energy enters in addition. With increasing coverage (0.5-1.19 ML) the vacant -1$^{st}$ Si layer slowly fills up, but the depletion in the Co composition is still retained. In this coverage range the amount of Co atoms increases in the surface layer as well as in the subsurface (up to -6$^{th}$ layer). So the main diffusing species at these coverages seems to be Co in the Si lattice. A $Co_2Si$ phase (Co/Si ratio of about 0.67) could not be found in contrast to the observation by Gallego *et al.* [4.15]. On the other hand, at 0.93 ML coverage, the first evidence of 1 ML of a $CoSi_3$ phase is found at the surface. This metastable silicide phase formation can be attributed to the lack of sufficient Co atoms to form more stable silicide phases. For 1.19 ML the Co content in the surface Si layer is 0.5 (Co/Si ratio), which is the expected saturation coverage for the fourfold hollow surface adsorption sites as suggested by Meyerheim *et al.* [4.6]

**Monolayer coverage**

Figure 4.5(a) shows Co HRBS spectra and RUMP simulations for Co coverages of 2.02 and 2.93 ML. The Co content (Co/Co+Si) in each Si monolayer, as obtained from the RUMP simulation, is shown in Fig. 4.5(b). Since a more or less perfect Si lattice with a few Co interstitials can not be assumed at these high coverages, the $x$ axis is again in units of $6.87\times10^{14}$ atoms/cm$^2$. For 2.02 ML and 2.93 ML, silicide-like phases (CoSi and $CoSi_2$) can be observed at the surface.

The existence of Si at the very surface [see Fig. 4.5(c)] gives clear evidence of the out-diffusion of Si atoms through the grown Co film. In particular for the Co coverage of 2.933 ML a stoichiometric composition of a CoSi phase of 3 ML in thickness is observed at the surface. By careful analysis of the data in this work, the growth of metallic Co on the Si surface at these coverages can be ruled out (as suggested by Cho *et al*. [4.8]). A metallic Co phase would enter the RUMP simulation through its higher Co concentration (besides a change in the stopping power) and would lead to a higher HRBS yield. Furthermore, there should be a shift in the high-energy edge of Si. Both predictions are incompatible with my experimental data. Evidently, for 2.02 and 2.93 ML, Co atoms grow on the Si surface and simultaneously Si atoms diffuse out through the growing Co film to maintain the silicide growth. These results are in good agreement with the results of Meyerheim *et al.* [4.6] and Rangelov *et al.* [4.9].

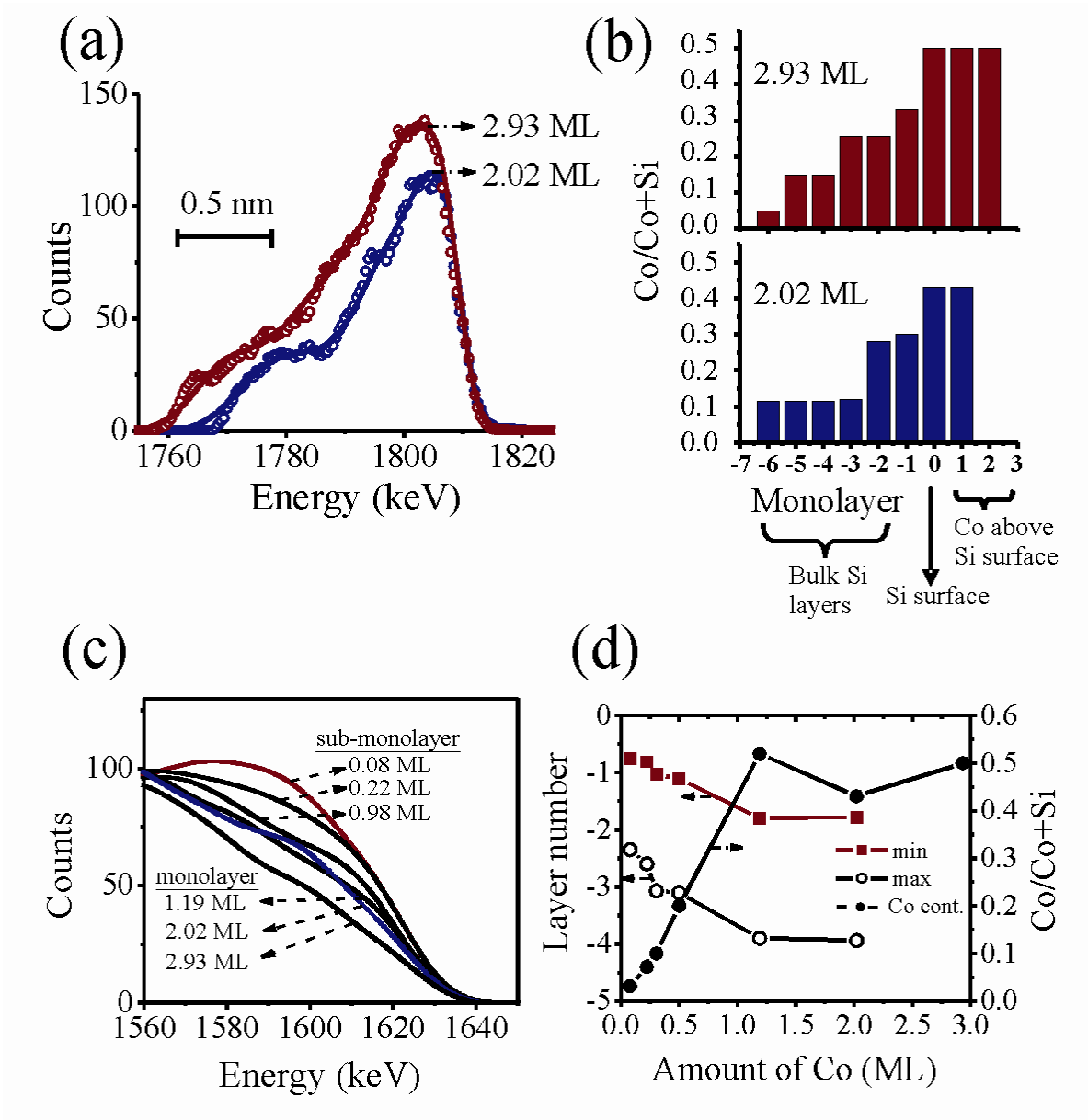


Fig. 4.5: **(a)** Co on Si (100), higher coverage (2.02 and 2.93 ML). Co edge of HRBS spectra (circles) and RUMP simulation (solid lines). **(b)** Co concentration (Co atoms per total number of atoms) in subsequent layers (each $6.87\times10^{14}$ atoms/cm$^2$ thick) of the sample as obtained from the RUMP simulation. The 0$^{th}$ layer is the topmost Si layer; -1, -2, -3, -4, and -5 are subsequent layers in the bulk and 1, 2 are Co layers above the initial Si surface. The latter indicate the growth of silicide at the surface. **(c)** High-energy edge of the HRBS spectra of Si for Co coverages from 0.08 to 2.93 ML on a Si (100) surface. The Si signal extends to the sample surface at all Co coverages. A smoothing procedure has been applied to the spectra to ease the discerniability. **(d)** Co content (Co atoms per total number of atoms) in the 0$^{th}$ Si layer (right scale) and position of the Co depletion (min.) and subsurface maximum (max., both left scale) versus the amount of evaporated Co on Si (100). The depletion points (min) and the maxima (max) were obtained by 4$^{th}$ order polynomial fits to the data of Fig. 1(c). The 0$^{th}$ layer saturates at about 0.5.

The Co content (Co/Co+Si) in the $0^{th}$ layer of the Si (100) sample is plotted in Fig. 4.5(d) as a function of the total evaporated amount of Co (full circles). At a Co coverage of 1.19 ML, the $0^{th}$ Si layer saturates at a Co concentration of ~ 0.5 which is in good agreement with the saturation concentration (0.5) of the proposed Co atomic positions, i.e. fourfold hollow sites in every second row of the Si (100) surface.

**Magnetic properties of 2.9 ML of Co on Si (100)**

The Si sample with 2.9 ML of evaporated Co (this yield 3 ML of CoSi phase at the surface, followed by diffused in Co) was capped with 3 nm of Au and the magnetic behavior (magnetization curve) measured with a SQUID magnetometer at room temperature.

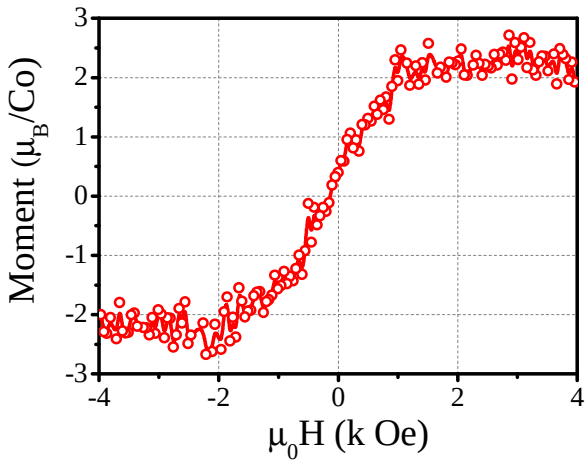


Fig. 4.6: The magnetization curve for 2.93 ML of Co on Si (100) measured at room temperature.

The thin silicide-like layer was found to be ferromagnetic and have remanence of $M_R$ = 0.436 $\mu_B$/Co and coercive field of $\mu_0$H = 128 Oe (see Fig. 4.6). The saturation magnetic moment was found to be 2.3 $\mu_B$ per Co atom, which is even higher than the bulk magnetic moment of Co (1.7 $\mu_B$). Recently theoretical work based on first principle calculations predicts that such ultra thin silicide layers show ferromagnetic order [4.21]. So my experimental observations support the theoretical prediction that the ultra thin silicide films have ferromagnetic order even at room temperature.

## 4.3 Fe-Si (100) interface at room temperature

Fe having 45 % spin polarization at room temperature is a very attractive material for spin injection into Si [4.2]. The spin injection efficiency largely depends on the interface structure between Fe and Si [4.4]. Because of short coherence length of spin polarization, electron spin

phenomena can only occur across a few nm thick interface region. So spin injection from Fe into Si strongly depend on the interface structure. Atomic scale control of the interface is thus the prerequisite for the realization of spin injection, which require well understanding of surface mixing behavior during growth of such heterostructure.

### 4.3.1 Initial stages of growth of Fe on Si (100)

On the *growth* of Fe on a Si (100) surface Ruehrnschopf *et al.* [4.22] concluded that Fe grows in a layer by layer mode for higher coverages except the reaction in the sub-monolayer coverage. However, Klaesges *et al.* [4.23] and Gomoyunova *et al.* [4.24] suggested that a strong chemical reaction between Fe and Si results in a disordered Fe/Si overlayer. About the *thickness of the reacted layer* at the interface, Gallego *et al.* [4.25] revealed that Si diffuses to the surface for less than 8 ML and metallic Fe grows for coverages higher than 8 ML. Alvarez *et al.* [4.26] found that above the coverage of 5 ML the reaction slows down and metallic Fe grows with some Si atoms still dissolved in the Fe matrix. Ruehrnschopf *et al.* [4.22] could not detect any interdiffusion whereas Klaesges *et al.* [4.23] estimated the interface silicide thickness to be around ~ 2 nm. The *chemical composition* of the interface layer at different stages of growth for the low coverage regime doesn't seem to be not settled yet. Konuma *et al.* [4.27] concluded that 5 ML of Fe evaporated on Si mixes strongly and forms a FeSi-like phase. However Klaesges *et al.* [4.23] can differentiate between different silicides for different coverages. Up to a coverage of 3 ML of Fe on Si the authors could see non-stoichiometric intermixing. For coverages grater than 4 ML a $Fe_3Si$-like phase is formed having a thickness around 2 nm. For coverages greater than 10 ML the silicide formation abruptly ends and the spectra resemble that of bulk Fe.

To some extent the disagreement between different authors may be due to slightly different experimental conditions (Si surface preparation, deposition rate, Fe thickness calibration, sensitivity of the measuring technique, etc.). In this study, the Fe depth distribution and Fe/Si composition at initial stages of Fe growth on Si (100) are presented, as obtained by an *in situ* HRBS experiment at room temperature. From the RUMP fitting of my experimental results I obtained information about growth mode, thickness of the reacted layer and formation of different phases at very initial stages at the room temperature. This result has significant implications for spin injection from Fe into Si.

**Results and discussion**

Two different set of experiments are presented here: one for very initial stages of Fe growth (0.0325 – 0.12 ML) and other for higher coverages (0.28 – 9.1 ML). The *in situ* HRBS measurements were performed using 2 MeV $N^+$ ions at incidence angles of 2° to the sample surface and at a scattering angle of 37.5°. Fe with 4N purity was evaporated from 0.0325 ML to 9.3 ML from an effusion cell on a cleaned Si (100) surface. The HRBS spectrum of the Fe distribution for the coverage of 0.0325 ML is shown in Fig. 4.7(a). The spectrum shows three distinct peaks which correspond to Fe atoms in three well defined depths in the Si lattice. In order to obtain more detailed information about the Fe depth distribution, the Fe spectrum was simulated by the program RUMP. In these simulations the Si sample was subdivided into thin sublayers containing exactly $6.87\times10^{14}/cm^2$ Si atoms and the appropriate amount of Fe atoms added up. As one can see from Fig. 4.7(a) the simulation fits HRBS date very well. From the sharp high-energy edge of HRBS spectra 3D-island growth of Fe at this coverage can be excluded.

Fig. 4.7(b) shows the Fe concentration in the different sublayers as obtained from the RUMP simulation for 0.0325 ML of Fe coverage. According to these results the top-most layer is a layer of Si atoms with a few Fe atoms ($0^{th}$ layer). The next layer, layer '-1' is the next (100) Si layer; it is depleted of Fe as is layer -3 which is completely free of Fe. The data indicate that at a coverage as low as 0.0325 ML, Fe atoms have apparently diffused into the Si bulk up to the $-4^{th}$ layer. The amount of diffused-in Fe atoms is even higher than the amount of Fe in the Si surface. The Fe atoms are, however, by no means homogeneously distributed over this range. As Fig. 4.7(b) shows, every second Si layer is depleted of Fe, thus giving an oscillatory Fe distribution in the Si lattice.

Fig. 4.7(c) finally illustrates the distribution of the Fe atoms in the Si lattice and correlates this distribution with the peaks observed in the HRBS spectrum. The first peak at 1800 keV thus corresponds to Fe atoms in the $1^{st}$ Si layer, the second peak in the spectrum at 1790 keV to Fe atoms in the $-2^{nd}$ layer (2.7 Å from the Si surface), and the third peak to Fe atoms in the $-4^{th}$ layer (5.43 Å from the Si surface). The diffused in Fe atoms apparently tend to avoid occupy adjacent layers in Si lattice. This is similar to results on the diffusion microstructure of Ni in Si (100) [4.28] and the distribution of metal atoms in metal alloys like $Cu_3Au$ [4.29] close to the surface. A similar behavior is also found for the deposition of Co on Si (100) at -60°C (see Chapter 5 of this thesis). In these systems such a configuration is stabilized by the minimization of the Gibbs free energy, consisting of atomic binding, strain and surface energies, and the entropy of mixing.

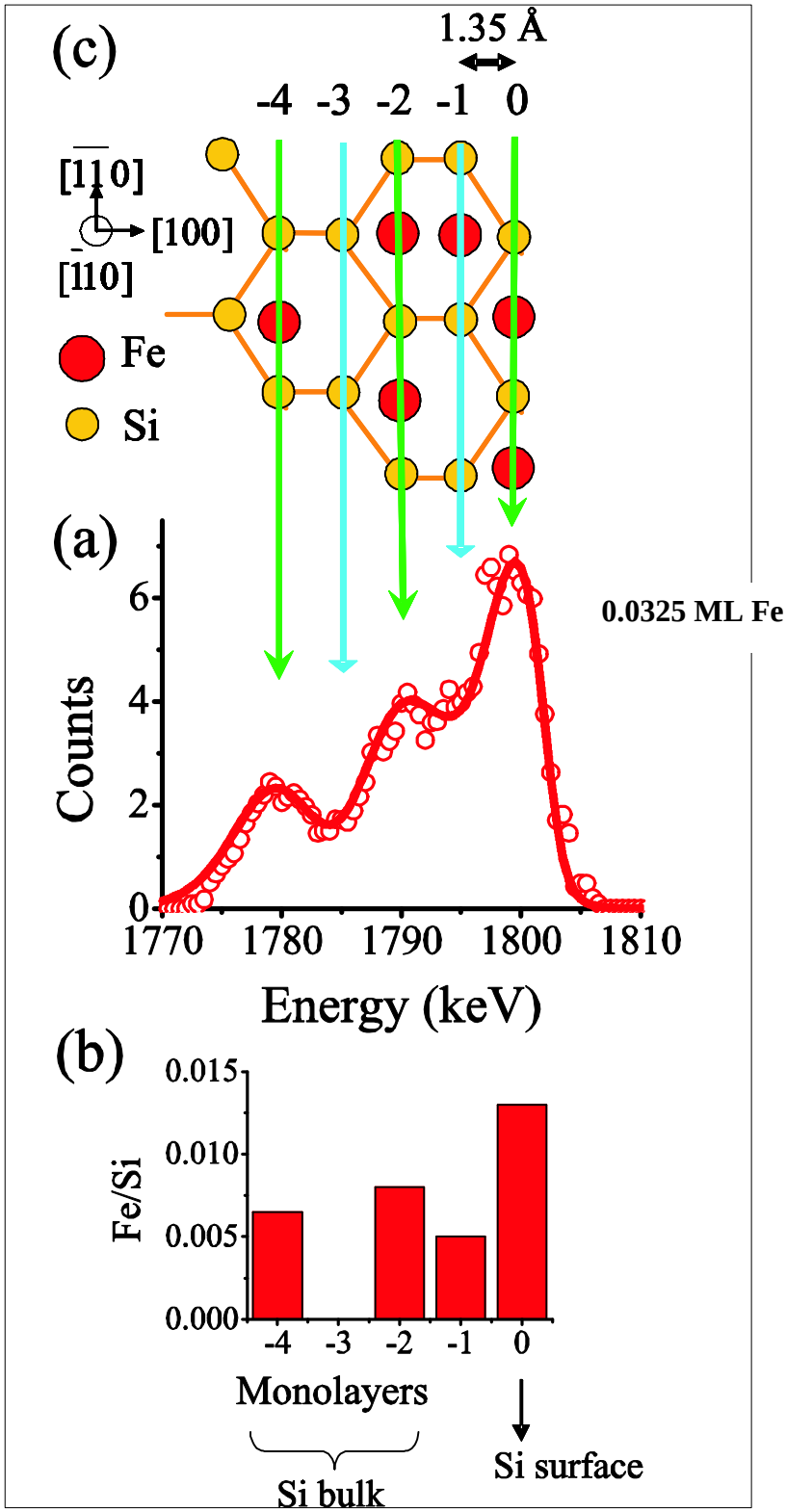


Fig. 4.7: 0.0325 ML of Fe evaporated on Si (100) at room temperature. **(a)** Fe edge of HRBS spectrum (circles) using 2 MeV $N^+$ ions and RUMP simulation (solid line). The peak at 1800 keV is due to backscattering from Fe in the $0^{th}$ layer (Si surface), the $2^{nd}$ peak at 1790 keV is due to Fe atoms in the -$2^{nd}$ Si layer and the $3^{rd}$ peak is due to Fe atoms in the -$4^{th}$ Si layer. **(b)** Fe concentration (Fe/Fe+Si) in the different Si (100) layers of the Si crystal as derived from the RUMP simulation. Each layer consists of $6.87\times10^{14}$ atoms/$cm^2$ Si plus some Fe atoms. Layer 0 is the $1^{st}$ Si layer; layers -1, -2 and -3 are subsequent layers in the Si bulk. **(c)** Projected atomic positions of diffused Fe atoms in the Si lattice showing atomic positions corresponding to the peaks of the HRBS spectrum.

With increasing coverage (from 0.068 – 1.41ML) no such oscillations could be observed in the Fe spectra (see Fig. 4.8). This indicates that the Si crystal structure is completely destroyed at these coverages. From the HRBS data it can also be seen that the high-energy edges of the HRBS spectra are not sharp, giving strong evidence for 3D-island growth of Fe-silicide phases. This island growth produces shadowing effects which result in a "rounding off" of the high-energy edge at glancing ion incidence [4.16]. This also means that strong inter-diffusion continues to occur, destroying the lattice structure of Si and resulting in the formation of amorphous silicide phases. At these coverages formation of definite silicide phases (e.g. $Fe_2Si$) and layer by layer growth could not be observed in contradiction to first results by Gallego *et al.* [4.25].

Figure 4.8(c) shows Fe HRBS spectra and RUMP simulations for Fe coverages of 2.5, 6.4 and 9.1 ML. The Fe content (Fe/Fe+Si) in each monolayer, as obtained from the RUMP simulation, is shown in Fig. 4.8(e). Since more or less perfect Si lattice with a few Fe interstitials can not be assumed at these high coverages, the $x$ axis is in units of $6.87\times10^{14}$ atoms/cm$^2$. The surface at higher coverage seems to now be smooth and homogeneous indicated by a sharp high-energy edge in the HRBS spectra. For the evaporation of 2.51 ML of Fe, 6 ML of $FeSi_2$ phase at the surface, 3 ML of $FeSi_3$ phase just below, and the rest 4 ML of inter-diffused layers having no definite phase were observed. For 6.4 ML of evaporated Fe, 7 ML of FeSi phase, 3 ML of $FeSi_2$ and 7 ML of $FeSi_3$ could be observed. At this coverage, three Si-rich phases were observed in contrast to the single FeSi phase observed by Konuma *et al.* [4.27]. For 9.167 ML of evaporated Fe, 6 ML of $Fe_3Si$, 9 ML of $Fe_2Si$ and 10 ML of a FeSi-like phase, having 2 ML of transition layers between the different silicide phases, were observed. There in particular is no sharp silicide/Si interface as stated by Klaesges *et al.* [4.23]. The thickness of all silicide phases formed for 9.167 ML is around 2 nm and still no pure metallic Fe has formed. It is to be noted that by RUMP simulation, distinctions can be made between the growth of pure Fe and silicide on a Si surface, from the stopping power which enters the simulation (it almost a factor of 2 different for Fe and e.g. FeSi) and from the height of the Fe peak. Further, looking at the HRBS spectra of the Si edge in Fig. 4.8(d), it is clear that there is no shift in the Si peak position. This gives clear indication that Si remains at the surface at all coverage even after 9.2 ML of Fe evaporation.

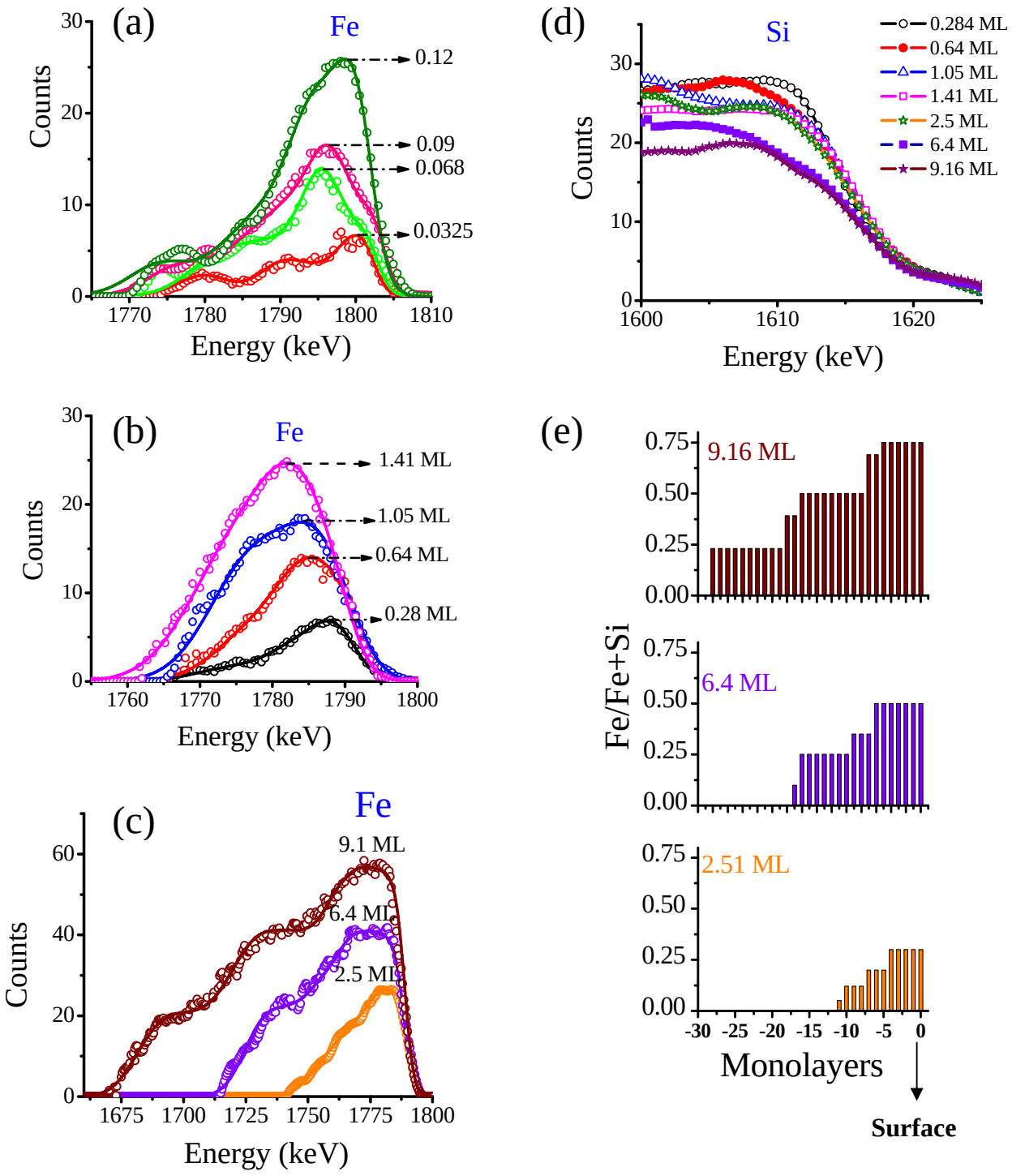


Fig. 4.8: Fe on Si (100), (0.0325-9.1 ML). **(a-c)** Fe edge of HRBS spectra (circles) and RUMP simulation (solid lines). **(d)** High-energy edge of the HRBS spectra of Si. Si atoms are found at the surface at all coverage. **(e)** Fe concentration (Fe atoms per total number of atoms) in subsequent layers (each $6.87\times10^{14}$ atoms/cm$^2$ thick) of the sample for the coverage of 2.5-9.1 ML, as obtained from the RUMP simulation.

The results presented here provide evidence for a silicide formation mechanism based on the interstitial defect model by Tu [4.7]. According to this model the in-diffused Co (or Fe) atoms occupy the tetrahedral interstitial voids in the Si lattice which requires very little activation energy. Charge transfer between adjacent Co (or Fe) and Si atoms occurs, and the local Si covalent bonds transform into weaker metal-like bonds. This interstitial atom-induced bond transformation produces the reduced Si bond strength needed to account for room temperature silicide formation.

From the knowledge gained from the above section, it is important to prohibit the in-diffusion of Co (or Fe) into the intestinal sites at the initial stages of growth and the out-diffusion of Si atoms in the latter stages. The diffusion of Co and Fe atoms as obtained from the experimental data and theoretical calculations existing in the literature is energetically favorable. To change the laws of nature, non-equilibrium growth conditions are necessary. In the next chapter interface studies under non-equilibrium growth conditions are presented.

# Chapter 5

# Ferromagnet-Si Schottky contact: Nonequilibrium growth of Co on Si

As discussed in chapter 2 and 4, it is highly desirable to fabricate Co/Si (100) heterostructures with atomically abrupt interfaces for spin injection into Si. Such sharp interfaces are typically unfavorable from thermodynamic equilibrium consideration but may be possible to grow using non equilibrium growth conditions. As understood from the growth of Co on Si (100) at room temperature from the previous chapter, diffused-in Co atoms occupying the tetrahedral interstitial sites are the main cause for the weakening of Si-Si bonds. These weakened bonds allow Si atoms to diffuse out to the surface and form silicide-like phases. The growth of Co on Si substrate strongly depends on the substrate preparation conditions. So in order to control and improve the interface, non-equilibrium growth conditions are necessary. (1) A simple solution would be to limit the inter-diffusion by lowering the growth temperature, preventing the atoms from finding energetically preferred positions. (2) Another compelling example is the “surfactant action” in heteroepitaxy, where the surfactant atoms float on the growth front while promoting layer-by-layer growth and sharp interfaces. In this chapter we will discuss these two growth modes for the Co/Si (100) system.

## 5.1 Low temperature growth of Co on Si (100) at -60 °C:

***Compositional oscillations of diffused Co atoms in Si lattice***

As mentioned in the previous chapter, diffused-in Co atoms occupying the tetrahedral interstitial sites are the main cause for the weakening of Si-Si bonds. These weakened bonds allow Si atoms to diffuse out to the surface and form silicide-like phases at room temperature.

Thus low temperature growth would prohibit the diffusion of Co into the Si lattice and reduce the formation of silicide phases at the interface [5.1].

In this section, the Co depth distribution and Co/Si composition at the initial stages of Co growth on Si (100) are investigated in an *in situ* experiment by HRBS at *low temperature* (-60 °C). From a RUMP fitting of the experimental results, the information are obtained about the main diffusing species, the thickness of the reacted Si layer and the different phases formed at -60 °C from very initial stages to fully metallic Co coverage.

### 5.1.1 Experimental

The *in situ* HRBS measurements were performed in an ultra high vacuum (UHV) system consisting of a preparation chamber, connected to a Pelletron accelerator, and an electrostatic spectrometer for energy analysis of scattered 2 MeV $N^+$ ions at incidence angles of 2° to the sample surface and at a scattering angle of 37.5°. n-Si (100) with resistivity of 4-10 O cm (p doped) were cleaned in UHV by flash heating at 950 °C. From this temperature the samples were slowly cooled down to -60 °C. The surface cleanness of the Si samples was verified by HRBS measurements. In the experiment both, the Co growth [0.1 to 5.93 ML, 1 ML = $6.87\times10^{14}$ atoms/cm$^2$ = number density of Si (100) layers] and the HRBS measurements were done keeping the Si substrate at -60 °C. Co with 4N purity was evaporated from an effusion cell. Before use the effusion cell was outgassed; no C or O contaminants were found during evaporation. The evaporation rate (0.05 ML/min) was calibrated by HRBS with an accuracy of about 5%. Each HRBS spectrum was taken on a new spot (size ~ 1 mm$^2$) to minimize the influence of radiation damage.

### 5.1.2 Submonolayer coverage

The HRBS spectrum of the Co distribution for the coverage of 0.1 ML is shown in Fig. 5.1 (a). The spectrum shows three distinct peaks which correspond to Co atoms in three well defined depths in the Si lattice: at the surface, below the surface and somewhat further inside. In order to obtain more detailed information about the Co depth distribution, the Co spectrum was simulated by the program RUMP. In these simulations the Si sample was subdivided into thin sublayers containing exactly $6.87\times10^{14}$/cm$^2$ Si atoms and the appropriate amount of Co atoms added up. The composition of each sublayer was varied (by varying the

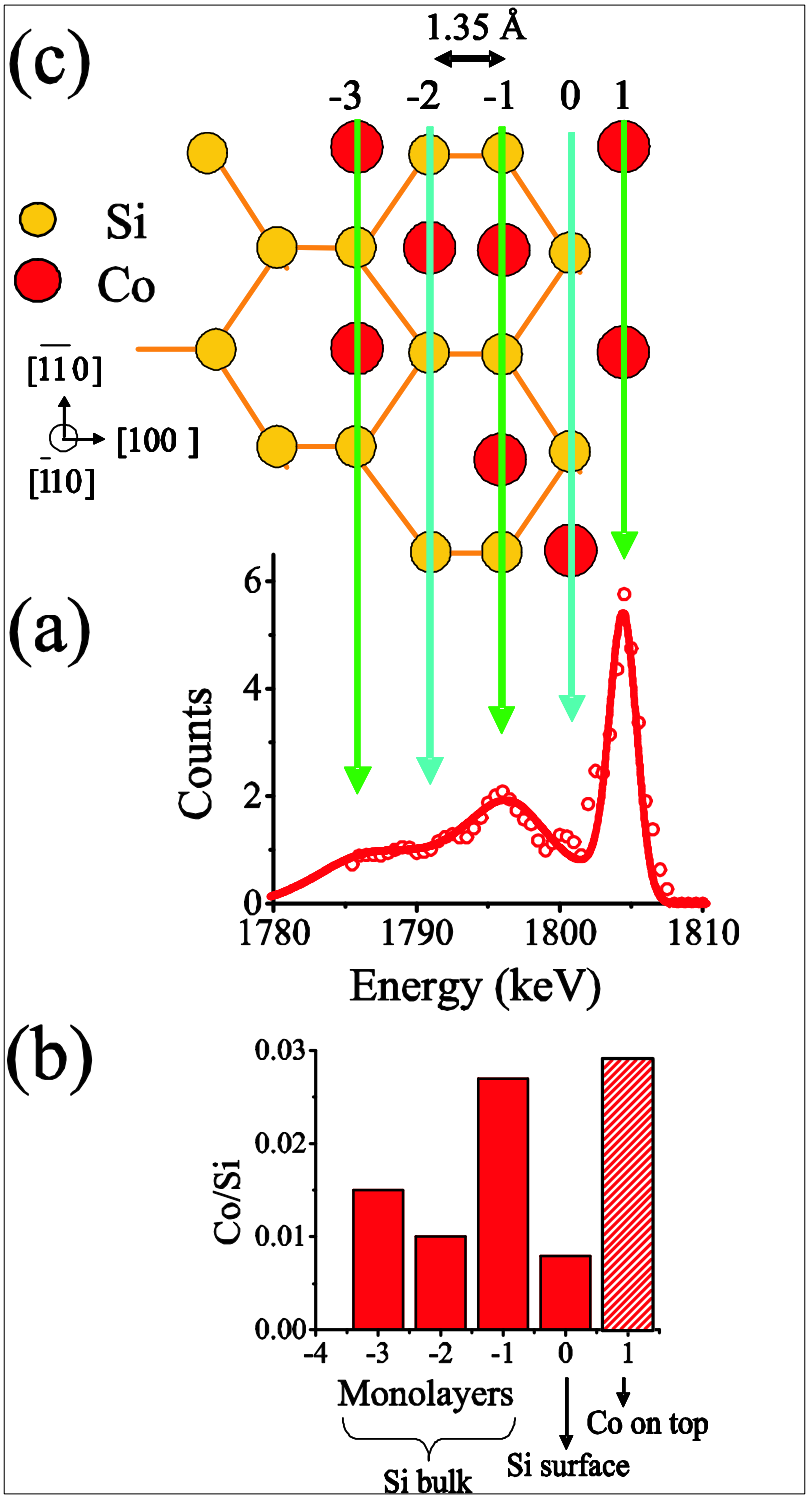


Fig. 5.1: 0.1 ML of evaporated Co on Si (100) at -60 °C. **(a)** Co edge of HRBS spectrum (circles) using 2 MeV $N^+$ ions and RUMP simulation (solid line). The peak at 1804 keV is due to backscattering from Co at the surface, the 2nd peak at 1796 keV is due to Co atoms in the -1st Si layer and the 3rd peak is due to Co atoms in the -3rd Si layer. **(b)** Co concentration (Co/Si) in the different Si (100) layers of the Si crystal as derived from the RUMP simulation. Each layer consists of $6.87\times10^{14}$ atoms/$cm^2$ Si plus some Co atoms. Layer 1 (hatched column) corresponds to Co atoms growing on top of the Si crystal, layer 0 is the 1st Si layer; layers -1, -2 and -3 are subsequent layers in the Si bulk (solid columns). **(c)** Projected atomic positions of diffused Co atoms in the Si lattice showing atomic positions corresponding to the peaks of the HRBS spectrum.

Co content) and the HRBS spectrum calculated for the assumed Co depth distribution until good agreement was achieved with the experimental data. At the small coverages of Fig. 5.1 (a) and also Fig. 5.2 (a) (0.1 - 1.3 ML), the Co atoms were assumed to be adsorbed on top of the Si surface and to occupy sites in the (100) Si layers, exclusively. The latter follows the results of Meyerheim *et al.* [5.2] indicating that at low Co coverage the Co atoms take tetrahedral interstitial sites in the Si lattice and four-fold hollow sites in the first Si layer which all are allocated on (100) Si planes. It is to be noted that one can exclude the growth of islands during Co deposition: From an Auger study Gallego *et al*. [5.3] derives layer-by-layer growth of Co with some Si intermixed during deposition at room temperature. Also from the HRBS data themselves this can be excluded: When island growth occurs, shadowing effects would become visible in the spectra at glancing incidence, resulting in a “rounding off” of the high-energy edge of the spectra [5.4]. No such effects are seen in our HRBS spectra. One can, however, not exclude clusters of Co which are incorporated inside the Si lattice. Most probably such clusters are present at very low coverage. In this case the concentrations given in the following are average concentrations of Co, averaged over the individual layers.

Fig. 5.1(b) shows the Co concentration in the different sublayers as obtained from the RUMP simulation for 0.1 ML of Co coverage. According to these results the top-most layer is a layer of Co atoms on top of the Si surface ($1^{st}$ layer). As a careful analysis of our data shows, it is free of Si atoms (the presence of Si atoms in this layer would enter the RUMP simulation through a different stopping power). As Fig. 5.1(a) shows, one can fit the experimental data very well in this way, which we can not do otherways. It should be noted that this result is different from results for Co growth on Si (100) at room temperature by our group [5.1] [see also Fig. 5.2(c)] and by Meyerheim *et al.* [5.2] where only an incorporation of Co in the top-most Si layer was observed. The next layer, layer ‘0’ in Fig. 5.1(b), is the top-most (100) Si layer; it is almost free of Co. Layers -1, -2, and -3 are subsequent layers below the Si surface. They all exhibit small amounts of Co. This means that at a coverage as low as 0.1 ML, Co atoms have apparently diffused into the Si bulk up to the $-3^{rd}$ layer. The amount of diffused-in Co atoms is even higher than the amount of Co on top of the Si surface. The Co atoms are, however, by no means homogeneously distributed over this range. As Fig. 5.1(b) shows, every second Si layer is depleted of Co, thus giving an oscillatory Co distribution in the Si lattice. This is similar to results on the diffusion microstructure of Ni in Si (100) [5.5] and the distribution of metal atoms in metal alloys like $Cu_3Au$ [5.6] close to the surface. In these systems such a configuration is stabilized by the minimization of the Gibbs free energy, consisting of atomic binding, strain and surface energies, and the entropy of mixing.

Fig. 5.1(c) finally illustrates the distribution of the Co atoms in the Si lattice and correlates this distribution with the peaks observed in the HRBS spectrum. The first peak at 1804 keV thus corresponds to Co atoms on top of the Si surface, the second peak in the spectrum at 1796 keV to Co atoms in the -1$^{st}$ layer (1.35 Å from the Si surface), and the third peak to Co atoms in the -3$^{rd}$ layer (4.05 Å from the Si surface).

With increasing coverage (from 0.36-1.3 ML) the amount of diffused-in Co increases as does the amount of Co on top of the Si surface [see Fig. 5.2(a)], but the oscillatory behavior in the HRBS spectra is still preserved. This can also clearly be seen in the results of the RUMP simulation of the spectra [Fig. 5.2(b)]. From this compositional analysis it further is clear that for all coverages metallic Co grows on top of the Si surface, in addition to diffused-in Co. The diffused-in Co atoms now fill up Si layers which were Co depleted before, but the oscillatory behavior of the Co distribution is still preserved: The 0$^{th}$ and -2$^{nd}$ layers remain depleted of Co at all coverages. The Co contents (Co/Si) in the layers +1 to -3 as obtained from Fig. 5.2(b) are plotted in Fig. 5.2(d) versus the evaporated amount of Co (0.1-1.3 ML). The slopes of the plots are indicative of the incorporation rates of Co at and below the surface at different Co coverages. The concentration of Co in layer 0 and layer -2 are lowest for all coverages. At very initial stages of growth (for 0.1 and 0.36 ML) the amounts of Co in layer 1 and layer 0 stay almost constant, while the amount of Co in layer -1 and -3 strongly increases [see also Fig. 5.2(b)]. This means that the strong in-diffusion of Co continues at this coverage leaving the Co content of the surface layer (layer 1) almost unaffected. It is to be noted that this is consistent with the suggestion by Horsfield *et al.* [5.7], based on a theoretical study, that bulk diffusion of Co in Si should be very fast, possibly faster than surface diffusion, and the experimental observation of Lee *et al.* [5.8] who find that bulk diffusion is much faster than surface diffusion at high temperature. The present observations find the same for small coverages even at -60 °C.

### 5.1.3 Comparison with room temperature measurements

For direct comparison with the low temperature growth data presented here, Co HRBS spectra of a sample grown at room temperature (22 °C, measured with 2 MeV $N^+$ ions, incidence angle 2.5°, scattering angle 37.5°) are presented in Fig. 5.2(c). As the figure shows, the distribution of Co in this sample is markedly different: i) At -60 °C the Co atoms at the surface occupy positions on top of the Si surface instead of being incorporated in the Si surface, as observed at 22 °C. This results in the formation of a pure Co surface layer at -60

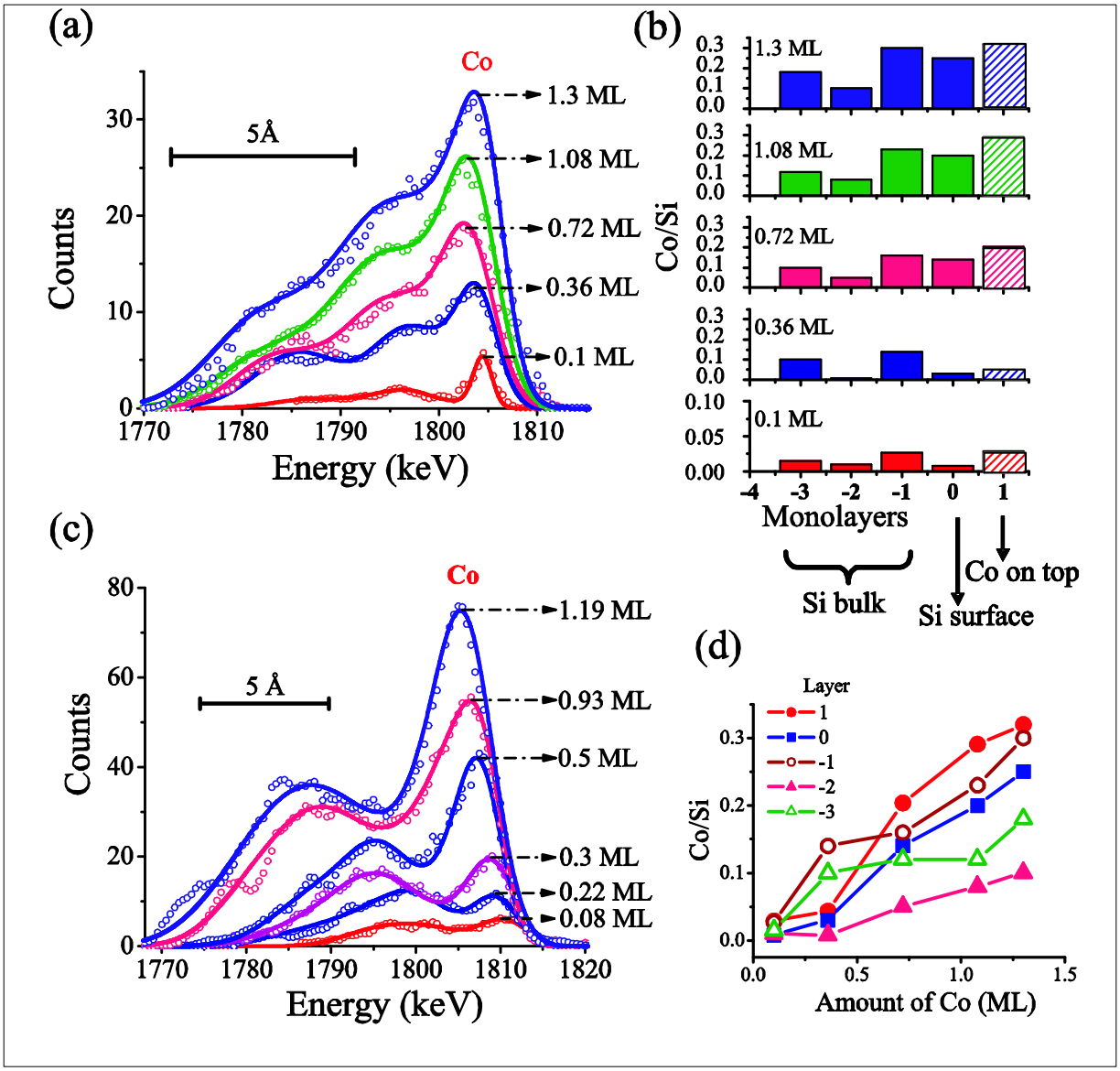


Fig. 5.2: **(a)** Co on Si (100), submonolayer coverage (0.1 to 1.3 ML) at -60 °C : Co edge of HRBS spectra (circles) using 2 MeV $N^+$ ions and RUMP simulations (solid lines). **(b)** Co concentration (Co/Si) in the different Si (100) layers of the Si crystal as derived from (a) by RUMP simulations. Each layer consists of $6.87\times10^{14}$ atoms/cm$^2$ Si plus some Co atoms. Layer 1 (hatched column) corresponds to Co atoms growing on top of the Si crystal, layer 0 is the 1$^{st}$ Si layer; layers -1, -2 and -3 are subsequent layers in the Si bulk (solid columns). Note: the y axis for 0.1 ML is scaled differently than the others. **(c)** HRBS spectrum of Co on Si (100) deposited at room temperature [11] (2 MeV $N^+$ ions, incidence angle 2.5°, sub-monolayer coverage: 0.08-1.19 ML): experimental data (circles) and RUMP simulations (solid lines). The peaks between 1805 and 1815 keV are due to backscattering from Co at the surface. A second peak in the range of 1785-1800 keV is due to subsurface Co enrichment in the Si bulk. **(d)** Co concentration (Co/Si) in the layers -3 to +1 of Fig. 5.2(b) versus the amount of evaporated Co (0.1 to 1.3 ML) on Si (100). As the figure shows, layers 0 and -2 are Co depleted compared to adjacent layers.

°C instead of the formation of a silicide surface layer at 22 °C ii) At -60 °C the in-diffusion of Co is strongly reduced. One can see directly from Fig. 5.2 that the Co atoms are localized closer to the surface at low temperature than at room temperature. The Co distribution shows a diffusion tail-like envelope at -60 °C which decays rapidly with increasing depth, while at room temperature a two-peak structure is found with surface and subsurface enrichment of Co. iii) For growth at -60 °C pronounced oscillations in the Co distribution are observed even for coverages above 1 ML (1.3 ML). At room temperature only indications of such oscillations can be seen for very low coverage. Apparently room temperature is sufficient to distribute the Co atoms more homogeneously over the different Si layers. Besides, at 22 °C, a subsurface-maximum in the Co distribution seems to be energetically more favorable.

### 5.1.4 Higher coverage

The consequences of such an inhibited Co in-diffusion at low temperature for the Co/Si interface structure are illustrated in Fig. 5.3 at higher coverage. There, for direct comparison with low temperature growth (5.93 ML of Co grown at -60 °C, Fig. 5.3(a)), an HRBS spectrum of 23.4 ML of Co grown on Si (100) at room temperature is shown in Fig. 5.3(b). Besides the Co spectra also the high-energy edges of the Si spectra are shown. For the measurements ion beams of 2 MeV $N^+$ ions [incidence angle 2.5°, Fig. 5.3(a)] and 2 MeV $He^+$ ions [incidence angle 5°, Fig. 5.3(b)] were used for -60 °C and 22 °C growth conditions, respectively. The scattering angle was 37.5° in both cases. The RUMP simulations of these spectra are shown as solid lines. [Since we can not assume a more or less perfect Si lattice with a few Co interstitials at this high coverage, the samples were subdivided into thin sublayers of the thickness of $6.87\times10^{14}$ atoms/cm$^2$ (Co+Si atoms) in the simulations]. For both cases the Co/Co+Si compositions at the interface are shown in the insets of Fig. 5.3, as obtained from the RUMP simulations. It is clearly evident that the interface structures at these two temperatures (besides attaining to different coverages) exhibit considerable differences. i) At -60 °C the interdiffusion of Co and Si is strongly reduced. As a consequence the growth of pure metallic Co starts much earlier than at 22 °C. Already at the deposition of 5.93 ML of Co one monolayer of metallic Co has formed. ii) The interdiffusion depths of Co and Si seem to be similar for both growth temperatures, but the amount of Co in the silicide phases is much smaller at -60 °C (4.93 ML of Co) than at 22 °C (17.4 ML of Co). iii) The silicide phases formed at the interface are quite different: At -60 °C only 1 ML of $Co_2Si$ and 3 ML of the CoSi phases are formed, followed by a long tail of low Co content silicides into the Si bulk. In contrast, at room temperature, well defined thick silicide layers of higher Co concentrations

are formed at the interface: 4 ML $Co_2Si$, 25 ML CoSi and 4 ML $CoSi_2$. The fraction of stoichiometric CoSi phase formed at the interface is much smaller for -60 °C (1.5 ML of pure Co, corresponding to 30 % of the total amount of Co in silicide phases) than for 22 °C (12.5 ML of pure Co, corresponding to 72 % of the total amount of Co in silicide phases).

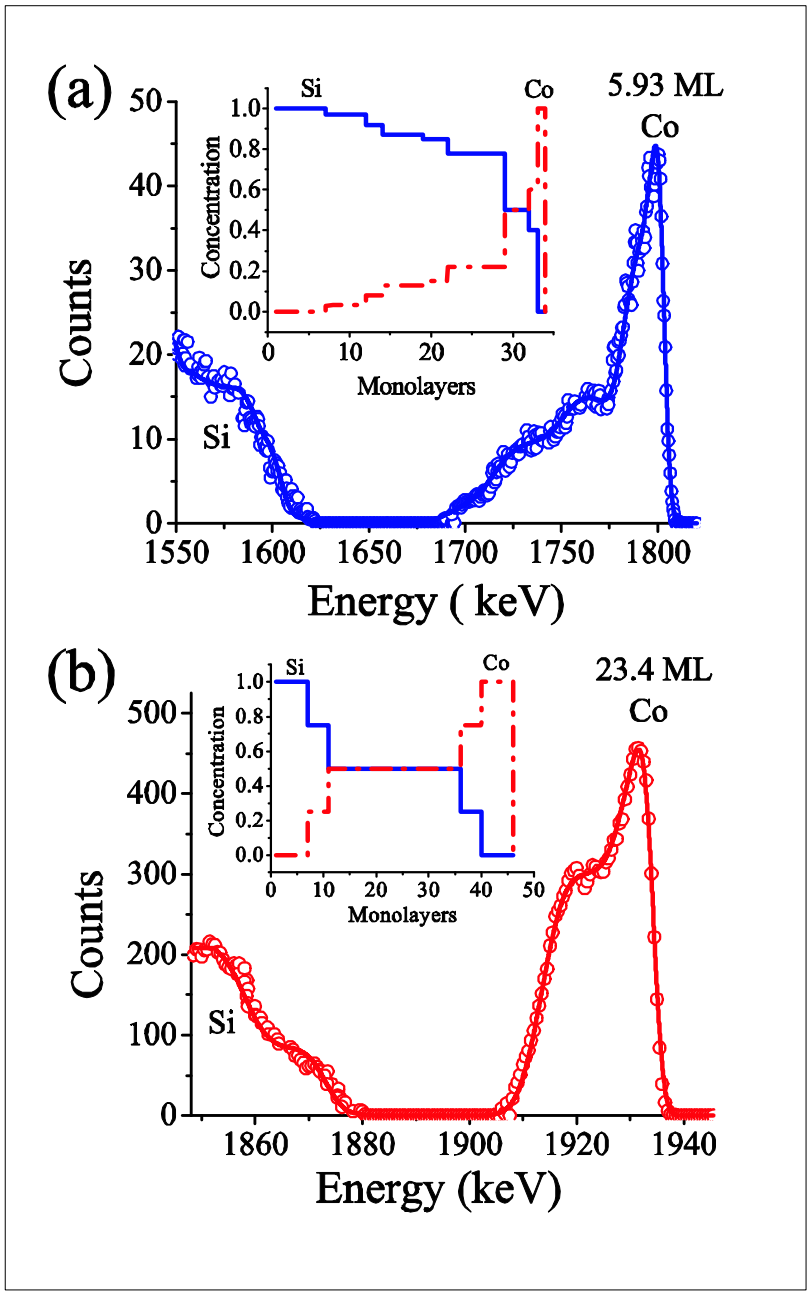


Fig. 5.3: HRBS spectra of both the Si and Co edges **(a)** 5.93 ML of Co deposited at -60 °C and **(b)** 23.42 ML of Co deposited at room temperature (22 °C), together with simulations of the spectra by RUMP (solid lines through the data). The insets show the Si and Co concentrations at the interface as obtained from the RUMP simulations.

As discussed above, at low temperature growth conditions the amount of Co diffusion into Si lattice could be suppressed, however, not able to decrease the silicide thickness substantially. However low temperature growth may give rise to poor crystal quality (of the Co film) and higher defect density. Overcoming these limitations is of crucial practical importance and represents a unique challenge in thin film growth. To decrease the silicide thickness again some other non equilibrium growth conditions are to be considered. Surfactant mediated growth is the other way which can reduce interface reactions and improve the crystalline quality.

## 5.2 Surfactant mediated growth of Co on Si (100)

As shown in the previous section, the amount of silicide phases formed at the interface at low temperature is drastically reduced but could not be stopped completely. However low temperature growth can give rise to poor crystal quality and higher defect density. Overcoming these limitations is of crucial practical importance and represents a unique challenge to the growth of Co on Si (100) with sharp interface.

Another compelling example of nonequilibrium growth is the “surfactant action” in heteroepitaxy. A significant breakthrough was achieved by using surfactants for the cases of hetero- and homo-epitaxial growth [5.9, 5.10]. The surfactant due to its lower surface free energy floats on the growth front to minimize the total energy of the system and hence reduces the interdiffusion. Experiments on surfactant mediated growth of Co on Cu [5.11], Co on GaAs [5.12] and Co on Ge [5.13] show that the surfactant floats on the Co overlayers, reduces interface reactions, improves the crystalline quality and drastically reduces the magnetic dead layer at the interface. Up to now there is no such attempt made for the surfactant-mediated growth of Co thin films on the Si, which is a very important heterostructure for spin injection experiments. The lower surface free energy of Sb in comparison to Co and Si, makes it a potential candidate for surfactant mediated growth. Sb can lower the surface free energy of the solid-vacuum interface and float on the growth front without significant incorporation into the growing film [5.14, 5.15]. The presence of 1 ML of Sb on the Si surface can make the evaporated Co atoms to land softly and hence stop them from diffusing into the Si lattice. As the Sb floats on the surface, it keeps the total energy of the system minimum and does not allow Si to diffuse out.

In this section, a study of the Sb mediated growth of Co on Si (100) has been performed in an *in situ* experiment where the quality of the Co film was analyzed during growth by

HRBS. In this studies the growth of Co on Si with and without Sb as surfactant are presented. The following issues were addressed which are important for the growth of Co on Si (100) with Sb as a surfactant: a) Does Sb behaves as a surfactant for the Si-Co heterostructure? b) Does Sb reduce the interface reaction by reducing the Co in-diffusion and Si out-diffusion? c) Is there any incorporation of Sb in the grown Co thin film?

### 5.2.1 Experimental

The cleaning of the Si (100) surface, the evaporation of the Co and Sb thin films and the *in situ* analysis by HRBS were carried out in an ultra high vacuum (UHV) system consisting of a preparation chamber, connected to a Pelletron accelerator, and equipped with an electrostatic spectrometer for energy analysis of scattered MeV ions. Two separate experiments were performed in these investigations: the growth of Co on a clean Si (100) surface without and with Sb as surfactant. For this purpose n-type Si (100) of size 2×2 $cm^2$ and resistivity 0.5 O cm was Shiraki [5.16] cleaned and immediately transferred into the UHV chamber. The samples were degassed over night and annealed at 750 °C for 2 hr. Then the samples were heated to 900 °C for 30 min and flash heated to 1050 °C for several short periods of time to achieve a clean, oxide-free surface. From these high temperatures the samples were slowly cooled down to room temperature (~ 1 °C /sec). The surface cleanness of the samples was verified by HRBS measurements.

Co with a high purity *(4N)* was evaporated from a high temperature effusion cell on to the clean Si (100) surface which was kept at room temperature. The evaporation rate was about 0.5 ML/min (1 ML = $6.87\times10^{14}$ atoms/$cm^2$). For Sb-mediated growth of Co on Si (100), Sb with high purity *(3N)* was sublimated from a low temperature effusion cell on to the clean Si (100) surface at the rate of 0.1 ML/min, followed by Co evaporation. The deposition rates were measured by a quartz microbalance and calibrated by HRBS with an accuracy of about 5%. HRBS measurements were carried out at the Sb, Co and Si high-energy edge in the backscattering spectra for different stages of Co evaporation. HRBS with monolayer depth resolution was achieved by the use of the high-resolution electrostatic spectrometer mentioned above. All the measurements were performed using 2 MeV $He^+$ ions at an incidence angle of 4.5° for the growth of Co on Si and 7.5° for the Sb mediated growth, and at a scattering angle of 37.5°. For all coverages, the HRBS spectra were taken on new spots (size ~ 1 $mm^2$) within the uniform evaporation region to minimize effects of radiation damage. For the magnetic measurements of Co on Si (100) with Sb and without Sb as surfactant, the samples were prepared by shadow mask evaporation technique.

### 5.2.2 Growth of Co on Si (100) without surfactant

In order to have a direct comparison at hand, in the first experiment Co (2 ML to 23.42 ML) was evaporated on Si (100) at room temperature without Sb as surfactant and HRBS spectra were taken at different stages of Co deposition. The evolution of the Co backscattering spectra with increasing coverage is shown in Fig. 5.4. The HRBS spectra reflect the composition and depth structure of the samples. The spectra in the range 1910 keV to 1935 keV are due to backscattering from the grown Co film, the spectra between 1850 keV to 1885 keV due to backscattering from the Si substrate. The spectra, in particular the steps in the Si and the small height of the Co spectra (for 2 ML to 16 ML of Co evaporation) give clear evidence for the formation of Co silicide. Furthermore, up to 16 ML of evaporated Co, the high-energy part of the Si spectrum does not shift its initial position. This means that Si is still present at the sample surface (out-diffusion through the Co film). For 23 ML of evaporated Co a step in the Co spectrum appears, in addition to the step in the Si spectrum. In addition to this, the shift of the high energy edge of the Si spectrum gives clear evidence for the growth of pure metallic Co on top of the silicide phases at the interface.

In order to obtain more detailed information about the depth distributions of Co and Si with monolayer depth resolution, the Co spectra were simulated by the program "RUMP". In these simulations, individual atomic layers (1 ML = $6.87\times10^{14}$ atoms/cm$^2$) were considered where each layer was allowed to have its individual composition of Co and Si. The results of these simulations are included in Fig. 5.4. For 2 ML and 3.48 ML of evaporated Co on Si, a CoSi-like phase is formed. For 6 ML and 11.83 ML of evaporated Co, a CoSi-like phase on the surface is followed by a $CoSi_2$-like phase at the interface. For 16 ML of evaporated Co, a $Co_2Si$ phase on the surface, followed by CoSi, and a $CoSi_2$-like phase at the interface are detected. No metallic Co could be found on the surface up to this coverage. Finally, for 23 ML of Co coverage, 7 ML of pure metallic Co grow on the surface, followed by $Co_2Si$, CoSi and $CoSi_2$ like phases at the interface. The thickness of the silicide layers at the interface for 23 ML case is calculated from the RUMP simulation. The total amount of Co atoms found in the interface silicide layer is 16.87 ML. This means that pure metallic Co grows only for coverages greater than 16.87 ML. This amount is slightly smaller than in the results of Meyerheim *et al.* [5.2] (19 ML). The Co is distributed over the thickness of 32 ML (24.2 Å) having different silicide compositions. The thickness of each silicide layer (from surface to interface) amounts to: $Co_2Si$ : 3.26 Å, CoSi : 18.77 Å, and $CoSi_2$ : 2.2 Å. The elemental distribution of Si and Co at the interface for 23 ML of evaporated Co on Si is shown in Fig. 5.6. Thus the experiment shows that Co and Si exhibit strong mixing at the interface; metallic Co starts to grow only after the

evaporation of about 17 ML of Co. The mixing at the Co-Si interface is due to in-diffusion of Co at the initial stages and out-diffusion of Si at higher coverages [5.1, 5.2].

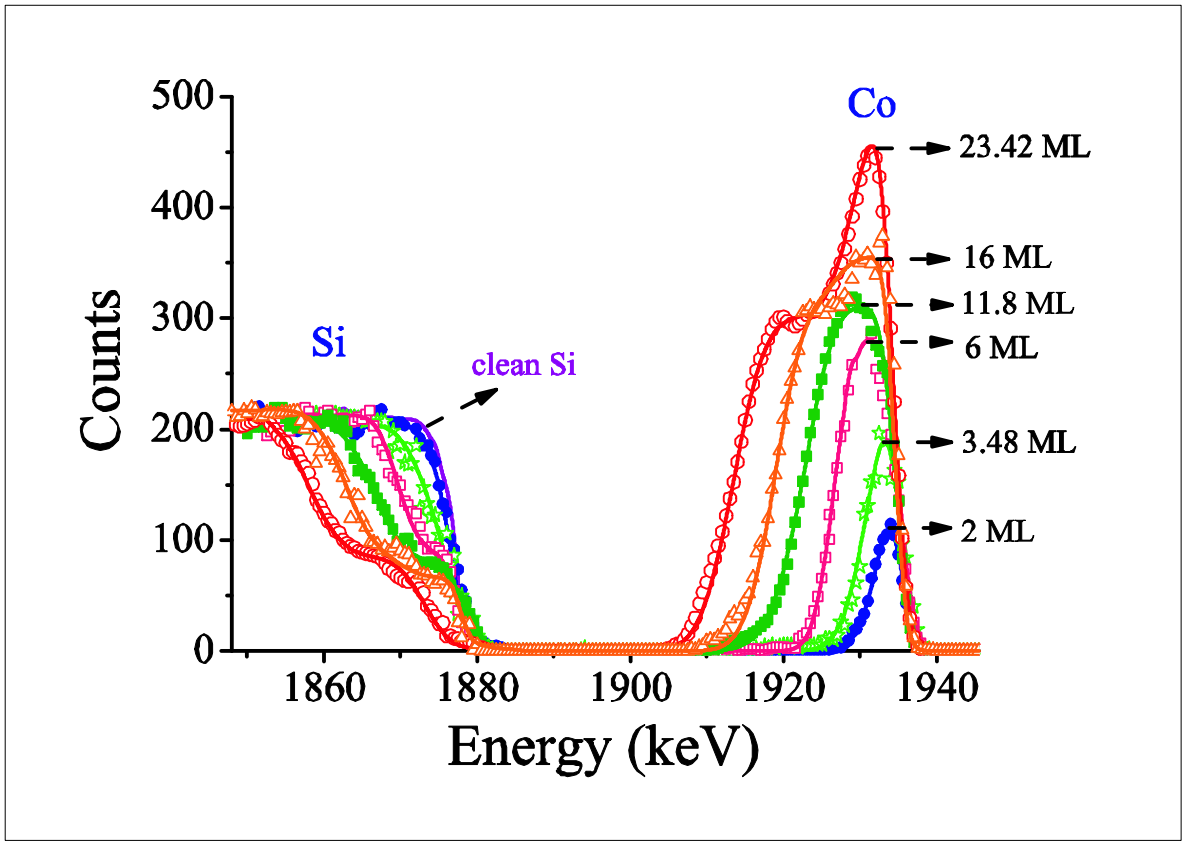


Fig. 5.4: Backscattering spectra (circles) and RUMP simulation (solid lines) for Co coverages from 2 ML to 23.48 ML on a Si (100) surface at room temperature without surfactant.

### 5.2.3 Growth of Co on Si (100) with surfactant

A substantial modification of the growth mode can be obtained by introducing a third element as a surfactant. If the surfactant lowers the surface free energy of both Co and Si, segregation of the surfactant will be strong during growth. For this purpose 1 ML of Sb was evaporated on a clean Si (100) surface. Subsequently Co films of increasing thickness were deposited on this substrate and the sample was analyzed by HRBS at the different stages of Sb and Co deposition. The HRBS spectra together with RUMP simulations are shown in Fig. 5.5 which also includes the spectra of the Si surface before and after Sb deposition. As shown in Fig. 5.5 the (Sb and Si) spectra of 1ML Sb on Si could be well simulated with RUMP under the simple assumption of one continuous layer of Sb ($0.687\times10^{14}$ at./cm$^2$). Only slight thickness

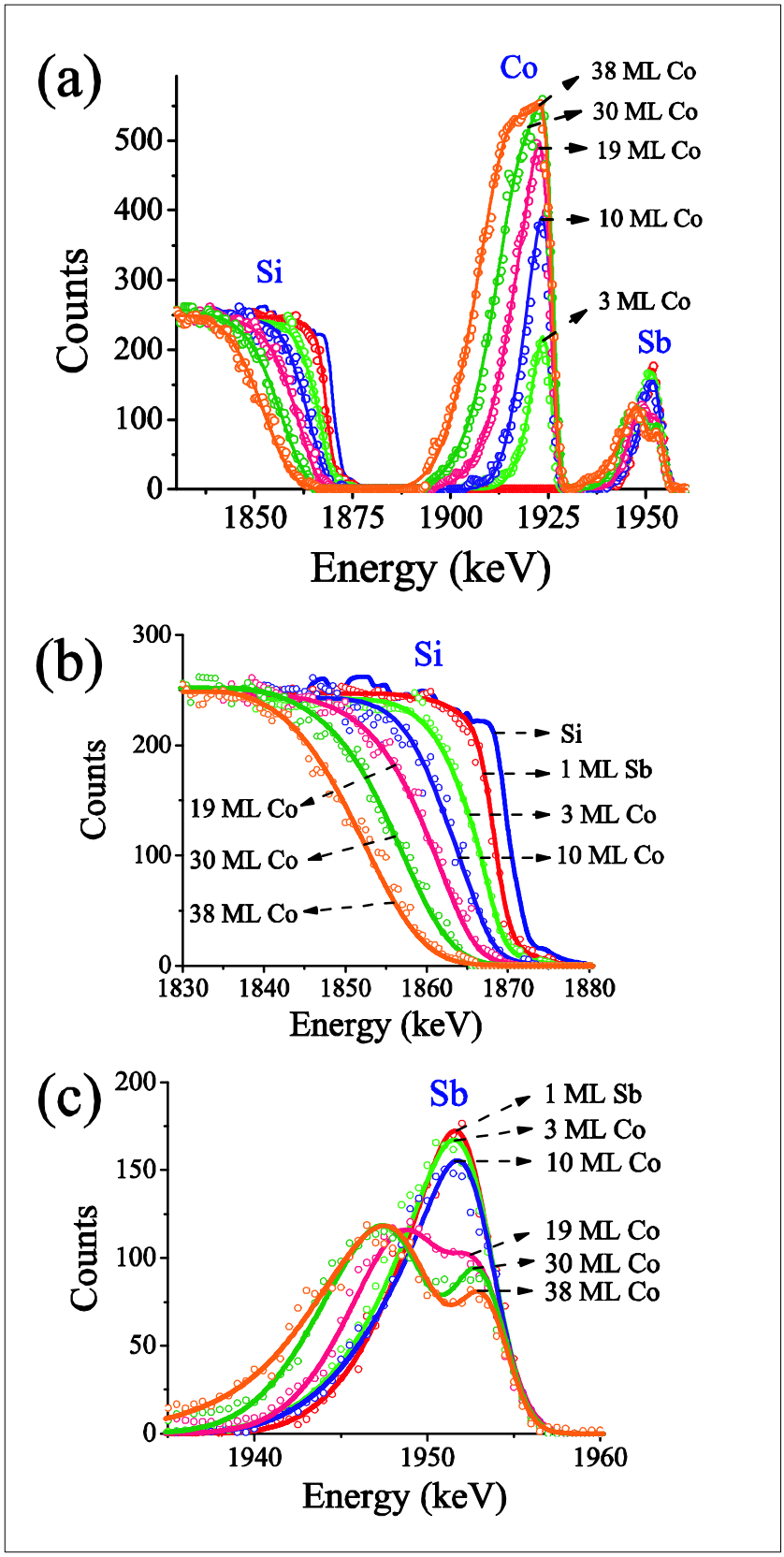


Fig. 5.5: Rutherford backscattering spectra (circles) and RUMP simulation (solid lines) for Sb mediated growth of Co on Si (100) **(a)** overview about the HRBS spectra during the deposition of Co (3 ML to 38 ML) on Si (100) surface **(b)** Shift of the high-energy Si edge during Sb and subsequent Co deposition **(c)** The modification of the Sb spectra with increasing Co coverage.

fluctuations of the Sb layer had to be assumed. This roughness is most likely a natural consequence of the large (16 %) difference in the covalent radii of Sb and Si [5.17]. The complete coverage of the Si surface by the Sb layer is clearly evident from the parallel shift of the Si high energy edge position from 1874.4 keV to 1872.1 keV after the Sb evaporation.

Fig. 5.5 also shows Rutherford backscattering spectra and RUMP simulations of Si, Co and Sb after the evaporation of increasing amounts of Co on the 1 ML Sb-terminated Si (100) surface. For 3 ML of Co the simple parallel shift in the Si high energy edge position gives a clear indication of the growth of metallic Co on the Si surface. From the RUMP simulation we could find that metallic Co grows on the surface with 1 ML of a $CoSi_2$-like phase at the interface. In contrast to the growth of Co on Si without Sb as surfactant, the inter-diffusion of Co and Si is drastically reduced for the Sb mediated growth. Apparently this diffusion and the intermixing are surface mediated and strongly hindered by the Sb surface layer. As soon as a Co atom has arrived at the surface, it is bonded to the surfactant, resulting in a strongly reduced surface mobility. Evidently the Sb layer on the surface reduces the in-diffusion of Co and the out-diffusion of Si through the Co overlayer. Looking at the shift in the Si high energy edge position for all coverages (3 ML to 38 ML) it is clear that a layer by layer growth of Co occurs. The absence of any step-like structures in the Si and Co spectra for Sb-mediated growth of Co on Si gives clear evidence that a much sharper interface has been formed for the Sb-mediated growth case. For 10 ML to 38 ML of Co evaporation, the total amount of Co in the interface silicide layer is ~ 5 ML which is distributed over a silicide thickness of 17.45 ML (1.3 nm). The thicknesses of different compositions of the silicides are: $CoSi_2$: 7.7 Å and $CoSi_4$ : 5.4 Å . So, the thickness of the interface silicide is reduced by about a factor of two to 1.3 nm for the growth of Co on Si with Sb as surfactant in contrast to a 2.4 nm thick silicide layer as observed for the growth without surfactant. From this it is clear that as well Co in-diffusion as Si out-diffusion is strongly reduced for the Sb mediated growth.

### 5.2.4 Sb incorporation in the grown Co film

A strong tendency for surface segregation is an important condition for the effectiveness of Sb as a surfactant. If we look at the Sb backscattering spectra for all Co coverages, we see that the Sb edge remains at the same energy position even after 38 ML of Co deposition. This indicates that the Sb floats on the Co surface, obeying its surfactant behavior; apparently the site exchange mechanism (as proposed by T. Ohno [5.18]) holds well for the Sb-Co-Si system. For the 3 ML and 10 ML case there is no change in the Sb spectra at all except a slight decrease in

the number of counts. This reduction in counts can be attributed to the surface roughness after Co evaporation. For the cases of 19 ML, 30 ML and 38 ML the spectra modify drastically, showing some incorporation of Sb in the grown Co film. This incorporation of Sb may be due to the relatively low temperature of growth (room temperature) and the increasingly Co film. In fact the bulk solubility limit of Sb in Co is well below 1 % at room temperature [5.19]. The elemental distributions of Si, Co and Sb at the interface for 23 ML of evaporated Co on Si are shown in Fig. 5.6.

### 5.2.5 Comparison of interface with and without surfactant

For the reason of comparison, concentration profiles of Si, Co and Sb are shown in Fig. 5.6 (lower panel) for growth of Co on Si without Sb (23 ML of Co) and in Fig. 5.6 (upper panel) for growth with Sb as surfactant (19 ML of Co). A drastic reduction of the intermixing at the Co-Si interface

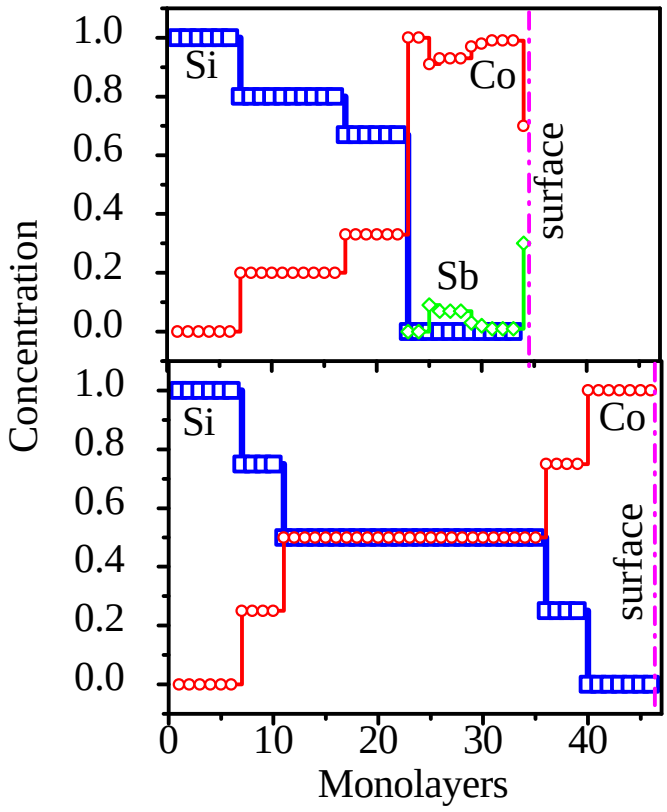


Fig. 5.6: **Upper panel**: Elemental distribution of Si, Co and Sb for growth of 23 ML of Co on Si without Sb as a surfactant (32 ML ~ 2.4 nm of silicide layers: $Co_2Si$: 3.26 Å, CoSi: 18.77 Å, and $CoSi_2$: 2.2 Å). **Lower panel**: Growth of 19 ML of Co on Si with Sb as a surfactant (17.5 ML ~ 1.3 nm of silicide layers: $CoSi_2$: 7.7Å and $CoSi_4$: 5.4 Å).

(from 32 ML to 17.5 ML) is seen when the surfactant is used. In the case of Sb mediated growth Si-rich phases ($CoSi_2$, $CoSi_4$) were found in comparison to more Co-rich phases as obtained in the case of no surfactant. In addition, Fig. 5.6 shows that there is some incorporation of Sb in the grown Co thin film.

### 5.2.6 Comparison of magnetic properties with and without surfactant

As understood from the growth of Co on Si (100), metallic Co starts to grow after 17 ML of evaporated Co and with surfactant mediated growth the interface is significantly improved. To study the magnetic properties of the silicide layers formed at the interface at room temperature and the effect of surfactant, 17 ML of Co was evaporated on Si (100) with and without Sb by use of a shadow mask. So the part of the sample grown without Sb must have consumed all Co to form silicide-like phases at the interface and the part grown with Sb must have improved interface quality. The magnetization curves of these two types of samples measured at 300 K are shown in Fig. 5.7.

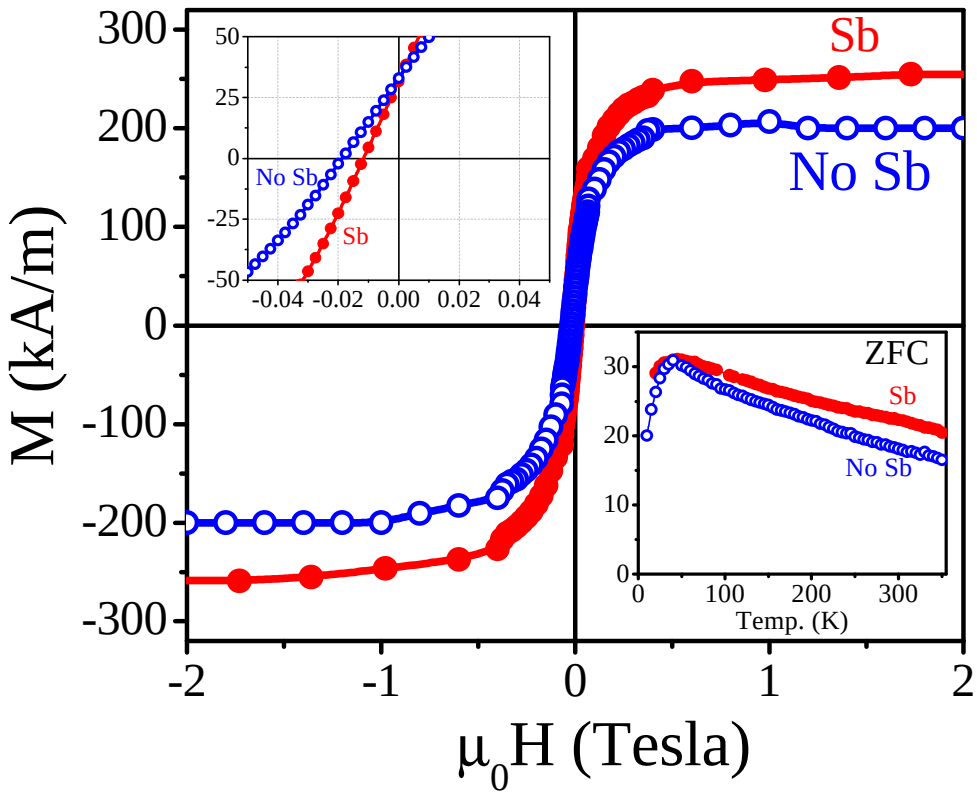


Fig. 5.7: Magnetic measurements of 17 ML Co on Si (100) with and without Sb: Magnetization curves at room temperature. **Upper inset**: Magnified version of magnetization curve showing clear remanence and coercive fields. **Lower inset**: Temperature dependence of remanent magnetization at zero applied zero.

There are two important results which are to be discussed here. (i) The sample grown without Sb (where all Co atoms are in silicide like phases) is magnetic even above room temperature. (ii) The sample grown with Sb as surfactant shows higher saturation magnetization, clearly indicating improved interface quality. The observation of higher magnetization is due to the improved interface (less silicide formation) by Sb mediated growth. The higher coercive field observed for the case of the sample grown without Sb, may be due to the fact that the silicide layers act as pinning centers. Furthermore, the comparison of the temperature dependences of the remanent magnetizations at zero applied field (ZFC) is shown in the lower inset of Fig. 5.7. A peak around 40 K in the ZFC curve for both the samples gives an evidence of the presence of an antiferromagnetic phase in the sample. However, the fast magnetization decay with temperature for the Co sample without surfactant gives clear evidence that the surfactant mediated growth Co has better magnetic properties.

This Sb mediated growth of Co on Si (100) proves to be useful to get a much sharper interface. The improved interface quality with Sb mediated growth is also reflected in magnetic measurements. Co with Sb mediated growth shows a higher magnetic moment.

## 5.3 Comparison of different growth modes: *(22 °C, -60 °C and with-Sb)*

For the reason of comparison, concentration profiles of Si, Co and Sb are shown in Fig. 5.8 for growth of Co on Si at room temperature (23 ML of Co), at -60 °C (5.96 ML of Co), and for growth with Sb as surfactant (19 ML of Co). Low temperature growth at -60 °C results in the formation of an interface silicide layers with low Co contents and only a very thin layer of stoichiometric CoSi composition when compared with room temperature deposition. At low temperature, the amount of Co diffused in is drastically reduced but the depth of diffusion is found to be similar to that of room temperature growth. A drastic reduction of the intermixing at the Co-Si interface (from 32 ML to 17.5 ML) is seen when the surfactant is used. In the case of Sb mediated growth Si rich phases ($CoSi_2$, $CoSi_4$) were found in comparison to more Co rich phases in the case without surfactant at room temperature. In addition there is some incorporation of Sb in the grown Co thin film. Due to the different thickness of the silicides formed at the interfaces for different growth modes, all experiments could not be performed with the same ion beam and same incidence angle. This would make a comparison of different ways of Co film growth easier. But one can do this on a computer. If one give the interface structure as derived from Fig. 5.8(a) in to a RUMP simulation with a 2 MeV N ion beam at an incidence angle of 2°, then we one directly compare the three growth modes in a RUMP

simulation of the HRBS spectra. The result is shown in Fig. 5.8(b). The differences of the different modes of growth are now clearly visible.

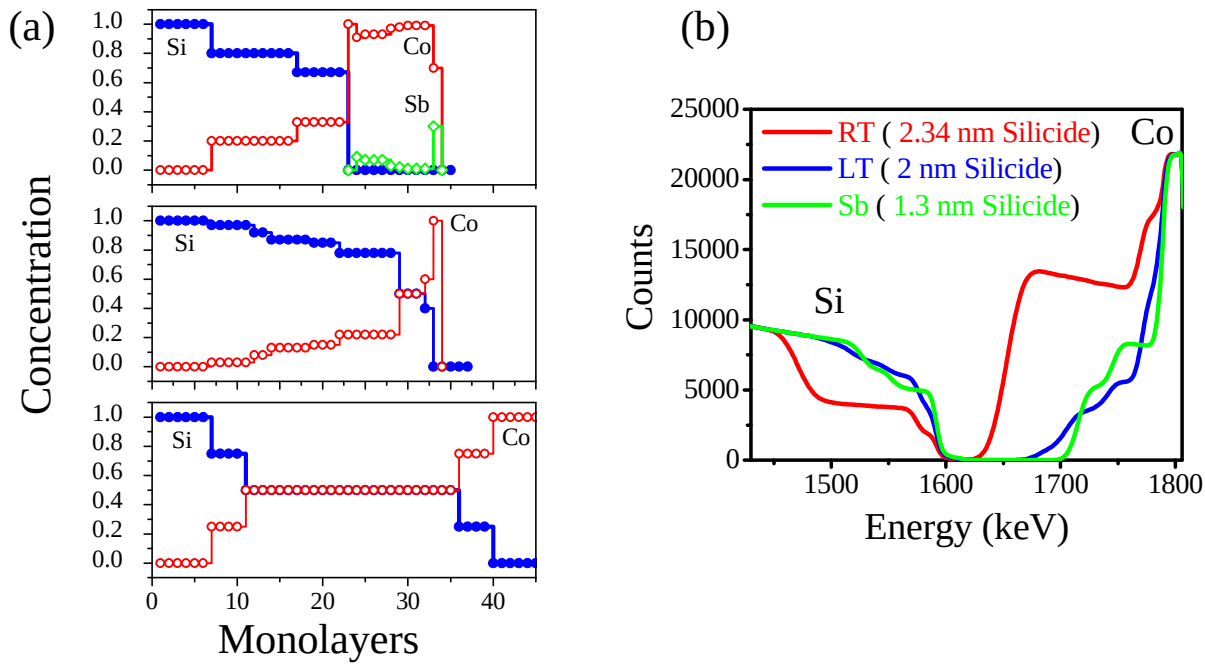


Fig. 5.8. **(a)** Elemental distribution of Si, Co and Sb for ***Bottom:*** growth of 23 ML of Co on Si at room temperature (32 ML ~ 2.4 nm of silicide layers: $Co_2Si$ : 3.26 Å, CoSi : 18.77 Å, and $CoSi_2$ : 2.2 Å), ***center:*** 5.93 ML of Co deposited at -60 °C : 2nm thick silicide phases at the interface having low Co content and ***Top:*** growth of 19 ML of Co on Si with Sb as a surfactant (17.5 ML ~ 1.3 nm of silicide layers: $CoSi_2$: 7.7Å and $CoSi_4$ : 5.4 Å ). **(b)** RUMP simulation for three different growth modes taking the data obtained from different experiments.

## 5.4 Problem in spin injection and detection in Schottky contact

It was shown in this chapter that the simple solutions can reduce the FM-Si inter-diffusion at the interface and improve the interface quality. 1) By lowering the temperature, so that the diffusion is drastically reduced, and the atoms are prevented from finding energetically preferred positions, and 2) by using Sb as surfactant for the growth of Co on Si. However these non equilibrium growth conditions could not stop the silicide formation completely. From this chapter we came to conclusion that it is not possible to obtain a sharp Co-Si interface and hence a direct ferromagnetic metal- Si Schottky contact can not be used for spin injection purpose.

Another way to get rid of both problems is to use a tunnel barrier between FM and Si for spin injection. Using a tunnel barrier has two advantages i) It forms a chemical barrier between the FM and the Si and ii) One will have a measurable magneto resistance due to the spin selective resistance of the tunnel barrier.

# Chapter 6

# MgO tunnel barrier for spin injection into Si

In this chapter the fabrication and characterization of ultra-thin MgO tunnel barriers on Si (100) is reported. Some of the properties of tunnel barriers (as mentioned in chapter 2) are addressed which are important for spin injection into Si: i) the MgO-Si (100) interface, ii) the crystallinity of ultra-thin MgO tunnel barriers, iii) the ferromagnetic metal-MgO interface, iv) the thermal stability of ferromagnetic metals on tunnel barriers, and finally v) the subject of low-resistant tunnel barriers. In the end of the chapter, a design of a spin injection device is proposed using the concept of spin injection into Si from ferromagnetic Co through a MgO tunnel barrier in non-local geometry.

## 6.1 Tunnel barriers for spin injection

As discussed in chapter 4, there exist thick silicide layers of different compositions at ferromagnet (FM) - Si interfaces [6.1, 6.2]. Various experimental measures were taken such as low-temperature growth or surfactant-mediated growth, but silicide formation could not be stopped fully. The silicide layer may be the main cause for spin-flip scattering and low spin injection efficiency [6.3, 6.4].

On the other hand, using an ultra-thin tunnel barrier between FM and Si will have three advantages: (i) form a chemical barrier between the FM and the Si, (ii) circumvent the conductivity mismatch problem, and (iii) in addition, act as a spin filter [6.5]. As discussed in chapter 2, the tunneling spin polarization is normally less than 50% when an $Al_2O_3$ tunnel barrier is used [6.6]. This is because of the amorphous nature of $Al_2O_3$, which causes scattering and depolarization of the injected spin polarized carriers. MgO can be produced as a crystalline tunnel barrier and, thus, allows coherent tunneling of spin polarized electrons. A

large polarization (~ 50 %) was obtained for FM/MgO/GaAs system, indicating that very efficient spin injection is possible using a MgO tunnel barrier [6.7]. Quite aside form the above mentioned disadvantage, the amorphous tunnel barriers ($Al_2O_3$, $SiO_2$, $Si_3N_4$) leave dangling bonds as electronic defects [6.8]. An alternative crystalline MgO tunnel barrier on Si would, in principle, have less dangling bonds and other electronic defects such as interface traps for charge carriers.

## 6.2 MgO tunnel barrier on Si (100)

The growth of epitaxial oxides on Si (100) is an expanding research topic with important technological applications in Si integrated circuits [6.9]. In the present study magnesium oxide (MgO) was chosen as tunnel barrier on Si for several reasons. i) It is chemically inert and thermally stable and should, therefore, result in sharp interfaces with both Si and ferromagnetic metals. (ii) MgO has a wide band gap (7.3 eV), ensuring a large band offset with Si to minimize leakage currents. (iii) The crystalline properties will facilitate coherent tunnelling of spin polarized electrons [6.10].

In section 6.3 the growth of ultra-thin MgO films on Si (100) by reactive molecular beam epitaxy is explored. Its interface with the Si substrate and the ferromagnetic metal has been studied by *in situ* HRBS and *ex situ* HR-TEM. The thermal stability of ultra-thin Co and Fe films on such MgO tunnel barriers have been verified by thermal annealing and *in situ* HRBS measurements. The issue of tailoring the resistance-area product of the ferromagnetic metal-MgO-Si structure has also been addressed by producing oxygen deficient tunnel barrier and by scaling the thickness of the MgO film.

## 6.3 Ultra-thin MgO-Si interfaces

MgO is a highly insulating crystalline solid with NaCl structure. The lattice constant of MgO is 4.211 Å, whereas that of Si is 5.431 Å, implying a direct lattice mismatch of - 22.5 %. But there is a near commensurate match with Si at a 4:3 ratio of the lattice constants (four MgO to three Si lattice constants). It is to be noted that epitaxial systems with large lattice mismatch (like MgO/Si) have been observed to have a structural transformation within a small number of monolayers (four monolayers in the case of Al/Si (111) with a - 25.4 % mismatch) [6.11]. Fork *et al*. first reported epitaxial growth of *thick* MgO films on Si (100) by pulse laser deposition [6.12]. The films had a cube-on-cube epitaxial relationship. The interface with Si

was found to be incommensurate but abrupt and free from secondary phases or obvious interdiffusion. The authors also could not find any growth of silicon-oxide at the MgO-Si interface. The MgO/Si (100) interface is expected to be incommensurate at the early stages of growth due to the large lattice mismatch. The minimization of the defect density in the epitaxial growth of an ultra-thin MgO film on Si (100) can be a real challenge. For the realization of a high tunnelling magneto-resistive effect the ultra-thin MgO barrier should have a good crystalline structure without pin-holes, and a sharp interface with the Si (100) substrate.

### 6.3.1 Sample preparation

Equilibrium thermodynamic data suggest that MgO is stable against the formation of interfacial compounds with Si. In the case of reactive molecular beam epitaxy where Mg is employed as the cation source along with an oxidising background source of $O_2$, kinetic limitations may supplant equilibrium considerations. Potential aggravating effects are: (i) substrate oxidation prior to initiation of film growth and (ii) magnesium silicide formation at the interface at RT. Mg atoms are believed to be adsorbed on cave sites on the Si (100) surface at very initial stages and, as the amount of Mg increases, a ~ 2 ML thick silicide is forming at the interface [6.13]. These two effects argue for opposite extremes in growth conditions, requiring a better understanding of their relative importance. It is important to find an appropriate growth regime that at least partially overcomes these effects.

In the sample preparation, precautions were taken to avoid the above mentioned effects. First 0.5 ML of Mg was evaporated on cleaned Si (100) which is expected to occupy the cave sites on the Si (100) surface and then oxygen was streamed into the chamber. In this way both, silicide formation and also the oxidation of Si could be avoided. In this way ultra-thin stoichiometric MgO films were prepared on Si (100) surface by evaporating Mg at a rate of 1 ML/min. and an oxygen pressure of $1\times10^{-7}$ mbar.

### 6.3.2 HRBS studies

HRBS is, perhaps, the most powerful tool for characterizing such ultra-thin MgO tunnel barriers in atomic details. The *in situ* HRBS measurements were carried out in an ultra high vacuum (UHV) system consisting of a preparation chamber, connected to a Pelletron accelerator, and an electrostatic spectrometer for energy analysis of scattered 2 MeV $N^+$ ions at an incidence angle of 10° to the sample surface and a scattering angle of 37.5° [6.14]. n-Si

(100) samples with resistivity 4-10 O-cm (P doped) were cleaned in UHV by flash heating at 1050 °C. The surface cleanness of the Si samples was verified by HRBS measurements. Before use the effusion cell was outgassed; no C or O contaminants were found during Mg evaporation. Ultra-thin MgO films were prepared on this Si (100) by evaporating Mg at a $1\times10^{-7}$ mbar oxygen partial pressure. The evaporation rate (1 Å/min) was calibrated by HRBS with an accuracy of about 5%. The sample was characterized *in situ* by high resolution RBS to obtain detailed information about the composition and thickness of the MgO tunnel barrier and about its interface structure with the Si (100) surface.

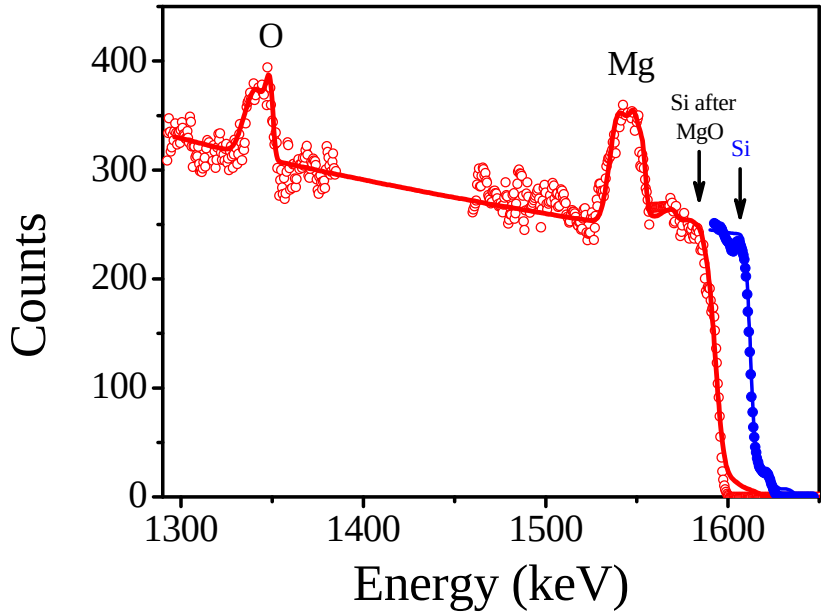


Fig. 6.1: HRBS spectra of the Si sample before and after MgO evaporation. Before evaporation: HRBS spectrum of the high-energy Si edge (solid blue circles) and RUMP simulation (solid blue line) of the clean Si. After MgO evaporation: HRBS spectrum at Si, Mg and O edges (open red circles) and RUMP simulation (solid red line) of the 1.5 nm thick MgO film as prepared on Si (100) surface. The spectrum shows that the MgO film is very uniform. A surplus oxygen at the surface of the MgO film is clearly visible.

Figure 6.1 shows the HRBS spectra of the Si sample before and after evaporation of MgO. Before the evaporation the sample was cleaned and no O or C contamination was found. The blue curve shows the high-energy edge of the cleaned Si sample (at 1620 keV). After the evaporation of MgO the Si surface edge is shifted parallel to lower energies (1600 keV). The two peaks observed on the Si background spectrum at 1560 keV and 1350 keV are due to the Mg and O content in the grown MgO thin film on the Si substrate, respectively. In order to obtain more detailed information about the thickness and composition of the MgO film and the structure of its interface with Si, the spectrum was simulated by the program RUMP [6.15]. In these simulations the sample was subdivided into thin sublayers of the

thickness of $6.87\times10^{14}$ atoms/cm$^2$ (this is the atomic density of the Si (100) planes). The composition of each sublayer was varied and the HRBS spectrum calculated for the assumed Mg and O concentrations and depth distributions until good agreement with the experimental data was achieved. From the simulations it was found that the grown MgO is 1.5 nm thick and exhibits the composition $Mg_{0.5}O_{0.5}$, with the exception of the surface layer (2 ML) which has the composition $Mg_{0.35}O_{0.65}$, i.e. exhibits an O surplus. This increased O content of the surface layer is well visible in Fig. 6.1 and may be due to the fact that some residual oxygen gas was left in the scattering chamber even after closing the oxygen bottle.

The almost parallel shift of the high-energy edge of Si gives strong evidence that the 1.5 nm thin MgO layer is quite uniform in thickness and that no island formation has occurred. From the RUMP simulation, a thickness fluctuation of only 2 ML is found in the MgO thin film. It is to be noted that in case of island growth the Si high-energy edge would not shift in a parallel manner. Besides, the almost trapezoidal shape of the Mg and O parts of the spectrum are indicative of a very homogeneous MgO layer. Island growth would result in a more triangular shape, as is observed in case of the Co spectra on top of the MgO film (see section 6.4.1). No such effects are seen in the HRBS spectra. The MgO-Si interface was found to be very sharp from the RUMP simulation, hence ruling out the formation of any silicide phase and the oxidation of the Si surface.

### 6.3.3 HR-TEM studies

In general, ultra-thin oxide barriers almost invariably contain defects. The presence of pin-holes in ultra-thin films is a real and significant problem. The relative contributions due to elastic tunneling through the insulating spacer layer and ballistic transport through the pin-hole can change the magnetoresistive response completely [6.16]. For the realization of a high tunnelling magneto-resistive effect the ultra-thin MgO barrier should have a good crystalline structure without pin-holes and a sharp interface with the Si (100) substrate. To verify these properties of the MgO barrier, HR-TEM studies were carried out.

Figure 6.2 shows an overview and the high resolution TEM micrograph of a Co/MgO(1.5 nm)/Si (100) heterostructure. The image shows an excellent morphology with rather smooth and flat layers. The MgO layer has crystalline structure and a very sharp interface with Si. The results are in quite good agreement with the result of the HRBS analysis. Also the HR-TEM shows that this MgO film does not have pin-holes.

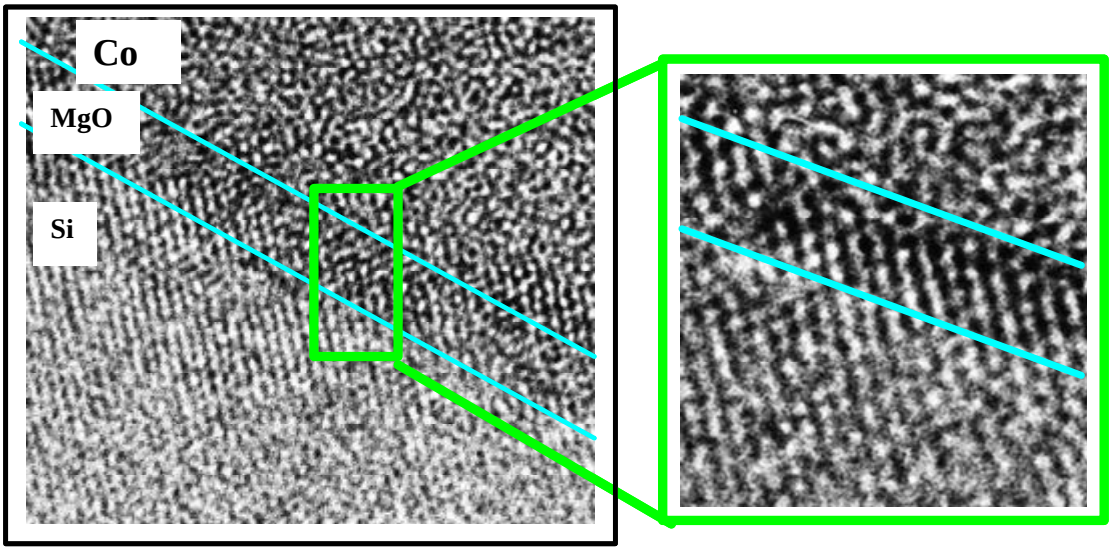


Fig. 6.2: HR-TEM cross-sectional micrograph of a Si (100)/MgO (1.5 nm)/Co structure. Epitaxial growth of MgO on Si is evident by the magnified version shown in the right panel. The lines have been added at the interfaces to aid the eye in distinguishing the layers of small contrast difference.

## 6.4 Ferromagnet-MgO interface

Structural perfection across the interface is a prerequisite for coherent tunnelling. Numerous experimental and theoretical works show that the nature of the bonding at the ferromagnetic metal/insulator interface plays the key role in the tunnelling process. Indeed, as the result of an interface reaction the electron tunnelling process can be strongly modified. Consequently, it becomes important to control the chemical quality of the interfacial layer.

Because of very different surface free energies of MgO (1.1 J/m$^2$) at the one hand and Co or Fe (~ 2.9 J/m$^2$) on the other hand, layer by layer growth is not favoured for ferromagnetic metals on MgO. However, the Co/MgO (100) interface as well as the Fe/MgO (100) interface are found to be model interfaces from the chemical, structural and magnetic point of view. Sicot *et al.* observed a weak hybridization between Co and MgO as well as an increase of the magnetic moment of Co in contact with MgO [6.17]. For the case of the Fe/MgO system, Tusche *et al.* have shown that Fe grows on MgO in a disordered structure, due to high surface free energy [6.18]. Tusche *et al.* and Meyerheim *et al.* found that one ML of Fe oxidises at the interface, but it is not clear whether the MgO is reduced or not [6.19]. On the other hand Sicot *et al.* could not find any FeO layer at the interface at all [6.17].

### 6.4.1 Growth of Co on MgO /Si (100)

Highly pure (*4N*) Co was grown on the MgO tunnel barriers described in section 6.3 from a properly degassed effusion cell. The evaporation rate (0.5 ML/min) was calibrated by HRBS with an accuracy of about 5%. The *in situ* HRBS measurements were carried out in an ultra high vacuum (UHV) system consisting of a preparation chamber, connected to a Pelletron accelerator, and an electrostatic spectrometer for energy analysis of scattered 2 MeV $N^+$ ions at an incidence angle of 8° to the sample surface and a scattering angle of 37.5°. The HRBS spectra for the evolution of the Co distribution are shown in Fig. 6.3 for Co coverages of 0.05 - 3 ML. The peak between 1800 and 1815 keV is due to $N^+$ ions backscattered by Co atoms adsorbed on the MgO tunnel barrier. From the very beginning of Co growth (0.05 ML) island growth is evident because of a long tail of the Co peaks towards lower energies (low energies correspond to large thicknesses). Referring to the results of Sicot *et al.*, the formation of a CoO layer at the interface could be excluded [6.17]. In order to obtain detailed information about the Co growth, the 3 ML Co spectrum is simulated by the program RUMP. It could best be fitted by assuming the growth of pure Co film of thickness 3 ML with a roughness of 2 ML (standard deviation).

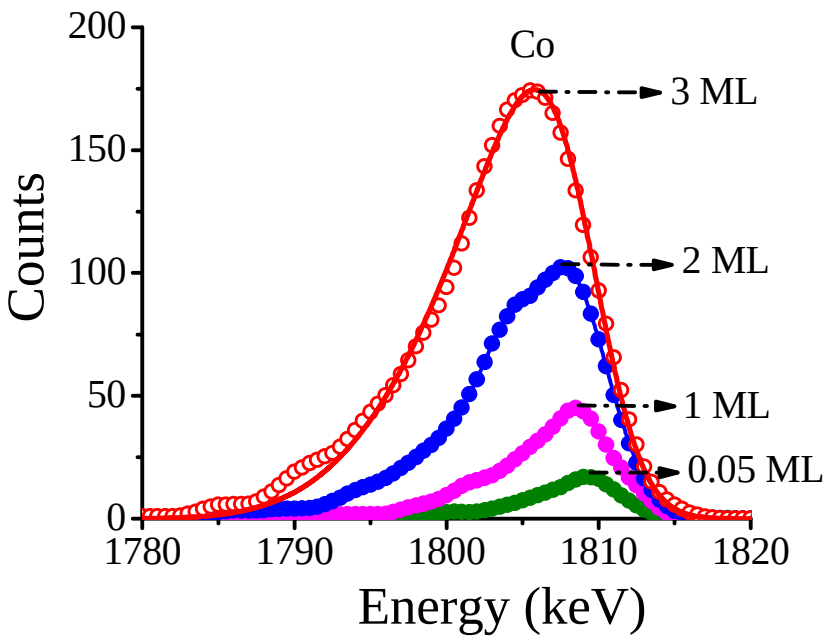


Fig. 6.3: Co on MgO tunnel barrier/Si (100) structure for 0.5 to 3 ML at room temperature: Co peaks of the HRBS spectra for 0.05 to 2 ML (solid circles, the lines are drawn to guide the eye) using 2 MeV $N^+$ ions. For 3 ML, the HRBS data (open circles) and the RUMP simulation (solid line) are presented.

### 6.4.2 Growth of Fe on MgO/Si (100)

Ultra thin Fe films were grown on MgO tunnel barriers and analyzed *in situ* in the way described in section 6.4.1, using 2 MeV $He^+$ ions at an incidence angle of 3° to the sample surface and a scattering angle of 37.5°. The HRBS spectra for the evolution of the Fe distribution are shown in Fig. 6.4 for Fe coverages of 0.05 - 4 ML. Also here island growth is evident from the very beginning (0.05 ML), because of the long tails in the HRBS spectra towards lower energies. Referring to the results of Sicot *et al.*, the formation of an FeO layer at the interface could be excluded [6.17]. In order to obtain more detailed information about the Fe growth, the 4 ML Fe spectrum is simulated by the program RUMP. It could be fitted by assuming the growth of pure Fe of thickness 4 ML with a roughness of 2.5 ML (standard deviation).

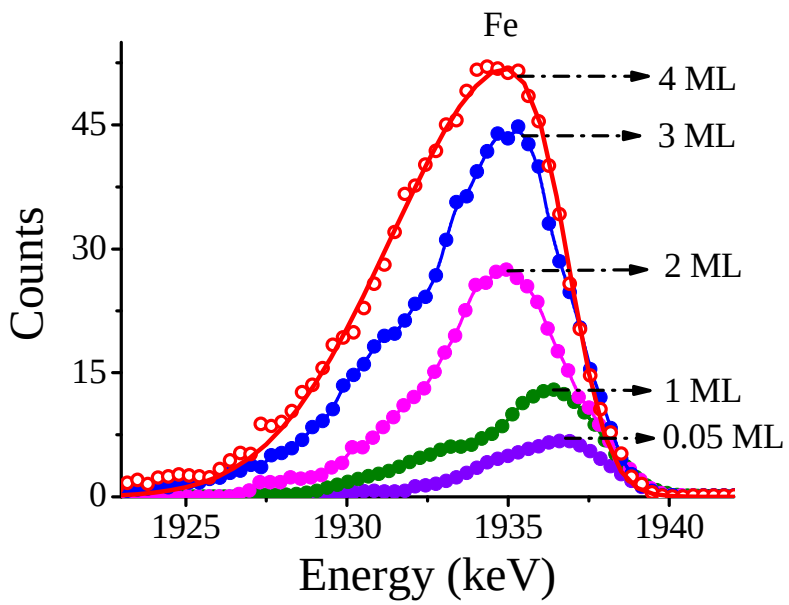


Fig. 6.4: Fe on MgO tunnel barrier/Si (100) structure for 0.5 to 4 ML at room temperature: Fe peak of the HRBS spectra for 0.05 to 3 ML (solid circles, the lines are drawn to guide the eye) using 2 MeV $N^+$ ions. For 4 ML, the HRBS data (open circles) and the RUMP simulation (solid line) are shown.

### 6.4.3 Thermal stability of ferromagnetic films deposited on the MgO tunnel barriers

A thermal stability study of the ferromagnetic films on the tunnel junctions is of significance, since the films (when integrated in a semiconductor chip) should withstand high-temperature treatments during existing semiconductor processes. On the other hand the thermal stability of

magnetic tunnel junctions is of considerable interest because their performance has been shown to improve upon annealing [6.20]. The thermal stability of the MBE-grown ferromagnet-MgO tunnel junctions on Si (100) has been studied by annealing them at 450°C for 15 min and analyzing them *in situ* by HRBS.

Fig. 6.5(a) shows the HRBS spectra of 3 ML of Co evaporated on such a MgO tunnelling barrier, in the as-prepared and the annealed state. As evident from the figure, the Co profile does not show any changes upon annealing which means that it is thermally stable up to 450 °C. The same applies for the 3 ML Fe film [see Fig. 6.5(b)]. The slight increase in the maximum count rate of the Fe spectrum after annealing is probably due to the fact that the Fe film becomes more homogenous after annealing. The great thermal stability of these Co and Fe films should be compared with the thermal behaviour of Co and Fe films on pure Si (100) substrates. In the latter case strong in-diffusion of the metals and out-diffusion of Si is observed (see chapter 4) which leads to pronounced silicide formation. Nothing like this is observed in the present case which means that the barrier is stable against diffusion and does not show pin holes to a larger amount.

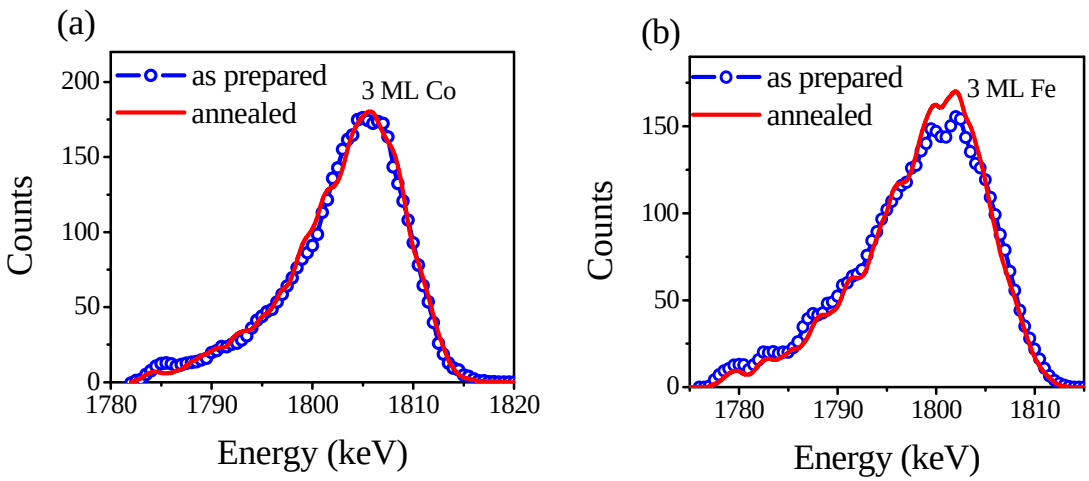


Fig. 6.5: Thermal stability of ferromagnetic metal on MgO tunnel barrier/Si (100) structures **(a)** HRBS spectra of 3 ML of Co as prepared (open circles) and after annealing at 450 °C for 15 min (solid line). **(b)** HRBS spectra of 3 ML of Fe as prepared (open circles) and after annealing at 450 °C for 15 min (solid line). No major changes are visible.

## 6.5 Optimization of resistance-area product

As discussed in chapter 2, a reasonable value of MR can only be obtained in the FM/I/Si/I/FM structure if the resistance-area (RA) product of both FM/I/Si contacts is relatively small [6.21]. It should be noted that the experimentally observed RA product values by Min *et al.*

for $Co/Al_2O_3/Si$ on low and high doped Si are far from the required range for the observation of spin injection effects [6.22].

The issue of tailoring the resistance-area product of a ferromagnetic metal-MgO-Si structure have been addressed by (i) producing tunnel barriers having less oxygen content and (ii) scaling down the thickness of the MgO film into the sub-nanometer regime. Both procedures should result in reduced resistivity of the tunnel barrier.

### 6.5.1 Oxygen deficient tunnel barrier

In a step to tailor the resistance of the MgO tunnel barrier, the O content in the barrier has been decreased. In the preparation by reactive molecular beam epitaxy, first a few monolayers of stoichiometric MgO were grown and then the O content was decreased towards the surface. This oxygen-deficient tunnel barrier has two advantages. 1) It will exhibit a lower resistance; 2) it will not oxidize the ferromagnet evaporated on this. Such an oxygen deficient MgO barrier was characterized *in situ* by HRBS and *ex situ* by HRTEM to get in-depth information about the composition, thickness, interface quality and structure.

Figure 6.6(a) shows the HRBS spectra before and after the evaporation of MgO on to the cleaned Si (100) surface. After evaporation of MgO the Si surface edge is again shifted parallel towards lower energies. The two peaks observed on the Si background, at 1560 keV and 1350 keV, which are due to Mg and O in the grown MgO thin film, now show a different structure than in case of Fig. 6.1. In order to obtain more detailed information about the thickness, the composition of the MgO film and the interface with Si, the spectrum was simulated by the program RUMP.

From the simulations it was found that the grown MgO film is 2 nm thick. The MgO is found to be stoichiometric $Mg_{0.5}O_{0.5}$ at the interface, but the surface is deficient of oxygen and enriched with Mg as desired. Besides, this can be already seen from the spectra. The almost parallel shift of the high-energy edge of Si gives strong evidence that the 2 nm $MgO_x$ layer is quite uniform in thickness and no island formation has occurred. The MgO-Si interface is found to be very sharp from the RUMP simulation, hence ruling out the formation of any silicide phase or oxidation of the Si surface.

Figure 6.6(b) shows the high resolution TEM micrograph of the $Co/MgO_x$(2 nm)/Si (100) heterostructure. The image shows an excellent morphology with extremely smooth, flat layers and free of pin-holes. This result is in quite good agreement with the HRBS analysis. But the MgO film in this case is found to be amorphous in structure. So by decreasing the

oxygen content in the grown MgO tunnel barrier, it apparently ended up with an amorphous structure.

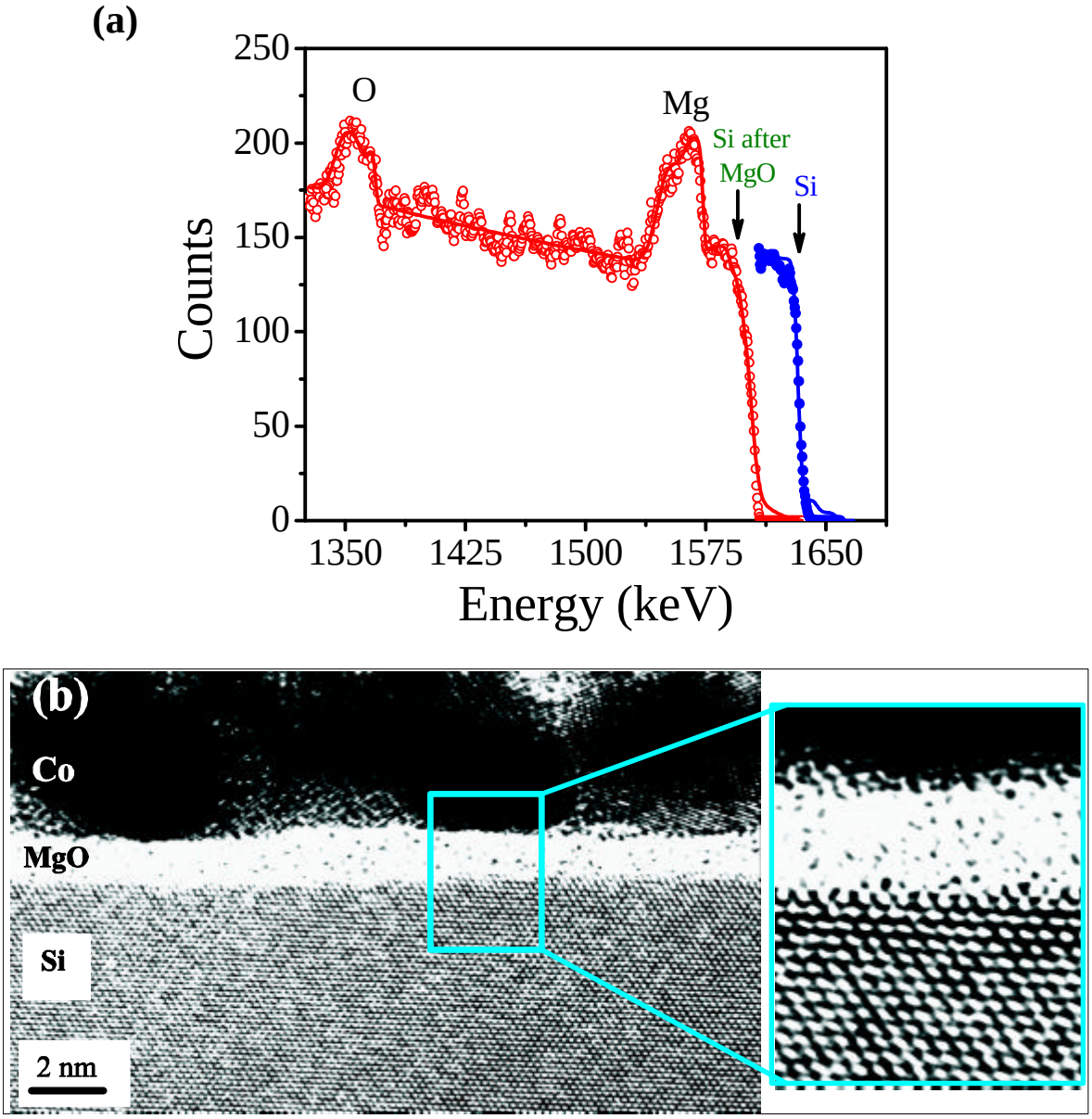


Fig. 6.6: **(a)** HRBS spectra of the Si sample before and after MgO evaporation. Before evaporation: HRBS spectrum of the high-energy edge Si edge (solid blue circles) and RUMP simulation (solid blue line) of the clean Si. After MgO evaporation: HRBS spectrum at Si, Mg and O edges (open red circles) and RUMP simulation (solid red line) of the 2 nm MgO as prepared on a Si (100) surface. **(b)** HR-TEM cross-sectional micrograph of a Si (100)/MgO (2 nm)/Co structure. The high resolution interface structure is shown on the right panel.

### 6.5.2 Scaling of MgO tunnel barrier thickness

Following the motivation to decrease the resistance-area product of the tunnel junctions as discussed in chapter 2, an ultra-thin MgO tunnel barrier with a thickness in the sub-nanometer

regime has also been fabricated. As the oxide thickness is decreased below 1 nm, meeting the reliability specifications is becoming challenging. Due to the large lattice mismatch between MgO and Si there might occur island growth at this thin film regime.

Ultra-thin MgO films were prepared on clean Si (100) by evaporating Mg at a $1\times10^{-7}$ mbar oxygen pressure with an evaporation rate of 1 Å/min. The HRBS spectra of the *in situ* analysis (using the same experimental conditions as described in section 6.3.2) are shown in Fig. 6.7; which gives detailed information about the composition and thickness of the MgO tunnel barrier and its interface structure with Si (100).

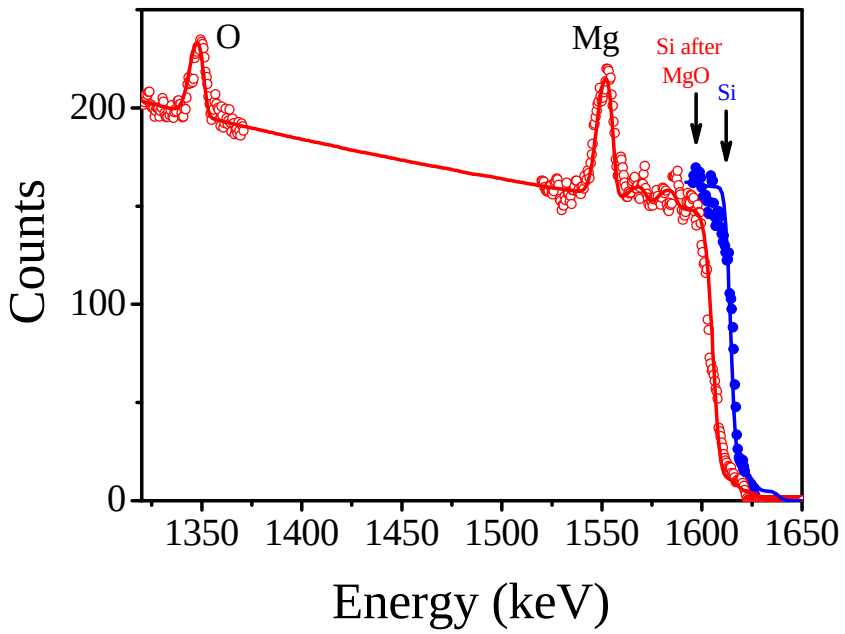


Fig. 6.7: HRBS spectra before and after MgO evaporation. HRBS spectra at the Si edge before MgO evaporation (solid blue circles) and RUMP simulation (solid blue line) of the clean Si. After MgO evaporation: HRBS spectra at the Si, Mg and O edges (open red circles) and RUMP simulation (solid red line) of the 7.35 Å thin MgO layer as prepared on the Si (100) surface.

The figure shows the HRBS spectra before and after evaporation of MgO. After evaporation of MgO, the Si surface edge is still shifted parallel towards lower energies. The two peaks at 1560 keV and 1350 keV are again due to Mg and O in the MgO thin film, respectively. From a RUMP simulation it is found that the grown MgO film is 7.35 Å thick and exhibits a composition of $Mg_{0.5}O_{0.5}$. The Si surface shifts towards lower energy which is due to complete coverage of the Si surface by the MgO layer. However the shift now is not fully parallel which gives evidence of slight thickness fluctuations of the MgO layer (~ 1 ML, as obtained from the RUMP simulation). The MgO-Si interface was found to be very sharp

from the RUMP simulation, hence ruling out the formation of any silicide phase or oxidation of the Si surface.

In the next section a proposal is presented for fabricating a spin injection device by using crystalline a tunnel barrier on Si (100).

## 6.6 Proposal for spin injection and detection in Si

The major challenge in the field of spintronics is to demonstrate efficient injection and detection of spin polarized carriers at room temperature. Thus far, spin transport has only been measured in direct-band gap semiconductors, below room temperature. My work is focused on the study of spin injection into silicon. The choice is motivated by large spin life times observed in silicon even at room temperature, owing to the weak spin orbit coupling. I have proposed the first electrical spin injection and electrical detection device on Si in March 2005. But due to fabrication difficulties the device could not be fabricated in time during my thesis. In the mean time Lou *et al.* have been able to show electrical detection of spin injection in GaAs in Feb. 2007 with the same electronic device [6.23]. Despite its exciting fundamental and technological promise, a demonstration of coherent spin transport in Si has remained elusive. The fabrication and realization of spin injection and detection device in Si is still a real challenge. In this section the proposal for electrical spin detection in Si which was thought to be done much before the work of the GaAs by Lou *et al.* is presented.

### 6.6.1 Spin injection device

Figure 6.8 shows my proposed spin injection and detection device. It consists of two Co electrodes sitting on a Si bar. The Co electrodes are separated from Si by a MgO tunnel barrier. The Si surface is heavily doped only below the two Co electrodes. The different aspect ratios of the Co electrodes were chosen for having two different switching fields so that the Co electrodes can be made parallel or anti-parallel by only sweeping the magnetic field for the measurement of magnetoresistance. The measurement was proposed to be made in non-local geometry, which minimizes the background effects by placing a spin detection electrode outside the path of the charge current. Spin polarized electrons can be injected from the first ferromagnetic electrode (Co1) into Si and a voltage can be measured between the second ferromagnetic electrode (Co2) and Si. Although the electrons will flow from Co 1 to contact 1

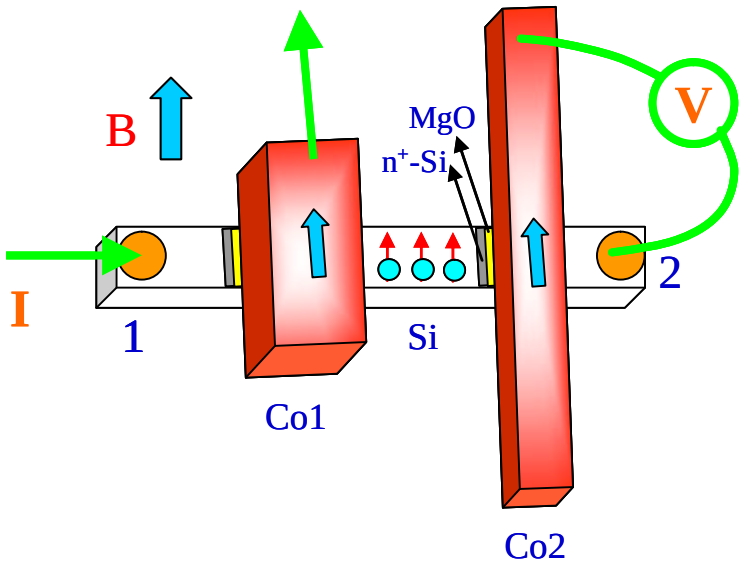


Fig. 6.8: Spin injection and detection concept, showing the injection of spin polarized electrons from Co1 electrode into Si through the MgO tunnel barrier and the detection by a second electrode Co2 in a non-local geometry.

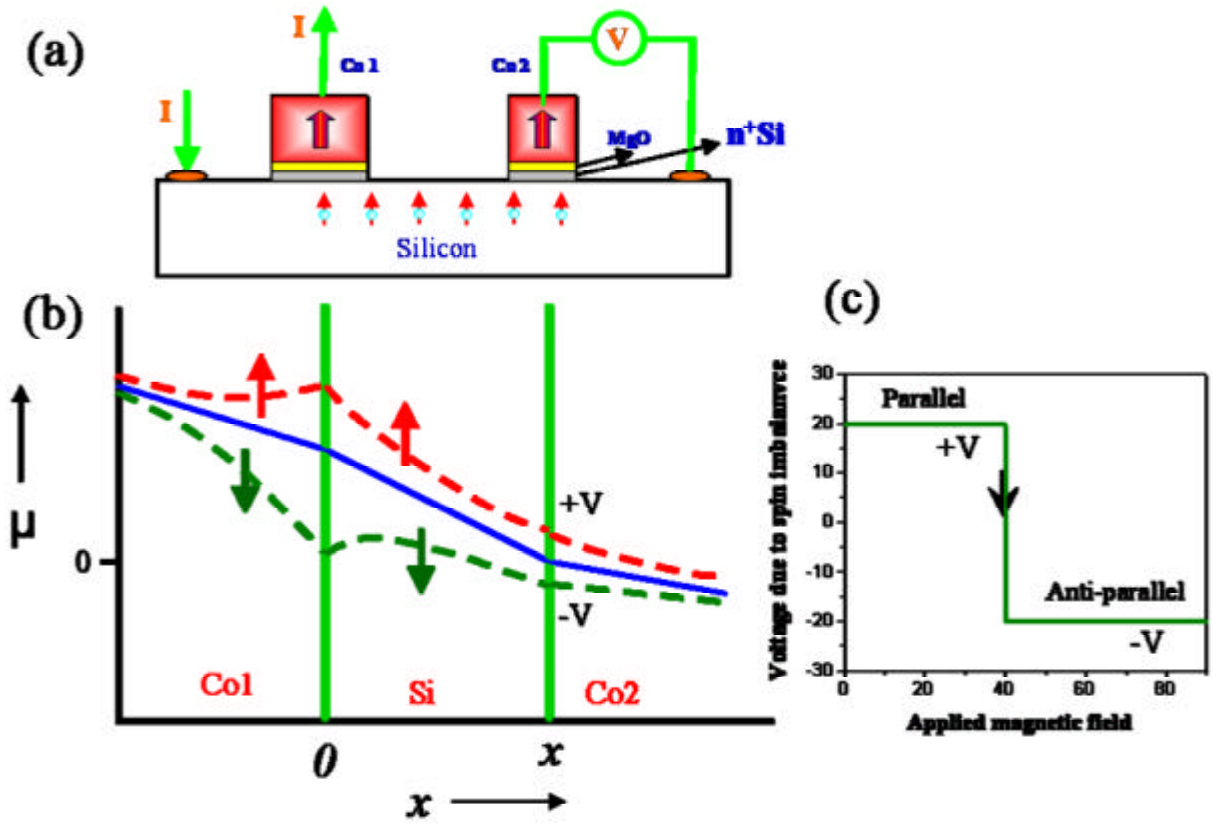


Fig. 6.9: **(a)** Cross section of the spin valve device, where the ferromagnetic spin injector (Co1) is separated from Si by a MgO tunnel barrier and $n^+$-Si layer. The second ferromagnetic electrode Co2 is used to detect the spin accumulation at a distance *x* from the injector. **(b)** Spatial dependence of spin up and spin down electrochemical potential (dashed line) in the device. The solid line indicates the electrochemical potential (voltage) of electrons in the absence of spin injection. **(c)** The expected change in the voltage signal in non local geometry for parallel and anti-parallel magnetization of Co1 and Co2.

through Si, a spin current can flow from the source in either direction, thus leading to stationary spin accumulation. This spin accumulation at the interface will extend over a characteristic spatial length given by the spin flip length. As the second ferromagnet (Co 2) is present within the spin diffusion length in Si, it can be used as a spin sensitive voltage probe to detect this spin accumulation.

The injected spin polarized electrons from Co1 through a tunnel barrier causes the densities (electrochemical potentials μ) of the spin up and spin down electrons in Si to become un-equal. The induced spin accumulation ( $m\uparrow - m\downarrow$ ) in Si can be detected by the Co2 contact via a tunnel barrier as a voltage drop. Sweeping the magnetic field, +/- V voltage can be measured for spin-up and spin-down electrons for parallel and anti parallel magnetization of the FMs respectively (see Fig. 6.9). For parallel alignment of Co1 and Co2, the voltage measured in the detector contact is only due to up spin electrons, and for anti-parallel alignment down spin electrons are measured. This gives rise to a spin valve signal. Measurements in this geometry will avoid many spurious side effects and what is measured is only the effect due to spin accumulation in Si.

## 6.7 Sample preparation for spin injection device

In this section the sample preparation for this spin injection device will be presented.

**(i) n-Si (100):** A n-Si (100) sample has been chosen as the base material for the spin injection device. The choice is motivated by long spin coherence lengths of electrons in n-type Si and the available states at $k$ = 0 in the (100) direction. In an all-electrical spin injection device where the ferromagnetic metals are used as spin injector, holes are unwanted due to their detrimental effect on the electron recombination and since the spin life times of holes is less than that of electrons. So moderate doping of n-type Si ($10^{16}$ atoms/cm$^3$) is chosen for long spin life times and spin diffusion lengths.

**(ii) Epitaxial n$^+$-Si layer:** Even with a tunnel barrier at the interface, a Schottky barrier forms at the interface due to band bending of Si. The formation of a Schottky barrier at the interface originates from an inability of the ultra thin tunnel barrier to support the difference in potentials between the Si and the FM on the other side of the tunnel barrier. As discussed in section 2.7.4, a n$^+$-Si layer ( $N_d^+ \geq 10^{20} cm^{-3}$) between FM and Si should be used to increase the spin injection current. The epitaxial n$^+$-Si layers were prepared by molecular

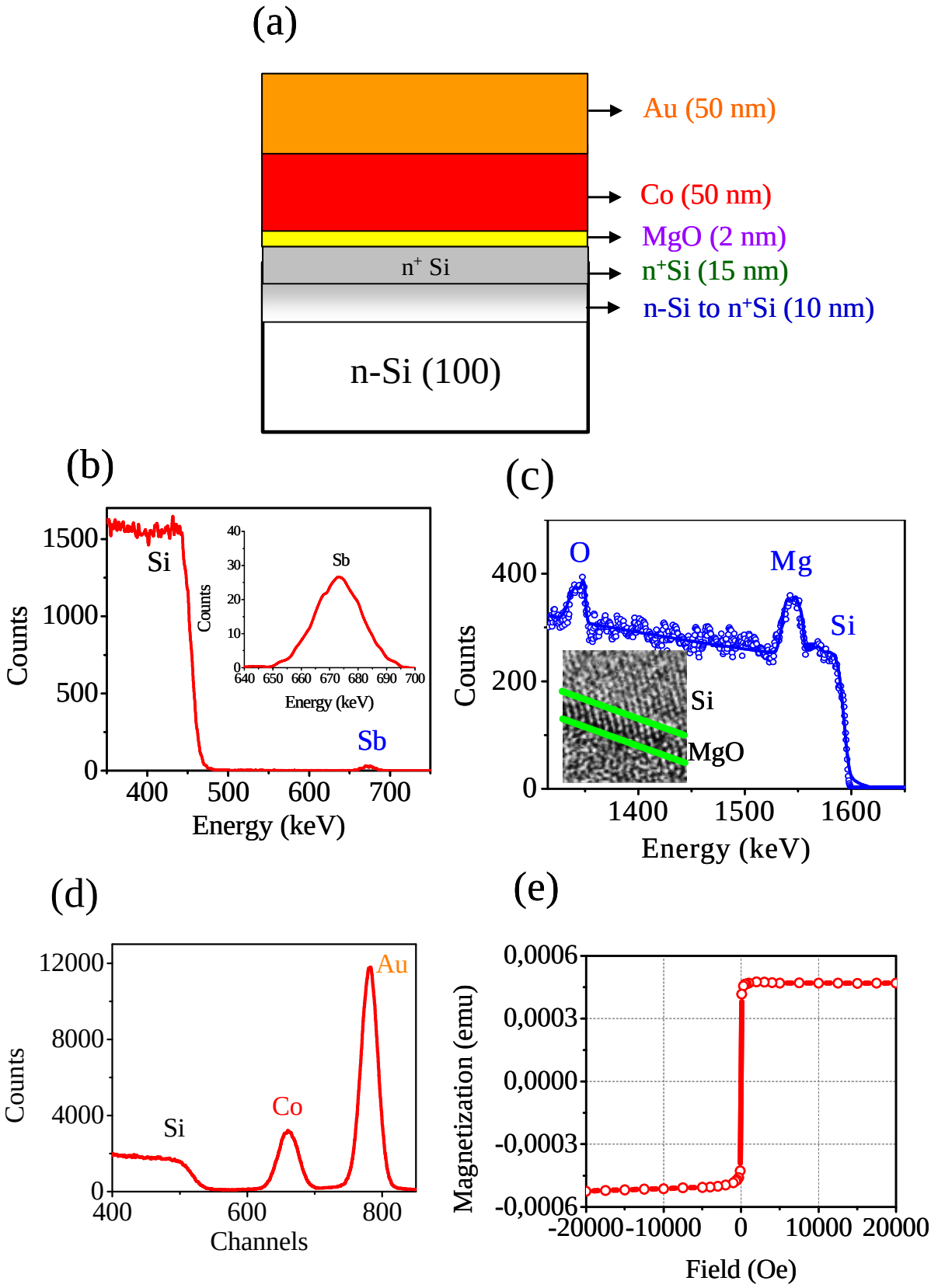


Fig. 6.10: **(a)** Structure of the prepared sample for fabrication of the spin injection device. **(b)** The RBS spectrum of the Sb-doped epitaxial $n^+$-Si layer. The inset shows the magnified version of the Sb profile. **(c)** HRBS spectrum of 2 nm MgO prepared on Si (100). The inset shows the HR-TEM micrograph of such a MgO tunnel barrier. **(d)** RBS spectrum of the sample shown in Fig.10 (a). **(e)** The magnetization loop of the 50 nm thin Co film of 25 $mm^2$ in size.

beam epitaxy using Arsenic as dopant in the following sequence. First a 15 nm thin $n^+$-Si sequential Antimony (Sb) doping starting at $N_d \approx 10^{16} atoms/cm^3$ at the substrate and increasing to $N_d \approx 10^{20} atoms/cm^3$ towards the surface was grown. Then a 15 nm thin $n^{++}$-Si layer ($N_d \approx 10^{20} atoms/cm^3$) on the surface was grown. The *ex situ* RBS characterization of such a sample is shown in the Fig. 6.10(b). The Sb doping profile can be clearly seen in the inset of the figure.

**(iii) MgO Tunnel barrier (2 nm)**

This Si sample was cleaned by a diluted HF solution and annealing under UHV conditions. A reactive molecular beam epitaxy approach has followed by evaporating Mg from an effusion cell in $1\times10^{-7}\,mbar$ of oxygen pressure for fabrication of the ultra thin MgO tunnel barrier. The resistance of the tunnel barrier can be tailored by controlling the oxygen exposure and thickness of the barrier as shown in section 6.5 of this chapter. The HRBS spectrrum and the HR-TEM micrograph of such a tunnel barrier are shown in Fig. 6.10(c).

**(iv) Ferromagnetic contacts**

50 nm of Co thin film was grown without breaking the vacuum to keep the interface clean. Then the film was capped with 50 nm Au for electrical contacts. The sample structure shown in Fig. 6.10(a) were characterized by RBS and SQUID. From the RBS measurement [shown in Fig. 6.10(d)], the thickness of Co and Au was found to be 50 nm each. The magnetization loop of the 50 nm Co film (sample size 5 mm × 5 mm) is shown in Fig. 6.10(e). The sample magnetization was found to be strongly in plane, which is highly desirable for our device structures.

## 6.8 Device structure

The device structure proposed is planned to be prepared by using e-beam lithography, focused ion beam, reactive ion etching and other semiconductor fabrication techniques.

### 6.8.1 Defining the ferromagnetic electrodes

The ferromagnetic stripes should have different coercive (switching) fields. In this way, parallel and anti parallel magnetization of the FM can be realized by sweeping the external

field. This can be achieved by fabricating FMs of different aspect ratios. The FM with higher width will have lower coecivity and will switch first and the 2$^{nd}$ electrode will switch at higher field. The second important thing is to achieve a single domain structure at least in the region where the FMs make contact with the tunnel barrier. This can be achieved by higher aspect ratios.

The dimensions of two Co electrodes are chosen as follows [6.24]

Co1: Thickness 50 nm, Size: (0.4×4) μm$^2$

Co2: Thickness 50 nm, Size: (0.2×12) μm$^2$

### 6.8.2 Channel length

Different devices were planned to be prepared, keeping the separation between the two electrodes in the range 200 nm – 1 $mm$ . By using different channel lengths, the spin diffusion length in Si can be measured.

### 6.8.3 Spin injection device

The proposed spin injection device is shown in Fig. 6.11. It consists of two ferromagnetic electrodes Co1 and Co2 separated by 200 nm on a n-Si channel. Highly doped $n^{++}$-Si should only be used just below the ferromagnetic electrodes to minimize the Schottky barrier width. The $n^{++}$-Si layer in the Si channel should be removed because the spin relaxation strongly depends on the doping concentration [6.25].

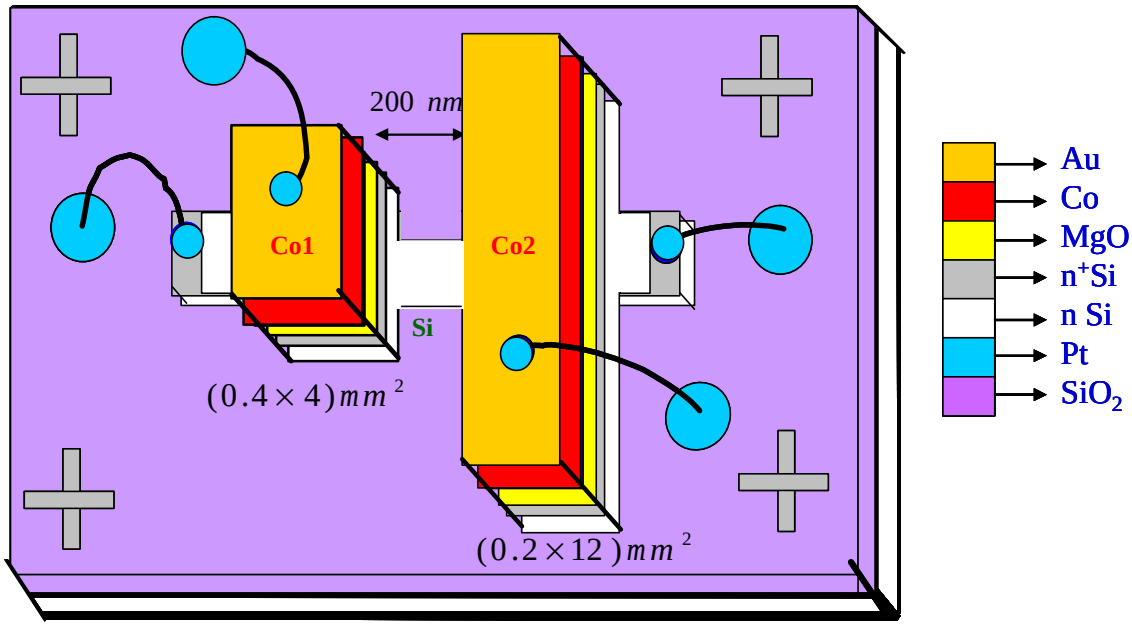


Fig. 6.11: Top view of the device structure for spin injection and detection in silicon: Spin polarized electrons can be injected from the 1st FM contact Co1 into Si through a MgO tunnel barrier and can be detected by Co2 through a second MgO tunnel barrier depending upon the relative magnetization of the Co electrodes. The Measurements are to be done in the depicted non-local geometry, which will avoid magnetoresistance of the ferromagnetic electrodes and stray Hall effects in the device structure.

# Chapter 7

# Mn doped Si for spin injection into Si

Most probably spin-polarized electrons can not be injected across a FM/Si Schottky contact due to its disordered interface structure. As extensively studied in chapter 4, multiple silicide phases form at the FM/Si interface at room temperature [7.1]. They may be the main cause for spin flip scattering and would drastically reduce the spin injection efficiency [7.2]. An alternative approach presented in chapter 6 for spin injection into Si is to insert a tunnel barrier between FM and Si [7.3]. This tunnel barrier will prohibit silicide formation at the FM/Si interface and also provide a high spin-dependent resistance. A third approach, which is presented in this chapter, is to use diluted ferromagnetic silicon (DMS) as spin injector instead of a metallic ferromagnet. These DMS also overcome the conductivity mismatch problem (observed in the case of ferromagnetic metal / Si heterostructures) by ensuring that the resistivities of the materials on both sides of the interface are comparable in magnitude [7.4].

## 7.1 Mn doped Si

Making Si a ferromagnetic semiconductor at room temperature by doping it with Mn to achieve the dominance of the long-range ferromagnetic interaction over the short-range antiferromagnetic interaction present in Mn bulk material can provide a promising candidate for spin injection into Si. Interestingly Mn-doped Si shows ferromagnetic behavior with a Curie temperature above room temperature in $Si_{0.95}Mn_{0.05}$ thin films [7.5], $Mn^+$-implanted Si [7.6], and $Mn^+$-implanted Si nanowires [7.7].

The ferromagnetic order in Mn-doped Si is believed to be due to long range interaction of Mn atoms, mediated by carriers, in the Si matrix. Carrier-mediated ferromagnetism has

great potential for making spin field effect transistors [7.8]. The nature and origin of this ferromagnetism, as well as its carrier mediation in Mn-doped Si still are points of discussion. Bolduc *et al*. [7.6] reported that in Mn-implanted samples the ferromagnetic exchange is hole mediated by comparing n-Si (n-type dopant, $10^{15}$ at./cm$^3$) and p$^+$-Si (p-type dopant,$10^{19}$ at./cm$^3$), where the carrier concentrations in n-Si and p$^+$-Si are quite different. There remains, however, the following controversy: if the ferromagnetism is only hole mediated, then n-Si should not show ferromagnetism. But, as they have demonstrated, it does show ferromagnetism. In another study Liu *et al*. [7.9] have shown that Mn-and B-doped Si thin films (p-type) show hole-mediated ferromagnetism. n-type Si samples were not studied in their work. So it carries importance to verify whether the ferromagnetism is mediated both by holes and electrons.

As the Mn atoms are known to be very fast diffusers in the Si lattice and to have a very low solubility, authors have only tried non-equilibrium ways like ion-implantation [7.6] and low temperature MBE growth [7.5] to dope Si with Mn. In these ways it is difficult to maintain the crystal quality of Si. Solid state diffusion, as one way to dope Si with Mn without much destruction of crystallinity, has not drawn much attention from the magnetism point of view. So it carries importance to find out whether Mn doped into Si by solid state diffusion, shows room temperature ferromagnetism. It is also interesting to see, whether ferromagnetism in solid state-diffused samples is mediated by carriers.

In order to answer on a few of these open questions, structural and magnetic properties of Mn-doped Si samples have been studied in this chapter. Ferromagnetic Si samples were prepared for this purpose in two different ways: i) by Mn ion implantation and ii) by solid state diffusion of Mn atoms. The origin of the ferromagnetism in such samples was studied by comparing the magnetic properties of p- and n-type Si samples with different dopant concentrations.

## 7.2 Sample preparation

Three types of Si (100) substrates were used in these experiments: p$^+$-Si (Boron: $1\times10^{19}$ atoms/cm$^3$), p-Si (Boron: $1\times10^{15}$ atoms/cm$^3$) and n-Si (Phosphous: $1\times10^{15}$ atoms/cm$^3$). The samples were treated in the following ways: i) In the case of Mn implantation: The samples were HF cleaned and degassed in UHV before implantation. For the study of the dose dependence of the ferromagnetism, the p$^+$-Si samples were implanted with 80 keV Mn$^+$ ions to the fluences of $5\times10^{15}$, $1\times10^{16}$, and $1\times10^{17}$ atoms/cm$^2$, which corresponds to Mn peak

concentrations of 0.4, 0.8, and 8 at. %, respectively. The carrier dependence of the ferromagnetism was studied on $p^+$-Si, p-Si and n-Si samples implanted by Mn ions to a fluence of $1\times10^{17}$ atoms/cm$^2$ and $1\times10^{16}$ atoms/cm$^2$. All the implantations were done at room temperature and the samples were subsequently rapid-thermally annealed at 850 °C for 5 min. ii) For the case of solid state diffusion, the Si substrates were cleaned by flash heating at 1050 °C in UHV. On these clean $p^+$-Si and n-Si surfaces, 4.12 ML of Mn were evaporated at room temperature and subsequently annealed at different temperatures (1 ML = $6.87\times10^{14}$ atoms/cm$^2$, this is the atomic density of the Si (100) planes). The growth and annealing of the manganese on the silicon substrate were studied *in situ* with high resolution RBS. Magnetic measurements were performed with a quantum design SQUID magnetometer. The size of all the samples taken for the SQUID measurements was 5×5 mm$^2$. To reveal the origin of ferromagnetism X-ray magnetic circular dichroism (XMCD) measurements were performed on a Mn-implanted Si sample.

## 7.3 Mn implanted Si

### 7.3.1 Lattice location of Mn atoms in Si lattice

After Mn-ion implantation, the implantation profiles were analyzed by RBS using a 1 MeV $He^+$ ion beam (incidence angle: 45°, scattering angle: 135°). The implantation profiles are found to be Gaussian with a projected range $R_p$ of about 70 nm as shown in Fig. 7.1(a) for three different fluences. The samples were also analyzed by RBS in combination with ion channeling to check for the implantation-induced damage and the lattice location of the Mn atoms with respect to the Si lattice. Fig. 7.1(b) shows such RBS-channeling spectra for the implantation fluence of $1\times10^{17}$ Mn ions/cm$^2$. From the comparison of the RBS-channeling spectra before and after annealing it is clear that the recrystallization during annealing started from the unperturbed Si bulk. The Mn implanted part partially recrystallized, but a major part is still full of defects. Further, it can be clearly seen that some out-diffusion of Mn occurred during annealing. To find out whether the Mn atoms are in interstitial or substitutional positions after annealing, the random and the channel spectra of the annealed samples were compared. As the spectra in Fig. 7.1(b) show, the Mn profile stayed the same in both cases, giving evidence that the majority of the implanted Mn atoms are not located on substitutional, i.e. Si sites with respect to the [100] crystallographic axis. Similar measurements were performed for the smaller implantation doses (not shown here); they show similar results, i.e. that the majority of the Mn atoms do not occupy substitutional sites in the Si lattice. It is to be

noted that according to density functional calculations interstitial Mn impurities in Si are energetically more stable than substitutional ones and that these interstitial Mn atoms show ferromagnetic ordering in the Si lattice [7.10]. The formation of Mn-silicide phases could not be observed within the detection limit of conventional XRD (Siemens D5005). However, the formation of manganese silicide clusters on nanometer scale can not be ruled out [7.11]. Finally, it is to be noted that our samples were implanted at room temperature and rapid-thermally annealed afterwards, to minimize the formation of silicide clusters.

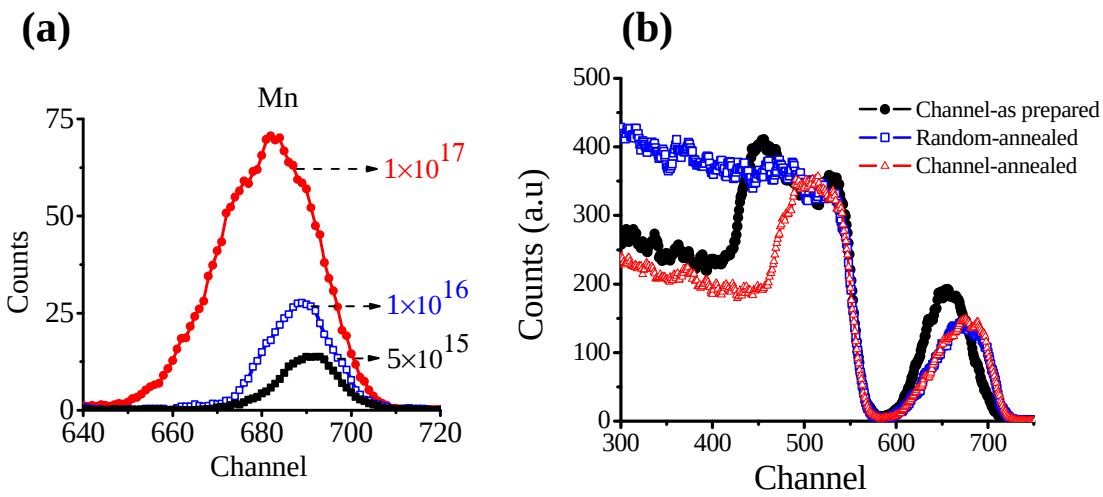


Fig. 7.1: **(a)** RBS depth profiles of Mn implanted in Si for three different fluences (atoms/cm$^2$). **(b)** RBS spectra of a p$^+$-Si sample implanted with 1×10$^{17}$ Mn ions/cm$^2$ : as implanted, ion beam incidence along [100] channel axis (solid circles); after annealing at 850 °C for 5 min., incidence along [100] axis (open triangles) and in random direction (open squares). (1 MeV He$^+$ ion beam, incidence angle: 45°, scattering angle: 135°).

### 7.3.2 Dose dependence of ferromagnetism

Magnetization curves (*M* vs *H*), measured at 300 K for all Mn implanted p$^+$-Si samples (Mn$^+$ ion implantation fluences 5×10$^{15}$, 1×10$^{16}$, and 1×10$^{17}$ ions/cm$^2$) are shown in Fig. 7.2. All three samples show room temperature ferromagnetism with remanence of $M_R$ ~ 0.12 ×10$^{-5}$ emu and coercivity of $\mu_0$H ~ 50 Oe. The linear background diamagnetism of Si was subtracted for all displayed data. As the figure shows, the saturation magnetization increases with the Mn content, but not proportional to the implantation dose. The magnetic saturation moment per Mn atom calculated for the 5×10$^{15}$ Mn ions/cm$^2$ sample amounts to about 1.2 Bohr magnetons ($\mu_B$). This value is by a factor of ~ 4.16 less than the moment of an isolated Mn atom of 5 $\mu_B$. The discrepancy is probably in part due to the strong antiferromagnetic coupling among the most closely spaced Mn atoms [7.12]. This low magnetic moment can also be due to disorder

effects which give rise to a wide distribution of exchange couplings and hopping integrals [7.13]. The calculated magnetic moment per Mn atom decreases with increasing implantation fluence: 1.2, 0.92 and 0.1 $\mu_B$ for the implantation fluences of $5\times10^{15}$, $1\times10^{16}$ and $1\times10^{17}$ $Mn^+$ ions/cm$^2$, respectively. This decrease is strong evidence that the short-range antiferromagnetic coupling is overcoming the long-range ferromagnetic interaction due to the closer spacing of the Mn ions [7.12].

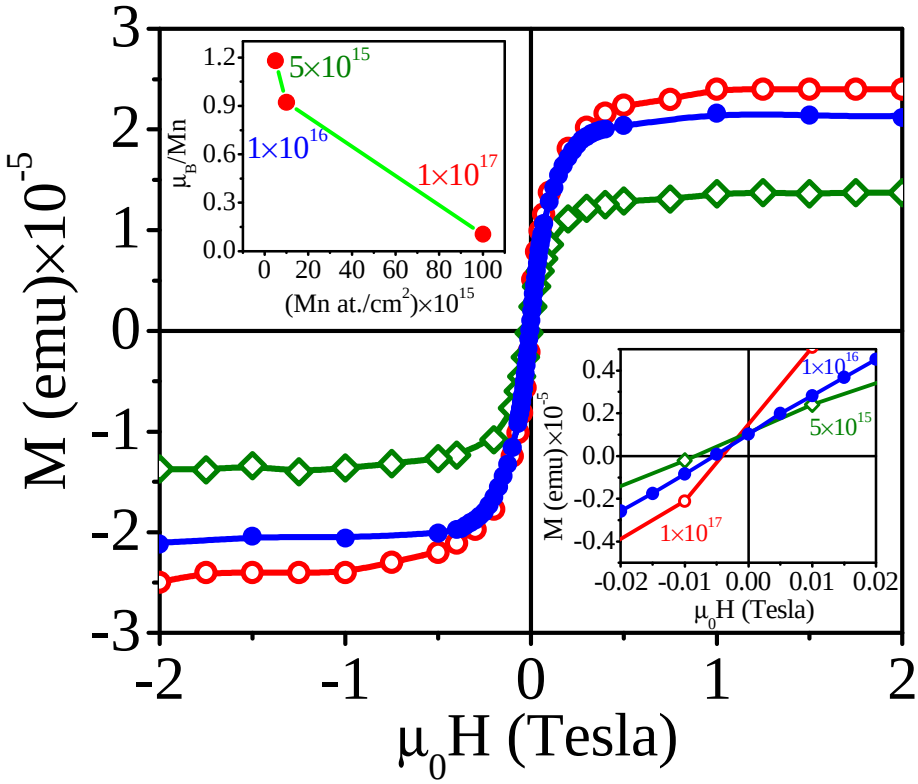


Fig. 7.2: Dose dependent ferromagnetism: Magnetization curves (*M* vs *H*) at 300 K for Mn implanted $p^+$-Si samples after rapid thermal annealing (implantation fluence Mn: $5\times10^{15}$, $1\times10^{16}$, and $1\times10^{17}$ atoms/cm$^2$). The magnetization increases with the Mn content in a non-linear fashion. The **lower inset** of the figure shows a magnified version of the *M* vs *H* curve around the origin to make remanence and coercive fields better visible. The **upper inset** of the figure shows the saturation magnetic moment per Mn atom vs. Mn implantation fluence.

Fig 7.3(a) and (b) illustrate the temperature dependence of magnetization (zero field cooled) for $p^+$-Si (B doped $1\times10^{19}$ atoms/cm$^3$) containing Mn implanted to fluences of $1\times10^{17}$ atoms/cm$^2$ and $1\times10^{16}$ atoms/cm$^2$, respectively. The ZFC curves of these two samples appear rather smooth without any abrupt change. It is clear from these measurements that there is no other low temperature magnetic phase present in the sample and that the Curie temperature of the sample is well above room temperature. The formation of any extra magnetic phase and nanocrystals would have resulted in a peak in the ZFC curve due to 'blocking' mechanism

owing to the competition between the thermal energy and the magnetic anisotropy energy of nanoparticles [7.14].

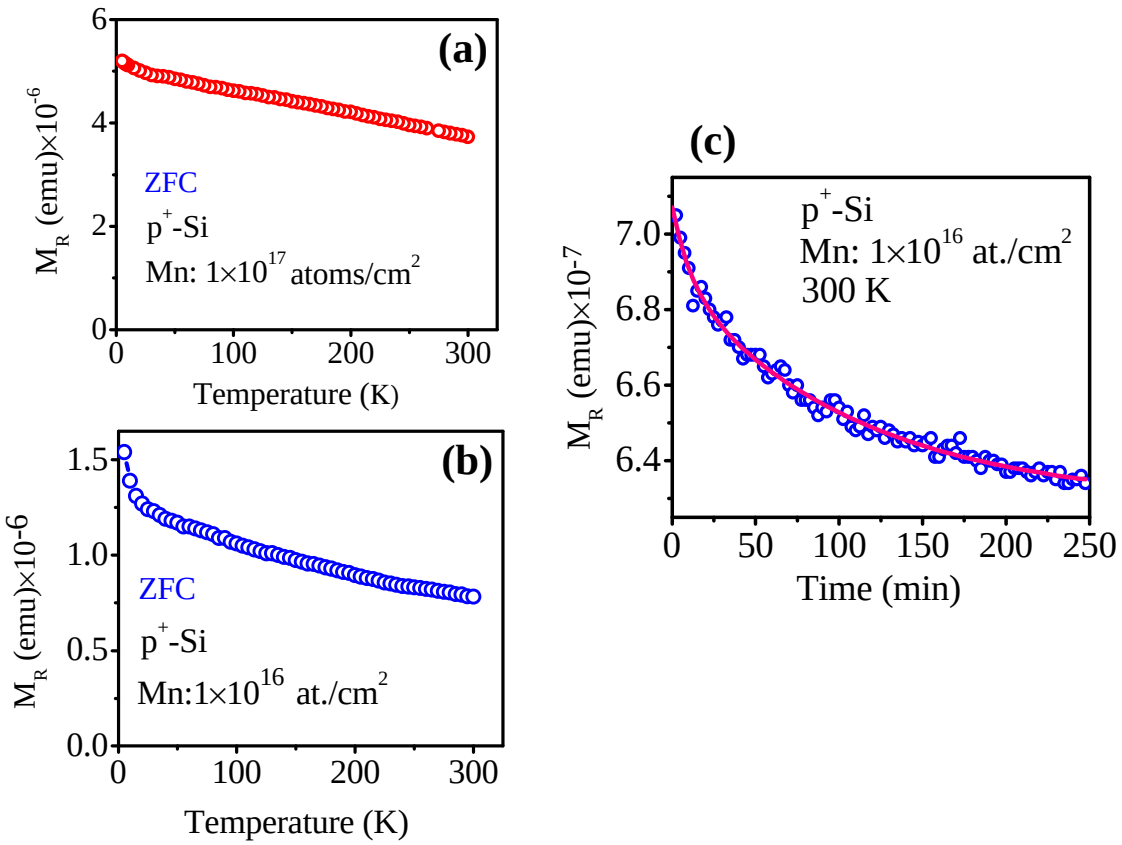


Fig. 7.3: Temperature dependence of remanent magnetization (zero field cooled curves) of Mn implanted in $p^+$-Si (B doped $1\times10^{19}$ atoms/cm$^3$) containing Mn implanted to fluence of **(a)** $1\times10^{17}$ atoms/cm$^2$ and **(b)** $1\times10^{16}$ atoms/cm$^2$. **(c)** Relaxation of the magnetization of $p^+$-Si (B doped $1\times10^{19}$ atoms/cm$^3$) containing Mn implanted to a fluence of $1\times10^{16}$ atoms/cm$^2$ after switching of the external field at 300 K. The solid line is the 2$^{nd}$ order exponential decay curve fit to the data.

The relaxation of the magnetization with respect to time was measured for $p^+$-Si (B-doped $1\times10^{19}$ atoms/cm$^3$) containing Mn implanted to a fluence of $1\times10^{16}$ atoms/cm$^2$ after switch-off of an external magnetic field at 300 K [Fig. 7.3(c)]. The sample obviously relaxes with time; however the relaxation is very small and the magnetization seems to reach equilibrium value after about 4 hr. This is an important fact because in many cases magnetism in diluted magnetic semiconductors turns out to be not stable with time. The solid lines in figure represents 2$^{nd}$ order exponential decay curve fit to the data points. From these measurements we can conclude that the ferromagnetic behavior of these samples persists well above room temperature and are quite stable with time.

### 7.3.3 Carrier-mediated ferromagnetism

In order to obtain information about the origin of this Mn-induced ferromagnetism in Si (whether hole mediated or electron mediated), Mn ions were implanted to a fluence of $1\times10^{17}$ ions/cm$^2$ and $1\times10^{16}$ ions/cm$^2$ into p$^+$-Si (Boron: $1\times10^{19}$ atoms/cm$^3$), p-Si (Boron: $1\times10^{15}$ atoms/cm$^3$) and n-Si (Phosphorus: $1\times10^{15}$ atoms/cm$^2$) samples. It should be pointed out in particular, that the hole concentration in p-Si and the electron concentration in the n-Si were the same, while the hole concentration in the p$^+$-Si sample was a factor of 10,000 higher.

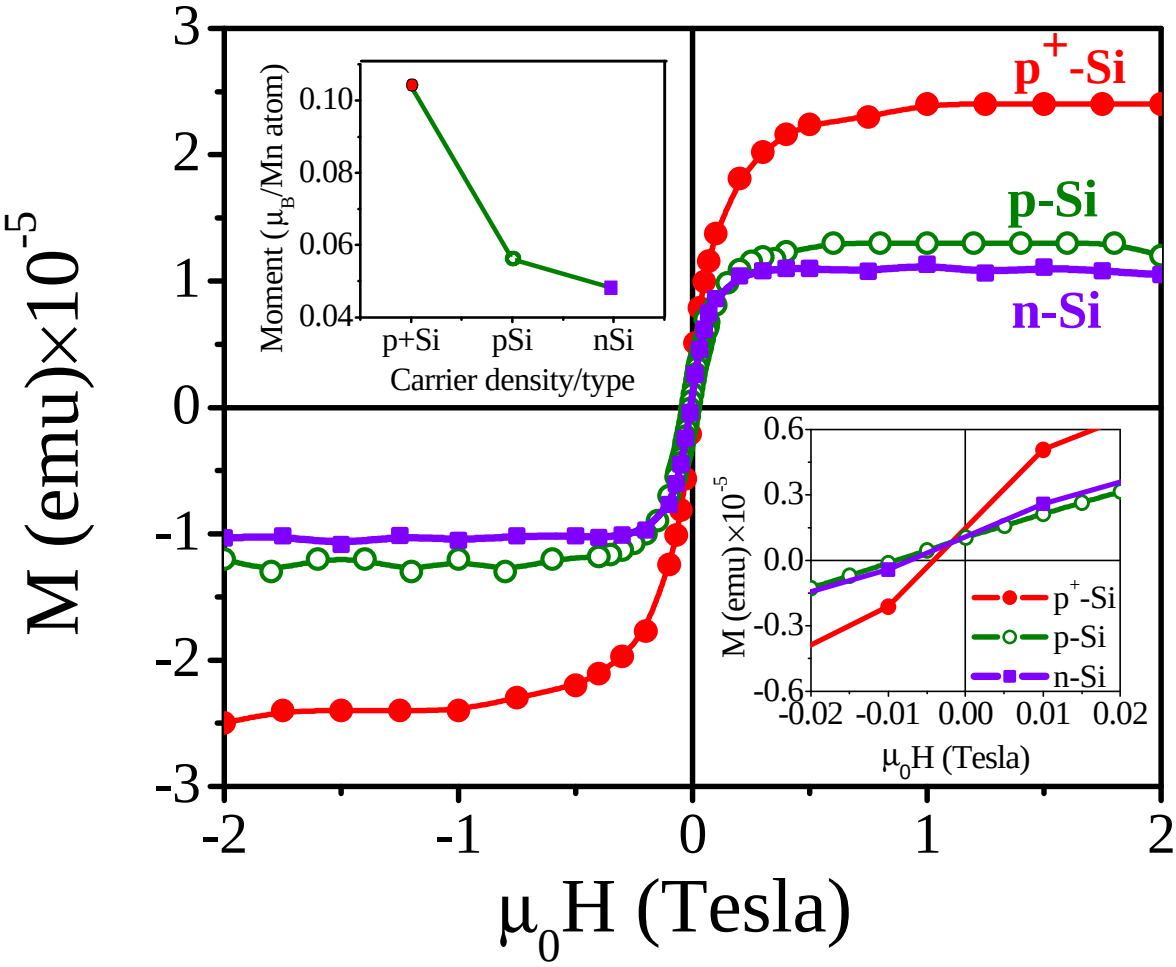


Fig. 7.4: Carrier-mediated ferromagnetism: Magnetization curves (*M* vs *H*) at 300 K for Mn ions of the fluence of $1\times10^{17}$ ions/cm$^2$ implanted into p$^+$-Si (Boron: $1\times10^{19}$ atoms/cm$^3$), p-Si (Boron: $1\times10^{15}$ atoms/cm$^3$) and n-Si (Phosphorus: $1\times10^{15}$ atoms/cm$^3$) samples. A higher hole concentration yields a higher magnetic moment. The latter is the same for equal concentrations of electronics and holes. The **lower inset** of the figure shows, however, a magnified version of the *M* vs *H* curve around the origin to make remanence and coercive fields better visible. The **upper inset** of the figure shows the saturation magnetic moment per Mn atom.

For the case of $1\times10^{17}$ Mn ions/cm$^2$ (Fig. 7.4), the p$^+$-Si sample shows a much higher magnetization than the n-Si sample in agreement with Bolduc *et al.* [7.6]. But the p-Si and n-Si samples (which have the same electron as hole concentrations) show almost the same saturation magnetization, remanence and coercive field at 300 K. Similar results are also observed in measurements at 5 K.

Similarly for the case of $1\times10^{16}$ Mn ions/cm$^2$ (Fig. 7.5), the p$^+$-Si sample shows a much higher magnetization than the n-Si sample. But the p-Si and n-Si samples (which have the same electron as hole concentrations) show almost the same saturation magnetization at 300 K.

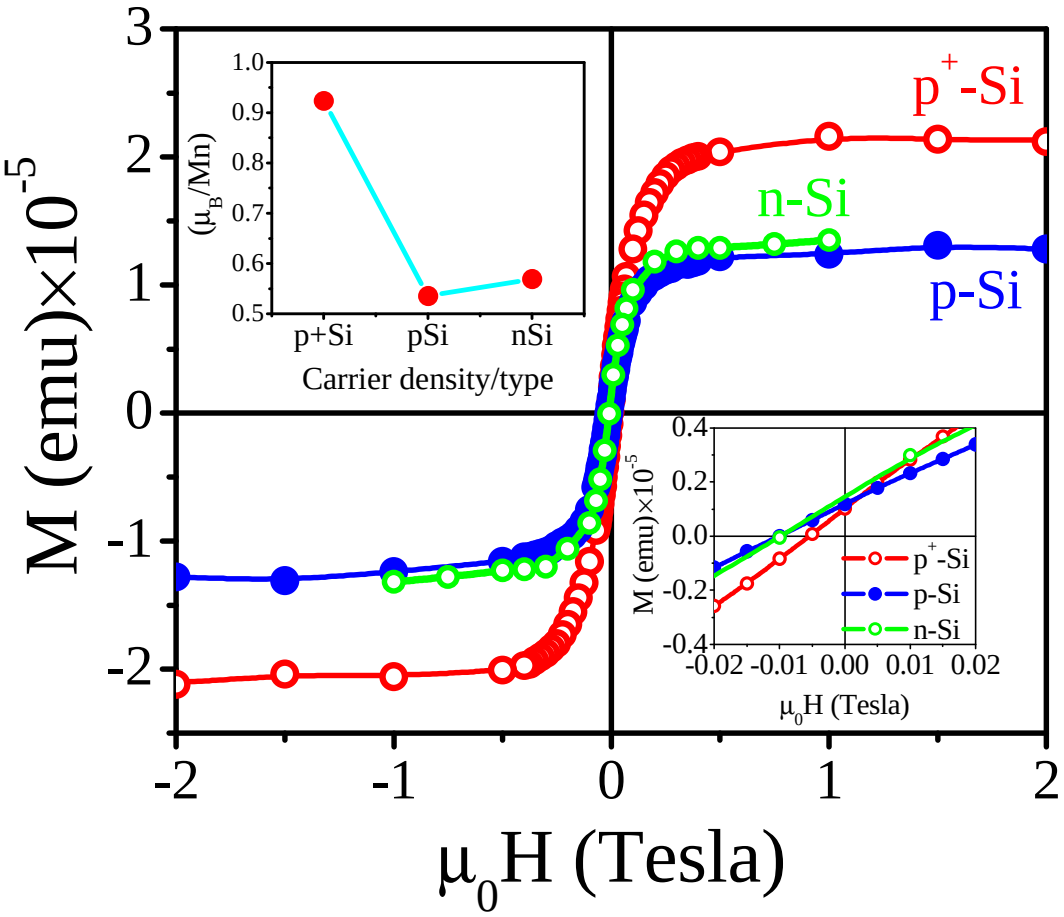


Fig. 7.5: Magnetization curves (*M* vs *H*) at 300 K for Mn ions of the fluence of $1\times10^{16}$ ions/cm$^2$ implanted into p$^+$-Si (Boron: $1\times10^{19}$ atoms/cm$^3$), p-Si (Boron: $1\times10^{15}$ atoms/cm$^3$) and n-Si (Phosphorus: $1\times10^{15}$ atoms/cm$^3$) samples. A higher hole concentration yields a higher magnetic moment. The latter is the same for equal concentrations of electronics and holes. The **Lower inset** of the figure shows a magnified version of the *M* vs *H* curve around the origin to make remanence and coercive fields better visible. The **Upper inset** of the figure shows the carrier dependence of the saturation magnetic moment per Mn atom.

These results give clear evidence that the magnetism in Mn-implanted samples is not mediated by holes alone, but apparently also by electrons. Thus, our results give evidence that the ferromagnetic ordering in Mn-implanted Si is due to the coupling of the localized Mn moments by charge carriers, i.e. both electrons and holes. As this observation can be reproduced for different samples, the effect can be taken as universal for Mn implanted into Si. With regard to carriers in Mn-doped Si: the energy levels induced by Mn are deep in the energy gap [7.15] and thus do not contribute significantly at 5 K. So at this low temperature only holes in p-type and electrons in n-type are the majority carriers.

### 7.3.4 Surface-magnetic properties of Mn implanted Si : X-ray magnetic circular dichroism (XMCD) measurements

To reveal the origin of ferromagnetism observed in Mn doped Si (how much each Mn atom contributes to magnetism), XMCD measurements were carried out on $1\times10^{17}$ Mn atoms/cm$^2$ implanted into $p^+$-Si (B doped: $1\times10^{19}$ atoms/cm$^3$) in collaboration with Mr. Thomas Tietze and Dr. Eberhard Goering (MPI für Metallforschung, Stuttgart). As the Mn implanted profile was 70 nm below the Si surface, the surface Si layer was etched away using diluted KOH solution. The magnetic behavior of the sample was then studied by XMCD at the $L_{2,3}$ Mn edge at room temperature at the PM III beam line at BESSY II. Total electron yield X-ray absorption spectra at the Mn edge were recorded for parallel ($\mu^+$) and antiparallel ($\mu^-$) alignment of the photo helicity with the applied fields (from B = 0 to 2 T) at room temperature. The measurements were done in normal incident geometry. The X-ray absorption spectra for B = 2 T is shown in Fig. 7.6. The XMCD ($\mu^+$- $\mu^-$) signal as obtained from the absorption spectra for B = 2 T is shown in the lower panel of the figure. At the $L_3$ edge a very low XMCD signal is obtained and no signal could be obtained at the $L_2$ edge. Absence of XMCD signal at $L_2$ edge may be due to the fact that there is a huge orbital moment on Mn atoms [7.16]. Applying the sum rule [7.17], an orbital magnetic moment of $1.42\times10^{-3}$ $\mu_B$ and a spin magnetic moment of $1.84\times10^{-3}$ $\mu_B$ were derived. The total magnetic moment ($3.261\times10^{-3}$ $\mu_B$) as obtained from the XMCD measurements is two orders of magnitude less than that observed in the SQUID measurement. The inset in the lower panel of the figure shows the total magnetic moment per Mn atom versus the magnetic filed. The absence of any XMCD signal at zero applied magnetic field gives clear evidence that there is no remanent magnetic moment on the Mn atoms. With increasing the magnetic field the total magnetic moment per Mn atom is found to increase linearly, which clearly reveals a

paramagnetic behavior (see inset of Fig.7.6). So manganese atoms on Si surface are in the paramagnetic state. These measurements do not explain the ferromagnetism observed in the sample.

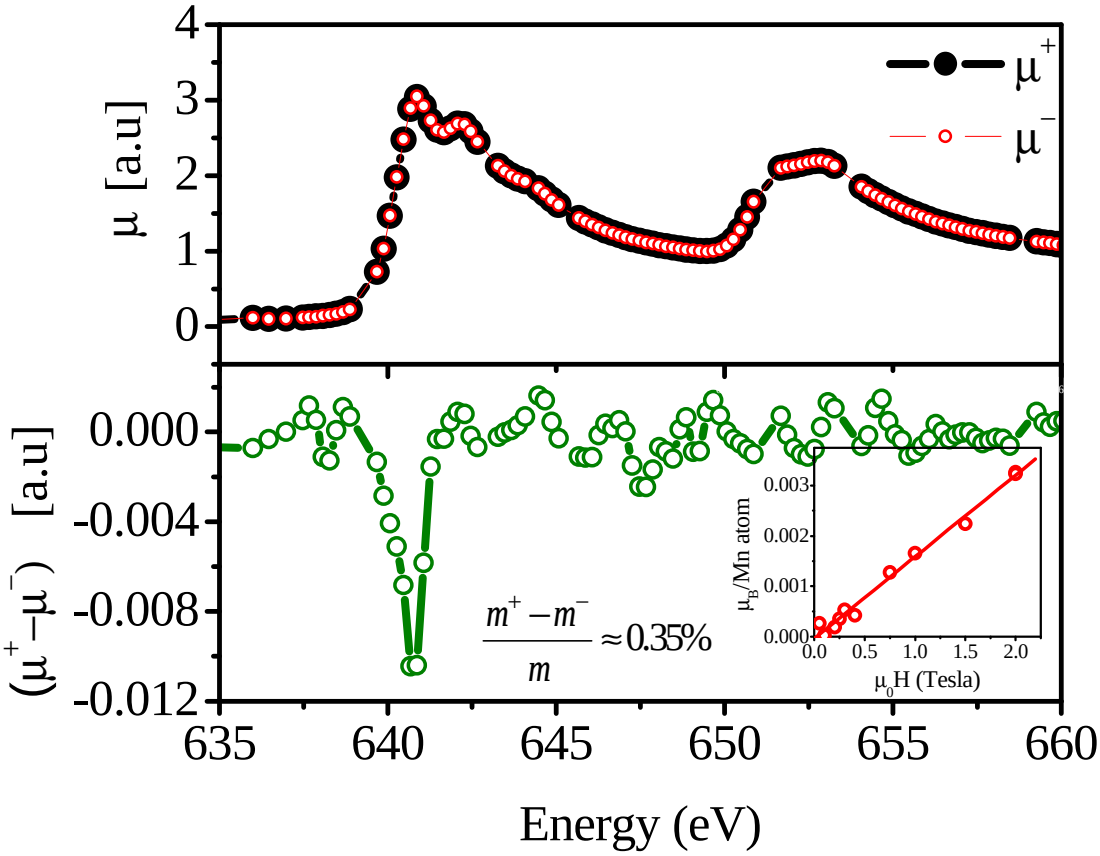


Fig. 7.6: **Upper panel:** TEY X-ray absorption spectra at the Mn $L_2$ and $L_3$ edges of the Mn implanted $p^+$-Si sample. The spectra recorded for parallel ($\mu^+$, black circles) and antiparallel ($\mu^-$, red circles) alignment of the photo helicity with the applied field B = 2 T at room temperature. **Lower panel:** XMCD ($\mu^+$- $\mu^-$) signal as obtained from the absorption spectra. The **inset** shows the total magnetic moment per Mn atom versus the magnetic filed. The straight line is the linear fit to data points.

In the total electron yield (TYE) mode applied here, the probing depth of XMCD measurements is given by the mean free path of the secondary photo electrons that escape the sample's surface, typically is in the range of 2 to 3 nm. So the results obtained from XMCD measurements presented here are only a surface effect, where Mn atoms may be in an oxidized state or in the $SiO_2$ matrix. Measurements in florescence yield (FY) mode, which can probe Mn atoms deeper inside the Si (~ 20 nm) or transmission mode are required to probe the actual moment of these Mn atoms deep in the Si lattice. So, up to now, magnetic moments of Mn atoms in Si lattice could not be measured successfully by XMCD. It is to be noted that

while Gambardella *et al.* have observed paramagnetic behavior of Mn-doped Ge by TEY mode, a ferromagnetic moment on Mn atoms could be revealed by the same authors by using florescence yield (FY) mode (where they probe Mn atoms deeper in Ge) [7.18].

To reveal more, whether there is any induced magnetic moments on the Si atoms by neighboring Mn atoms, absorption spectra at the Si $L_2$ and $L_3$ edges were recorded for parallel ($\mu^+$) and antiparallel ($\mu^-$) alignment of photo helicity (B = 0.5 T, room temperature). As shown in Fig. 7.7, no XMCD ($\mu^+$- $\mu^-$) signal could be obtained also for Si.

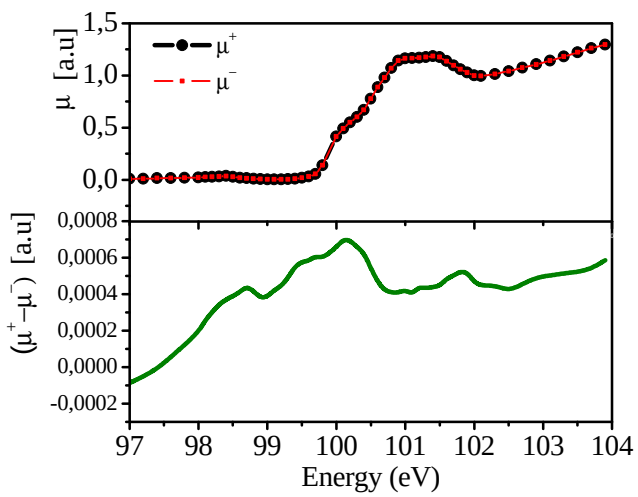


Fig. 7.7: **(Upper panel)** TEY x-ray absorption spectra at the Si $L_2$ and $L_3$ edges of the Mn implanted Si sample. The spectra recorded for parallel ($\mu^+$, black circles) and antiparallel ($\mu^-$, red square) alignment of photo helicity with applied field B = 0.5 T at room temperature. **(Lower panel)** No XMCD ($\mu^+$- $\mu^-$) signal could be obtained from the absorption spectra.

## 7.4 Mn doping by solid state diffusion

### 7.4.1 Growth of Mn on Si (100)

The second group of samples, we want to call them solid state diffusion samples in the following, were prepared by evaporation of Mn on clean Si substrates and subsequent annealing. Mn in the range 0.52 to 4.12 ML was evaporated on $p^+$-Si (Boron: $1\times10^{19}$ atoms/cm$^3$) and n-Si (Phosphorus: $1\times10^{15}$ atoms/cm$^3$), and HRBS spectra taken at the Mn and Si edges during evaporation, using 1 MeV $He^+$ ions at an incidence angle of 3.5° to the sample surface and a scattering angle of 37.5°. The spectra are shown in Fig. 7.8 (a). In order to obtain more detailed information, the spectra were simulated by the program RUMP. In these

simulations the sample was subdivided into thin sublayers of the thickness of $6.87\times10^{14}$ atoms/cm$^2$ (this is the atomic density of the Si (100) planes). The composition of each sublayer was varied and the HRBS spectrum calculated for the assumed Mn distribution until good agreement with the experimental data was achieved.

From the very beginning of the evaporation (0.5 ML of Mn) Mn diffuses into the Si in addition to growth of Mn on the Si surface. With increasing coverage an increasing amount of Mn atoms keep diffusing into the Si lattice. As the figure shows, the Si signal stays at the surface at all coverages, indicating that for all the coverages silicide-like phases are formed. At 4.12 ML of Mn, around 5 ML of $Mn_2Si$, followed by 2 ML of $MnSi_2$ are formed at the interface. We want to note that Mn atoms diffuse deep into the Si bulk already at room temperature, even for very low coverage (0.25 ML) with oscillatory concentrations (as observed with HRBS with monolayer depth resolution to be presented in section 7.5).

### 7.4.2 Annealing of Mn on Si (100)

The samples were then annealed in steps from 450 °C to 700 °C for different periods of time [see Fig. 7.8(b)]. Starting at lower temperature (450 °C) with the annealing causes Mn to diffuse into the Si bulk without sublimitation from the surface which would occur at high temperature (700 °C). The HRBS spectra shown in Fig. 7.8(b) were taken at 19° incidence angle and 37.5° scattering angle. A simulated spectrum of the as prepared sample for the same experimental geometry [derived from Fig. 7.8(a)] is shown here for comparison with the annealing results. Three important things could be observed during the annealing, as evident from the figure. i) The height of the Mn peak decreases, ii) the Mn profile reaches deeper into the Si, and iii) a peak appears on the high-energy edge of the Si spectrum which keeps on growing. From the first two points it is quite clear that in-diffusion of Mn and out-diffusion of Si takes place to form silicide-like phases at the surface. The appearance and growth of a surface peak, followed by a valley in the Si spectrum is due to ion channeling. After annealing at 700 °C, a strong decrease in the Mn intensity was observed at the surface: apparently the Mn diffuses into the bulk of the sample, there forming a low concentration silicide phase. The manganese atoms now seem to be more homogeneously distributed with some deficiency at the surface. The Mn concentration is about 2 at. %. Assuming a homogeneous distribution of Mn of 2 at %, this low concentration silicide phase reaches about 50 nm inside (as obtained from SIMS measurement). Then the samples were capped with 2 nm of Au.

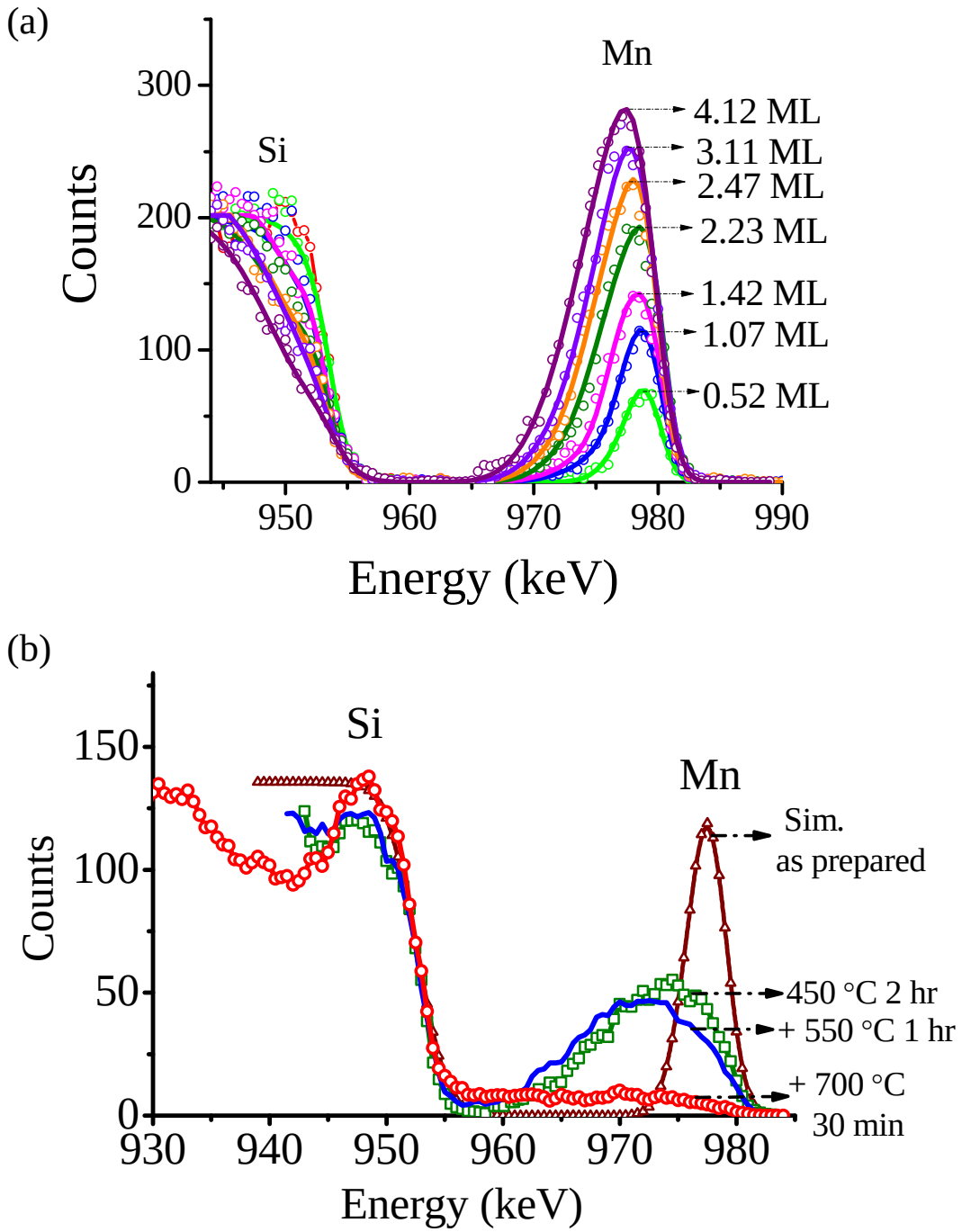


Fig. 7.8: HRBS spectra at both the Mn and Si edges of a solid-state grown sample using a 1 MeV $He^+$ ion beam: **(a)** During growth of Mn in the coverage range 0.52 ML to 4.12 ML (incidence angle: 3.5°, scattering angle: 37.5°) Mn silicide is formed at all steps. **(b)** After annealing at different temperatures for different times for 4.12 ML of deposited Mn (incidence angle: 19°, scattering angle: 37.5°). The Mn diffuses into the Si bulk. At 700 °C a more or less homogeneous silicide has formed with a Mn concentration of about 2 at %. A simulated spectrum of the as prepared (4.12 ML of Mn) sample [derived from Fig. 7.8(a)] is shown for same experimental geometry for direct comparison.

### 7.4.3 Ferromagnetism in Mn-diffused Si

Magnetization curves (*M* vs *H*) of the two samples ($p^+$-Si and n-Si) as measured at 300 K are shown in Fig. 7.9(a). Both samples show room temperature ferromagnetism with remanence of ~ $0.9 \times 10^{-5}$ emu and coercivity of ~ 50 Oe. $p^+$-Si ($10^{19}$ B/cm$^3$) shows higher remanence and higher coercivity than the n-Si sample ($10^{15}$ P/cm$^3$) (see the inset). But the certainly most striking result is that both samples exhibit the same saturation magnetization of 12 μemu – although the samples have by four orders of magnitude different carrier concentrations. Similar results are also observed for the measurements at 5 K. This means in particular, that in contrast to the samples prepared by ion implantation, the samples prepared by diffusion do apparently not show any carrier dependence of the ferromagnetism. This result seems to indicate that the ferromagnetic ordering of the Mn diffused into the Si is not due to coupling of the localized Mn moments by carriers. One way to explain this behavior could perhaps be the formation of small manganese-silicide clusters. Direct interaction between these clusters could give rise to the observed ferromagnetic order at room temperature. The saturation moment calculated from these data is about 1.8 Bohr magneton ($\mu_B$) per Mn atom. This value is by a factor of ~ 2.7 less than that of Mn atom having a moment of 5 $\mu_B$. We want to note that this value is, however, much higher than the values derived for the ion implanted samples.

Fig 7.9(b) illustrates the temperature dependence of magnetization (zero field cooled) for both $p^+$-Si and n-Si samples. The ZFC curves of these two samples appear rather smooth without any abrupt change. It is clear from these measurements that there is no other low temperature magnetic phase present in the sample and the Curie temperature of the sample is well above the room temperature. The relaxation of the magnetization with time was measured for both $p^+$-Si and n-Si samples after switch-off of an external magnetic field [Fig.7.9(c)]. The samples obviously relax, however the relaxations are very small. The n-Si sample relaxes faster than the $p^+$-Si sample in the beginning but slows down at longer time. The solid lines in the figure represent 2$^{nd}$ order exponential decay fits to the data points. From these measurements we can conclude that the ferromagnetic behavior of these samples persists well above room temperature and is quite stable with time.

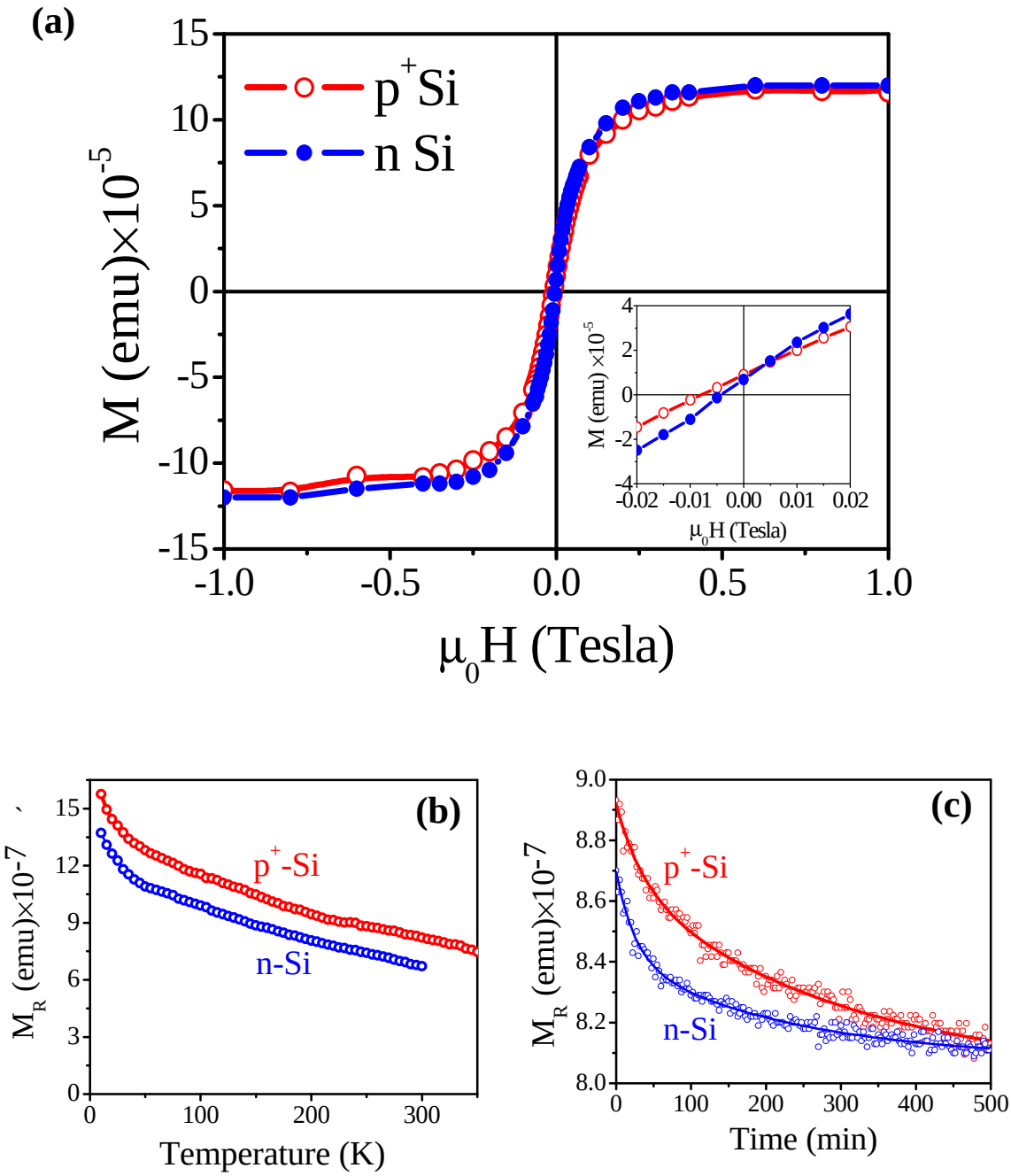


Fig. 7.9: **(a)** Magnetization curves (*M* vs *H*) at 300 K for the solid state grown samples with $p^+$-Si and n-Si. Both samples show the same saturation magnetization of 1.8 $\mu_B$/Mn atom, although their carrier concentrations differ by four orders of magnitude. The ***inset*** shows, for clarity, the magnified version of the remanence and coercive fields. **(b)** Temperature dependence of the remanent magnetization (zero field cooled curves) of $p^+$-Si and n-Si samples. **(c)** Relaxation of the magnetization of $p^+$-Si and n-Si samples at 300 K. The solid line is the 2$^{nd}$ order exponential decay fit to the data points.

## 7.5 Submonolayer Mn on Si (100): Natural existence of $Mn_xSi_{1-x}$/Si digital layers.

A recent density functional study showed that Si d doped with 0.25 ML of interstitial Mn is a half metallic ferromagnet [7.19]. Also a combined scanning tunneling microscopy (STM) study and density functional theory calculation suggests that Mn atoms occupy subsurface interstitial sites in the Si lattice for 0.25 ML of evaporated Mn on Si (100) [7.20]. But the disadvantage of the STM is that it can not probe the Mn atoms diffused deep into the Si lattice. Motivated by these results, the monolayer-resolved depth distribution of 0.25 ML of Mn on Si (100) has been studied by HRBS for a better understanding of the growth process.

The *in situ* HRBS measurements were performed using 2 MeV $N^+$ ions at incidence angles of 3.5° to the sample surface and at a scattering angle of 37.5°. Mn with 4N purity was evaporated from an effusion cell on a cleaned Si (100) surface. The HRBS spectrum of the Mn distribution for the coverage of 0.25 ML is shown in Fig. 7.10(a). The spectrum shows four distinct peaks which correspond to Mn atoms in four well defined depths in the Si lattice. In order to obtain more detailed information about the Mn depth distribution, the Mn spectrum was simulated by the program RUMP. In these simulations the Si sample was subdivided into thin sublayers containing exactly $6.87\times10^{14}/cm^2$ Si atoms and the appropriate amount of Mn atoms added up. Fig. 7.10(b) shows the Mn concentration in the different sublayers as obtained from the RUMP simulation. According to these results every second Si layers does not contain Mn atoms. The $0^{th}$, $-2^{nd}$, $-4^{th}$ and $-6^{th}$ layers are layer of Si atoms with a few Mn atoms. It is to be noted that all these layers contain almost equal amount of Mn atoms. The layers in between, the $-1^{st}$, $-3^{rd}$ and $-5^{th}$ layers are completely free of Mn. The data indicate that at a coverage as low as 0.25 ML, Mn atoms have apparently diffused into the Si bulk up to the $-6^{th}$ layer. As Fig. 7.10(b) shows, every second Si layer is free of Mn, thus giving an oscillatory Mn distribution in the Si lattice. Fig. 7.10(c) finally illustrates the distribution of the Mn atoms in the Si lattice and correlates this distribution with the peaks observed in the HRBS spectrum. The diffused in Mn atoms apparently tend to avoid to occupy adjacent layers in the Si lattice. This is similar to results on the diffusion microstructure of Ni in Si (100) [7.21] and the distribution of metal atoms in metal alloys like $Cu_3Au$ [7.22] close to the surface.

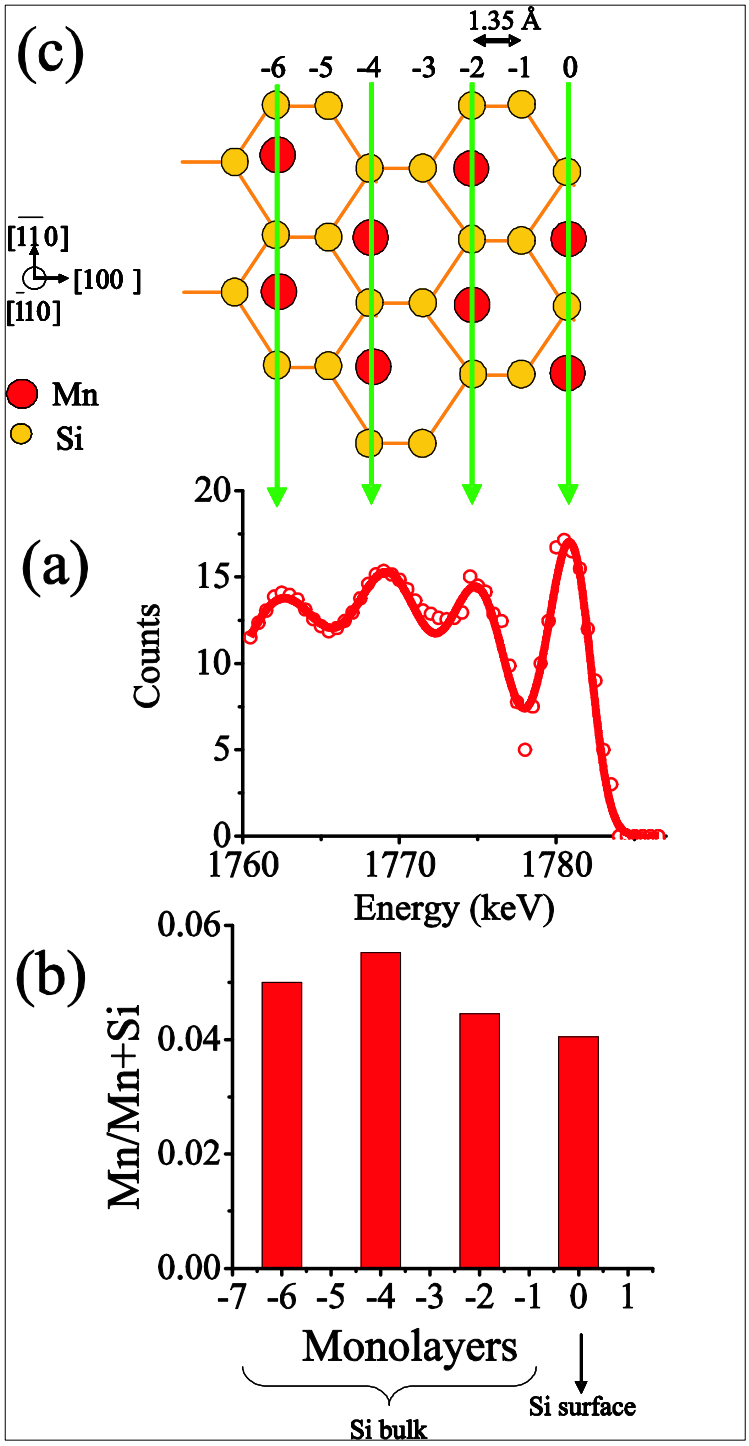


Fig. 7.10: 0.25 ML of Mn evaporated on Si (100) at room temperature. **(a)** Mn edge of HRBS spectrum (circles) using 2 MeV $N^+$ ions and RUMP simulation (solid line). The peak at 1781 keV is due to backscattering from Mn in the $0^{th}$ layer (Si surface), the $2^{nd}$ peak at 1774 keV is due to Mn atoms in the $-2^{nd}$ Si layer and the $3^{rd}$ peak is due to Mn atoms in the $-4^{th}$ Si layer. **(b)** Mn concentration (Mn/Mn+Si) in the different Si (100) layers of the Si crystal as derived from the RUMP simulation. Each layer consists of $6.87\times10^{14}$ atoms/cm$^2$ Si plus some Mn atoms. Layer 0 is the $1^{st}$ Si layer; layers -1, -2 and -3 are subsequent layers in the Si bulk. **(c)** Projected atomic positions of diffused Mn atoms in the Si lattice showing atomic positions corresponding to the peaks of the HRBS spectrum.

A similar behavior is also found for the deposition of very small amounts of Fe on Si (100) at room temperature and Co on Si (100) at -60 °C (see chapter 4 and 5 of this thesis). In these systems such a configuration is stabilized by the minimization of the Gibbs free energy, consisting of atomic binding, strain and surface energies, and the entropy of mixing. So there exists a natural $Mn_xSi_{1-x}$/Si digital layered structure for 0.25 ML of Mn on Si (100).

# Chapter 8

# Summary

The efficient spin injection into semiconductors could pave the way to a new generation of electronics devices such as spin memories, spin transistors, and spin quantum computers [8.1]. The most important semiconductor for industrial application, Si has been studied for the purpose of spin injection extensively in this thesis. In this thesis three different concepts for spin injection into Si have been addressed: ***(1) spin injection through a ferromagnet-Si Schottky contact, (2) spin injection using MgO tunnel barriers in between the ferromagnet and Si, and (3) spin injection from Mn-doped Si (DMS) as spin aligner.***

## 8.1 FM-Si Schottky contact for spin injection

In principle, spin-polarized electrons can be injected into Si across the interface. As discussed in chapter 2, the main problem for spin injection across a Schottky contact is the need for atomically sharp FM-Si interfaces [8.2]. In such a heterostructure of a ferromagnetic thin film on a Si substrate, any structural disorder at the interface would drastically reduce the spin polarization at the interface and, hence, the spin injection efficiency [8.3].

### 8.1.1 FM-Si interface at room temperature

The two candidates of ferromagnetic metals considered here were Co and Fe. Co films as grown in a MBE system on clean Si (100) with the substrate at room temperature exhibit a highly textured hcp (0001) structure. The non epitaxial growth characteristic as seen in these

studies is attributed to room temperature growth, the high lattice mismatch between Co and Si (100), and an interface reaction. Strong intermixing (around 32 ML) is seen by HRBS with extended disorder at the interface and new magnetic phases, having a Curie temperature below room temperature. The Co atoms present in this silicide phase have a magnetic moment and coercive field different from Co atoms in pure Co. These Co atoms are centers for spin flip scattering at the interface and would reduce the spin injection efficiency into silicon.

To be able to improve the interface qualities one needs to understand the atomic processes involved in the formation of such silicide phases. In order to obtain more detailed insight into the formation of such silicide phases the initial stages of growth of Co and Fe were studied *in situ* by HRBS with monolayer depth resolution.

**Growth of Co on Si (100)**

For the case of Co, the deposition of Co on Si (100) was studied *in situ* at very initial stages (0.08 ML to 3 ML) by HRBS [8.4]. It was found that Co evaporated on Si (100) at room temperature – besides occupying sites in the first Si layer – diffuses deep (up to $4^{th}$ layer) into the Si bulk already at very small Co coverages (about 0.1 ML). There it forms a subsurface maximum in the concentration which is separated from Co at the surface by a Co-denuded zone. With increasing coverage (about 1 ML) this denuded zone fills up with Co. At the surface the Co/Si ratio reaches the value of 0.5 for 1 ML coverage. At higher Co coverages (up to 2.93 ML) silicide-like phases with increasingly higher Co content (Co/Co+Si up to 0.5) are formed. Apparently these silicide phases are formed by Si out-diffusion through the growing Co film. A $3\times6.87\times10^{14}$ atoms/cm$^2$ thick CoSi phase could be observed for 2.93 ML Co coverage. This silicide phase is found to be ferromagnetic at room temperature. No metallic Co film is formed at these coverages. The experiment further gives clear evidence that Co is the main diffusing species for the Co coverage range 0.08 ML to 1.19 ML, while Si is the main diffusing species for 2.02 and 2.93 ML of evaporated Co. The metallic Co starts to grow only for coverages larger than 16.8 ML. The thicknesses of the silicide layers formed at the interface for 23 ML of evaporated Co (from surface to bulk) amount to: $Co_2Si$ : 3.26 Å, CoSi : 18.77 Å, and $CoSi_2$ : 2.2 Å.

**Growth of Fe on Si (100)**

For the case of Fe films grown on Si (100) at room temperature (0.0325 ML to 9.1 ML Fe), various silicide phases are formed with the Fe content increasing from the interface to the surface. For the case of 0.0325 monolayer of Fe on Si, pronounced oscillations in the Fe concentration were observed due to preferential occupation of Fe atoms in the alternative Si layers. For the coverages 0.068-1.41 ML no definite silicide phase could be observed. But there is strong inter-diffusion of Si and Fe forming a solid solution with a rough surface. For the coverage of 2.51 ML a signature of a $FeSi_3$ phase could be seen. For the higher coverage of 6.4 ML of evaporated Fe, 7 ML of FeSi, 3 ML of $FeSi_2$ and 7 ML of $FeSi_3$ could be observed. Up to this coverage Si-rich silicide phases are formed in contradiction to the results of Klasges *et al.*, where the authors observed Fe rich phases at the interface [8.5]. For 9.17 ML of evaporated Fe, Fe-rich silicide phases could be observed, consisting of: 6 ML of $Fe_3Si$, 9 ML of $Fe_2Si$ and 10 ML of a FeSi-like phase. These silicide phases have 2 ML of transition layers in between. The silicide phases formed for 9.17 ML are around 2 nm thick and still no metallic pure Fe has formed. At these higher coverages the surface looks smooth and homogeneous.

Last, but not least, the results presented here provide evidence for a silicide formation mechanism based on the interstitial defect model by Tu [8.6]. According to this model the in-diffused Co (or Fe) atoms occupy the tetrahedral interstitial voids in the Si lattice which requires very little activation energy. Charge transfer between adjacent Co (or Fe) and Si atoms occurs, and the local Si covalent bonds transform into weaker metal-like bonds. This interstitial atom-induced bond transformation produces the reduced Si bond strength needed to account for room temperature silicide formation.

### 8.1.2 FM-Si interface for non-equilibrium growth conditions

As understood, it was important to prohibit the in-diffusion of Co into interstitial sites at the initial stages of growth and the out-diffusion of Si atoms in the latter stages. The diffusion of Co and Fe atoms, as obtained from the experimental data and theoretical calculations existing in the literature, is energetically favorable. So in order to control and improve the interface, non-equilibrium growth conditions were followed (i) by lowering the growth temperature and (ii) by surfactant-mediated growth. In chapter 5 these two growth modes were discussed for the FM/Si (100) system.

**Low temperature growth of Co on Si (100)**

For the case of low temperature growth, the Co depth distribution has been measured with monolayer depth resolution in *in situ* HRBS experiments for Co deposition in the range 0.1 - 1.3 ML at -60 °C. Already at very low coverage Co diffusion into the bulk Si has been observed. The amount of in-diffused Co is, however, less than at room temperature. Also at -60 °C, Co is the main diffusing species. In contradiction to room temperature growth, Co atoms form layers of pure Co on top of the Si surface already at very low coverage. Every second Si layer, starting with the first Si layer, is Co depleted. This leads to an oscillatory Co distribution in the Si lattice which is preserved up to higher coverages (1.3 ML). Thus by low temperature evaporation we have not only achieved reduced diffusion of Co atoms into the Si lattice, but also reduced out-diffusion of Si which leads to the growth of metallic Co at the surface right from the beginning. For thicker layers of deposited Co, the low temperature growth at -60 °C results in the formation of an interface silicide layer with low Co content and only a very thin layer of stoichiometric CoSi composition when compared with room temperature deposition. There a thick layer of stoichiometric CoSi layer is formed. However low temperature growth may give rise to poor crystal quality (of the Co film) and higher defect density. Overcoming these limitations is of crucial practical importance and represents a unique challenge in thin film growth.

**Surfactant-mediated growth of Co on Si (100)**

The lower surface free energy of Sb in comparison to Co and Si, makes it a potential candidate for surfactant mediated growth [8.7]. By the use of one monolayer of Sb adsorbed on a Si (100) surface, Co-Si intermixing at the interface is strongly reduced in comparison to the interface without Sb as surfactant. Without Sb, intermixing of 2.42 nm in thickness (silicide layers) was found at the interface, which was reduced to 1.3 nm by the use of Sb. The Sb due to its lower surface free energy floats on the growth front to minimize the total energy of the system and hence reduces the interdiffusion of both Co and Si. Si-rich silicide phases were found at the interface in the case of Sb-mediated growth in comparison to Co-rich phases without Sb as surfactant. Only for higher Co coverages, we could observe that a small amount of Sb is incorporated in the grown Co film. This could be due to the employed room temperature growth (instead of growth at elevated temperatures) and an increasingly rougher Co film. This Sb-mediated growth of Co on Si (100) proves to be useful to get a much sharper interface. The

improved interface quality with Sb-mediated growth is also reflected in magnetic measurements. Co with Sb-mediated growth shows a higher magnetic moment.

It was shown that simple solutions can reduce the FM-Si inter diffusion at the interface and improve the interface quality. However these non-equilibrium growth conditions could not stop the silicide formation completely. However these investigations bring out some new interesting physics of the buried ferromagnet-Si interfaces.

### 8.1.3 Problems in spin injection and detection in Schottky contact

1. As seen in the previous section, a major problem for spin injection in a FM-Si Schottky contact is the existence of a silicide phases at the interface. The ferromagnetic metal atoms present in this silicide phase have a magnetic moment and coercive field different from ferromagnetic atoms in pure film. These diffused-in ferromagnetic atoms are centers for spin flip scattering at the interface and would reduce the spin injection efficiency into silicon. The real challenge in this field is to find a magnetically sharp FM-Si interface.
2. A second point consists in the fact that it is not possible to get the Schottky barrier at both ends (injector and detector). When the injection is done by reverse biasing the injector FM-Si Schottky contact, the detector end will be automatically forward biased (not having a Schottky barrier). This will violate the spin dependent tunneling rules and we will end up with detecting both spin directions.

## 8.2 MgO tunnel barrier for spin injection into Si

On the other hand, using an ultra-thin tunnel barrier between FM and Si will have three advantages: (i) form a chemical barrier between the FM and Si, (ii) circumvent the conductivity mismatch problem, and (iii) in addition act as a spin filter [8.8]. In chapter 6 the fabrication and characterization of ultra-thin crystalline MgO tunnel barriers on Si (100) was presented. Some of the important properties required for tunnel barriers on Si have been addressed. Ultra-thin stoichiometric MgO tunnel barriers with sharp interface with Si (100), very homogeneous, without pin-holes, and crystalline in structure could be fabricated by reactive molecular beam epitaxy. Co and Fe on an ultra thin MgO tunnel barrier were found to have island-like growth with a rough surface. Ultra-thin Co and Fe films are found to be thermally quite stable up to 450 °C, which is important for the integration into integrated circuits. In a move to decrease the resistance of the tunnel barrier, we have fabricated oxygen-

deficient tunnel barriers and sub-nanometer thin tunnel barriers. Oxygen-deficient tunnel barriers were found out to be amorphous, but to have a sharp interface with Si (100) and to be homogeneous. Also uniform, ultra-thin tunnel barriers of sub-nanometer thickness could be successfully prepared. In conclusion, Fe/MgO/Si (100) and Co/MgO/Si (100) systems are promising for spin injection into Si.

An electrical spin injection and detection device on Si has been proposed in section 6.7. It consists of a two Co electrodes sitting on the Si bar. The Co electrodes are separated from Si by a MgO tunnel barrier. The spin detection was proposed to be made in non-local geometry (as already realized for the spin injection in metallic systems [8.9]). This non-local geometry the background effects by placing a spin detection electrode outside the path of the charge current. Spin polarized electrons can be injected from the first ferromagnetic electrode (Co1) into Si in reverse bias condition. If spin polarized electrons can be injected successfully and a spin imbalance extends to some distance in Si then a voltage can be measured between the second ferromagnetic electrode (Co2) and Si.

## 8.3 Mn doped Si for spin injection

For spin injection purpose, instead of contacting the Si with a ferromagnetic metal, the contact could be made with another semiconductor, one with ferromagnetic properties. This solves the conductivity mismatch problem by ensuring that the resistivities of the materials on both side of the interface are comparable in magnitude [8.10]. Si-based diluted magnetic semiconductor samples were prepared by doping Si with Mn by two different methods i) by Mn ion implantation and ii) by in-diffusion of Mn atoms (solid state growth). Interestingly Mn-doped Si shows ferromagnetic order with a Curie temperature above room temperature in both types of samples.

### 8.3.1 Mn implanted Si

In the case of implanted samples, Mn atoms do not substitute Si sites. The implanted samples show room temperature ferromagnetism as measured by a SQUID magnetometer. The magnetic moment per Mn atom is found to decrease with increasing implantation dose. It has been observed that the implanted samples show carrier mediated ferromagnetism and, more importantly, mediated by both holes and electrons in contrast to statements in the literature. This result is very promising because complimentary spin MOSFETs (CMOS, both n–MOS and p-MOS) can be fabricated based on both electron and hole mediated ferromagnetism in

Mn-implanted Si. Due to the oxidation of the surface and other chemical effects during etching of surface Si layer, the XMCD measurements at the Mn edge could not see any ferromagnetic behaviour of these samples. The magnetic moment per Mn atom as obtained from the XMCD experiments is by two orders of magnitude less than that obtained from the SQUID measurements.

### 8.3.2 Solid state growth of Mn doped Si

For evaporation of Mn on Si (100), Mn atoms diffuse deep into the Si bulk already at room temperature, even for very low coverage (0.25 ML) with an oscillatory concentration depth profile as observed by HRBS with monolayer depth resolution. This results in natural $Mn_xSi_{1-x}$/Si digital layers on the surface. After annealing a 4 ML thick Mn film on a Si (100) surface up to 700°C, a 10 nm thick, low-Mn concentration silicide phase is formed having a Mn concentration of ~ 2 at. %. Surprisingly, the samples prepared by this solid state diffusion process show room-temperature ferromagnetism having a magnetic moment of 1.8 $\mu_B$ per Mn atom, which is much higher than that of the ion-implanted samples. In contrast to ion-implanted samples the ferromagnetism in these samples does not show any carrier mediation.

This Si-based diluted magnetic semiconductor is a relatively new material system. So in-depth understanding of the magnetic properties is required before using them for spin injection purpose.

# Chapter 9

# Zusammenfassung

Eine effiziente Spininjektion in Halbleiter könnte den Weg ebnen für eine Generation neuer elektronischer Bausteine wie Spin-Speicher, Spin-Transistoren oder Spin-Quanten-Computer [8.1]. Als wichtigster Halbleiter für die industrielle Anwendung wurde Silizium in dieser Arbeit zum Zwecke der Spininjektion ausführlich untersucht. Drei verschiedene Konzepte zur Spininjektion wurden in dieser angesprochen: (1) Spininjektion durch einen Ferromagnet-Silizium Schottky-Kontakt, (2) Spininjektion durch eine MgO-Tunnelbarriere zwischen dem Ferromagnet und Silizium und (3) Spininjektion aus Mn-dotiertem Silizium (DMS) zur Ausrichtung des Spins.

## 9.1 FM-Si Schottky-Kontakt für die Spininjektion

Im Prinzip können spinpolarisierte Elektronen aus einem Ferromagneten in Silizium injiziert werden. Wie in Kapitel 2 diskutiert, besteht das Hauptproblem für die Spininjektion durch einen Schottky-Kontakt darin, daß man eine atomar scharfe Grenzschicht benötigt [8.2]. In einer derartigen Heterostruktur aus einer dünnen ferromagnetischen Schicht auf Silizium würde jeder strukturelle Defekt in der Grenzschicht die Spininjektion durch die Grenzschicht deutlich reduzieren und damit die Effizienz der Spininjektion [8.3].

### 9.1.1 FM-Si-Grenzschicht bei Zimmertemperatur

Die beiden Kandidaten an ferromagnetischen Metallen, die in dieser Arbeit betrachtet wurden, waren Kobalt und Eisen. Dünne Kobaltfilme, wie sie auf einem Si (100)-Substrat mittels MBE bei Zimmertemperatur hergestellt werden, weisen eine stark texturierte hcp (0001)-Struktur auf. Das nicht-epitaktische Wachstum beruht auf Wachstum bei Zimmertemperatur, starker Gitterfehlanpassung zwischen Co und Si und einer Grenzflächenreaktion. Mit HRBS wird eine starke Durchmischung (32 ML) an der Grenzfläche beobachtet mit neuen magnetischen Phasen, deren Curie-Temperatur unterhalb Zimmertemperatur liegt. Die magnetischen Momente und Koerzitivfelder der Co-Atome in diesen Silizid-Phasen unterscheiden sich von denjenigen in reinem Kobalt. Diese Co-Atome sind Zentren für Spinflip-Streuung in der Grenzfläche und würden die Effizienz der Spininjektion in Silizium reduzieren.

Um diese Grenzflächen zu verbessern, muß man die atomaren Prozesse, die zur Bildung derartiger Silizidphasen führen, besser verstehen. Um detailliertere Einsicht in die Bildung dieser Silizide zu erlangen, wurde das Anfangsstadium des Wachstums dünner Co- und Fe-Schichten auf Si (100) in situ mittels hochauflösender Ionenstreuung mit Monolagen-tiefenauflösung untersucht.

**Wachstum von Co auf Si (100)**

Die Abscheidung von Co auf Si (100) wurde in situ mittels HRBS im Anfangsstadium (o.o8 – 3 ML) untersucht [8.4]. Dabei wurde gefunden, daß Co aufgedampft auf Si (100) bereits bei Zimmertemperatur und sehr geringen Bedeckungsgraden (ungefähr 0,1 ML) weit ins Volumen der Si-Probe diffundiert (bis zur 4. Atomlage) – neben einem Rest, der in der ersten Siliziumlage bleibt. Das Co-Tiefenprofil besitzt im Volumeninneren ein zweites Maximum neben einem 1. Maximum an der Probenoberfläche. Beide sind durch eine Co-verarmte Schicht getrennt. Mit zunehmender Bedeckung (ca 1 ML) wird diese Co-verarmte Schicht mit Co aufgefüllt. An der Oberfläche wird dabei ein Co/Si Verhältnis von 0,5 erreicht (bei 1 ML Bedeckung). Bei höherer Bedeckung (bis etwa 3 ML) werden Silizide mit zunehmend höherem Co-Gehalt (bis Co/Co+Si = 0,5) gebildet. Anscheinend entstehen diese Silizide durch Ausdiffusion von Si durch die wachsende Silizidschicht. Eine $3\times6{,}87\times10^{14}$ Atome/cm² dicke CoSi-Schicht (= 3 Monolagen) wird bei einer Co-Bedeckung von 0,93 ML beobachtet.

Diese Schicht ist bei Zimmertemperatur ferromagnetisch. Kein metallisches Co wird bei dieser Bedeckung gebildet. Das Experiment gibt ferner darüber Auskunft, daß bei kleinen Bedeckungsgraden (0,01 bis 1,19 ML) Co die diffundierende Spezies ist, während dies bei höheren Bedeckungsgraden (2,02 bis 2,93 ML) Si ist. Die Bildung von metallischem Co beginnt erst bei Bedeckungsgraden oberhalb von 16,8 ML. Die Dicken der Silizide, die bei einer Bedeckung von 23 ML Kobalt gebildet werden, betragen (von der Oberfläche ins Innere): $Co_2Si$ : 3,26 Å, CoSi : 18,77 Å, $CoSi_2$ : 2,2 Å.

**Wachstum von Eisen auf Si (100)**

Im Falle des Wachstums von Fe-Filmen auf Si (100) bei Zimmertemperatur (0,0325 ML bis 9,1 ML Fe) bilden sich Silizide mit wachsendem Fe-Gehalt von der Grenzschicht zur Oberfläche. Im Falle von 0,0325 ML Fe auf Si werden ausgeprägte Oszillationen der Fe-Konzentration beobachtet, was seine Ursache darin hat, daß vorzugsweise jede zweite Si-Atomlage von Fe-Atomen besetzt wird. Für niedrige Bedeckungsgrade (0,068 bis 1,14 ML Fe auf Si) konnten keine ausgeprägten Silizid-Phasen beobachtet werden, aber eine starke Durchmischung von Si und Fe mit einer rauhen Oberfläche. Bei einem Bedeckungsgrad von 2,51 ML konnte eine Andeutung einer $FeSi_3$-Phase beobachtet werden, aber ohne scharfe Grenzschicht zum Si-Substrat. Für den höheren Bedeckungsgrad von 6.4 ML Fe auf Si wurden 7 ML FeSi, 3 ML $FeSi_2$ und 7 ML $FeSi_3$ beobachtet. Bis zu diesem Bedeckungsgrad bilden sich Si-reiche Phasen, im Widerspruch zu Berichten von Klasges et al., worin die Autoren über Fe-reiche Phasen an der Grenzschicht berichten [8.5]. Für 9,17 ML Fe auf Si wurden Fe-reiche Silizidphasen beobachtet: 6 ML $Fe_3Si$, 9 ML $Fe_2Si$, und 10 ML einer FeSi-ähnlichen Phase mit 2 ML Übergangsschicht zwischen den Silizid-Phasen. Insgesamt besitzen die Silizid-Phasen eine Dicke von etwa 2 nm, ohne daß sich eine Schicht aus reinem Eisen gebildet hätte.

Zum Schluß sollte erwähnt werden, daß die Resultate dieser beiden Kapitel einen Mechanismus für die Silizid-Bildung nahelegen, wie er von Tu [8.6] vorgeschlagen wurde, und der auf einem Zwischengitter-Defektmodell basiert. Gemäß diesem Mechanismus diffundieren zunächst Co- (oder Fe-) Atome, welche sich zunächst auf Tetraederplätzen befinden, ins Siliziumgitter. Dies erfordert nur eine geringe Aktivierungsenergie. Danach erfolgt ein Ladungstransfer zwischen den Co- bzw. Fe-Atomen und den Si-Atomen, wobei sich die kovalente Si-Bindung in eine metallähnliche Bindung verwandelt. Diese Änderung

der Bindung hat eine Reduzierung der Bindungsstärke der Si-Atome zur Folge, wie sie für die Bildung von Siliziden benötigt wird.

### 9.1.2 Wachstum von FM-Si Grenzflächen unter Nichtgleichgewichtsbedingungen

Wie aus den letzten Abschnitten hervorgeht, ist es für die Struktur der Co/Si- oder Fe/Si-Grenzfläche wichtig, eine Eindiffusion von Co oder Fe bereits zu Beginn des Aufdampfprozesses und die Ausdiffusion von Si zu einem späteren Stadium zu verhindern. Dabei ist, wie aus experimentellen und theoretischen Arbeiten hervorgeht, die Eindiffusion von Co oder Fe über Zwischengitterplätze in einem frühen Stadium energetisch begünstigt. Um nun die FM-Si-Grenzschicht zu verbessern, wurden zwei Nichtgleichgewichtsverfahren verfolgt: (i) Wachstum des Metallfilms bei niedrigerer Substrattemperatur (bisher Zimmertemperatur) und (ii) Wachstum mit Hilfe eines Stoffes, welcher die Oberflächenenergie senkt (surfactant-mediated growth). In Kapitel 5 werden diese beiden Verfahren zur Verbesserung der FM/Si (100)-Grenzschicht diskutiert.

**Wachstum dünner Co-Schichten auf Si (100) bei niedriger Temperatur**

In diesem Falle wurde die Co-Tiefenverteilung während des Aufdampfens bei –60° C in situ mittels HRBS mit Monolagentiefenauflöseng untersucht (Bedeckung: 0,1 bis 1,3 ML). Bereits bei sehr niedriger Bedeckung mit Co wird eine Diffusion von Co ins Volumeninnere beobachtet. Die Menge an eindiffundiertem Co ist jedoch geringer als bei Zimmertemperatur. Auch bei –60° C ist Co zunächst die diffundierende Spezies. Im Gegensatz zum Wachstum bei Zimmertemperatur bilden die Co-Atome bereits bei geringem Bedeckungsgrad Lagen aus reinem Co auf der Si-Oberfläche. Jede zweite Atomlage, angefangen bei der obersten Lage, ist verarmt an Co. Dies führt zu einer oszillierenden Co-Verteilung im Siliziumgitter, was bis zu höheren Bedeckungsgraden (1,3 ML) hin anhält.

Insgesamt wurde durch das Aufdampfen auf ein kaltes Substrat nicht nur eine reduzierte Eindiffusion von Co, sondern auch eine reduzierte Ausdiffusion von Si erreicht, was von Beginn an zu Wachstum von reinen Co-Schichten auf der Oberfläche führt. Bei dickeren Lagen erhält man an der Grenzfläche eine vergleichsweise dicke Silizid-Schicht mit niedrigem Co-Gehalt und eine – im Vergleich zu Aufdampfen bei Zimmertemperatur – nur

sehr dünne stöchiometrische CoSi-Schicht (bei Aufdampfen bei Zimmertemperatur ist diese CoSi-Schicht sehr dick). Jedoch scheint Aufdampfen bei tiefer Temperatur zu Co-Filmen mit schlechter Kristallqualität und hoher Defektdichte zu führen. Diese Defizite zu überwinden ist von erheblicher Bedeutung und stellt eine echte Herausforderung beim Wachstum derartiger dünner Filme dar.

**Wachstum dünner Co-Schichten auf Si (100) mittels Stoffen, welche die Oberflächenenergie senken (surfactant-mediated growth)**

Die niedrige Oberflächenenergie von Sb im Vergleich zu Co und Si macht Sb zu einem potentiellen Kandidaten für diese Art des Wachstums [8.7]. Wie die Messungen gezeigt haben, wird durch eine einzige Monolage an Sb auf Si (100) das Mischen von Co und Si an der Grenzfläche stark unterdrückt. Ohne Sb wurde eine Mischungsdicke (Silizide) von 2,42 nm beobachtet, mit Sb wird diese auf 1,3 nm reduziert. Sb schwimmt dank seiner niedrigen Oberflächenenergie auf der Oberfläche, minimiert dadurch die Energie des Gesamtsystems und reduziert damit die Interdiffusion von Co und Si. An der Grenzfläche wurden Si-reiche Phasen gefunden im Gegensatz zur Abscheidung ohne Sb, wobei Co-reiche Phasen gefunden wurden. Bei dickeren Filmen wird etwas Sb im Co-Film inkorporiert. Dies könnte an der Aufdampfung bei Zimmertemperatur liegen (statt bei höherer Temperatur) und an der zunehmend rauheren Oberfläche des Co-Films.

Insgesamt erweist sich Sb nützlich, um ein schärfere Grenzfläche zwischen Co-Film und Si-Substrat zu erhalten. Die verbesserte Qualität der Grenzfläche zeigt sich auch in den magnetischen Messungen. Es wird ein höheres magnetisches Moment der Co-Atome beobachet.

Wie in den beiden letzten Abschnitten gezeigt, kann man mit einfachen Hilfsmitteln die Durchmischung von Co und Si an der Grenzfläche vermindern und eine deutliche Verbesserung der Qualität der Grenzschicht erreichen. Jedoch ließ sich damit die Durchmischung nicht vollständig verhindern. Allerdings haben diese Untersuchungen neue interessante Details über FM-Si-Grenzflächen geliefert.

### 9.1.3 Probleme bei der Spininjektion und –detektion am Schottky-Kontakt

1. Wie aus den letzten Abschnitten ersichtlich, besteht ein Hauptproblem bei der Spininjektion am Schottky-Kontakt in der Bildung von Silizid-Phasen an der Grenzfläche. Die ferromagnetischen Atome in dieser Silizid-Phase besitzen magnetische Momente und Koerzitiv-Kräfte, die sich von denjenigen im reinen Ferromagneten deutlich unterscheiden. Die eindiffundierten ferromagnetischen Atome sind außerdem Zentren für Spinflip-Streuung an der Grenzfläche und würden die Effizienz der Spininjektion in Si reduzieren. Gelöst werden könnten diese Probleme, wenn man magnetisch scharfe FM/Si-Grenzflächen herstellen könnte.

2. Ein zweites Problem besteht darin, daß man keine Schottky-Barrieren an beiden Enden eines Bauteils (bei der Injektion und bei der Detektion) erzielen kann. Wenn der Injektions-Kontakt in Sperrrichtung betrieben wird, wird der Detektions-Kontakt automatisch in Durchlassrichtung (d.h. ohne Schottky-Barriere) betrieben. Auf diese Weise geht am Detektions-Kontakt die Spinfilterwirkung verloren, und man detektiert beide Spinrichtungen in gleicher Weise.

## 9.2 MgO-Tunnel-Barriere für die Spininjektion in Silizium

Auf der anderen Seite besitzt die Verwendung einer ultradünnen Tunnelbarriere zwischen dem Ferromagneten und Silizium drei wesentliche Vorteile: (i) sie bildet eine chemische Barriere zwischen dem Ferromagneten und Silizium, (ii) durch sie kann das Problem der mangelnden Leitfähigkeitsanpassung (conductivity mismatch) gelöst werden, und (iii) wirkt sie selbst als Spinfilter [8.8]. In Kapitel 6 werden die Herstellung und Charakterisierung ultradünner MgO-Tunnelbarrieren auf Si (100) beschrieben. Dabei werden wichtige Eigenschaften derartiger Tunnelbarrieren auf Si angesprochen. Es konnten ultradünne stoichiometrische MgO-Tunnelbarrieren (etw 2 nm dick) mit scharfer Grenzfläche zur Si (100)-Oberfläche mittels reaktiver Molekularstrahlepitaxie hergestellten werden. Sie sind sehr homogen, lochfrei und kristallin in ihrer Struktur. Ultrdünne Co- und Fe-Filme auf einer solchen MgO-Tunnelbarriere wachsen unter Inselbildung mit einer rauhen Oberfläche. Diese Filme bleiben thermisch stabil bis 450 °C, was wichtig für die Integration in elektronische Bauelemente ist. Um den Tunnelwiderstand dieser Barrieren zu reduzieren wurden MgO-Filme mit unterstoichiometrischem Sauerstoffgehalt und subnanometerdicke Barrieren

hergestellt. Filme mit Sauerstoff-Defizit werden amorph, besitzen aber eine scharfe Grenzflächen mit Si (100) und sind homogen. Auch subnanometerdicke Barrieren konnten erfolgreich hergestellt werden. Zusammenfassend läßt sich sagen, daß Systeme zur Spininjektion in Si (100) auf der Basis von Fe/MgO/Si und Co/MgO/Si sehr erfolgversprechend sind.

In Abschnitt 6.7 wird eine Vorrichtung zur Spininjektion in Si und zur elektrischen Detektion vorgestellt, die auf derartigen Tunnelbarrieren basiert. Die Vorrichtung besteht aus zwei Co-Kontakten auf einem Si-Chip. Die Co-Elektroden sind durch MgO-Tunnelbarrieren vom Si-Substrat getrennt. Als Methode zur elektrischen Spindetetektion wird eine Messung in nicht-lokaler Geometrie vorgeschlagen, wie sie bereits erfolgreich zur Injektion in Metalle eingesetzt wurde [8.9]. Die Methode minimiert störende Untergrundeffekte, indem sie die Elektrode zur Spindetektion außerhalb des Strompfades plaziert. Spinpolarisierte Elektronen werden bei dieser Technik von einer ersten Co-Elektrode (Co1) in Si injiziert. Liegt erfolgreiche Spininjektion vor, so kann dies an Hand des Auftretens einer Spannung zwischen Si und der zweiten ferromagnetischen Elektrode (Co2) festgestellt werden.

## 9.3 Mn-dotiertes Silizium für die Spininjektion

Statt Si mit einem ferromagnetischen Metall in Kontakt zu bringen, kann man zur Spininjektion Si auch mit einem anderen Halbleiter, einem mit ferromagnetischen Eigenschaften in Kontakt bringen. Dies würde sofort das Problem der schlechten elektrischen Anpassung lösen, da die Materialien auf beiden Seiten der Grenzschicht vergleichbare spezifische Widerstände besitzen [8.10]. Solche verdünnten magnetischen Halbleiter (DMS) auf Si-Basis wurden durch Dotieren von Si mit Mn auf zwei Arten hergestellt: i) durch Mn-Ionenimplantation und ii) durch Eindiffusion von Mn-Atomen in Si (solid state growth). Interessanterweise ist Mn-dotiertes Si in beiden Fällen ferromagnetisch mit einer Curie-Temperatur oberhalb von Zimmertemperatur.

### 9.3.1 Mn-implantiertes Silizium

Im Falle der Implantation besetzen die Mn-Atome keine substitutionellen Plätze in Silizium. Die Proben zeigen Ferromagnetismus bei Zimmertemperatur, wie aus SQUID-Messungen

hervorgeht. Das magnetische Moment pro Mn-Atom nimmt mit zunehmender Implantationsdosis ab. Der Ferromagnetismus wird durch Ladungsträger vermittelt, und zwar – wie sich bei den Untersuchungen herausstellte - durch Elektronen und Löcher, im Gegensatz zu Spekulationen aus der Literatur (nur Löcher). Diese Resultate sind sehr vielversprechend, da auf diese Weise Spin-CMOSFETs (CMOS bedeutet n-MOS und p-MOS) hergestellt werden können, die auf Löcher- und Elektronen-vermitteltem Ferromagnetismus beruhen. Mittels XMCD an der Mn-L-Kante in Reflexion konnte allerdings kein ferromagnetisches Verhalten festgestellt werden, was möglicherweise an der starken Oxidation der Proben und einer Veränderung durch chemisches Abätzen liegen kann. Das magnetische Moment pro Mn-Atom, wie es sich aus diesen Messungen ergibt, ist um etwa zwei Größenordnungen kleiner als das aus den SQUID-Messungen.

### 9.3.2 Festkörper-Wachstum von Mn-dotiertem Silizium

Beim Aufdampfen von Mn-Atomen diffundieren diese bereits bei Zimmertemperatur und niedrigen Bedeckungsgraden (0,25 ML) bis tief ins Innere des Silizium-Substrats. Mittels HRBS mit Monolagen-Tiefenauflösung wird eine oszillatorische Tiefenverteilung beobachtet: Jede zweite Siliziumlage bleibt dabei Mn-frei; man spricht von natürlichen digitalen $Mn_xSi_{1-x}$/Si-Lagen an der Oberfläche. Nach Anlassen einer 4 ML dicken Mn-Schicht auf Si (100) bei Temperaturen bis 700 °C bildet sich eine ca 10 nm dicke Silizid-Schicht niedriger Mn-Konzentration mit einem Mn-Gehalt von ca 2 at %. Überraschenderweise zeigen die so hergestellten Schichten Ferromagnetismus bei Zimmertemperatur mit einem magnetischen von 1,8 $\mu_B$ pro Mn-Atom, was viel höher ist als bei den implantierten Proben. Im Gegensatz zu den ionen-implantierten Proben scheint der Ferromagnetismus dieser Proben nicht durch Ladungsträger vermittelt zu werden.

Diese verdünnten magnetischen Halbleiter auf der Basis von Silizium stellen eine neue Klasse von Materialien dar. Bevor sie zur Spininjektion verwendet werden können, sind jedoch weitere Untersuchungen und ein besseres Verständnis ihrer Eigenschaften erforderlich.

# Bibliography

## Chapter 1


**[1.1]** G. Moore, *Electronics* **38**, 19, April 1965.

[1.2] G. A. Prinz, *Science* **282**, 1660 (1998); I. Žutic, J. Fabian, and S. Das Sarma, *Rev. Mod. Phys*. **76**, 323 (2004).

[1.3] S. A. Wolf *et al.*, *Science* **294**, 1488 (2001); D. D. Awschalom and M. E. Flatté, *Nature Phys*. **3**, 153 (2007).

[1.4] S. Datta and B. Das, *Appl. Phys. Lett*. **56**, 665 (1990).

[1.5] P. R. Hammar, B. Bennet, M. Yang, and M. Johnson, *Phys. Rev. Lett.* **83**, 203 (1999).

[1.6] X. Lou, C. Adelmann, S. A. Crooker, E. S. Garlid, J. Zhang, S. M Reddy, S. D. Flexner, C. J. Palmstrøm, and P. A. Crowell, *Nature Phys*. **3**, 197 (2007).

[1.7] F. G. Monzon, H. X. Tang, and M. L. Roukes, *Phys. Rev. Lett.* **84**, 5022 (2000).

[1.8] G. Schmidt *et al*., *Phys. Rev. B* **62**, 4790 (2000).

[1.9] E. I. Rashba, *Phys. Rev. B* **62**, R16267 (2000).

[1.10] M. I. D'ykonov, V. I. Perel', Theory of optical spin orientation of electrons and nuclei in semiconductors', North Holland, Amsterdam, 1984, pp.11-50 and 73-129.

[1.11] H. J. Zhu, M. Ramsteiner, H. Kostial, M. Wassermeier, H. P. Schonherr, and H. K. Ploog, *Phys. Rev. Lett.* **87**, 16601 (2001).

[1.12] A. T. Hanbicki, B. T. Jonker, G. Itskos, G. Kioseoglou, and A. Petrou, *Appl. Phys. Lett*. **80**, 1240 (2002).

[1.13] V. F. Motsnyi, J. De Boeck, J. Das, W. Van Roy, G. Borghs, E. Goovaerts, and V. I. Safarov, *Appl. Phys. Lett.* **81**, 265 (2002).

[1.14] X. Jiang, R. Wang, R. M. Shelby, R. M. Macfarlane, S. R. Bank, J. S. Harris, and S. S. P. Parkin, *Phys. Rev. Lett.* **94**, 056601 (2005).

[1.15] R. Fiederling, M. Keim, G. Reuscher, W. Ossau, G. Schmidt, A. Waag, and L. W. Molenkamp, *Nature* **402**, 787 (1999); Y. Ohno, D. K. Young, B. Beschoten, F. Matsukura, H. Ohno, and D. D. Awschalom, *Nature* **402**, 790 (1999).

[1.16] A. G. Aronov and G. E. Pikus, *Sov. Phys. Semicond*. **10**, 698 (1976); I. Žutic, J. Fabian, and S. Erwin, *Phys. Rev. Lett*. **97**, 026602 (2006).

[1.17] M. Johnson and R. H. Silsbee, *Phys. Rev. Lett*. **55**, 1790 (1985).

[1.18] F. J. Jedema, H. B. Heersche, A. T. Filip, J. J. A. Baselmans, and B. J. vanWees,

*Nature* **416**, 713 (2002); F. J. Jedema, A. T. Filip, and B. J. van Wees, *Nature* **410**, 345 (2001).

**Chapter 2**

**[2.1]** G. A. Prinz, *Science* **282**, 1660 (1998); S. A. Wolf *et al.*, *Science* **294**, 1488 (2001); D. D. Awschalom and M. E. Flatté, *Nature Phys.* **3**, 153 (2007).

[2.2] N. F. Mott, *Adv. Phys.* **13**, 325 (1964), D. C. Jiles, Introduction to Magnetism and Magnetic Materials, Chapman & Hall publication, 1990.

[2.3] M. B. Stearns, *Phys. Rev. B* **8**, 4383 (1973).

[2.4] J. B. Gadzuk, *Phys. Rev.* **182**, 416 (1969); M. B. Stearns, *Phys. Rev. B* **6**, 3326 (1972).

[2.5] I. A. Campbell, A. Fert, and A. R. Pomeroy, *Phil. Mag.* **15**, 977 (1967); A. Fert and I. A. Campbell, *J. Phys. F* **6**, 849 (1976).

[2.6] R. J. Soulen *et al.*, *Science* **282**, 85 (1998).

[2.7] A. G. Arnov and G. E. Pikus, *Sov. Phys. Semicond.* **10**, 698 (1976).

[2.8] J. F. Gregg, I. Petej, E. Jouguelet, and C. Dennis, *Journal of Physics: Applied Physics* **35**, R121 (2002).

[2.9] R. M. Stroud, A. T. Hanbiki, Y. D. Park, G. Kioseoglou, A. G. Petukhov, B. T. Jonker, G. Itskov, and A. Petrou, *Phys. Rev. Lett.* **89**, 166602 (2002).

[2.10] J. M. MacLaren, X. G. Zhang, W. H. Butler, and X. Wang, *Phys. Rev. B* **59**, 5470 (1999); O. Wunnicke *et al.*, *Phys. Rev. B* **65**, 241306 (2006).

[2.11] C. H. Li *et al.*, *Appl. Phys. Lett.* **85**, 1544 (2004).

[2.12] D. K. Guthrie, L. E. Harrell, G. N. Henderson, P. N. First, T. K. Gaylord, E. N. Glytsis, and R. E. Leibenguth, *Phys. Rev. B* **54**, 16972 (1996).

[2.13] D. L. Smith, E. Y. Lee, and V. Narayanamurti, *Phys. Rev. Lett.* **80**, 2433 (1998).

[2.14] I. Žutic, J. Fabian, and S. Das Sarma, *Rev. Mod. Phys.* **76**, 323 (2004).

[2.15] J. Strand, X. Lou, C. Adelmann, and B. D. Schultz, *Phys. Rev. B* **72**, 155308 (2005); D. D. Awschalom, M. E. Flatte, and N. Samarth, *Scientific American* **286**, 66 (2002).

[2.16] S. Datta and B. Das, *Appl. Phys. Lett.* **56**, 665 (1990).

[2.17] P. R. Hammar, B. Bennet, M. Yang, and M. Jonson, *Phys. Rev. Lett.* **83**, 203 (1999).

[2.18] F. G. Monzon, H. X. Tang and M. L. Roukes, *Phys. Rev. Lett.* **84**, 5022 (2000); B. J. van Wees, *Phys. Rev. Lett.* **84**, 5023 (2000); P. R. Hammar, B. R. Bennett, M. J. Yang, and M. Johnson, *Phys. Rev. Lett.* **84**, 5024 (2000).

[2.19] M. Johnson and R. H. Silsbee, *Phys. Rev. Lett.* **55**, 1790 (1985).

[2.20] F. J. Jedema, H. B. Heersche, A. T. Filip, J. J. A. Baselmans, and B. J. vanWees, *Nature* **416**, 713 (2002); F. J. Jedema, A. T. Filip, and B. J. van Wees, *Nature* **410**, 345 (2001).

[2.21] X. Lou, C. Adelmann, S. A. Crooker, E. S. Garlid, J. Zhang, S. M Reddy, S. D. Flexner, C. J. Palmstrøm, and P. A. Crowell, *Nature Phys.* **3**, 197 (2007).

[2.22] A. T. Filip, B. H. Hoving, F. J. Hedema, B. van Wees, B. Dutta, and G. Borghs, *Phys. Rev. B* **62**, 9996 (2006).

[2.23] G. Schmidt *et al.*, *Phys. Rev. B* **62**, 4790 (2000).

[2.24] E. I. Rashba, *Phys. Rev. B* **62**, R16267 (2000).

[2.25] P. R. Hammar and M. Johnson, *Phys. Rev. Lett.* **88**, 066806 (2002).

[2.26] M. I. D'ykonov, V. I. Perel', Theory of optical spin orientation of electrons and nuclei in Semiconductors', North Holland, Amsterdam, 1984, pp.11-50 and 73-129.

[2.27] A. T. Hanbicki, B. T. Jonker, G . Itskos, G. Kioseoglou, and A. Petrou, *Appl. Phys. Lett.* **80**, 1240 (2002).

[2.28] V. F. Motsnyi, J. De Boeck, J. Das, W. Van Roy, G. Borghs, E. Goovaerts, and V. I. Safarov, *Appl. Phys. Lett*. **81**, 265 (2002).

[2.29] X. Jiang, R. Wang, R. M. Shelby, R. M. Macfarlane, S. R. Bank, J. S. Harris, and S. S. P. Parkin, *Phys. Rev. Lett.* **94**, 056601 (2005).

[2.30] Y. Ohno, D. K. Young, B. Beschoten, F. Matsukura, H. Ohno, and D. D. Awschalom, *Nature* **402**, 790 (1999).

[2.31] S. A. Crooker, M. Furis, X. Lou, C. Adelmann, D. L. Smith, C. J. Palmstrøm, and P. A. Crowell, *Science*, **309**, 2191 (2005).

[2.32] C. L. Dennis, J. F. Gregg, G. J. Ensell, and S. M. Thompson, *J. Appl. Phys.* **100**, 043717 (2006).

[2.33] D. R. Loraine, D. I. Pugh, H. Jenniches, R. Kirschman, S. M. Thompson , W. Allen, C. Sirisathikul, and J. F. Gregg, *J. Appl. Phys.* **87**, 5161 (2000).

[2.34] Y. Q. Jia, R. C. Shi, and S. Y. Chou, *IEEE Trans. Mag*. **32**, 4707 (1996).

[2.35] S. Hacia, T. Last, S. F. Fischer, and U. Kunze, *J. Phys. D* **37**, 1310 (2004).

[2.36] S. P. Dash, D. Goll, and H. D. Carstanjen, *Appl. Phys. Lett.* **90**, 132109 (2007).

[2.37] H. L. Meyerheim, U. Doebler, and A. Puschmann, *Phys. Rev. B* **44**, 5738 (1990).

[2.38] S. M. Thompson, D. Pugh, D. Loraine, C. L. Dennis, J. F. Gregg, Silicon-based Spin Electronics Devices: Spintronics materials and technology, Taylor & Francies (2007).

[2.39] S. M. Sze, Physics of semiconductor devices, John Wiley & Sons, Inc 2$^{nd}$ edition (1981).

[2.40] W. H. Butler, X. G. Zhang, T. C. Schulthess, and J. M. MacLaren, *Phys. Rev. B* **63**, 054416 (2001); J. Mathon and A. Umerski, *Phys. Rev. B* **63**, 220403 (2001).

[2.41] X. Jiang, R. Wang, R. M. Shelby, R. M. Macfarlane, S. R. Bank, J. S. Harris, and S. S. P. Parkin, *Phys. Rev. Lett*. **94**, 056601 (2005); S. S. P. Parkin *et al.*, *Nature Materials* **3**, 862 (2004). Yuasa *et al*., *Nature materials* **3**, 868 (2004).

[2.42] S. Mukhopadhyay and I. Das, *Phys. Rev. Lett*. **96**, 026601 (2006).

[2.43] Wang, X. Jiang, R. M. Shelby, R. M. Macfarlane, S. S. P. Parkin, S. R. Bank, and J. S. Harris, *Appl. Phys. Lett.* **86**, 052901 (2005).

[2.44] A. Fert and H. Jaffrès, *Phys. Rev. B* **64**, 184420 (2001).

[2.45] B. C. Min, K. Motohashi, C. Lodder, and R. Jansen, *Nature Materials* **5**, 817 (2006).

[2.46] R. Fiederling, M. Keim, G. Reuscher, W. Ossau, G. Schmidt, A. Waag, and L. W. Molenkamp, *Nature* **402**, 787 (1999); Y. Ohno, D. K. Young, B. Beschoten, F. Matsukura, H. Ohno, and D. D. Awschalom, *Nature* **402**, 790 (1999).

[2.47] F. M. Zhang, X. C. Liu, J. Gao, X. S. Wu, Y. W. Du, H. Zhu, J. Q. Xiao, and P. Chen, *Appl. Phys. Lett.* **85**, 786 (2004).

[2.48] M. Bolduc, C. Awo-Affouda, A. Stollenwerk, M. B. Huang, F. G. Ramos, G. Agnello, and V. P. LaBella, *Phys. Rev. B* **71**, 033302 (2005).

[2.49] H. W. Wu, C. J. Tsai, and L. J. Chen, *Appl. Phys. Lett*. **90**, 043121 (2007).

[2.50] H. Ohno, D. Chiba, F. Matsukura, T. Omiya, E. Abe, T. Dietl, Y. Ohno and K. Ohtani, *Nature* **408**, 944 (2000); Y. D. Park, A. T. Hanbicki, S. C. Erwin, C. S. Hellberg, J. M. Sullivan, J. E. Mattson, T. F. Ambrose, A. Wilson, G. Spanos, and B. T. Jonker, *Science* **295**, 651 (2002).

[2.51] G. M. Dalpian, A. J. R. da Silva, and A. Fazzio, *Phys. Rev. B* **68**, 113310 (2003); X. Luo, S. B. Zhang, and S. H. Wei, *Phys. Rev. B* **70**, 033308 (2004).

[2.52] H. Wu, P. Kratzer, and M. Scheffler, *Phys. Rev. Lett.* **98**, 117202 (2007).

[2.53] X. C. Liu, Z. H. Lu, Z. L. Lu, L. Y. Lv, X. S. Wu, F. M. Zhang, and Y. W. Du *J. Appl. Phys.* **100**, 073903 (2006).

[2.54] G. Schütz, W. Wagner, W. Wilhelm, P. Kienle, R. Zeller, R. Frahm, G. Materlik, *Phys. Rev. Lett.* **58**, 737 (1987).

**Chapter 3**

**[3.1]** L. Maissel and R. Glang, Handbook of Thin Film Technology, McGraw-Hill, 1970.

[3.2] Milton Ohring, The Materials Science of Thin Films, Academic press, 2002.

[3.3] S. P. Dash, D. Goll, and H. D. Carstanjen, *Appl. Phys. Lett*. **90**, 132109 (2007); H. L. Meyerheim, U. Doebler, and A. Puschmann, *Phys. Rev. B* **44**, 5738 (1990).

[3.4] K. N. Tu, *Appl. Phys. Lett*. **27**, 145 (1975).

[3.5] D. R. Loraine, D. I. Pugh, H. Jenniches, R. Kirschman, S. M. Thompson , W. Allen, C. Sirisathikul, and J. F. Gregg, *J. Appl. Phys*. **87**, 5161 (2000).

[3.6] J. W. Meyer, E. Rimini, Ion beam Handbook for materials analysis, Academic press, 1977; W. K. Chu, J. W. Mayer, M. A. Nicolet, Back Scattering spectrometry, Academic press, 1978; K. W. Chu, *Phys. Rev. A* **13**, 2057 (1976).

[3.7] L. R. Doolittle and M. O. Thompson, RUMP, Computer Graphics Service, 2002.

[3.8] Th. Enders, M. Rilli, and H. D. Carstanjen, *Nucl. Instrum. Methods Phys. Res. B* **139**, 239, (1992).

[3.9] H. D. Carstanjen, *Nucl. Instrum Methods Phys. Res. B* **136**, 1183 (1998).

[3.10] K. Kimura, K. Ohshima, and M. Mannami, *Phys. Rev. B* **63**, 235303 (2001).

[3.11] A. Ishizaki and Y. Shiraki, *J. Electrochem. Soc*. **133**, 666 (1986).

[3.12] W. Buckel and R. Kleiner, Superconductivity, WILEY-VCH, 2nd edition, 2004.

[3.13] J. Clarke, *Scientific American* **271**, 46 (1994).

**Chapter 4**

**[4.1]** S. A. Wolf, D. D. Awschalom, R. A. Buhrman, J. M. Daughton, S. von Molnár, M. L. Roukes, A. Y. Chtchelkanova, D. M. Treger, *Science* **294**, 1488 (2001); I. Žutic, J. Fabian, and Das Sarma, *Rev. Mod. Phys.* **76**, 323 (2004); D. D. Awschalom and M. E. Flatté, *Nature Phys*. **3**, 153 (2007).

[4.2] R. J. Soulen *et al.*, *Science* **282**, 85 (1998); A. G. Arnov and G. E. Pikus, *Sov. Phys. Semicond.* **10**, 698 (1976).

[4.3] S. P. Dash, D. Goll, and H. D. Carstanjen, *Appl. Phys. Lett*. **90**, 132109 (2007).

[4.4] D. R. Loraine, D. I. Pugh, H. Jenniches, R. Kirschman, S. M. Thompson , W. Allen, C. Sirisathikul, and J. F. Gregg, *J. Appl. Phys*. **87**, 5161 (2000); Y. Q. Jia, R. C. Shi, and S.Y. Chou, *IEEE Trans. Mag.* **32**, 4707 (1996); S. Hacia, T. Last, S. F. Fischer, and U. Kunze, *J. Phys. D* **37**, 1310 (2004).

[4.5] D. C. Jiles, Introduction to Magnetism and Magnetic Materials, Chapman & Hall, 1990.

[4.6] H. L. Meyerheim, U. Doebler, and A. Puschmann, *Phys. Rev. B* **44**, 5738 (1990).

[4.7] K. N. Tu, *Appl. Phys. Lett.* **27**, 145 (1975).

[4.8] W. S. Cho, J. Y. Kim, N. G. Park, I. W. Lyo, K. Jeong, S. S. Kim, D. S. Choi, C. N. Whang, and K. H. Chae, *Surf. Sci.* **453**, L309 (2000).

[4.9] G. Rangelov, P. Augustin, J. Stober, and Th. Fauster, *Phys. Rev. B* **49**, 7535 (1994).

[4.10] V. Scheuch, B. Voigtaender, and H. P. Bonzel, *Surf. Sci.* **372**, 71 (1997).

[4.11] V. Gomoyunova, I. I. Pronin, N. R. Gall, S. L. Molodtsov, and D. V. Vyalykh, *Tech. Phys. lettes* **29**, 496 (2001).

[4.12] A. P. Horsfield and H. Fujitani, *Phys. Rev. B* **63**, 235303 (2001).

[4.13] Th. Enders, M. Rilli, and H. D. Carstanjen, *Nucl. Instrum Methods Phys. Res. B* **136**, 1183 (1992).

[4.14] L. R. Doolittle and M. O. Thompson, RUMP, Computer Graphics Service, 2002.

[4.15] J. M. Gallego, R. Miranda, S. Molodtsov, C. Laubschat, and G Kaindl, *Surface Sci*. **239**, 203 (1990).

[4.16] K. Kimura, K. Ohshima, and M. Mannami, *Phys. Rev. B* **63**, 235303 (2001).

[4.17] P. Horsfield and H. Fujitani, *Phys. Rev. B* **63**, 235303 (2001).

[4.18] M. Y. Lee and P. A. Bennett, *Phys. Rev. Lett.* **75**, 4460 (1995).

[4.19] B. P. Uberuaga, M. Leskovar, A. P. Smith, H. Jónsson, and M. Olmstead, *Phys. Rev. Lett.* **84**, 2441 (2000).

[4.20] O. G. Shpyrko, R. Streitel, V. S. K. Balagurusamy, A. Y. Grigoriev, M. Deutsch, B. M. Ocko, M. Meron, B. Lin, P. S. Pershan, *Science* **313**, 77 (2006).

[4.21] H. Wu, P. Kratzer, and M. Scheffler, *Phys. Rev. B* **72**, 144425 (2005).

[4.22] K. Ruehrnschopf , D. Borgmann, and G. Welder, *Thin Solid Films* **280**, 171, (1996).

[4.23] Klaesges *et al.*, *Phys. Rev. B* **56**, 10801 (1997).

[4.24] Gomoyunova *et al*., *Tech. Phys.* **50**, 106 (2005).

[4.25] M. Gallego and R. Miranda, *J. Appl. Phys.* **69**, 1377 (1991); M. Gallego *et al.*, *Phys. Rev. B* **46**, 13339 (1992).

[4.26] J. Alvarez *et al.*, *Phys. Rev. B* **45**, 14042 (1992).

[4.27] K. Konuma *et al.*, *J. Appl. Phys.***73**, 1104 (1993).

[4.28] Y. Chang and J. L. Erskine, *Phys. Rev. B* **26**, 4766 (1982).

[4.29] H. Reichert, P. J. Eng, H. Dosch, and I. K. Robinson, *Phys. Rev. Lett.* **74**, 2006 (1995).

**Chapter 5**

**[5.1]** S. P. Dash, D. Goll, and H. D. Carstanjen, *Appl. Phys. Lett*. **90**, 132109 (2007).

[5.2] H. L. Meyerheim, U. Doebler, and A. Puschmann, *Phys. Rev. B* **44**, 5738 (1990).

[5.3] J. M. Gallego, R. Miranda, S. Molodtsov, C. Laubschat, and G. Kaindl, *Surf. Sci*. **239**, 203 (1990).

[5.4] K. Kimura, K. Ohshima, and M. Mannami, *Phys. Rev. B* **52**, 5737 (1995).

[5.5] Y. Chang and J. L. Erskine, *Phys. Rev. B* **26**, 4766 (1982).

[5.6] H. Reichert, P. J. Eng, H. Dosch, and I. K. Robinson, *Phys. Rev. Lett.* **74**, 2006 (1995).

[5.7] P. Horsfield and H. Fujitani, *Phys. Rev. B* **63**, 235303 (2001).

[5.8] M. Y. Lee and P. A. Bennett, *Phys. Rev. Lett.* **75**, 4460 (1995).

[5.9] M. Copel, M. C. Reuter, E. Kaxiras, and R. M. Tromp, *Phys. Rev. Lett.* **63**, 632 (1989); C. Humphreys, *Nature* **341**, 689 (1989).

[5.10] M. Copel, M. C. Reuter, M. H. Hoegen, and R. M. Tromp, *Phys. Rev. B* **42**, 11682 (1990).

[5.11] J. Camarero *et al.*, *Phys. Rev. Lett.* **76**, 4428 (1996).

[5.12] M. Izquierdo *et al.*, *Phys Rev. Lett.* **94**, 187601 (2005).

[5.13] H. W. Chang, J. S. Tsay, Y. L. Chiou, K. T. Huang, W. Y. Chan, and Y. D. Yao, *J. Appl. Phys.* **99**, 08J705 (2006)

[5.14] M. Copel, M. C. Reuter, M. H. Hoegen, and R. M. Tromp, *Phys. Rev. B* **42**, 11682 (1990).

[5.15] M. H. Hoegen, J. Falta, M. Copel, and R. M. Tromp, *Appl. Phys. Lett.* **66**, 487 (1994).

[5.16] A. Ishizaki and Y. Shiraki, *J. Electrochem. Soc*. **133**, 666 (1986).

[5.17] D. H. Rich, F. M. Leibsle, A. Samsavar, E. S. Hirschorn, T. Miller, and T. C. Chiang, *Phys. Rev. B* **39**, 12758 (1989).

[5.18] T. Ohno, *Phys. Rev. Lett.* **73**, 460 (1994).

[5.19] H. Okamoto, *Journal of Phase Equilibria and Diffusion* **26**, 198 (2005).

**Chapter 6**

**[6.1]** S. P. Dash, D. Goll, and H. D. Carstanjen, *Appl. Phys. Lett.* **90**, 132109 (2007).

[6.2] H. L. Meyerheim, U. Doebler, and A. Puschmann, *Phys. Rev. B* **44**, 5738 (1990).

[6.3] D. R. Loraine *et al.*, *J. Appl. Phys.* **87**, 5161 (2000).

[6.4] Y. Q. Jia, R. C. Shi, and S. Y. Chou, *IEEE Trans. Magn.* **32**, 4707 (1996).

[6.5] E. I. Rashba, *Phys. Rev. B* **62**, R16267 (2000), G. Schmidt *et al.*, *Phys. Rev. B* **62**, 4790 (2000).

[6.6] V. F. Motsnyi, J. De Boeck, J. Das, W. Van Roy, G. Borghs, E. Goovaerts, and V.

I. Safarov, *Appl. Phys. Lett.* **81**, 265 (2002).

[6.7] X. Jiang, R. Wang, R. M. Shelby, R. M. Macfarlane, S. R. Bank, J. S. Harris, and S. S. P. Parkin. *Phys. Rev. Lett.* **94**, 056601 (2005); S. S. P. Parkin *et al*., *Nature Matererials* **3**, 862 (2004). Yuasa *et al.*, *Nature materials* **3**, 868 (2004).

[6.8] C. J. Först, C. R. Ashman, K. Schwarz, and P. E. Blöchl, *Nature* **427**, 53 (2004); A. I. Kingon, J. Maria, and S. K. Streiffer, *Nature* **406**, 1032 (2000); D. A. Muller, T. Sorsch, S. Moccio, F. H. Baumann, K. Evans-Lutterodt, and G. Timp *Nature* **399**, 758 (1999); E. H. Nicolian and J. R. Brews, *MOS Physics and Technology*, Second edition, Wiley- Interscience, New York, (1982).

[6.9] C. J. Foerst, C. R. Ashman, K. Schwarz, and P. E. Bloechl, *Nature* **427**, 53 (2004).

[6.10] W. H. Butler, X. G. Zhang, T. C. Schulthess, and J. M. MacLaren, *Phys. Rev. B* **63**, 054416 (2001); J. Mathon and A. Umerski, *Phys. Rev. B* **63**, 220403 (2001).

[6.11] P. Chen, D. Bolmont, and C. A. Sebenne, *J. Phys. C* **17**, 4897 (1984).

[6.12] D. K. Fork, F. A. Ponce, J. C. Tramontana, and T. H. Geballe, *Appl. Phys. Lett.* **58**, 2294 (1991).

[6.13] M. R. J. van Buuren, C. L. Griffiths, H. van Kempen, *Surf. Sci.* **314**, 172 (1994); P. Hutchison, M. M. R. Evans, and J. Nogami, *Surf. Sci.* 411, 99 (1998); Cho *et al. Surf. Sci.* **523**, 30 (2003).

[6.14] Th. Enders, M. Rilli, and H. D. Carstanjen, *Nucl. Instrum Methods Phys. Res. B* **136**, 1183 (1992).

[6.15] L. R. Doolittle and M. O. Thompson, RUMP, Computer Graphics Service, 2002.

[6.16] S. Mukhopadhyay and I. Das, *Phys. Rev. Lett*. **96**, 026601 (2006).

[6.17] M. Sicot, S. Andrieu, F. Bertran, and F. Fortuna, *Phys. Rev. B* **72**, 144414 (2005).

[6.18] C. Tusche *et al.*, *Phys. Rev. Lett.* **95**, 176101 (2005).

[6.19] H. L. Meyerheim *et al.*, *Phys. Rev. Lett.* **87**, 076102 (2001).

[6.20] Wang, X. Jiang, R. M. Shelby, R. M. Macfarlane, S. S. P. Parkin, S. R. Bank, and J. S. Harris, *Appl. Phys. Lett.* **86,** 052901 (2005).

[6.21] A. Fert and H. Jaffrès, *Phys. Rev. B* **64**, 184420 (2001).

[6.22] B. Min, K. Motohashi, C. Lodder, and R. Jansen, *Nature Materials* **5**, 817 (2006)

[6.23] X. Lou, C. Adelmann, S. A. Crooker, E. S. Garlid, J. Zhang, S. M Reddy, S. D. Flexner, C. J. Palmstrøm, and P. A. Crowell, *Nature Phys*. **3**, 197 (2007).

[6.24] F. J. Jedema, H. B. Heersche, A. T. Filip, J. J. A. Baselmans, and B. J. vanWees ; *Nature* **416**, 713 (2002).

[6.25] J. M. Kikkawa and D. D. Awschalom, *Phys. Rev. Lett*. **80**, 4313 (1998).

**Chapter 7**

**[7.1]** S. P. Dash, D. Goll, H. D. Carstanjen, *Appl. Phys. Lett.* **90**, 132109, (2007).

[7.2] D. R. Loraine, D. I. Pugh, H. Jenniches, R. Kirschman, S. M. Thompson , W. Allen, C. Sirisathikul, and J. F. Gregg, *J. Appl. Phys.* **87**, 5161 (2000).

[7.3] X. Jiang, R. Wang, R. M. Shelby, R. M. Macfarlane, S. R. Bank, J. S. Harris, and S. S. P. Parkin, *Phys. Rev. Lett.* **94**, 056601 (2005).

[7.4] R. Fiederling, M. Keim, G. Reuscher, W. Ossau, G. Schmidt, A. Waag, and L. W. Molenkamp, *Nature* **402**, 787 (1999); Y. Ohno, D. K. Young, B. Beschoten, F. Matsukura, H. Ohno, and D. D. Awschalom, *Nature* **402**, 790-792 (1999); H. Ohno, *Science* **281**, 951 (1998).

[7.5] F. M. Zhang, X. C. Liu, J. Gao, X. S. Wu, and Y. W. Du, H. Zhu, J. Q. Xiao, P. Chen, *Appl. Phys. Lett.* **85**, 786 (2004).

[7.6] M. Bolduc, C. Awo-Affouda, A. Stollenwerk, M. B. Huang, F. G. Ramos, G. Agnello, V. P. LaBella, *Phys. Rev. B* **71** 033302 (2005).

[7.7] H. W. Wu, C. J. Tsai, and L. J. Chen, *Appl. Phys. Lett.* **90**, 043121 (2007).

[7.8] H. Ohno, D. Chiba, F. Matsukura, T. Omiya, E. Abe, T. Dietl, Y. Ohno, and K. Ohtani, *Nature* **408**, 944 (2000); Y. D. Park, A. T. Hanbicki, S. C. Erwin, C. S. Hellberg, J. M. Sullivan, J. E. Mattson, T. F. Ambrose, A. Wilson, G. Spanos, and B. T. Jonker, *Science* **295**, 651 (2002).

[7.9] X. C. Liu, Z. H. Lu, Z. L. Lu, L. Y. Lv, X. S. Wu, F. M. Zhang, and Y. W. Du *J. Appl. Phys.* **100**, 073903 (2006).

[7.10] G. M. Dalpian, A. J. R. da Silva, and A. Fazzio, *Phys. Rev. B* **68**, 113310 (2003); X. Luo, S. B. Zhang, and S. H. Wei, *Phys. Rev. B* **70**, 033308 (2004).

[7.11] A. Wolska, K. Lawniczak-Jablonska, M. Klepka, M. S. Walczak, and A. Misiuk, *Phys. Rev. B* **75**, 113201 (2007); S. Zhou *et al.*, *Phys. Rev. B* **75**, 085203 (2007).

[7.12] T. Dietl, H. Ohno, F. Matsukura, J. Cibert, and D. Ferrand, *Science* **287**, 101 (2000).

[7.13] M. Berciu and R. N. Bhatt, *Phys. Rev. Lett.* **87**, 107203 (2000).

[7.14] O. D. Jayakumar *et al.*, *Nanotechnology* **17**, 1278 (2006); D. P. Norton *et al.*, *Appl. Phys. Lett.* **82**, 239 (2003); N. Theodoropoulou *et al.*, *Phys. Rev. Lett.* **89**, 107203 (2002).

[7.15] K. Graff, Metal impurities in silicon device fabrication, Springer, Berlin, 1995.

[7.16] E. Goering, S. Gold, and A. Bayer, Appl. *Phys. A* **78**, 855 (2004).

[7.17] B. T. Thole, P. Carra, F. Sette, and G. V. Laan, *Phys.Rev.Lett.* **68**, 1943 (1992).

[7.18] P. Gambardella *et al*., *Phys. Rev. B* **75**, 125211 (2007).

[7.19] H. Wu, P. Kratzer, and M. Scheffler, *Phys. Rev. Lett.* **98**, 117202 (2007).

[7.20] M. R. Krause, A. J. Stollenwerk, J. Reed, V. P. LaBella, M. Hortamani, P. Kratzer, and M. Scheffler to be published.

[7.21] Y. Chang and J. L. Erskine, *Phys. Rev. B* **26**, 4766 (1982).

[7.22] H. Reichert, P. J. Eng, H. Dosch, and I. K. Robinson, *Phys. Rev. Lett.* **74**, 2006 (1995).

**Chapter 8 and Chapter 9**

**[8.1]** G. A. Prinz, *Science* **282**, 1660 (1998); S. A. Wolf *et al., Science* **294**, 1488 (2001); D. D. Awschalom and M. E. Flatté, *Nature Phys.* **3**, 153 (2007).

[8.2] D. R. Loraine, D. I. Pugh, H. Jenniches, R. Kirschman, S. M. Thompson , W. Allen, C. Sirisathikul, and J. F. Gregg, *J. Appl. Phys.* **87**, 5161 (2000); Y.Q. Jia, R. C. Shi, and S. Y. Chou, *IEEE Trans. Mag.* **32**, 4707 (1996); S. Hacia, T. Last, S. F. Fischer, and U. Kunze, *J. Phys. D* **37**, 1310 (2004).

[8.3] R. M. Stroud, A. T. Hanbiki, Y. D. Park, G. Kioseoglou, A. G. Petukhov, B. T. Jonker, G. Itskov, and A. Petrou, *Phys. Rev. Lett.* **89**, 166602 (2002)

[8.4] S. P. Dash, D. Goll and H. D. Carstanjen, *Appl. Phys. Lett*. **90**, 132109 (2007).

[8.5] Klaesges *et al.*, *Phys. Rev. B* **56**, 10801 (1997).

[8.6] K. N. Tu, *Appl. Phys. Lett*. **27**, 145 (1975).

[8.7] C. Humphreys, *Nature* **341**, 689 (1989); M. Copel, M. C. Reuter, E. Kaxiras and R.M. Tromp, *Phys. Rev. Lett*. **63**, 632 (1989).

[8.8] X. Jiang, R. Wang, R. M. Shelby, R. M. Macfarlane, S. R. Bank, J. S. Harris, and S. S. P. Parkin, *Phys. Rev. Lett*. **94**, 056601 (2005); S. S. P. Parkin *et al*., *Nature Materials*. **3**, 862 (2004). Yuasa *et al., Nature materials,* **3**, 868 (2004).

[8.9] F. J. Jedema, H. B. Heersche, A. T. Filip, J. J. A. Baselmans, and B. J. vanWees, *Nature* **416**, 713 (2002); F. J. Jedema, A. T. Filip, and B. J. van Wees, *Nature* **410**, 345 (2001).

[8.10] R. Fiederling, M. Keim, G. Reuscher, W. Ossau, G. Schmidt, A. Waag, and L. W. Molenkamp, *Nature* **402**, 787 (1999); Y. Ohno, D. K. Young, B. Beschoten, F. Matsukura, H. Ohno, and D. D. Awschalom, *Nature* **402**, 790 (1999).

# Acknowledgement

A journey is easier when you travel together. This thesis is the result of three years of work whereby I have been accompanied and supported by many people. It is a pleasant aspect that I have now the opportunity to express my gratitude to all of them.

- My deepest gratitude goes to my promoter ***Prof. Dr. H. D. Carstanjen***, who has given me this unique opportunity to carry out this research work in the Max-Planck-Institut für Metallforschung. In spite of his busy schedule, he always found adequate time to supervise me during experiments. He encourages independent thinking and gave me the freedom to try out new things. I have immensely benefited from his in-depth experimental knowledge, stimulating discussions, valuable inputs and continuous encouragement. His enthusiasm and integral view on research and his mission for providing 'only high-quality work and not less', has made a deep impression on me.
- I am greatly indebted to ***Prof. Dr. G. Denninger*** and ***Prof. Dr. G. Mahler*** for agreeing to be the referees of my thesis.
- I am greatly indebted to ***Dr. Dagmar Goll*** for being such a wonderful advisor. I thank her for her invaluable guidance, support, discussions and critical evaluation at each and every stage of my progress.
- I am greatly indebted to ***Prof. G. Schütz*** for her valuable discussions, encouragement, her interest in my research work and providing me modern experimental facilities for carrying out such research.
- I wish to express my profound gratitude to ***Dr. Á. Szokefalvi-Nagy*** and ***Dipl. Ing. M. Bechtel*** for their help during the HRBS experiments.
- I wish to express my profound gratitude to ***Dr. E. Göring, Mr. Thomas Tietze*** and ***Mr. E. Amaladass*** for their interest in my research and the XMCD measurements.
- I would like to thank ***Dr. F. Phillipp*** and ***Mr. P. Kopold*** for HR-TEM measurements on the MgO tunnel barriers.
- I would like to thank my friend ***Dr. P. K. Sahoo*** for preparing Mn implanted Si samples for my research at very short notice.
- I would like to thank ***Prof. E. Kasper*** and ***Dr. M. Oehme*** of the Institute of Semiconductor Engineering at the University of Stuttgart for preparing epitaxial $n^+$-Si layer.

- My many thanks to all the colleagues of both the Max-Planck Institutes for their assistance during my research and hearty thanks to my friends who made my stay at Stuttgart pleasant and enjoyable.
- I feel a deep sense of gratitude for my mother, ***Smt. Sulochana Dash*** and father, ***Prof. Dr. Jagannath Prasad Dash*** who formed part of my vision and taught me the good things that really matter in life. I am grateful for my sisters ***Ratnamanjari Dash*** *and* ***Snehamanjari Dash***, and brother ***Biswamohan, and my brother-in-laws Dr. S. N. Dash and Engg. M. Rath*** for rendering me the sense and the value of brotherhood. *I am very grateful towards my beloved wife* ***Alaka Tripathy*** *for her love and patience during the Ph.D. period, and helping me in finalizing the thesis. At last I would like to thank all of my family members and relatives who have always encouraged me to achieve my goal.*

# Curriculum Vitae

| | |
|---|---|
| Name | Saroj Prasad Dash |
| Date and Place of Birth | 26.05.1975, Kendrapara (Orissa, India) |
| Nationality | Indian |
| 2004 – 2007 | **Ph.D.** at the Max-Planck-Institut für Metallforschung, Stuttgart, Germany<br>Title: "*Towards Spin Injection into Silicon*". |
| 2003 – 2004 | Project Associate, Indian Institute of Technology (IIT), Delhi, India<br>"Improvement of electrical properties of Si-$SiO_2$ interface in metal-oxide-Si structure by back surface $Ar^+$ ion implantation" and "NiTi thin film for MEMS devices" |
| 2001 – 2003 | **Master of Technology (M.Tech.) in Solid State Materials**,<br>Indian Institute of Technology (IIT), Delhi, India<br>Thesis Title: "Exploring the possibility of tailoring the lattice parameter of Si by $Ar^+$ ion implantation". |
| 1999 – 2001 | Project Assistant, Institute of Physics, India. |
| 1995 – 1998 | **M. Sc. (Physics)**, Utkal University, India<br>Specialization: Electronics |
| 1994 – 1997 | **B. Sc. (Physics)**, Utkal University, India. |
| 1992 – 1994 | **10+2 Science** (Physics, Mathematics, Chemistry, Biology), C.H.S.E., Orissa, India. |

# Part of this work has been published or will be published

## Publications

- **S. P. Dash**, D. Goll, and H. D. Carstanjen, Subsurface enrichment of Co in Si (100) at room temperature, *Appl. Phys. Lett.* **90**, 132109 (2007).
- **S. P. Dash**, D. Goll, and H. D. Carstanjen, Near-surface compositional oscillations of Co in Si (100) at low temperature, to be submitted.
- **S. P. Dash**, D. Goll, T. Tietze, E. Göring, P. K. Sahoo, and H. D. Carstanjen, Ferromagnetism in Mn doped Si, to be submitted.
- **S. P. Dash**, D. Goll, and H. D. Carstanjen, Improvement of Co/S(100) interface by surfactant mediated growth, manuscript in preparation.
- **S. P. Dash**, D. Goll, and H. D. Carstanjen, MgO tunnel barriers on Si (100) for spin injection, manuscript in preparation.
- **S. P. Dash**, D. Goll, and H. D. Carstanjen, Initial stages of growth of Fe on Si (100) at room temperature, manuscript in preparation.

## Conference contributions

- **S. P. Dash**, D. Goll, Á. Szokefalvi-Nagy, and H. D. Carstanjen, Co-Si interfaces for spin injection into Si, Poster presentation at Spintronics summer school, Wittenberg, Germany, 2004.
- **S. P. Dash**, Initial stages of growth of Co on Si (100), *Oral presentation* at Deutsche Physikalische Gesellschaft spring meeting and European condensed matter conference, Dresden, 2005.
- **S. P. Dash**, D. Goll, T. Tietze, E. Göring, E. Amaladass, and H. D. Carstanjen, Making Si a ferromagnet, Poster presentation at Spin transport work shop, Bad Honnef, Germany, 2007.